First-Row Transition Metal Complexes of Dipyrrinato Ligands: Synthesis and Characterization

HARVARD UNIVERSITY
Graduate School of Arts and Sciences

DISSERTATION ACCEPTANCE CERTIFICATE

The undersigned, appointed by the

Department of Chemistry & Chemical Biology

have examined a dissertation entitled:

First-Row Transition Metal Complexes of Dipyrrinato Ligands: Synthesis and Characterization

presented by : Austin B. Scharf

candidate for the degree of Doctor of Philosophy and hereby certify that it is worthy of acceptance.

Signature _____

Typed name: Professor Theodore Betley

Signature _____

Typed name: Professor Eric Jacobsen

Signature _____

Typed name: Professor Cynthia Friend

Date: 21 June 2013

First-Row Transition Metal Complexes of Dipyrrinato Ligands: Synthesis and Characterization

A dissertation presented

by

Austin B. Scharf

to

The Department of Chemistry and Chemical Biology

in partial fulfillment of the requirements
for the degree of
Doctor of Philosophy
in the subject of
Chemistry

Harvard University

Cambridge, Massachusetts

June 2013

Dissertation Adviser: Professor Theodore A. Betley Austin B. Scharf

First-Row Transition Metal Complexes of Dipyrrinato Ligands: Synthesis and Characterization

Abstract

A library of variously-substituted dipyrrins and their first-row transition metal (Mn, Fe, Cu, Zn) complexes have been synthesized, and the effects of peripheral substituents on the spectroscopic, electrochemical, and structural properties of both the free-base dipyrrins and their metal complexes has been explored. The optical and electrochemical properties of the free dipyrrins follow systematic trends; with the introduction of electron-withdrawing substituents in the 2-, 3-, 5-, 7-, and 8-positions of the dipyrrin, bathochromic shifts in the absorption spectra are observed, oxidation becomes more difficult, and reduction becomes more facile. Similar effects are seen for iron(II) dipyrrinato complexes, where peripheral substitution of the dipyrrinato ligand induces red-shifts in the absorption spectra and increases the oxidation potential of the bound iron. Steric interactions between the peripheral halogens and the 5-substituent of the dipyrrinato ligand can induce distortion of the ligand from planarity, resulting in widely varying ^{57}Fe Mössbauer quadrupole splitting ($|\Delta E_Q|$) parameters.

The coordination number and geometry of metal atoms bound to widely-varied dipyrrinato ligands was analyzed by X-ray crystallography. Sterically encumbered substituents in the ligand 1- and 9-positions allowed the isolation of several three-coordinate species, including dipyrrinato complexes of Fe(II), Cu(I), and Cu(II). Less sterically demanding 1- and 9-substituents, such as mesityl, adamant-1-yl, and *tert*-butyl generally favored the formation of four-coordinate structures. Five-coordinate complexes could be crystallographically

characterized with weakly coordinating anionic donor ligands (e.g. triflate). Each of these coordination numbers was analyzed by the angular overlap model to generate electronic configuration diagrams.

A series of free-base dipyrrin and metal dipyrrinato complexes bearing the 1- and 9-substituent Q (Q = 2′,4′,6′-$Ph_3C_6H_2$) were synthesized, and their luminescence spectra were obtained. This series included highly luminescent Zn(II) and Li(I) dipyrrinato complexes (Φ_F = 0.67 and 0.51, respectively), the first appreciably luminescent dipyrrinato complexes of paramagnetic metals (Φ_F = 0.015 to 0.03), and the first molecular species containing Mn(II) to phosphoresce at room temperature (Φ_P = 0.015).

Table of Contents

to my students

Acknowledgements

My career in chemistry began at Bethany Christian High School, under the tutelage of Mike Goertzen, who taught me the wonders of stoichiometry with a very odd rap, and continued through my undergraduate career at the University of Richmond, then as I worked as a synthetic organic chemist at Pfizer, and finally during my graduate studies at Harvard University.

I owe many thanks to my chemistry professors and colleagues at the University of Richmond, where I spent way too much time in Gottwald Science Center. Professor John T. Gupton, my undergraduate research advisor, and Dr. Edie Banner, then a post-doc in his lab, were excellent mentors as they guided my synthesis of Rigidin E and taught me the ins and outs of working in a synthetic organic chemistry lab. To this day, they are the only reason I know what a Curtius Rearrangement is. They also spoiled me with a Biotage automated chromatography system, which would haunt me throughout my "poor" years at Harvard. Professors Bill Myers, Michael Leopold, and Carol Parish taught me that high expectations and high praise lead to a productive education – even if I've now forgotten many of the topics from their classes. John Solano, Laura Barrosse-Antle, Katie Watkins, and Sarah Remmert were my closest compatriots in the Gottwald Center, and they taught me nearly as much as the entire chemistry faculty.

My colleagues at Pfizer taught me more about adult life than they did about chemistry – though they taught me an awful lot about that, too – and my heartfelt thanks go to them. In particular, Dr. Ted W. Johnson and Guy McClellan took me under their wings from my first day as the youngest member of the Drug Discovery team in June of 2006. Their expertise and friendship showed me that a career in chemistry could be both challenging and rewarding. Dr. Steve Tanis taught me as much about organic chemistry – and good beer – as any professor I've

ever had. Wendy Taylor, Dave Alexander, Stephanie Scales, and the late Justin Kroupa helped me bridge the gap between work and play, and taught me that even a very productive life should involve a hefty amount of fun.

At Harvard, I have countless people to thank. I owe many thanks to Ted Betley, who recognized my passion for teaching and encouraged me to pursue it, even when it hampered my research. Thanks also to Jim Anderson, Alan Saghatelian, Gregg Tucci, and (especially) Ryan Spoering, whose teaching and mentorship reminded me that my passion for teaching was worth pursuing. I couldn't have made it through these five years without Graham, Tamara, and Libby, my classmates and dear friends, who kept me sane and kept a smile on my face – most of the time, anyway – through the successes and failures that every graduate student faces. The friendship and support of my other labmates, especially Alison and Matt, were fantastic.

In terms of the actual *science* of this dissertation, my labmates and colleagues in the chemistry department have been invaluable. In particular, Evan and Graham guided me through every step of DFT calculations; Alison, Graham, and Shao were my tutors and mentors for X-ray crystallography; László helped me figure out how the spectrofluorimeter works; and my other labmates have all provided valuable insights and suggestions as my projects waxed and waned. Libby Hennessy (ETH), Evan King (ERK), Graham Sazama (GTS), Guy Edouard (GAE), Matt Taylor (MJTW), Diana Iovan (DAI), and Art Bartolozzi (ARB) provided me with compounds to analyze or use in my own projects; I have tried to acknowledge each of those instances with their initials throughout the text. Thanks are also due to Professor Xiaowei Zhuang for the generous use of her spectrofluorimeter, and Dr. Yu-Shen Cheng at ChemMatCARS, APS, for his assistance with single crystal data obtained there, and Dr. Zvi Blank at Complete Analysis

Laboratories for putting up with huge shipments of air-sensitive materials for elemental analysis and only rarely being grumpy about it.

Of course, my family and friends have been extraordinarily supportive, and I thank them all for bearing with me while I complained about faulty fluorimeters, shoddy spectrometers, stubborn syntheses, and distressing diffractometers, among many other things they knew almost nothing about.

But above all, I thank my students, for whom I came to grad school, and for whom I finish it. They kept me smiling throughout these five years, kept me learning, and kept me motivated to power through. Their "*aha!*" moments and heartfelt curiosity about the workings of the world, and especially chemistry, are the sparks that feed my passion for education, and what will continue to inspire me to teach.

List of Schemes

Chapter 2

Chapter 3

Chapter 4

List of Figures

Chapter 1

Chapter 2

Chapter 3

Chapter 4

Chapter 5

List of Tables

Chapter 2

Chapter 3

Chapter 4

Chapter 5

List of Chemical Abbreviations, Acronyms, Symbols, and Units

Å	**Å**ngstrom (10^{-10} m)
A or Amp	**amp**ere
A or Abs	**abs**orbance
acac	**ac**etyl**ac**etonate ($C_5H_7O_2^-$)
Ad	**ad**amant-1-yl
Anal.	elemental **anal**ysis
APS	**A**dvanced **P**hoton **S**ource at Argonne National Lab
Ar	**ar**yl
BFP	3′,5′-**b**is(tri**f**luoromethyl)**p**henyl [3′,5′-$(CF_3)_2C_6H_3$)]
BODIPY	**bo**ron difluoride **dipy**rrinato complex
br.	**br**oad (in reference to spectral peak shape)
^{13}C	**c**arbon-**13**
calc'd	**calc**ulate**d**
CCD	**c**harge-**c**oupled **d**evice
cm^{-1}	wavenumbers; inverse **c**enti**m**eters
Cp	**c**yclo**p**entadienyl ($C_5H_5^-$)
CSA	**c**amphor **s**ulfonic **a**cid
CV	**c**yclic **v**oltammetry or **c**yclic **v**oltammogram
δ	NMR chemical shift (ppm), or Mössbauer isomer shift ($^{mm}/_{s}$)
d	doublet in NMR
D or *d*	**d**euterium
D	integrated area under a luminescence emission curve
DCE	1,2-**d**i**c**hloro**e**thane
DCM	**di**chloro**m**ethane
DCP	2′,6′-**di**chloro**p**henyl (2′,6′-$Cl_2C_6H_3$)
dd	doublet of doublets in NMR
DDQ	2,3-**d**ichloro-5,6-**d**icyano-benzo**q**uinone
ΔE_Q	Mössbauer nuclear quadrupole splitting
DFT	**d**ensity **f**unctional **t**heory
DMF	**di****m**ethyl **f**ormamide
dpma	**di****p**yrro**m**eth**a**ne
e	**e**lementary charge, 1.602×10^{-19} coulombs
ε	**e**psilon; molar **e**xtinction coefficient
η^n	eta, **h**apticity; the number, n, of contiguous atoms of a ligand bound to a metal
E	electrochemical potential, voltage
$E_{½}$	half-wave potential
E_{pa}	**a**nodic **p**eak potential
E_{pc}	**c**athodic **p**eak potential

equiv.	molar **equiv**alents
ESI	**e**lectro-**s**pray **i**onization
Et	**et**hyl
Φ	quantum yield
Φ_F	quantum yield of **f**luorescence
Φ_P	quantum yield of **p**hosphorescence
Fc	**f**erro**c**ene [$(C_5H_5)_2Fe^{II}$]
Fc^+	**f**erro**c**enium [$(C_5H_5)_2Fe^{III}]^+$
h	**h**ours
^1H	proton (**h**ydrogen-**1**)
HMDS	**h**exa**m**ethyl **d**i**s**ilazide
HOMO	**h**ighest **o**ccupied **m**olecular **o**rbital
I	electrical current
I	**i**ntensity of incident light
IR	**i**nfra**r**ed (spectroscopy)
IUPAC	**I**nternational **U**nion of **P**ure and **A**pplied **C**hemistry
J	coupling constant in NMR
K	**k**elvin
λ	**l**ambda; wave**l**ength
λ_{max}	wavelength of **max**imum absorption or emission
L	neutral, **L**-type, dative ligand
LC	**l**iquid **c**hromatography
LUMO	**l**owest **u**noccupied **m**olecular **o**rbital
m	**m**ultiplet in NMR
m-	***m****eta*, denoting a 1,3-relationship on a benzene ring
M	**m**olar (moles per liter)
Me	**me**thyl
Mes	**mes**ityl, 2′,4′,6′-trimethylphenyl (2′,4′,6′-$(CH_3)C_6H_2$)
min	**min**utes
mol	**mol**es
m*M*	**m**illi**m**olar (millimoles per liter)
mmol	**m**illi**mol**es
MS	**m**ass **s**pectrometry
ν	**n**u; frequency
n	refractive index
nb	**n**on-**b**onding
NBS	**N**-**b**romo**s**uccinimide
*n*Bu	**n**ormal (linear) **bu**tyl ($-CH_2CH_2CH_2CH_3$)
NCS	**N**-**c**hloro**s**uccinimide
NIR	**n**ear-**i**nfra**r**ed

NIS	**N-i**odo**s**uccinimide
nm	**n**ano**m**eter (10^{-9} m)
NMR	**n**uclear **m**agnetic **r**esonance
o-	***o****rtho*, denoting a 1,2-relationship on a benzene ring
OAc	**ac**etate
OTf	**t**ri**f**late (trifluoromethane sulfonate)
p-	***p****ara*, denoting a 1,4-relationship on a benzene ring
Ph	**ph**enyl
PMT	**p**hoto**m**ultiplier **t**ube
ppm	**p**arts **p**er **m**illion
PPTS	**p**yridinium ***p****ara*-**t**oluene **s**ulfonate
py	**py**ridine
q	**q**uartet in NMR
Q	2′,4′,6′-triphenylphenyl (**q**uadraphenyl)
Q	nuclear **q**uadrupole moment
R	generic organic group
s	**s**inglet in NMR
s or sec	**sec**onds
S	molecular **s**pin quantum number (Σm_s)
S_n	**s**inglet electronic state ($n = 0$: ground state; $n > 0$: excited states)
spt	**se****pt**et in NMR
t	**t**riplet in NMR
T	**t**emperature
*t*Bu	**t**ertiary **bu**tyl ($-C(CH_3)_3$)
td	**t**riplet of **d**oublets in NMR
THF	**t**etra**h**ydro**f**uran
TMS	**t**ri**m**ethyl**s**ilyl ($-Si(CH_3)_3$)
T_n	**t**riplet electronic state
TOF	**t**ime-**o**f-**f**light
UV	**u**ltra**v**iolet
Vis	**vis**ible
VSEPR	**V**alence **S**hell **E**lectron **P**air **R**epulsion Theory
wrt	**w**ith **r**espect **t**o
X	halide (chloride, bromide, or iodide)

Chapter 1: Electronic and Geometric Structures of Oligopyrrole Complexes

1.1 Introduction

The biological chemistry of oligopyrroles and their metal complexes is truly vast. Pyrroles and their derivatives play key roles in the biological functioning of virtually all organisms on Earth, from archaea[1] to humans. They are key chemical players in photosynthesis,[2] metabolism,[3] oxygen transport, and a host of other processes.[4] The unique electronic and structural characteristics of these oligopyrroles and their complexes endow them with a wide range of functions and properties.

The three most common functions of pyrrole-based cofactors in biology are as pigments,[5] as ligand architectures for the support of transition metals,[6] and as mediators or participants in redox chemistry.[7] Oligopyrroles in biological systems are typically highly conjugated molecules, allowing them to absorb light in the visible region of the electromagnetic spectrum. This is one of their key purposes in photosynthetic organisms, where the light-harvesting chromophores in chloroplasts are chlorophylls, highly-decorated tetrapyrrole macrocycles supporting a dicationic magnesium atom (Figure 1.1).[8] A variety of other metals can be supported by oligopyrrole

---

1 Jahn, D.; Verkamp, E.; Soll, D. *Trends Biochem. Sci.* **1992**, *17*, 215.

2 (a) Concepcion, J. J.; House, R. L.; Papanikolas, J. M.; Meyer, T. J. *Proc. Natl. Acad. Sci. U.S.A.* **2012**, *109*, 15560. (b) Cook, S. A.; Borovik, A. S. *Nat. Chem.* **2013**, *5*, 259. (c) Cox, N.; Pantazis, D. A.; Neese, F.; Lubitz, W. *Acc. Chem. Res.*, ahead of print. (d) Sartorel, A.; Bonchio, M.; Campagna, S.; Scandola, F. *Chem. Soc. Rev.* **2013**, *42*, 2262. (e) Scheer, H. *Adv. Photosynth. Respir.* **2006**, *25*, 1.

3 Carlsen, C. U.; Moller, J. K. S.; Skibsted, L. H. *Coord. Chem. Rev.* **2005**, *249*, 485.

4 Li, Zhang, ed. Heme Biology: The Secret Life of Heme in Regulating Diverse Biological Processes. World Scientific Publishing: Singapore, 2011.

5 Maitland, P. Quarterly Reviews, Chemical Society **1950**, 4, 45.

6 Murakami, Y. et al. Transition Metal Complexes of Pyrrole Pigments, I-XIX. Various publications, 1968-1981.

7 Bellelli, A.; Brunori, M.; Brzezinski, P.; Wilson, M. T. *Methods (San Diego, CA, U. S.)* **2001**, *24*, 139.

8 Wu, S. M.; Rebeiz, C. A. *J. Biol. Chem.* **1985**, *260*, 3632.

macrocycles, including cobalt, which is supported by a large corrin-based ligand platform in methylcobalamin, also known as Vitamin B12.[9] Iron is bound by a porphyrin in the heme proteins,[4] which regulate oxygen transport (hemoglobin and myoglobin, among others) and carry out oxidative metabolism (the cytochrome family). In heme proteins, the oligopyrrole ligand is often implicated in the redox catalysis performed by the proteins, such as serving as an electron reservoir in the catalytic cycle of Cytochrome P450.[10]

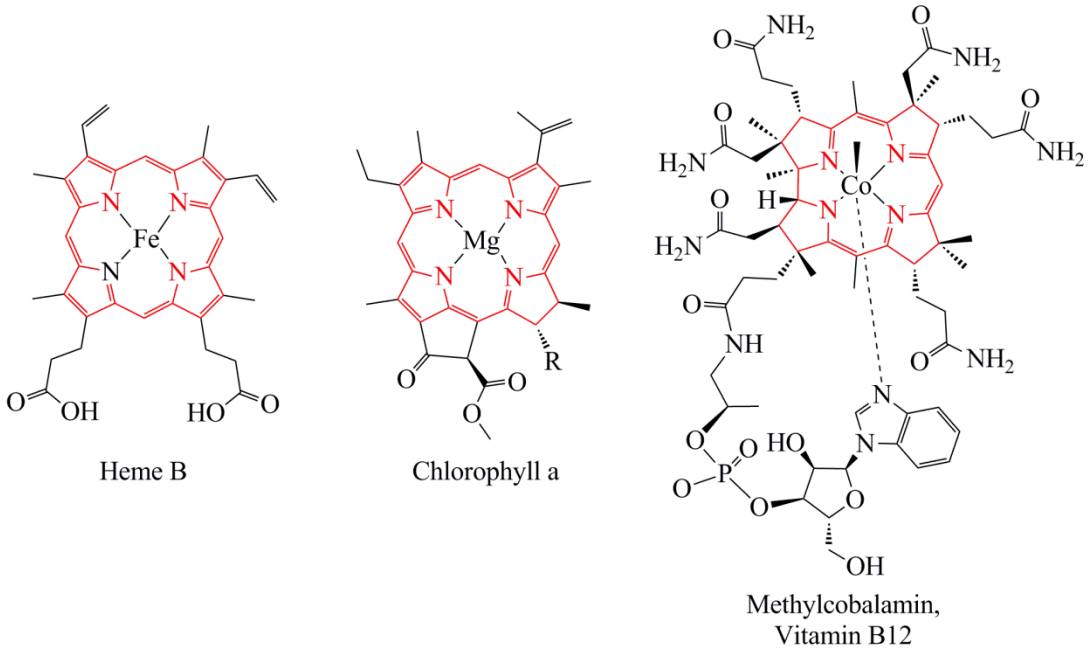

Figure 1.1. Biological molecules featuring oligopyrroles with bound metals; portions in red are the oligopyrroles.

In order to better understand the chemistry of oligopyrroles and their metal complexes, researchers have synthesized a host of oligopyrroles. In some cases this is to better understand the biological functions of these systems, in other cases they are synthesized for their utility as

[9] (a) Rossi, M.; Glusker, J. P.; Randaccio, L.; Summers, M. F.; Toscano, P. J.; Marzilli, L. G. *J. Am. Chem. Soc.* **1985**, *107*, 1729. (b) Randaccio, L.; Furlan, M.; Geremia, S.; Slouf, M.; Srnova, I.; Toffoli, D. *Inorg. Chem.* **2000**, *39*, 3403.

[10] Ortiz de Montealllano, P. R., Ed.; *Cytochrome P450: Structure, Mechanism, and Biochemistry*; 4 ed.; Kluwer Academic/Plenum Publishers: New York, 2005.

pigments or dyes,[11] catalysts or co-catalysts,[12] or building-blocks for three-dimensional supramolecular architectures,[13] among other applications. Some of the most commonly synthesized are the porphyrins, fully conjugated tetrapyrrole macrocycles connected by methine linkages (Figure 1.2). Their tetrapyrrolic cousins, the chlorins, bacteriochlorins, and isobacteriochlorins, differ from porphyrins in the degree of conjugation in the macrocyclic π-systems. All of these systems can be synthesized by the polycondensation of pyrrole with aldehydes;[14] most of these syntheses are poor-yielding and require rigorous chromatographic purification.

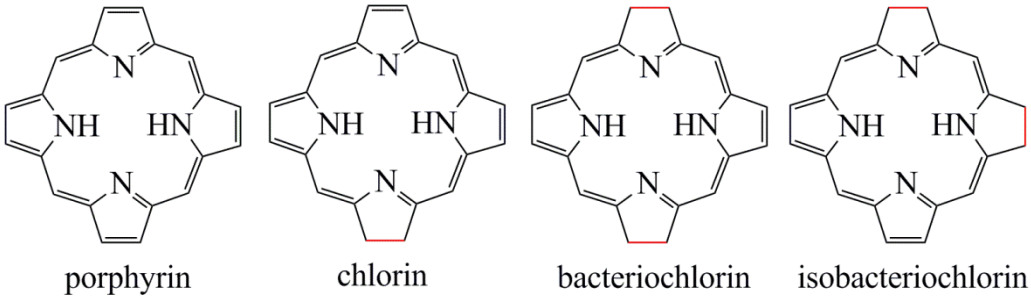

Figure 1.2. Members of the porphyrin family of tetrapyrrole macrocycles; red bonds indicate sites of saturation relative to the parent porphyrin.

Other tetrapyrrole macrocycles are commonly encountered in biology, such as corroles and corrins (Figure 1.3),[15] though they are less frequently synthesized in the lab. Some tetrapyrrole macrocycles, such as the non-conjugated porphyrinogens[16] and the N-substituted

[11] Senge, M. O. *Nachr. Chem.* **2004**, *52*, 273, and references therein.
[12] Kadish, K. M.; Smith, K. M.; Guilard, R., Eds.; *The Porphyrin Handbook*; Academic Press: New York, 2003; Vol. 1-20.
[13] (a) Maeda, H. *Eur. J. Org. Chem.* **2007**, 5313. (b) Nabeshima, T.; Akine, S.; Ikeda, C.; Yamamura, M. *Chem. Lett.* **2010**, *39*, 10.
[14] (a) Rothemund, P. *J. Am. Chem. Soc.* **1935**, *57*, 2010. (b) Rothemund, P. *J. Am. Chem. Soc.* **1936**, *58*, 625. (c) Petit, A.; Loupy, A.; Maiuardb, P.; Momenteaub, M. *Syn. Comm.* **1992**, *22*, 1137. (d) Pereira, M. M.; Monteiro, C. J. P.; Peixoto, A. F. *Targets Heterocycl. Syst.* **2008**, *12*, 258.
[15] Melent'eva, T. A. *Russ. Chem. Rev.* **1983**, *52*, 641.
[16] (a) Kraeutler, B. *Chimia* **1987**, *41*, 277. (b) Floriani, C. *Chem. Commun. (Cambridge, U.K.)* **1996**, 1257. (c) Gale, P. A.; Anzenbacher, P., Jr.; Sessler, J. L. *Coord. Chem. Rev.* **2001**, *222*, 57.

porphyrazines,[17] are not found in biological systems, but are nevertheless important as ligands in transition-metal mediated reactions and as molecular dyes.

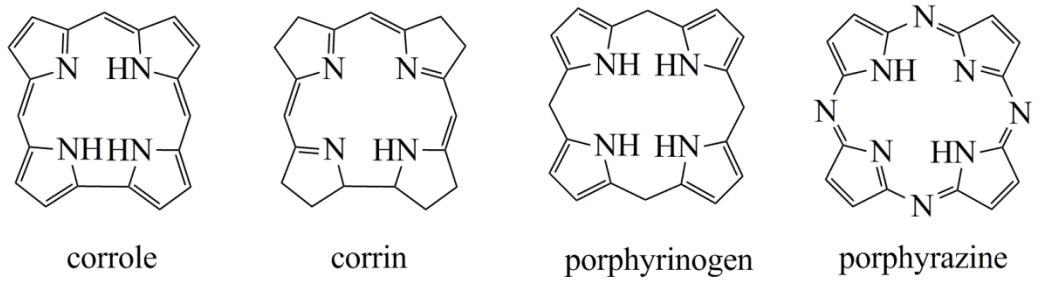

Figure 1.3. Various tetrapyrrole macrocycles.

In addition to tetrapyrrole macrocycles, a variety of other macrocyclic oligopyrroles are also known, including the tripyrrolic subporphyrins,[18] pentapyrrolic sapphyrins,[19] and hexapyrrolic hexaphyrins[20] (Figure 1.4). These porphyrin analogs can be synthesized by similar routes as porphyrins, and are often found as some of the byproducts in porphyrin syntheses.

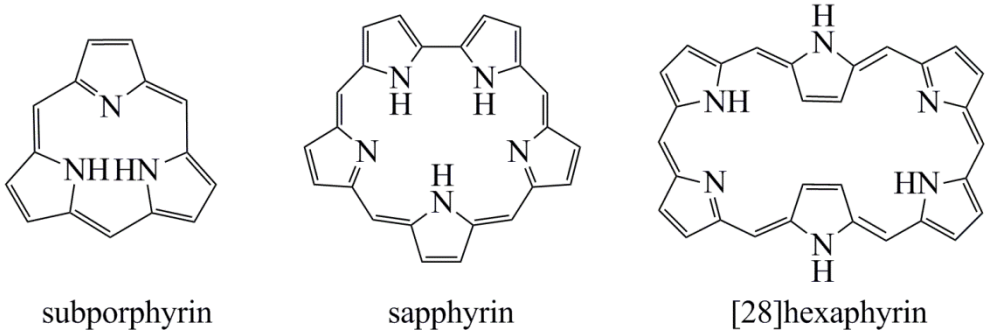

Figure 1.4. Contracted and expanded porphyrin analogs.

[17] (a) Rodriguez-Morgade, M. S.; Stuzhin, P. A. *J. Porphyrins Phthalocyanines* **2004**, *8*, 1129. (b) Fuchter, M. J.; Zhong, C.; Zong, H.; Hoffman, B. M.; Barrett, A. G. M. *Aust. J. Chem.* **2008**, *61*, 235. (c) Lukyanets, E. A.; Nemykin, V. N. *J. Porphyrins Phthalocyanines* **2010**, *14*, 1.

[18] (a) Torres, T. *Angew. Chem., Int. Ed.* **2006**, *45*, 2834. (b) Inokuma, Y.; Osuka, A. *Dalton Trans.* **2008**, 2517. (c) Osuka, A.; Tsurumaki, E.; Tanaka, T. *Bull. Chem. Soc. Jpn.* **2011**, *84*, 679.

[19] (a) Sessler, J. L.; Cyr, M. J.; Burrell, A. K. *Synlett* **1991**, 127. (b) Sessler, J. L.; Davis, J. M. *Acc. Chem. Res.* **2001**, *34*, 989. (c) Pareek, Y.; Ravikanth, M.; Chandrashekar, T. K. *Acc. Chem. Res.* **2012**, *45*, 1801.

[20] Misra, R.; Chandrashekar, T. K. *Acc. Chem. Res.* **2008**, *41*, 265, and references therein.

Several types of acyclic oligopyrroles have also been studied,[21] largely in the context of the biological metabolism of porphyrins and their macrocyclic cousins, but also as pigments, ligand platforms for metal complexes, conductive organic materials, building blocks for macrocyclic oligopyrroles, and as monomers for the synthesis of supramolecular architectures.

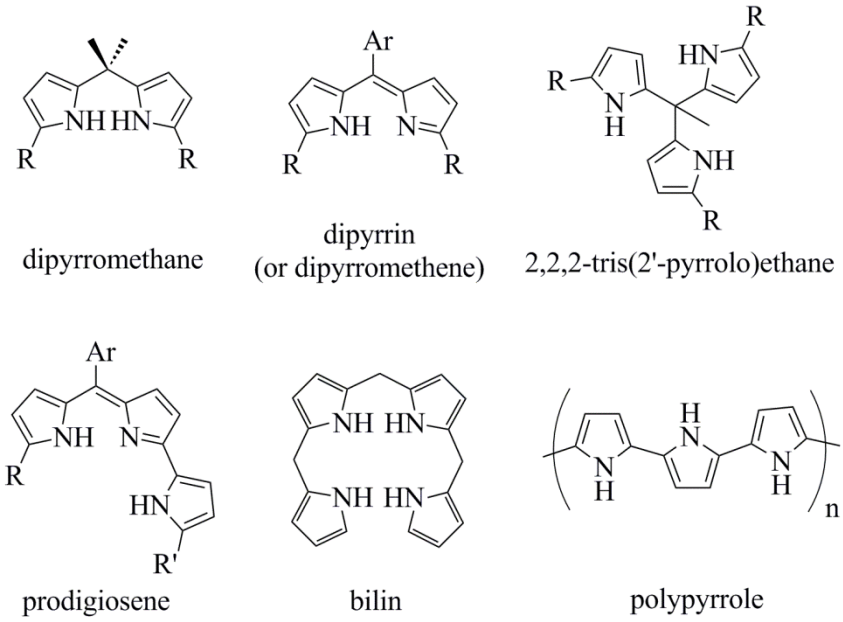

Figure 1.5. Examples of synthetically accessible acyclic oligopyrroles.

These acyclic systems are generally easier to synthesize than their macrocyclic relatives, while still maintaining many of their desirable properties: the ability to bind metals, highly absorptive conjugated π-systems, and potential for redox-activity.

In the cases of all these oligopyrroles, variations in substitution patterns on the periphery of the pyrrole framework allows significant modification of the properties of the compounds and

[21] (a) King, E. R.; Betley, T. A. *J. Am. Chem. Soc.* **2009**, *131*, 14374. (b) Lindsey, J. S. *Acc. Chem. Res.* **2010**, *43*, 300. (c) Sazama, G. T.; Betley, T. A. *Inorg. Chem.* **2010**, *49*, 2512. (d) Sazama, G. T.; Betley, T. A. *Organometallics* **2011**, *30*, 4315. (d) Thompson, A.; Bennett, S.; Gillis, H. M.; Wood, T. E. *J. Porphyrins Phthalocyanines* **2008**, *12*, 918. (e) Mizutani, T.; Yagi, S. *J. Porphyrins Phthalocyanines* **2004**, *8*, 226. (f) Rockwell, N. C.; Lagarias, J. C. *ChemPhysChem* **2010**, *11*, 1172. (g) Inomata, K. *Heterocycles* **2012**, *85*, 2879. (h) Li, X.; Malardier-Jugroot, C. *Macromolecules* **2013**, *46*, 2258.

their metal complexes. A detailed understanding of these substituent effects in oligopyrrole species, and in particular of dipyrrins, is the aim of this dissertation.

1.2 Systematic Variations in the Properties of Oligopyrroles and their Metal Complexes

In order to modulate the photophysical properties and reactivity of oligopyrrolic systems, nature has employed a number of strategies.[12] Among these are (1) chelation to various metals, (2) functionalization directly on the pyrrole, and (3) functionalization at carbons between pyrrole units (referred to as *meso* positions). These variations have effects on the geometric structure, electronic structure, and reactivity of oligopyrrole complexes. Our attention in this section will focus on those oligopyrroles linked by methine (=C–) bridges, as these are the most relevant to the dipyrrins discussed in the body of this dissertation. These are the porphyrins, chlorins, corrins, corroles, subporphyrins, sapphyrins, and hexaphyrins, though some of these classes of compounds are much less studied than others.

1.2.1 Variations in Geometric Structure

Most oligopyrroles, especially macrocyclic ones, are essentially planar, which maintains a conjugated system between pyrrole subunits. Deviations from planarity can be engendered by a number of factors. Subporphyrins, due to the ring-strain inherent in the contracted macrocycle, are significantly domed,[18] and exist exclusively as their boron chelates; these molecules have been studied as intermediates between planar and spherical aromaticity.[22] The planarity of some porphyrins is diminished by coordination to metals; low-valent Ti(II) porphyrins are known to be slightly domed[23] and heavy-metal porphyrinates are also frequently domed slightly, since the

[22] Chen, Z.; King, R. B. *Chem. Rev.* **2005**, *105*, 3613.
[23] Woo, L. K.; Hays, J. A.; Jacobson, R. A.; Day, C. L. *Organometallics* **1991**, *10*, 2102.

large metal ion cannot easily fit in the planar binding pocket of the porphyrin ligand;[24] these deviations from planarity are associated with the lower stability and higher reactivity of these non-planar oligopyrroles.[12] Even larger deviations from the planarity of porphyrins and corroles are brought about by steric interactions on the periphery of the macrocycles. Though β-octaalkyl porphyrins and corroles generally remain near planarity, those bearing larger substituents in the β or *meso* positions can undergo saddling or ruffling distortions. For instance, β-octabromoporphyrins are generally ruffled, especially in cases where the *meso*-substituents also bear bulky groups in their *ortho* positions.[25] The degree of ruffling or saddling in these molecules is often quantitatively measured by the angle χ,[26] which is the dihedral angle between two Cα–Cβ bonds linked by a methine group (Figure 1.6). Other types of distortions are measured by other geometric parameters; for instance, doming is typically measured by the distance between the N4 mean plane and the porphyrin mean plane.

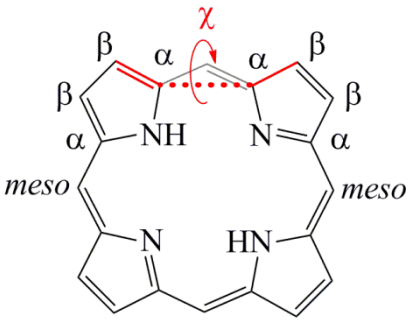

Figure 1.6. Illustration of the dihedral angle χ on a porphyrin, as well as the conventional nomenclature of the α, β, and *meso*- positions.

[24] Lemon, C. M.; Brothers, P. J.; Boitrel, B. *Dalton Trans.* **2011**, *40*, 6591.
[25] Mandon, D.; Ochsenbein, P.; Fischer, J.; Weiss, R.; Jayaraj, K.; Austin, R. N.; Gold, A.; White, P. S.; Brigaud, O.; Battioni, P.; Mansuy, D. *Inorg. Chem.* **1992**, *31*, 2044.
[26] Cullen, D. L.; Desai, L. V.; Shelnutt, J. A.; Zimmer, M. *Struct. Chem.* **2001**, *12*, 127.

1.2.2 Variations in Absorption

One of the most notable properties of oligopyrrole systems is their ability to absorb light in the visible region of the electromagnetic spectrum. In all conjugated oligopyrroles and their metal complexes, the primary absorption occurs in the visible region of the spectrum and is due to $\pi \rightarrow \pi^*$ excitation from the singlet ground state to the second singlet excited state ($S_0 \rightarrow S_2$); this absorption is referred to in porphyrins as the Soret band, and that terminology is also frequently used in analogous systems.[12] A second $\pi \rightarrow \pi^*$ excitation to a lower singlet excited state (S_1) is also usually observed, and is called the Q band. These absorptions typically occur at wavelengths (λ_{max}) between 400 and 600 nm in the conjugated oligopyrroles,[27] though extension of the π-system by appending benzo-fused units to the pyrrole backbone can extend these absorption bands into the near infrared (NIR) or infrared (IR) regions;[28] for instance, tin naphthalocyanines have intense NIR absorption bands ranging from 770 to 900 nm (Figure 1.7).[29] The intensity of these absorption bands can be described by the molar extinction coefficient, ε, which is defined by Beer's Law (Equation 1.1).

$$Abs = \varepsilon \times l \times C \qquad \text{(Eq. 1.1)}$$

Here, *Abs* is the (unitless) absorbance of a solution at a given wavelength, *l* is the path length of the incident light through the solution in centimeters (cm), and *C* is the concentration of the solution in molarity (*M*). Extinction coefficients above 10^5 $M^{-1}cm^{-1}$ are quite rare, but these highly absorptive naphthalocyanines have ε on the order of 3×10^6 $M^{-1}cm^{-1}$, and are therefore

[27] Falk, H. The Chemistry of Linear Oligopyrroles and Bile Pigments; Springer-Verlag Wien: New York, 1989.
[28] Mori, H.; Tanaka, T.; Osuka, A. *J. Mater. Chem. C* **2013**, *1*, 2500.
[29] Jakubikova, E.; Campbell, I. H.; Martin, R. L. *J. Phys.Chem. A* **2011**, *115*, 9265.

frequently used as efficient chromophores in solar cells[30] and photodiodes,[31] where near infrared absorption is exceptionally important.

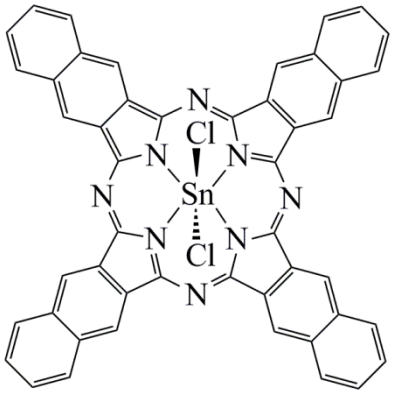

Figure 1.7. Tin(IV) naphthalocyanine with λ_{max} in the NIR region and $\varepsilon > 3 \times 10^6\ M^{-1}cm^{-1}$.

The wavelengths of these absorptions are sensitive to the substitution of the naphthalocyanine, with substituents closest to the tetrapyrrole core having the most significant effect on the absorption maximum. This substituent-dependence on the λ_{max} of chromophoric oligopyrroles is universal. Halide, alkyl, aryl, and alkoxy substituents in the β-positions of the pyrrole subunits generally cause bathochromic (red) shifts in the absorption spectra relative to their non-substituted analogs.[32] Hypsochromic (blue) shifts in oligopyrrole absorption spectra are more rarely observed, but are common upon coordination of the oligopyrrole to an open-shell, d^6–d^9 transition metal, where metal $d\pi \rightarrow$ ligand π^* back-donation raises the energy of the oligopyrrole LUMO, thereby increasing the energy of HOMO $\rightarrow$ LUMO (or LUMO+1) absorption.[12]

[30] (a) Imahori, H.; Umeyama, T.; Ito, S. *Acc. Chem. Res.* **2009**, *42*, 1809. (b) Qian, G.; Wang, Z. Y. *Chem. - Asian J.* **2010**, *5*, 1006.
[31] Sowell, J.; Strekowski, L.; Patonay, G. *J. Biomed. Opt.* **2002**, *7*, 571.
[32] Wertsching, A. K.; Koch, A. S.; DiMagno, S. G. *J. Am. Chem. Soc.* **2001**, *123*, 3932.

1.2.3 Variations in Emission

Molecular luminescence, or the emission of light from individual molecules, is closely linked to the absorption of light by molecular species.[33] Upon absorption of a photon of visible light, an electron is promoted from one orbital to another, higher-energy orbital, resulting in an excited-state species. This excited state species rapidly relaxes to the lowest vibrational energy state of the electronic excited state, and then can relax back to the singlet ground state (S_0) by a number of pathways, including collisional energy transfer to other molecules, internal conversion, resonant energy transfer to non-emissive species, intersystem crossing to a triplet excited state, emission of a photon of slightly lower energy than the absorbed photon, or any combination of these (Figure 1.8).[34] When emission occurs directly from the singlet excited state (S_n, $n \geq 1$), the phenomenon is called fluorescence; when intersystem crossing to a triplet excited state (T_n, $n \geq 1$) occurs before emissive relaxation to S_0, this luminescence is called phosphorescence. The efficiency of luminescence emission is characterized by the emission quantum yield, Φ, defined by Equation 1.2.

$$\Phi = \frac{\#\ of\ photons\ emitted}{\#\ of\ photons\ absorbed} \qquad \text{(Eq. 1.2)}$$

Emission is also characterized by the difference in energy between the absorbed photon and the emitted photon; this is known as the Stokes shift. The majority of molecules that luminesce are rigid, conjugated species; the conjugated oligopyrroles discussed here meet this criterion, and are often luminescent. Any structural variation that increases the rigidity of a luminophore generally increases Φ. In oligopyrroles, this is often achieved by extension of the π-system by

[33] Thompson, M. *MRS Bull.* **2007**, *32*, 694.
[34] (a) Parkhurst, L. J. *Pract. Spectrosc.* **2001**, *25*, 5. (b) Balzani, V.; Bergamini, G.; Campagna, S.; Puntoriero, F. *Top. Curr. Chem.* **2007**, *280*, 1.

benzannulation,[28] or by the introduction of bulky *meso*-aryl-substituents, which restrict rotation about the C_{meso}–C_{aryl} bond.

Phosphorescence is characterized by large Stokes shifts (generally > 150 nm) and long excited-state lifetimes; because of these long lifetimes, non-radiative relaxation pathways become kinetically competitive with photon emission, so quantum yields of phosphorescence are generally much lower than for fluorescence. Phosphorescence can be enhanced by the incorporation of heavy atoms either into the structure of the oligopyrrole complex, or into the solvent. Heavy atoms enhance spin-orbit coupling, thereby increasing the probability of intersystem crossing, and raising the probability of $T_n \rightarrow S_0$ phosphorescence.[35] This is most clearly observed in oligopyrrole systems that are bound to second- and third-row transition metals, which generally phosphoresce rather than fluoresce, as in the case of Ir(III) corroles,[36] which efficiently phosphoresce at ambient temperature (Φ_P = 0.012). Heavy halogens, particularly bromine and iodine, can also enhance spin-orbit coupling,[37] thereby enhancing phosphorescence emission, though this has not been extensively studied in oligopyrrole complexes.

[35] Elbjeirami, O.; Rawashdeh-Omary, M. A.; Omary, M. A. *Res. Chem. Intermed.* **2011**, *37*, 691.
[36] Palmer, J. H.; Durrell, A. C.; Gross, Z.; Winkler, J. R.; Gray, H. B. *J. Am. Chem. Soc.* **2010**, *132*, 9230.
[37] Melo, J. I.; Maldonado, A. F.; Aucar, G. A. *J. Chem. Phys.* **2012**, *137*, 214319/1.

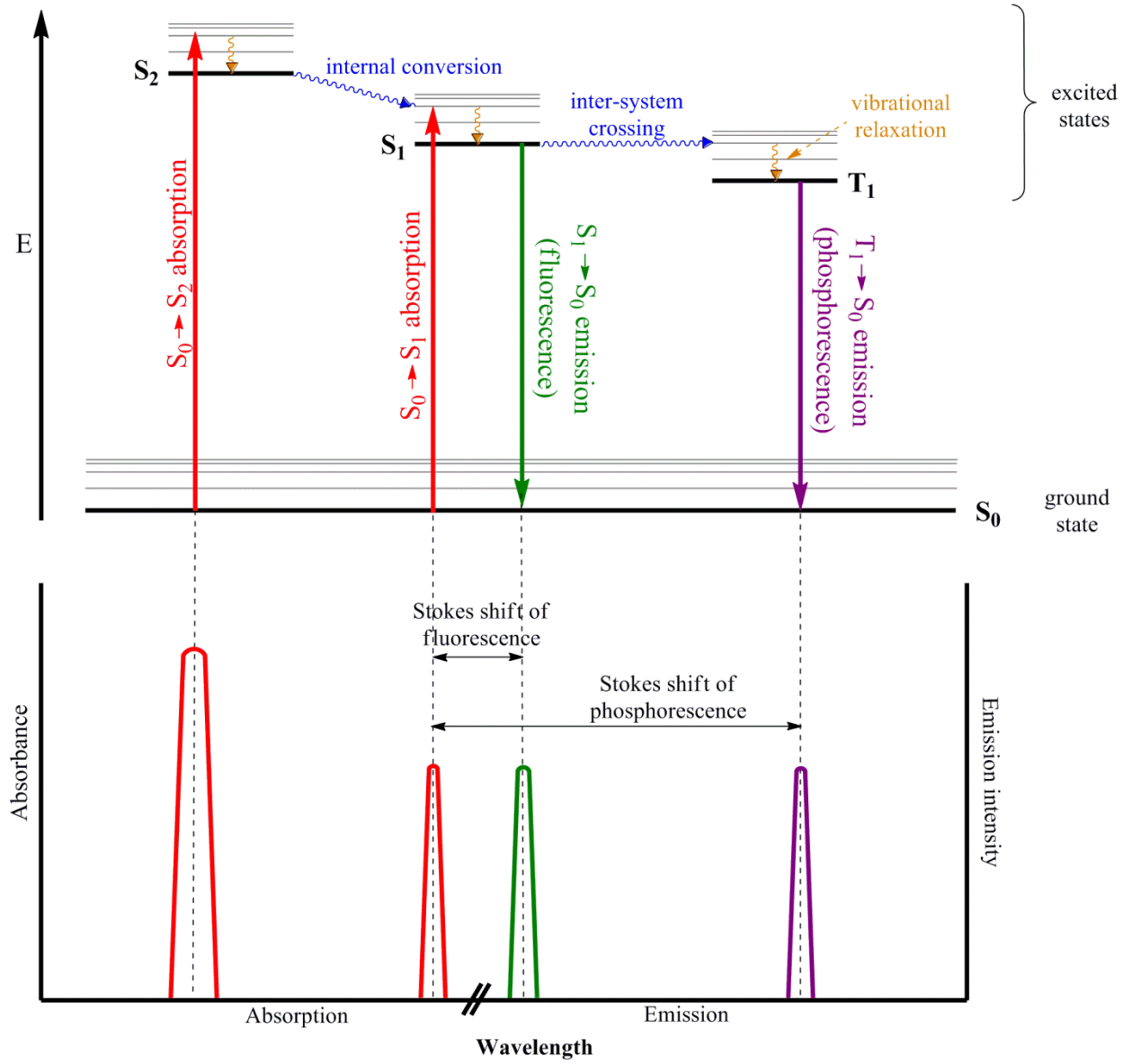

Figure 1.8. Jablonski diagram (top) illustrating absorption (red), fluorescence emission (green), and phosphorescence emission (purple), and correlating with absorption and emission spectra (bottom). Vibrational relaxation, internal conversion, and inter-system crossing are non-radiative pathways of relaxation to the ground state. Gray lines indicate vibrational excited states within a given electronic state.

1.2.4 Variations in Redox Properties

Most oligopyrroles are redox active molecules, and can undergo both one-electron oxidation and one-electron reduction reversibly.[38] This redox activity plays a crucial role in the oxidative catalysis carried out by the heme cofactor of Cytochrome P450,[10] in which the

[38] Bhyrappa, P.; Sankar, M.; Varghese, B. *Inorg. Chem.* **2006**, *45*, 4136.

porphyrin supplies an electron (is oxidized) in the catalytic cycle; one of the active intermediates in the cycle is generally accepted to be an iron(IV) oxo supported by a porphyrin radical cation. This allows the heme cofactor to perform challenging oxidation chemistry. The introduction of electron-withdrawing substituents on the periphery of the oligopyrrole generally makes the complex more difficult to oxidize, but more susceptible to reduction; while the introduction of electron-donating groups has the opposite effect.[39] These structural variations in oligopyrrole complexes modify their redox capabilities, allowing them to support metals in oxidation states 0 to +6.[12]

1.3 Dipyrrins and Their Complexes

Dipyrrins, also known as dipyrromethenes, pyrromethenes, dipyrrylmethenes, and a host of other names, are possibly the most well-studied of the synthetic linear oligopyrroles. They can be viewed as "hemi-porphyrins," and many of their electronic and geometric features reflect this similarity (Figure 1.9). Their ease of synthesis, robustness, exceptional photophysical properties (both aborptivity and luminescence), and highly variable architecture make them extremely versatile compounds. For an excellent, comprehensive review on the chemistry of dipyrrins and their chelates, see Wood and Thompson, 2007.[40] In general, substituent effects on the optical and electrochemical properties of dipyrrins and their chelates parallel the larger oligopyrroles described in Section 1.2, though systematic studies of these substituent effects in dipyrrin-based systems are lacking.[41] There are two key differences between dipyrrins and their macrocyclic

[39] (a) Takeuchi, T.; Gray, H. B.; III, W. A. G. *J. Am. Chem. Soc.* **1994**, *116*, 9730. (b) Hodge, J. A.; Hill, M. G.; Gray, H. B. *Inorg. Chem.* **1995**, *34*, 809. (c) Grinstaff, M. W.; Hill, M. G.; Birnbaum, E. R.; Schaefer, W. P.; Labinger, J. A.; Gray, H. B. *Inorg. Chem.* **1995**, *34*, 4896. (d) Kadish, K. M.; Lin, M.; Caemelbecke, E. V.; Stefano, G. D.; Medforth, C. J.; Nurco, D. J.; Nelson, N. Y.; Krattinger, B.; Muzzi, C. M.; Jaquinod, L.; Xu, Y.; Shyr, D. C.; Smith, K. M.; Shelnutt, J. A. *Inorg. Chem.* **2002**, *41*, 6673.

[40] Wood, T. E.; Thompson, A. *Chem. Rev.* **2007**, *107*, 1831, and references therein.

[41] Scharf, A. B.; Betley, T. A. *Inorg. Chem.* **2011**, *50*, 6837.

relatives: (1) the ability to functionalize the 1- and 9-positions of dipyrrins and (2) the flexibility to bind metals in geometries other than square planar.

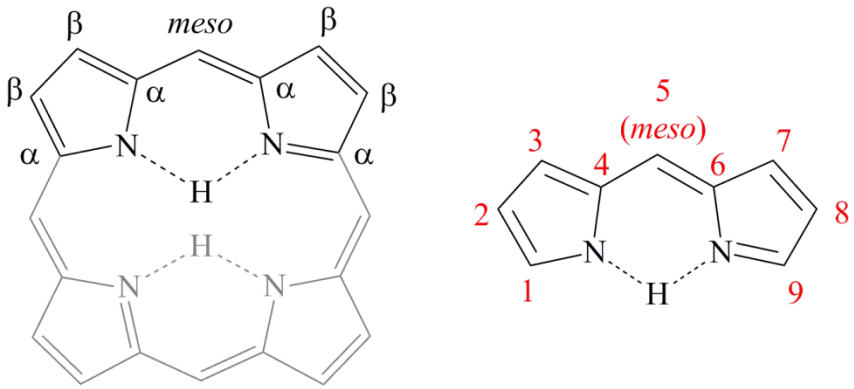

Figure 1.9. The core structure and labeling scheme for a porphyrin, left, and for a dipyrrin, right, showing IUPAC numbering, and emphasizing the similarity between porphyrins and dipyrrins.

1.3.1 Free-Base Dipyrrins

There have been relatively few studies of uncomplexed, or free-base, dipyrrins reported in the chemical literature. Dipyrrins are present in biological systems as metabolites of porphyrins, and are part of a group of oligopyrroles called bile pigments. When symmetrically substituted, they display C_s symmetry, indicating the equivalence of the 1 and 9, 2 and 8, 3 and 7, and 4 and 6 positions. These molecules are intense chromophores (like their macrocyclic cousins, Sections 1.1 and 1.2.2), and their other properties are reviewed in the book *The Chemistry of Linear Oligopyrroles and Bile Pigments*.[27]

1.3.2 Boron Difluoride Dipyrrinato (BODIPY) Complexes

Deprotonated dipyrrins, referred to a dipyrrinato ligands, can serve as monoanionic, bidentate ligands for both main-group elements and transition metals. Boron-difluoride dipyrrinato complexes, commonly referred to as BODIPYs (Figure 1.10), are undoubtedly the

best-studied of these chelates.[42] BODIPYs are most often found in optical applications, as they are strongly absorptive in the visible region of the electromagnetic spectrum and are frequently luminescent.

There is a large body of literature on how various substitution patterns and structural variations affect the photophysical properties of BODIPYs. The introduction of functionality directly onto the dipyrrin core in positions 1, 2, 3, 7, 8, and 9 has a wide range of effects on the properties of these molecules, while substitution of the *meso* position generally has a less pronounced effect, except on the intensity of luminescence from emissive species (see Section 1.2.3).

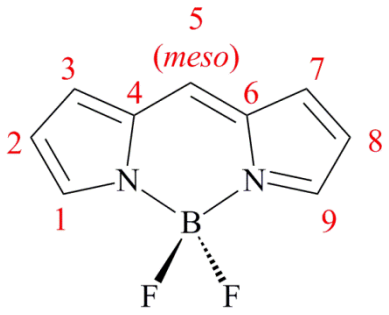

Figure 1.10. General structure of BODIPY dyes.

1.3.3 Main-Group Dipyrrinato Complexes

In addition to the abundant BODIPY class of dipyrrinato complexes, a number of other main-group dipyrrin-based molecules have been synthesized and studied as well. A large number of these complexes are homoleptic bis- or tris-dipyrrinato species of Mg(II), Ca(II), Al(III), Ga(III), In(III), Tl(I), and Tl(III).[40] These homoleptic complexes of main-group compounds generally adopt geometries as predicted by VSEPR theory: bis(dipyrrinato) complexes are generally approximately tetrahedral, and tris complexes are generally octahedral. Other main-

[42] (a) Benniston, A. C.; Copley, G. *Phys. Chem. Chem. Phys.* **2009**, *11*, 4124. (b) Loudet, A.; Burgess, K. *Chem. Rev.* **2007**, *107*, 4891. (c) Ziessel, R.; Ulrich, G.; Harriman, A. *New J. Chem.* **2007**, *31*, 496. (d) Ulrich, G.; Ziessel, R.; Harriman, A. *Angew. Chem., Int. Ed.* **2008**, *47*, 1184.

group dipyrrinato complexes include heteroleptic complexes of Li(I), Na(I), K(I),[43] Al(III),[44] Si(IV),[45] Sn(II), and Sn(IV).[46] The properties of the main-group chelates of dipyrrinato ligands are a growing area of research, and their use in the construction of supramolecular architectures and as fluorophores is only recently developing.[47]

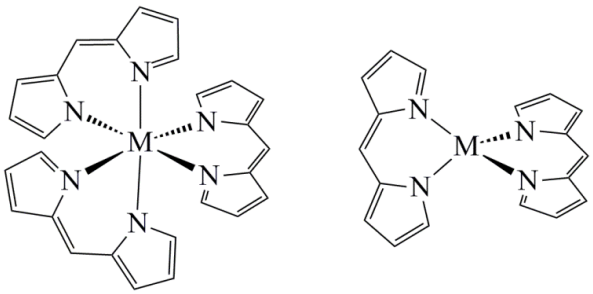

Figure 1.11. General structures of homoleptic tris(dipyrrinato), left, and bis(dipyrrinato) complexes. Only the Λ enantiomer of the tris(dipyrrinato) complex is shown arbitrarily.

1.3.4 Transition Metal Dipyrrinato Complexes

The first dipyrrinato complexes of transition metals were reported as early as the 1930s,[48] but they have only recently received a resurgence of attention for their potential applications in metal-organic frameworks,[49] fluorescence labeling,[50] light-harvesting arrays,[51] coordination polymers,[52] and catalysis.[53] While there is a vast body of literature on the effects of ligand variation on the optical properties of BODIPY dyes, as well as the experimental properties of

[43] Ali, A. A.-S.; Cipot-Wechsler, J.; Crawford, S. M.; Selim, O.; Stoddard, R. L.; Cameron, T. S.; Thompson, A. *Can. J. Chem.* **2010**, *88*, 725.
[44] Thoi, V. S.; Stork, J. R.; Magde, D.; Cohen, S. M. *Inorg. Chem.* **2006**, *45*, 10688.
[45] Sakamoto, N., Ikeda, C., Yamamura, M., and Nabeshima T., *J. Am. Chem. Soc.*, **2011**, *133*, 4726–4729.
[46] Crawford, S. M.; Al-Sheikh, A. A.; Cameron, T. S.; Thompson, A. *Inorg. Chem.* **2011**, *50*, 8207.
[47] Baudron, S. A. *Dalton Trans.* **2013**, *42*, 7498, and references therein.
[48] Fischer, H.; Orth, H. *Die Chemie des Pyrrols*; Akademische Verlagsgesellschaft MBH: Leipzig, 1937; Vol. 2.
[49] (a) Cohen, S. M.; Halper, S. R. *Inorg. Chim. Acta* **2002**, *341*, 12. (b) Murphy, D. L.; Malachowski, M. R.; Campana, C. F.; Cohen, S. M. *Chem. Commun.* **2005**, *44*, 5506. (c) Stork, J. R.; Thoi, V. S.; Cohen, S. M. *Inorg. Chem.* **2007**, *46*, 11213. (d) Halper, S. R.; Cohen, S. M. *Inorg. Chem.* **2005**, *44*, 486.
[50] Filatov, M. A.; Lebedev, A. Y.; Mukhin, S. N.; Vinogradov, S. A.; Cheprakov, A. V. *J. Am. Chem. Soc.* **2010**, *132*, 9552.
[51] Yu, L.; Muthukumaran, K.; Sazanovich, I. V.; Kirmaier, C.; Hindin, E.; Diers, J. R.; Boyle, P. D.; Bocian, D. F.; Holten, D.; Lindsey, J. S. *Inorg. Chem.* **2003**, *42*, 6629.
[52] (a) Halper, S. R.; Malachowski, M. R.; Delaney, H. M.; Cohen, S. M. *Inorg. Chem.* **2004**, *43*, 1242. (b) Do, L.; Halper, S. R.; Cohen, S. M. *Chem. Commun.* **2004**, 2662.
[53] (a) King, E. R.; Hennessy, E. T.; Betley, T. A. *J. Am. Chem. Soc.* **2011**, *133*, 4917. (b) Hennessy, E. T.; Betley, T. A. *Science* **2013**, *340*, 591.

free-base and metallo-porphyrins and other macrocyclic oligopyrrole species (see Section 1.2), there has been little systematic exploration of how peripheral ligand variations affect the chemistry of transition-metal dipyrrinato complexes.[41]

1.4 Summary of Chapters

Chapter 2 describes the synthesis and characterization of a wide range of free-base dipyrrins, variably substituted in the 1-, 2-, 3-, 5- (*meso*-), 7-, 8-, and 9-positions. The effects or aryl and alkyl substitution in the 1- and 9-positions, halogenation in the 2-, 3-, 7-, and 8-positions, and haloaryl substitution in the 5-position on the optical and electrochemical properties of these complexes is explored.

Chapter 3 describes the synthesis of iron(II) dipyrrinato complexes and the effects of ligand halogenation and *meso*-fluoroarylation on the spectroscopic, electrochemical, and structural properties of the complexes. While halogenation and *meso*-fluoroarylation cause predictable and systematic changes in the optical and redox properties of these iron complexes, the effects of those ligand modifications on the structural and Mössbauer spectroscopic properties are less intuitive, but are analyzed here.

In **Chapter 4**, the synthesis of a broader range of transition metal dipyrrinato complexes is described, including 3-, 4-, and 5-coordinate metal complexes. The structural differences between these complexes are described, and their idealized d-orbital splitting diagrams baesd on the method of angular overlap[54] are presented.

Finally, in **Chapter 5**, the luminescent properties of the derivatives and transition metal chelates of 1,9-bis(2′,4′,6′-triphenylphenyl)dipyrrins are discussed. The first paramagnetic,

[54] Jorgensen, C. K., Pappalardo, R., and Schmidtke, H. H. *J. Chem. Phys.*, **1963**, *39*, 1422.

appreciably luminescent dipyrrinato complexes are presented, as is the first complex of manganese(II) that is known to phosphoresce at room temperature in the solution state.

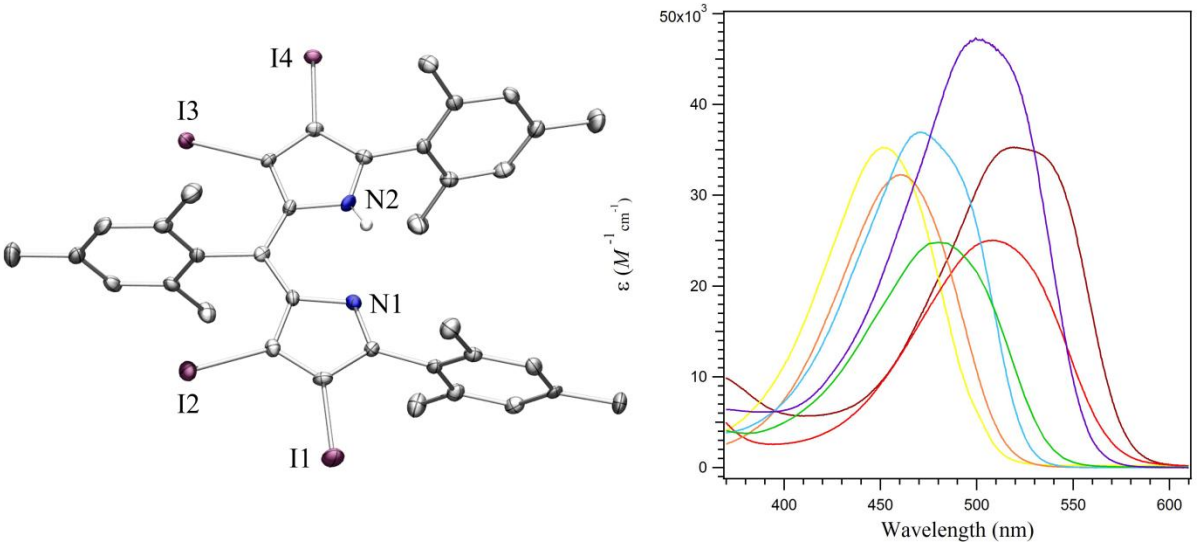

Chapter 2: Synthesis of and Characterization of Dipyrrins[55]

2.1 Synthesis of Dipyrrins

C_s or C_2 symmetric dipyrrins can be readily synthesized on large scale by the reaction of two equivalents of an appropriate 2-substituted pyrrole with one equivalent of an aldehyde or acetal under acidic catalysis, followed by two-electron oxidation by 2,3-dichloro-5,6-dicyano-1,4-benzoquinone (DDQ) or other chemical oxidants.[56] The dipyrrin can be isolated either as the hydrohalide salt if the oxidation is worked up under strongly acidic conditions, or as the free base if milder conditions are used. The pyrrole and aldehyde or acetal can bear a range of functionalities, but simple 2-alkyl or 2-aryl pyrroles and aryl aldehydes or acetals are typically used.

[55] This chapter was adapted with permission from Scharf, A. B.; Betley, T. A. *Inorg. Chem.* **2011**, *50*, 6837.
[56] Fischer, H.; Elhardt, E. *Z. Physiol. Chem.* **1939**, *257*, 61.

Scheme 2.1. Synthesis of dipyrrins

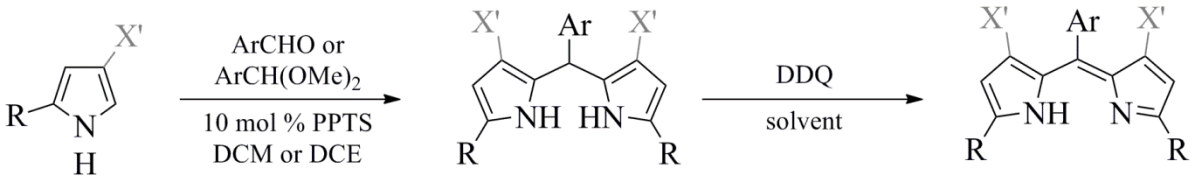

For Ar = mesityl (Mes), the acetal was used; for Ar = haloaryl, the aldehyde could be used. Heat was required for the condensation to occur with the bulky R = 2′,4′,6′-$Ph_3C_6H_2$ (Q). X′ = H or Me. Several solvents could be used for the DDQ oxidation step; dichloromethane, acetone, and hexanes were the most commonly used.

Our protocol involves the condensation of a 2-aryl or 2-alkyl pyrrole with mesitaldehyde dimethyl acetal or a haloaryl aldehyde in chlorinated solvent (dichloromethane or dichloroethane) with pyridinium *p*-toluene sulfonate catalyst; occasionally heat is required. Passage through a silica plug and concentration in vacuo typically yields the non-conjugated dipyrromethane (dpma) cleanly. Oxidation with DDQ can be performed in a wide variety of solvents, including acetone, dichloromethane, and hexane (Scheme 2.1). Work-up typically involves concentration of the crude reaction mixture in vacuo, suspension or dissolution in ethyl acetate, followed by several aqueous washes to remove the hydroquinone byproduct. If further purification is required, trituration from cold acetonitrile or pentanes, or column chromatography with basic alumina stationary phase and hydrocarbon eluent can be used, though either purification method generally results in significantly decreased yields.

Subsequent functionalization of the 2-, 3-, 7-, and 8-positions of the dipyrrin can be achieved via halogenation with N-halosuccinimides (NXS, X = Cl, Br, I) in tetrahydrofuran (THF),[57] or with molecular iodine in dimethyl formamide (DMF) under basic conditions.[58]

[57] (a) Bhyrappa, P.; Sankar, M.; Varghese, B. *Inorg. Chem.* **2006**, *45*, 4136. (b) Chumakov, D. E.; Khoroshutin, A. V.; Anisimov, A. V.; Kobrakov, K. I. *Chem. Heterocycl. Compd. (New York, NY, U.S.)* **2009**, *45*, 259.

[58] Gupton, J. T.; Banner, E. J.; Scharf, A. B.; Norwood, B. K.; Kanters, R. P. F.; Dominey, R. N.; Hempel, J. E.; Kharlamova, A.; Bluhn-Chertudi, I.; Hickenboth, C. R.; Little, B. A.; Sartin, M. D.; Coppock, M. B.; Krumpe, K. E.; Burnham, B. S.; Holt, H.; Du, K. X.; Keertikar, K. M.; Diebes, A.; Ghassemi, S.; Sikorski, J. A. *Tetrahedron* **2006**, *62*, 8243.

Bromination is possible on almost all dipyrrins studied herein, and can be achieved regioselectively at the 3- and 8-positions if only two equivalents of NBS are used; this regioselectivity is presumably a result of the more sterically encumbered environment at the 3- and 7-positions of the dipyrrin as there is little electronic differentiation between the two positions. One-dimensional NMR analysis was inconclusive in determining this regioselectivity, but it was unequivocally confirmed by X-ray crystallographic analysis of the 2,8-dibromodipyrrin **($^{Br;\,H}_{Mes}$L^{Mes})H** (Figure 2.1). If four or more equivalents of NBS are used, complete tetrabromination is observed within minutes to hours of addition of NBS, depending on the nucleophilicity of the dipyrrin.

Scheme 2.2. Halogenation of dipyrrins

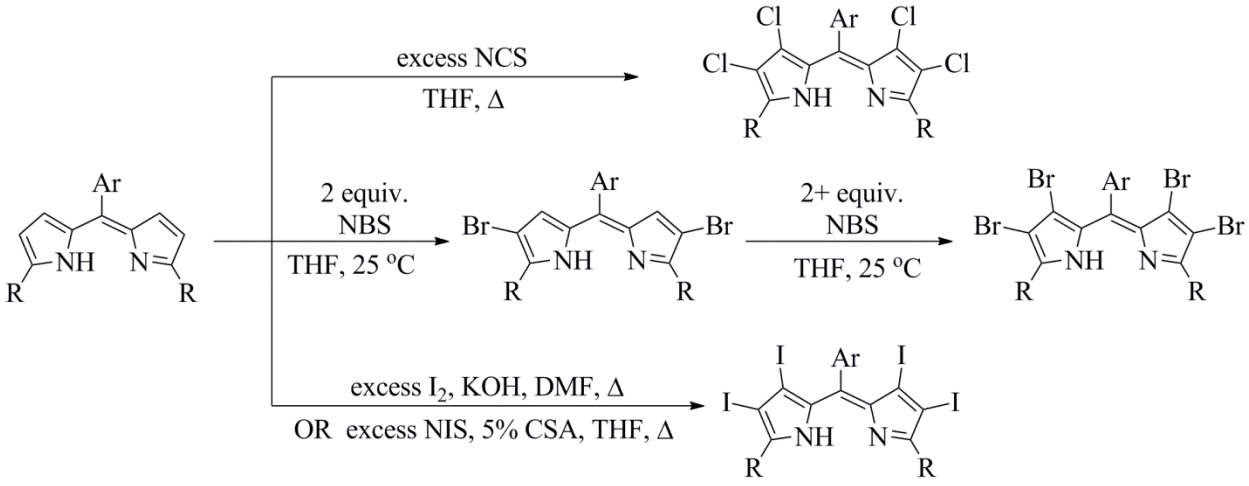

Chlorination and iodination generally require increased temperatures, longer reaction times, and/or acid catalysis, if halogenation can be achieved at all. We have been unable to isolate any regioselectively chlorinated or iodinated products, even with only one or two equivalents of halogenating agent, and only tetrachlorinated and tetraiodinated dipyrrins could be obtained cleanly. These dipyrrins are abbreviated **($^{X;\,X'}_{Ar}$L^{R})H** throughout this dissertation (Figure 2.2), where X is the 2- and 8- substituent, X′ is the 3- and 7- substituent, Ar is the 5- or *meso*

subsituent, and R is the 1- and 9- or flanking substituent. If X = X′, a single character will appear in the left superscript, which denotes the 2-, 3-, 7-, and 8-substituent.

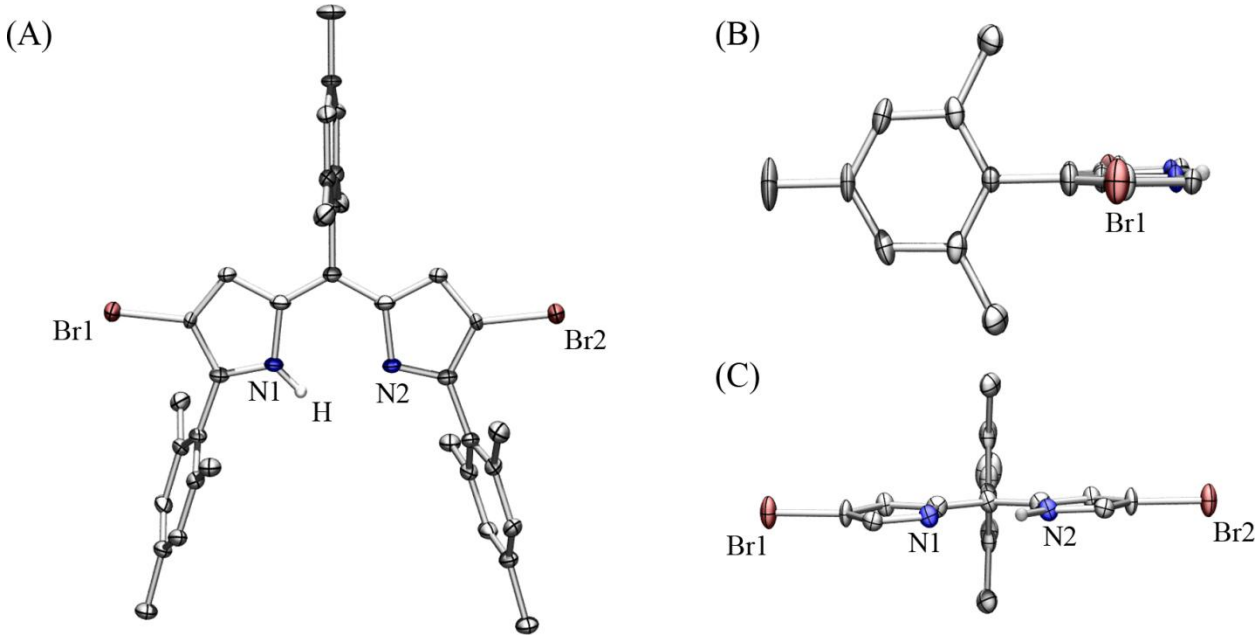

Figure 2.1. Solid-state molecular structure of $(^{Br;\,H}_{Mes}L^{Mes})H$ with ellipsoids drawn at the 50% probability level. Hydrogen atoms, except the N-H, have been omitted for clarity, and the N-H hydrogen has been arbitrarily placed on N1. (A) Whole molecule, illustrating regioselectivity of dibromination. (B) Side view, illustrating planarity of the dipyrrin core; flanking mesityl groups have been omitted for clarity. (C) Front view, illustrating the orthogonality of the dipyrrin with the *meso*-mesityl group (see Section 3.6 for further discussion); flanking mesityl groups have been omitted for clarity. Gray, C; blue, N; maroon, Br.

Occasionally, benzylic halogenation competed with pyrrolic halogenation. This could be avoided by the use of inhibitor-free THF, oxygen-free reaction conditions, and protection of the reaction vessel from ambient light to prevent photo-induced homolysis of the halogenation reagent and the generation of halide radicals.

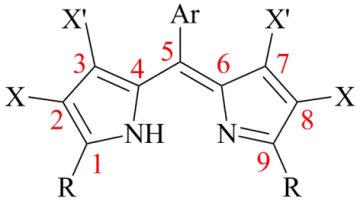

Figure 2.2. Generic structure of dipyrrins

Table 2.1. Dipyrrins studied herein

Entry	Abbreviation	R	Ar	X	X′
1	$(^{H}_{Mes}L^{Mes})H$	Mes	Mes	H	H
2	$(^{Cl}_{Mes}L^{Mes})H$	Mes	Mes	Cl	Cl
3	$(^{Br;\ H}_{Mes}L^{Mes})H$	Mes	Mes	Br	H
4	$(^{Br}_{Mes}L^{Mes})H$	Mes	Mes	Br	Br
5	$(^{I}_{Mes}L^{Mes})H$	Mes	Mes	I	I
6	$(^{H}_{C_6F_5}L^{Mes})H$	Mes	C_6F_5	H	H
7	$(^{Cl}_{C_6F_5}L^{Mes})H$	Mes	C_6F_5	Cl	Cl
8	$(^{Br}_{C_6F_5}L^{Mes})H$	Mes	C_6F_5	Br	Br
9	$(^{H}_{BFP}L^{Mes})H$	Mes	3′,5′-$(CF_3)_2C_6H_3$	H	H
10	$(^{Br}_{BFP}L^{Mes})H$	Mes	3′,5′-$(CF_3)_2C_6H_3$	Br	Br
11	$(^{H}_{Mes}L^{tBu})H$	*t*Bu	Mes	H	H
12	$(^{Cl}_{Mes}L^{tBu})H$	*t*Bu	Mes	Cl	Cl
13	$(^{Br}_{Mes}L^{tBu})H$	*t*Bu	Mes	Br	Br
14	$(^{H}_{DCP}L^{tBu})H$	*t*Bu	2′,6′-$Cl_2(C_6H_3)$	H	H
15	$(^{H}_{Mes}L^{Ad})H$	Ad	Mes	H	H
16	$(^{Cl}_{Mes}L^{Ad})H$	Ad	Mes	Cl	Cl
17	$(^{Br}_{Mes}L^{Ad})H$	Ad	Mes	Br	Br
18	$(^{H}_{C_6F_5}L^{Ad})H$	Ad	C_6F_5	H	H
19	$(^{H}_{DCP}L^{Ad})H$	Ad	2′,6′-$Cl_2(C_6H_3)$	H	H
20	$(^{Br}_{DCP}L^{Ad})H$	Ad	2′,6′-$Cl_2(C_6H_3)$	Br	Br
21	$(^{H}_{Mes}L^{Q})H$	2′,4′,6′-$Ph_3(C_6H_2)$	Mes	H	H
22	$(^{Br}_{Mes}L^{Q})H$	2′,4′,6′-$Ph_3(C_6H_2)$	Mes	Br	Br
23	$(^{I}_{Mes}L^{Q})H$	2′,4′,6′-$Ph_3(C_6H_2)$	Mes	I	I
24	$(^{H;\ Me}_{DCP}L^{Me})H$	Me	2′,6′-$Cl_2(C_6H_3)$	H	Me

Abbreviations used: Mes = 2′,4′,6′-trimethylphenyl, mesityl; BFP = 3′,5′-**b**is(tri**f**luoromethyl)**p**henyl; DCP = 2′,6′-**di**chloro**p**henyl; *t*Bu = *tert*-butyl (–$C(CH_3)_3$); Ad = adamant-1-yl; Q = 2′,4′,6′-triphenylphenyl; Me = methyl.

2.2 Characterization of Dipyrrins

All the dipyrrins synthesized in this study were characterized by ^{1}H and ^{13}C NMR, high-resolution ESI-MS, and UV/Vis spectroscopy; when appropriate, ^{19}F NMR, cyclic voltammetry (CV), and luminescence spectroscopy (Chapter 5) were also performed.

2.2.1 Nuclear Magnetic Resonance

NMR studies confirmed the C_s (or C_2) symmetry of the dipyrrins, which show diagnostic peaks above 11 ppm for the N-H proton and two clean doublets (or occasionally higher order multiplets, if coupling to the N-H proton can be resolved) for the pyrrolic C-H protons between 5 and 6 ppm. This high degree of symmetry is consistent with either rapid N-H tautomerization or a *bona fide* 3-center, 4-electron bond between the N-H-N unit.

High-resolution ^{13}C NMR spectra allowed the determination of carbon-fluorine coupling constants for **($_{BFP}^{H}L^{Mes}$)H**, $^{1}J_{C\text{-}F}$ = 272, $^{2}J_{C\text{-}F}$ = 32, and $^{3}J_{C\text{-}F}$ = 3.8 Hz, in accord with previous reports of similar fluoroaryl groups.[59] Due to the extensive coupling for the perfluorophenyl groups, no such $J_{C\text{-}F}$ values could be extracted for those species. While the ^{13}C NMR spectra of all compounds showed the appropriate number of peaks in the expected chemical shift ranges, no rigorous assignments were attempted.

2.2.2 Mass Spectrometry

Positive-ion mode electrospray ionization mass spectrometry showed molecular ion peaks for $^{m}/_{z}$ = $[M+H]^{+}$ for all dipyrrins. For all dipyrrins, but especially those that were polyhalogenated, isotope patterns were consistent with the assigned structures and formulae.

[59] Yakelis, N. A.; Bergman, R. G. *Organometallics* **2005**, *24*, 3579.

2.2.3 UV/Vis Spectroscopy

Dipyrrins are intensely colored molecules, due to their high degree of conjugation and associated small HOMO/LUMO gap.[27] Visible light absorption by $\pi \rightarrow \pi^*$ excitation occurs in the range 450–550 nm for the dipyrrins studied here, with molar extinction coefficients (ε) in excess of 15,000 $M^{-1}cm^{-1}$ and as high as 50,000 $M^{-1}cm^{-1}$ (Table 2.2 and Figure 2.3). These characteristic absorptions result in colors ranging from bright yellow for the smallest dipyrrins to intense dark reddish-purple for the largest, though the majority of the complexes studied herein are bright orange when pure.

The identity of the 5- (or *meso*-) aryl group has a minor effect on the absorption characteristics of dipyrrins, presumably because it is oriented roughly orthogonal to the chromophoric dipyrrin plane. Its effect on the energies of the HOMO and LUMO are therefore purely inductive. Electron-poor aryl groups such as perfluorophenyl (C_6F_5), 3′,5′-bis(trifluoromethyl)phenyl (BFP), or 2′,6′-dichlorophenyl (DCP) cause a slight red-shift in the wavelength of maximum absorption relative to the more electron-rich mesityl group (on average, by 8, 8, and 5 nm, respectively).

Halogenation of the pyrrole backbone has a more pronounced effect on λ_{max} because both inductive and resonance effects play a role in the relevant π system of the dipyrrins. The magnitude of the induced red-shift increases with the size of the halogen and decreases with electronegativity;[60] chlorination causes a less significant shift than bromination, which in turn is less dramatic than for iodination (on average, 18, 24, and 36 nm for tetrahalogenation, respectively). Dibromination in $\mathbf{(^{Br;\,H}_{Mes}L^{Mes})H}$ causes a 7 nm bathochromic shift, slightly less than

[60] ACS Online Periodic Table. http://acswebcontent.acs.org/games/pt.html. American Chemical Society: 2007.

half the effect observed for $(^{Br}_{Mes}L^{Mes})H$. The effects of the *meso* substituent and the pyrrolic halogens are nearly additive.

Table 2.2. UV/Vis spectroscopic details[a] of dipyrrins

Entry	Dipyrrin	λ_{max} (nm)	ε^b ($M^{-1}cm^{-1}$)
1	$(^{H}_{Mes}L^{Mes})H$	464	31,600
2	$(^{Cl}_{Mes}L^{Mes})H$	480	24,800
3	$(^{Br;\ H}_{Mes}L^{Mes})H$	471	49,000
4	$(^{Br}_{Mes}L^{Mes})H$	485	26,700
5	$(^{I}_{Mes}L^{Mes})H$	503	47,200
6	$(^{H}_{C_6F_5}L^{Mes})H$	472	31,700
7	$(^{Cl}_{C_6F_5}L^{Mes})H$	490	27,900
8	$(^{Br}_{C_6F_5}L^{Mes})H$	496	30,700
9	$(^{H}_{BFP}L^{Mes})H$	473	26,200
10	$(^{Br}_{BFP}L^{Mes})H$	492	28,000
11	$(^{H}_{Mes}L^{tBu})H$	447	29,300
12	$(^{Cl}_{Mes}L^{tBu})H$	466	25,900
13	$(^{Br}_{Mes}L^{tBu})H$	472	39,700
14	$(^{H}_{DCP}L^{tBu})H$	450	33,800
15	$(^{H}_{Mes}L^{Ad})H$	453	29,200
16	$(^{Cl}_{Mes}L^{Ad})H$	471	36,900
17	$(^{Br}_{Mes}L^{Ad})H$	478	36,100
18	$(^{H}_{C_6F_5}L^{Ad})H$	461	32,300
19	$(^{H}_{DCP}L^{Ad})H$	458	15,300
20	$(^{Br}_{DCP}L^{Ad})H$	486	39,400
21	$(^{H}_{Mes}L^{Q})H$	507	25,000
22	$(^{Br}_{Mes}L^{Q})H$	520	35,300
23	$(^{I}_{Mes}L^{Q})H$	539	34,900
24	$(^{H;\ Me}_{DCP}L^{Me})H$	451	35,300

[a] Spectra obtained in dichloromethane at 0 °C with a maximum scan rate of 600 nm/min. [b] Average extinction coefficients calculated from a minimum of four concentrations.

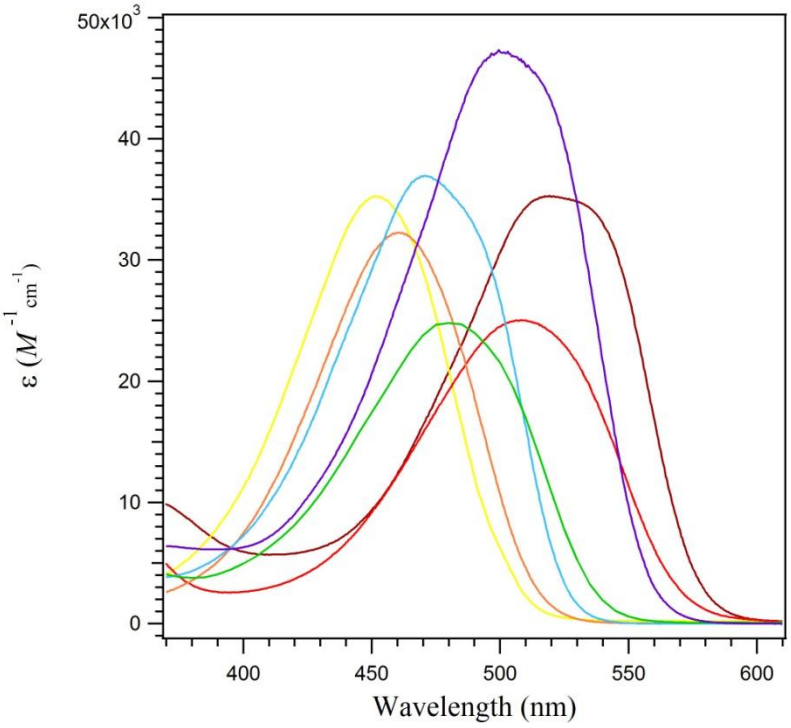

Figure 2.3. Representative UV/Vis spectra of dipyrrins, showing the full range of λ_{max} values. Spectra obtained at room temperature in dichloromethane; average ε values calculated from a minimum of four concentrations. Yellow, $(^{H;\,Me}_{DCP}L^{Me})H$; orange, $(^{H}_{C_6F_5}L^{Ad})H$; light blue, $(^{Cl}_{Mes}L^{Ad})H$; green, $(^{Cl}_{Mes}L^{Mes})H$; purple, $(^{I}_{Mes}L^{Mes})H$; red, $(^{H}_{Mes}L^{Q})H$; maroon, $(^{Br}_{Mes}L^{Q})H$.

2.2.4 Cyclic Voltammetry

Dipyrrins are redox-active molecules and can undergo both one-electron oxidation and one-electron reduction.[27, 61] The reversibility of the redox events depends on the specific substitution of the dipyrrin. In this study, only those dipyrrins with R = Mes were investigated by electrochemistry.

Cyclic voltammetry revealed fully- or quasi-reversible one-electron oxidation events for all the dipyrrins studied electrochemically (0.1 m*M* analyte concentration in dichloromethane, 0.1 *M* (nBu$_4$N)(PF$_6$) supporting electrolyte, scan rate = 250 $^{mV}/_{s}$, glassy carbon working electrode, nonaqueous Ag^+/Ag reference electrode, platinum wire counter-electrode, under a

[61] Ribo, J. M.; Farrera, J.-A.; Claret, J.; Grubmayr, K. *Bioelectrochem. Bioenerg.* **1992**, *29*, 1.

nitrogen atmosphere at 25 °C). Fully-reversible waves in cyclic voltammetry, when purely diffusion-limited, have a minimum separation between the anodic and cathodic peak potentials ($|E_{pa} - E_{pc}|$) of 57 mV per electron transferred; the majority of the quasi-reversible oxidation waves observed here had $|E_{pa} - E_{pc}|$ between 70 and 85 mV, well within the accepted range for fully reversible events in relatively concentrated solutions. The major exception was **(**$^{\mathbf{Cl}}_{\mathbf{Mes}}$**L**$^{\mathbf{Mes}}$**)H**, for which the peak separation was 148 mV; this could indicate a multi-electron process, or, more likely, a slightly slower electron-transfer process than in the other species.

For the nonhalogenated dipyrrins **(**$^{\mathbf{H}}_{\mathbf{Mes}}$**L**$^{\mathbf{Mes}}$**)H**, **(**$^{\mathbf{H}}_{\mathbf{C_6F_5}}$**L**$^{\mathbf{Mes}}$**)H**, and **(**$^{\mathbf{H}}_{\mathbf{BFP}}$**L**$^{\mathbf{Mes}}$**)H**, the initial one-electron oxidation was pseudo-reversible if the potential was not increased beyond ~0.8 V (vs. $[Cp_2Fe]^{+/0}$; all subsequent voltage measurements are referenced to this redox couple). If the potential was swept further anodically, a second quasi-reversible one-electron oxidation could be seen, which renders the first oxidation event fully irreversible. We attribute this behavior to the formation of a diradical which can intramolecularly and irreversibly couple, akin to the coupling observed for the similar dipyrromethanes when subjected to electrochemical oxidation.[21a] The presence of halogens on the backbone blocks this coupling pathway, hence, the oxidations in the cases of the halogenated dipyrrins are fully reversible. The onset of oxidation was seen at 470 mV for **(**$^{\mathbf{H}}_{\mathbf{Mes}}$**L**$^{\mathbf{Mes}}$**)H**; the introduction of fluoroaryl groups in the *meso* position of the dipyrrin, as in **(**$^{\mathbf{H}}_{\mathbf{C_6F_5}}$**L**$^{\mathbf{Mes}}$**)H** and **(**$^{\mathbf{H}}_{\mathbf{BFP}}$**L**$^{\mathbf{Mes}}$**)H**, shifted this potential by approximately +100 mV. Halogenation had a more pronounced effect on the oxidation potential of the dipyrrin, anodically shifting the oxidation by as much as +500 mV for the most electronegative chlorine substituents (Table 2.3). There was a correlation between the sum of the Pauling electronegativities of the pyrrole backbone 2,3,7,8-(X/X′-) substituents and the oxidation potential of the dipyrrin; as more electronegative substituents are added to the dipyrrin backbone, it becomes significantly more

difficult to oxidize. The effects of *meso*-substitution and backbone halogenation are additive; the greatest anodic shift of the oxidation potential is observed for the 5-perfluorophenyl tetrachlorodipyrrin **($_{C_6F_5}^{Cl}$L^{Mes})H**, which has an onset of oxidation approximately +600 mV from **($_{Mes}^{H}$L^{Mes})H**.

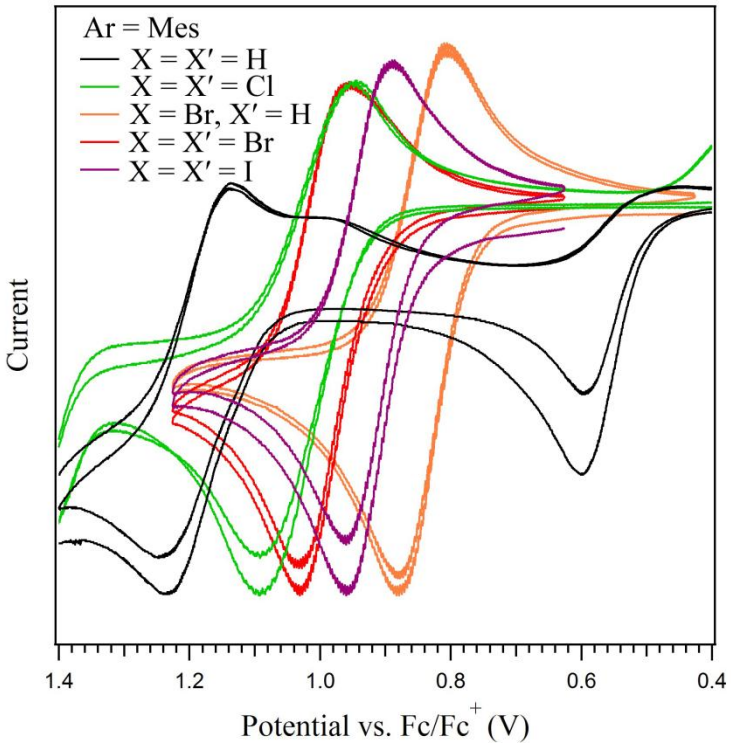

Figure 2.4. Effect of halogenation on dipyrrin oxidation potential. Cyclic voltammograms obtained in CH_2Cl_2 at 25 °C, with 0.1 *M* (nBu$_4$N)(PF$_6$) as the supporting electrolyte and a scan rate of ≤ 250 mV/s. Black, **($_{Mes}^{H}$L^{Mes})H**; green, **($_{Mes}^{Cl}$L^{Mes})H**; orange, **($_{Mes}^{Br;\,H}$L^{Mes})H**; red, **($_{Mes}^{Br}$L^{Mes})H**; purple, **($_{Mes}^{I}$L^{Mes})H**.

Electrochemical reduction of the dipyrrins was also reversible or quasi-reversible across the series, with the exception of **($_{C_6F_5}^{Cl}$L^{Mes})H**, for which reduction was irreversible. The parent dipyrrin **($_{Mes}^{H}$L^{Mes})H** was the most difficult to reduce, with $E_{½}$ = –2.0 V; this reduction wave was also very broad, with $|E_{pa} - E_{pc}|$ = 232 mV. Introduction of electron-withdrawing substituents in the backbone 2-, 3-, 7-, 8- and/or 5-(*meso*-) positions made reduction more facile. 5-Fluoroarylation shifted the reduction potentials by +100 to +200 mV, and tetrahalogenation

shifted the potential by roughly +450 mV. It is interesting to note that most of these reduction events are reversible, indicating that stable halide anions are not expelled on the time-scale of the voltammetric experiment. All cyclic voltammograms are presented in Section 2.4.3.

Table 2.3. Electrochemical characterization of dipyrrins with R = Mes

Dipyrrin	$E_{½}$(ox)[a] (V)	$\lvert E_{pa} - E_{pc}\rvert$ (mV)[b]	$E_{½}$(red)[a] (V)	$\lvert E_{pa} - E_{pc}\rvert$ (mV)[b]	ΣEN[c] (Pauling)
$(^{H}_{Mes}\mathbf{L}^{Mes})\mathbf{H}$	0.520[d]	—	−1.999	232	8.80
$(^{Cl}_{Mes}\mathbf{L}^{Mes})\mathbf{H}$	1.018	148	−1.558	71	12.64
$(^{Br;\,H}_{Mes}\mathbf{L}^{Mes})\mathbf{H}$	0.842	75	−1.763	72	10.32
$(^{Br}_{Mes}\mathbf{L}^{Mes})\mathbf{H}$	0.994	75	−1.544	63[e]	11.84
$(^{I}_{Mes}\mathbf{L}^{Mes})\mathbf{H}$	0.925	70	−1.547	64[e]	10.64
$(^{H}_{C_6F_5}\mathbf{L}^{Mes})\mathbf{H}$	0.676[d]	—	−1.707	75	8.80
$(^{Cl}_{C_6F_5}\mathbf{L}^{Mes})\mathbf{H}$	1.144	85	−1.264[d]	—	12.64
$(^{Br}_{C_6F_5}\mathbf{L}^{Mes})\mathbf{H}$	1.139	79	−1.251	67	11.84
$(^{H}_{BFP}\mathbf{L}^{Mes})\mathbf{H}$	0.636[d]	—	−1.720	73	8.80

[a] Cyclic voltammetry performed in dichloromethane containing 0.1 *M* (nBu$_4$N)(PF$_6$) at 25 °C; maximum scan rate of 250 mV/s; glassy carbon working electrode, nonaqueous Ag^+/Ag reference electrode, and platinum wire counterelectrode; referenced to $[Cp_2Fe]^{+/0}$. [b] Separation between the voltages of the cathodic and anodic peak currents. [c] The sum of the Pauling electronegativity values of the 2-, 3-, 7-, and 8-positions (X/X′), taken from the ACS online periodic table; H = 2.20, Cl = 3.16, Br = 2.96, I = 2.66.[60] [d] Irreversible; values reported are the potentials at peak half-maximum. [e] Anodic peaks were somewhat obscured by a closely overlapping subsequent wave.

2.3 Conclusions

A wide variety of C_s symmetric dipyrrins can readily be synthesized by established routes. Variations in the substituents at all modifiable positions (1-, 2-, 3-, 5-, 7-, 8-, and 9-) can be achieved through straightforward synthetic routes. Substituents at the 1- and 9-positions are installed by the use of readily available 2-substituted pyrroles. 5-Aryl substituents are installed by the use of aryl aldehydes or acetals, many of which are commercially available or readily synthesized. Halogenation of the dipyrrin with N-halosuccinimides or molecular iodine leads to

functionalization of the 2-, 3-, 7-, and 8-positions. These structural variations lead to predictable and systematic changes in the electronic absorption spectra and the redox potentials for one-electron oxidation and reduction of the dipyrrins.

2.4 Experimental Methods

2.4.1 General Synthetic Considerations

Dipyrrin syntheses were performed under an atmosphere of air. Solvents were purchased from VWR or Aldrich and used as received. Chloroform-*d* and benzene-d_6 for aerobic use were purchased from Cambridge Isotope Labs and used as received. Organic reagents, main-group inorganic reagents, silica, neutral alumina (Brockmann I), and Celite® 545 used for aerobic dipyrrin syntheses were purchased from typical chemical suppliers and used as received, unless otherwise noted. N-chloro-, N-bromo-, and N-iodosuccinimide were purchased from Aldrich and recrystallized from boiling deionized water prior to use. 2-Mesityl,[62] 2-adamant-1-yl, 2-*tert*-butyl, and 2-(2′,4′,6′-triphenyl)phenyl pyrroles[53a] and mesitaldehyde dimethyl acetal[63] were synthesized according to literature procedures.

2.4.2 Characterization and Physical Measurements

Nuclear magnetic resonance experiments were performed on Varian Mercury 400, Varian Unity/Inova 500, or Agilent DD2 600 spectrometers. ^{1}H and ^{13}C NMR chemical shifts are reported relative to $SiMe_4$ using the chemical shift of residual solvent peaks as reference. ^{19}F

[62] Rieth, R. D.; Mankad, N. P.; Calimano, E.; Sadighi, J. P. *Org. Lett.* **2004**, *6*, 3981.
[63] Ji, N.; O'Dowd, H.; Rosen, B. M.; Myers, A. G. *J. Am. Chem. Soc.* **2006**, *128*, 14825.

chemical shifts are reported relative to external $CFCl_3$. Spectra were processed using the ACDLabs SpecManager v. 12 software package.

Mass spectrometry was performed at the Harvard University FAS Center for Systems Biology Mass Spectrometry and Proteomics Resource Laboratory on an Agilent 6210 TOF LC/MS with a dual nebulizer ESI source operating in positive ion mode.

UV/Visible spectra were recorded on a Varian Cary 50 UV/Visible Spectrometer, with a scan rate of 100–300 nm/min. Extinction coefficients were determined from a minimum of four concentrations per sample, and were calculated by a linear regression fit of the absorbance vs. concentration data.

Cyclic voltammetry experiments were carried out using a CH Instruments CHI660C Electrochemical Workstation. The supporting electrolyte was 0.1 *M* (nBu$_4$N)(PF_6) in dichloromethane. A glassy carbon working electrode, platinum wire counter electrode, and a non-aqueous Ag^+/Ag reference electrode (10 m*M* $AgNO_3$ in acetonitrile) were used. The concentration of each analyte was ~0.1 m*M*. Scan rates were 100–500 $^{mV}/_{s}$, depending on the sample. Each scan was referenced to internal Fc^+/Fc; when overlapping redox waves or electron transfer between species in solution obscured the reference peaks, external Fc^+/Fc was used instead.

X-ray crystallographic characterization of **($^{Br;\,H}_{Mes}L^{Mes}$)H** and **($_{Mes}{}^{I}L^{Mes}$)H** was performed at the at the Harvard Center for Crystallographic Studies. Data was obtained on a Bruker three-circle platform goniometer equipped with an Apex II CCD and an Oxford cryostream cooling device. Radiation was from a graphite fine focus sealed tube Mo Kα (λ = 0.71073 Å) source. Crystals were mounted on a cryoloop or glass fiber pin using Paratone-N oil. Structures were collected at 100 K. All data was collected as a series of φ and ω scans. All data was integrated

using SAINT and scaled with a multi-scan absorption correction using SADABS.[64] The structures were solved by direct methods or Patterson maps using SHELXS-97 and refined against F^2 on all data by full matrix least squares with SHELXL-97.[65] All non-hydrogen atoms were refined anisotropically. Hydrogen atoms were placed at idealized positions and refined using a riding model. Full experimental details for all compounds characterized by x-ray diffraction can be found in the Appendix.

2.4.3 Synthetic Procedures

Scheme 2.3. Condensation to form dipyrromethanes

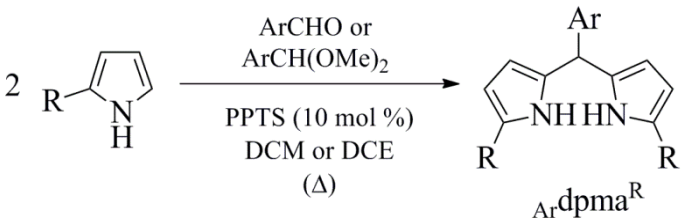

General procedure for condensation with aldehydes or acetals. To a stirring, room temperature solution of 2-substituted pyrrole (2 equiv.) in dichloromethane (DCM) or dichloroethane (DCE) was added the aromatic aldehyde or acetal (1 equiv.), followed by pyridinium *p*-toluene sulfonate (PPTS, 10 mole %). The reaction mixture was allowed to stir for 12–24 hours, then was passed through a plug of silica to remove the acid catalyst and residual water. The plug was washed with excess dichloromethane and the eluent was concentrated in vacuo to afford the dipyrromethanes, abbreviated $_{Ar}$**dpma**^{R}, where Ar is the 5-substituent and R is the 1,9-substituent.

[64] *APEX2 Software Suite*, Bruker AXS: Milwaukee, WI, 2009.
[65] Sheldrick, G. *Acta Crystallogr. Sect. A* **2008**, *64*, 112.

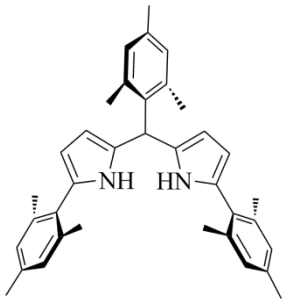

$_{Mes}$**dpma**^{Mes}.[21a] 2-Mesityl pyrrole, mesitaldehyde dimethyl acetal, DCM solvent, room temperature, up to 24 h; >56% yield. ^{1}H NMR (500 MHz, $CDCl_3$) δ ppm 2.12 (s, 3H), 2.13 (s, 18H), 2.15 (s, 6H), 5.61 (s, 1H, methanetriyl-C*H*), 6.02 (apparent t, *J* = 3 Hz, [pyrrole-C*H*]$_2$), 6.08 (apparent t, *J* = 3 Hz, [pyrrole-C*H*]$_2$), 6.73 (s, 2H, {[*meso*-Mes]CH}$_2$), 6.78 (s, 4H, {[flanking-Mes]CH}$_2$), 6.99 (br. s, 2H, N-*H*).

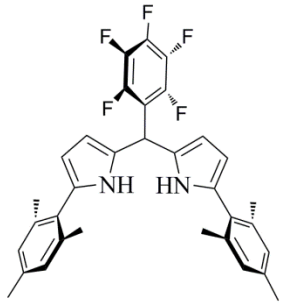

$_{C_6F_6}$**dpma**^{Mes}. 2-Mesityl pyrrole, perfluorobenzaldehyde, DCM solvent, room temperature, 24 h. Activated molecular sieves were also added to the reaction mixture. Triturated from cold dichloromethane; 58% yield. ^{1}H NMR (500 MHz, $CDCl_3$) δ ppm 2.12 (s, 12H, [*o*-*Me*$_2$(C_6H_2Me)]$_2$), 2.33 (s, 6H, [*p*-*Me*($C_6H_2Me_2$)]$_2$), 5.98 (m, 2H + 1H, [pyrrole-C*H*]$_2$ and methanetriyl-C*H*), 6.11 (t, *J* = 2.93 Hz, 2H, [pyrrole-C*H*]$_2$), 6.94 (s, 4H, [$Me_3C_6H_2$]$_2$), 7.91 (br. s., 2H, N*H*). ^{13}C NMR (125 MHz, $CDCl_3$) δ ppm 20.78, 21.28, 33.62, 107.89, 108.82, 127.72, 128.34, 130.05, 130.52, 138.03, 138.62. ^{19}F NMR (375 MHz, $CDCl_3$) δ ppm –161.2 (td, *J* = 22.5 Hz & 7.5 Hz, 2F, *m*-F), –156.27 (t, *J* = 20.6 Hz, 1F, *p*-F), –142.11 (d, *J* = 16.8 Hz, 2F, *o*-F). HR-MS (ESI$^+$, $^{m}/_{z}$ for [M+H]$^+$) calc'd for [$C_{33}H_{29}F_5N_2$+H]: 549.2324, found 549.2329.

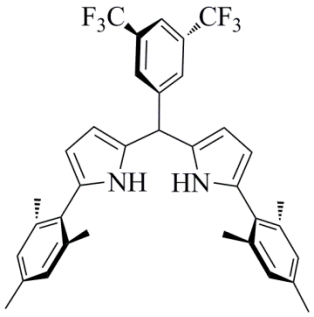

$_{BFP}$**dpma**^{Mes}. 2-Mesityl pyrrole, 3,5-bis(trifluoromethyl)benzaldehyde, DCM solvent, room temperature, 48 hours. Activated molecular sieves were also added to the reaction mixture. Recrystallized from cold hexanes; 87.7% yield. ^{1}H NMR (500 MHz, $CDCl_3$) δ ppm 2.14 (s, 12 H, [*o*-*Me*$_2$(C_6H_2Me)]$_2$), 2.33 (s, 6H, [*p*-*Me*($C_6H_2Me_2$)]$_2$), 5.69 (s, 1H, methanetriyl-C*H*), 5.95 (m, 2H, [pyrrole-C*H*]$_2$), 6.01 (m, 2H, [pyrrole-C*H*]$_2$), 6.94 (s, 4H, [$Me_3C_6H_2$]$_2$), 7.76 (s, 2H + 2H, *o*-H_2($C_6H_1(CF_3)_2$) and [N*H*]$_2$), 7.82 (s, 1H, *p*-*H*($C_6H_2(CF_3)_2$). ^{13}C NMR (125 MHz, $CDCl_3$) δ ppm 20.73, 21.28, 43.90, 108.50, 108.80, 121.18 (spt, $^{3}J_{C\text{-}F}$ = 3.8 Hz), 123.57 (q, $^{1}J_{C\text{-}F}$ = 272 Hz), 128.31, 128.76 (q, $^{3}J_{C\text{-}F}$ = 3.8 Hz), 130.15, 130.45, 130.52, 131.95 (q, $^{2}J_{C\text{-}F}$ = 32 Hz), 138.09, 138.60, 145.57. ^{19}F NMR (375 MHz, $CDCl_3$) δ ppm −63.19 (s, 6F). HR-MS (ESI$^+$, m/z for [M+H]$^+$) calc'd for [$C_{35}H_{32}F_6N_2$+H]: 595.2542, found 595.2456.

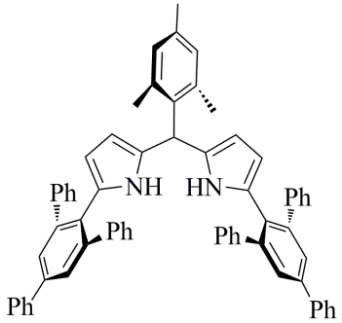

$_{Mes}$**dpma**^{Q}.[53a] 2-(2′,4′,6′-triphenyl)phenyl pyrrole, mesitaldehyde dimethyl acetal, DCE solvent, 100 °C, 96 h. Subject to aerobic oxidation and was not isolated, but carried directly forward to the dipyrrin.

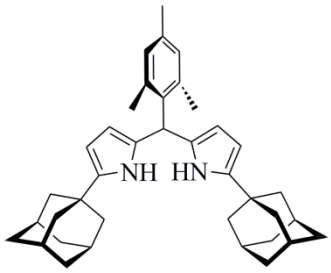

$_{Mes}$**dpma**^{Ad}.[53a] Mesitaldehyde dimethyl acetal, DCM solvent, room temperature, 16 h. Activated molecular sieves were also added to the reaction mixture. Recrystallized from cold hexanes; 69% yield. ^{1}H NMR (500 MHz, $CDCl_3$) δ ppm 1.68–1.82 (m, apparent quartet, 12H), 1.86 (d, *J* = 2.29 Hz, 12H), 1.99–2.15 (m, 12H), 2.31 (s, 3H, *p*-Me [Mes]), 5.66–5.76 (m, 2H, [pyrrole-C*H*]$_2$), 5.78–5.86 (m, 2H + 1H, [pyrrole-C*H*]$_2$ and methanetriyl-C*H*), 6.87 (s, 2H, *m*-H [Mes]), 7.80 (br. s, 2H, N-*H*).

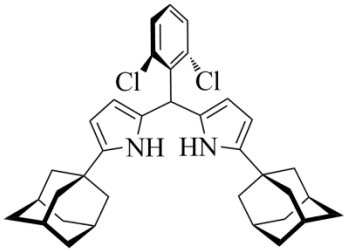

$_{DCP}$**dpma**^{Ad}.[53b] 2-Adamant-1-yl pyrrole, 2,6-dichlorobenzaldehyde, DCM solvent, room temperature, 16 h. Activated molecular sieves were also added to the reaction mixture. 92.3% yield. ^{1}H NMR (600 MHz, $CDCl_3$) δ ppm 1.73–1.85 (m, apparent quartet, 12H), 1.91 (d, *J* = 2.64 Hz, 12H), 2.10 (br. s, 6H), 5.90 (apparent t, *J* = 2 Hz, 2H, [pyrrole-C*H*]$_2$), 5.96 (dd, *J* = 2 Hz & 0.6 Hz), 6.46 (s, 1H, methanetriyl-C*H*), 7.17 (t, *J* = 8.05 Hz, 1H, *p*-H), 7.37 (br. s, 2H, *m*-H), 8.11 (br. s, 2H, N-*H*).

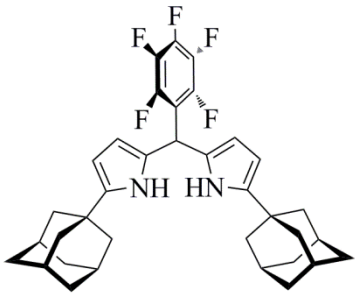

$_{C_6F_6}$**dpma**^{Ad}. 2-Adamant-1-yl pyrrole, perfluorobenzaldehyde, DCM solvent, room temperature, 16 h. Activated molecular sieves were also added to the reaction mixture. Recrystallized from cold pentanes; 53% yield. ^{1}H NMR (500 MHz, $CDCl_3$) δ ppm 1.70–1.83 (m, apparent quartet, 12H), 1.87 (d, *J* = 2.29 Hz, 12H), 2.07 (br. s, 6H), 5.82–5.87 (m, 2H + 1H, [pyrrole-C*H*]$_2$ and methanetriyl-C*H*), 5.88–5.92 (m, 2H, [pyrrole-C*H*]$_2$), 7.92 (br. s, 2H, N-*H*). ^{13}C NMR (125 MHz, $CDCl_3$) δ ppm 28.75, 33.50, 36.95, 43.02, 102.14, 107.27, 126.45, 143.34; extensive C-F coupling obscures the perfluorophenyl ^{13}C signals. ^{19}F NMR (375 MHz, $CDCl_3$) δ ppm –161.96 (td, *J* = 21 Hz & 7 Hz, 2F, *m*-F), –156.84 (t, *J* = 21 Hz, 1F, *p*-F), –142.31 (br. s, 2F, *o*-F). HR-MS (ESI$^+$, $^m/_z$ for $[M+H]^+$) calc'd for $[C_{35}H_{37}F_5N_2+H]$: 581.2950, found 581.2980.

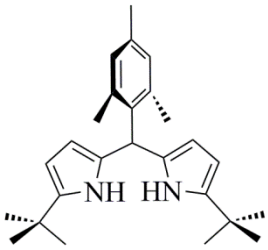

$_{Mes}$**dpma**$^{t\text{Bu}}$[53a]. 2-*tert*-Butyl pyrrole, mesitaldehyde dimethyl acetal, DCM solvent, room temperature, 16 h. Activated molecular sieves were also added to the reaction mixture; 85% yield. ^{1}H NMR (500 MHz, $CDCl_3$) δ ppm 1.12 (s, 18H, *t*Bu), 5.74 (m, 2H, [pyrrole-C*H*]$_2$), 5.85 (m, 2H + 1H, [pyrrole-C*H*]$_2$ and methanetriyl-C*H*), 6.88 (s, 2H, *m*-H[Mes]), 7.76 (br. s, 2H, N-*H*).

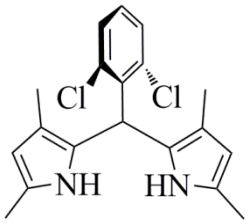

$_{DCP}$**dpma**^{Me}. 2,4-dimethyl pyrrole, 2,6-dichlorobenzaldehyde, DCM solvent. This molecule was susceptible to aerobic oxidation and was not isolated, but was carried directly on to the dipyrrin.

Scheme 2.4. Oxidation with DDQ

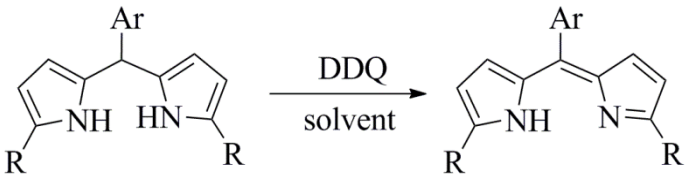

General procedure for oxidation with DDQ. To a stirring, room temperature solution of dipyrromethane in acetone, hexanes, or dichloromethane was added 2,3-dichloro-4,5-dicyanobenzoquinone (DDQ, 1 equiv.); immediate color change was typically observed. After stirring for 1–24 hours, the solvent was removed in vacuo, the residue was taken up in ethyl acetate, washed with saturated aqueous sodium bicarbonate, water, and brine. If the material was insoluble or mildly soluble in the organic layer, it was directly collected by vacuum filtration (*isolation method A)*. If the material was soluble in the organic layer, it was dried over sodium or magnesium sulfate, filtered, and concentrated in vacuo to afford the free-base dipyrrins (*isolation method B)*. Several methods for purification could be employed, depending on the solubility characteristics of the specific dipyrrin. *Purification method A*: Trituration from cold acetonitrile. *Purification method B*: Trituration from cold pentanes. *Purification method C*: Column chromatography on a neutral or basic alumina column, eluting with hexanes.

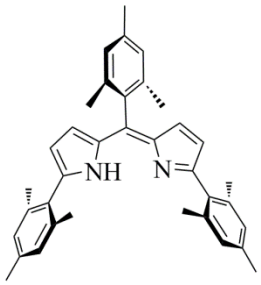

($_{Mes}^{H}$L^{Mes})H.[21a] Acetone solvent, 6 h reaction time. Isolation method A; no purification necessary; 70% yield. ^{1}H NMR (500 MHz, $CDCl_3$) δ ppm 2.22 (s, 6H, [*o*-*Me*($C_6H_2Me_2$)]$_2$ (*meso*-Mes)), 2.23 (s, 12H, [*o*-*Me*$_2$(C_6H_2Me)]$_2$ (flanking Mes)), 2.32 (s, 6H, [*p*-*Me*($C_6H_2Me_2$)]$_2$ (flanking Mes)), 2.40 (s, 3H, [*p*-*Me*($C_6H_2Me_2$)]$_2$, (*meso*-Mes)), 6.23 (d, *J* = 4.12 Hz, 2H, [pyrrole-C*H*]$_2$), 6.42 (d, *J* = 3.89 Hz, 2H, [pyrrole-C*H*]$_2$), 6.92 (s, 4H, [$Me_3C_6H_2$]$_2$ (flanking Mes)), 6.97 (s, 2H, [$Me_3C_6H_2$]$_2$ (*meso*-Mes)). UV/Vis (CH_2Cl_2, 25 °C) λ_{max} = 464 nm, ε = 31,600 $M^{-1}cm^{-1}$.

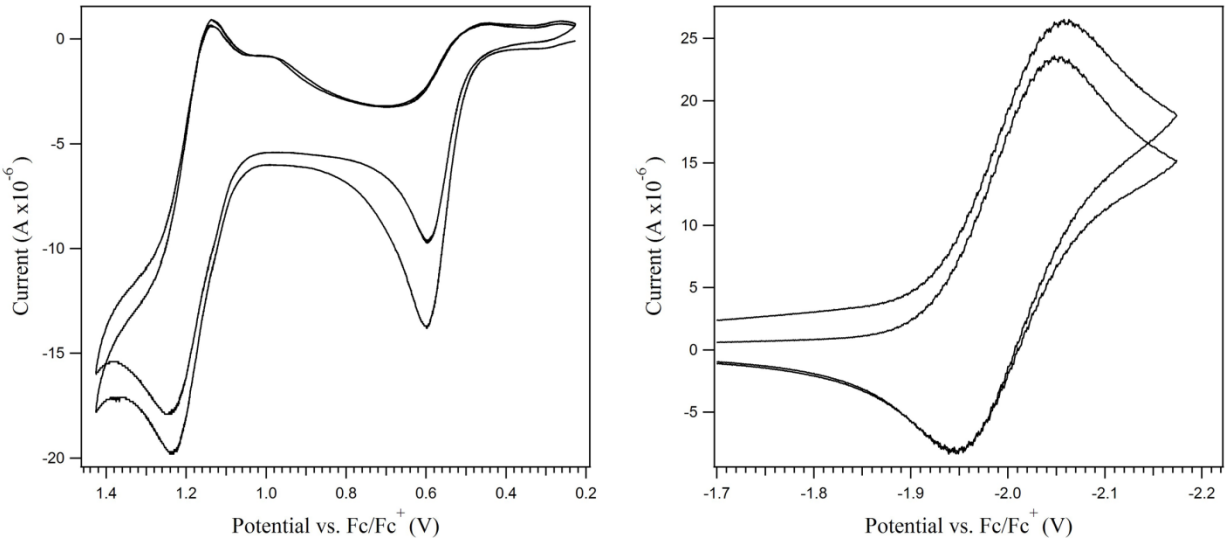

Figure 2.5. Cyclic voltammograms of **($_{Mes}^{H}$L^{Mes})H**. Oxidation, left; reduction, right. For experimental details, see page 32.

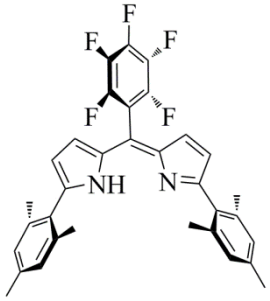

($_{C_6F_5}^{H}$L^{Mes})H. Acetone solvent, 24 h reaction time. Isolation method A; purification method C; 31% yield. ^{1}H NMR (500 MHz, $CDCl_3$) δ ppm 2.24 (s, 12H, [*o*-*Me*$_2$(C_6H_2Me)]$_2$), 2.33 (s, 6H, [*p*-*Me*($C_6H_2Me_2$)]$_2$), 6.35 (d, *J* = 4.12 Hz, 2H, [pyrrole-C*H*]$_2$), 6.53 (d, *J* = 4.12 Hz, 2H, [pyrrole-C*H*]$_2$), 6.94 (s, 4H, [$Me_3C_6H_2$]$_2$), 12.35 (br. s., 1H, N*H*). ^{13}C NMR (125 MHz, $CDCl_3$) δ ppm 20.93, 21.33, 29.96, 120.88, 121.94, 126.67, 128.73, 131.31, 137.34, 138.44, 140.28, 156.63; extensive C-F coupling obscures the ^{13}C signals of the perfluorophenyl group. ^{19}F NMR (376 MHz, C_6D_6) δ ppm –161.76 (td, *J* = 22.5 Hz & 7.5 Hz, 2F, *o*-F), –153.08 (t, *J* = 22.5 Hz, 1F, *p*-F), –139.10 (dd, *J* = 22.5 Hz & 3.75 Hz, 2F, *m*-F). UV/Vis (CH_2Cl_2, 25 °C) λ_{max} = 473 nm, ε = 31,700 $M^{-1}cm^{-1}$. HR-MS (ESI$^+$, m/z for $[M+H]^+$) calc'd for [$C_{33}H_{27}F_5N_2$+H]: 547.2167, found 547.2205.

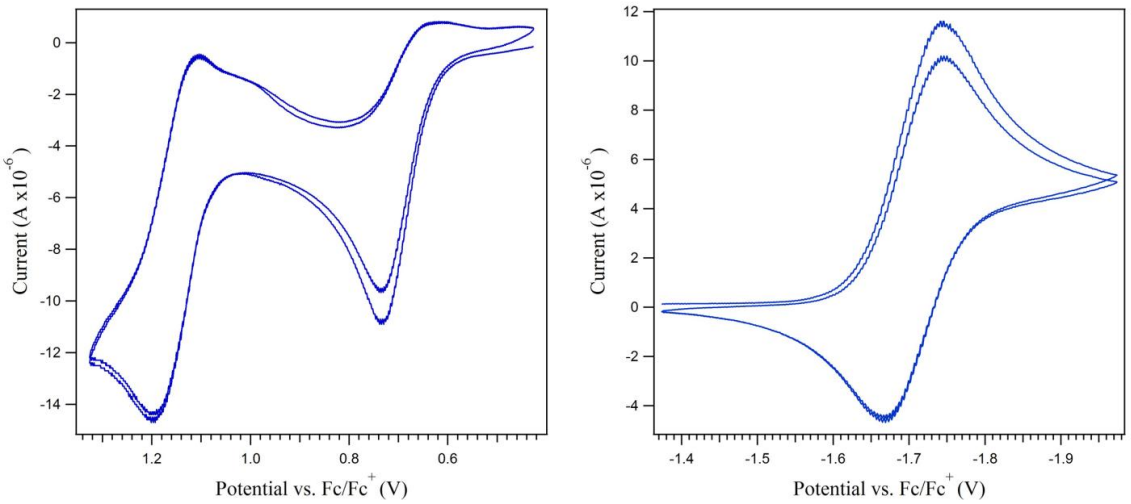

Figure 2.6. Cyclic voltammograms of **($_{C_6F_5}^{H}$L^{Mes})H**. Oxidation, left; reduction, right. For experimental details, see page 32.

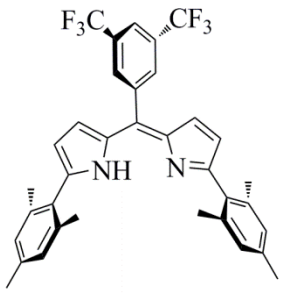

($_{BFP}^{H}L^{Mes}$)H. Acetone solvent, 24 h reaction time. Isolation method A, no purification required; 68% yield. ^{1}H NMR (500 MHz, $CDCl_3$) δ ppm 2.25 (s, 12H, [*o*-*Me*$_2$(C_6H_2Me)]$_2$), 2.33 (s, 6H, [*p*-*Me*($C_6H_2Me_2$)]$_2$), 6.37 (d, *J* = 4.12 Hz, 2H, [pyrrole-C*H*]$_2$), 6.50 (d, *J* = 4.12 Hz, 2H, [pyrrole-C*H*]$_2$), 6.95 (s, 4H, [$Me_3C_6H_2$]$_2$), 8.05 (s, 1H, *p*-*H*($C_6H_2(CF_3)_2$), 8.12 (s, 2H, *o*-H_2($C_6H_1(CF_3)_2$)), 12.59 (br. s., 1H, N*H*). ^{13}C NMR (125 MHz, $CDCl_3$) δ ppm 20.93, 21.33, 120.69, 122.68, 123.50 (q, $^{1}J_{C\text{-}F}$ = 273 Hz), 127.89, 128.73, 131.02, 131.33, 131.44, 131.60, 135.62, 137.29, 138.41, 139.91, 140.43, 156.24. ^{19}F NMR (375 MHz, $CDCl_3$) δ ppm −3.06 (s, 6F, -CF_3). UV/Vis (CH_2Cl_2, 25 °C) λ_{max} = 472 nm, ε = 28,000 $M^{-1}cm^{-1}$. HR-MS (ESI$^+$, $^m/_z$ for $[M+H]^+$) calc'd for [$C_{35}H_{30}F_6N_2$+H]: 593.2386, found 593.2423.

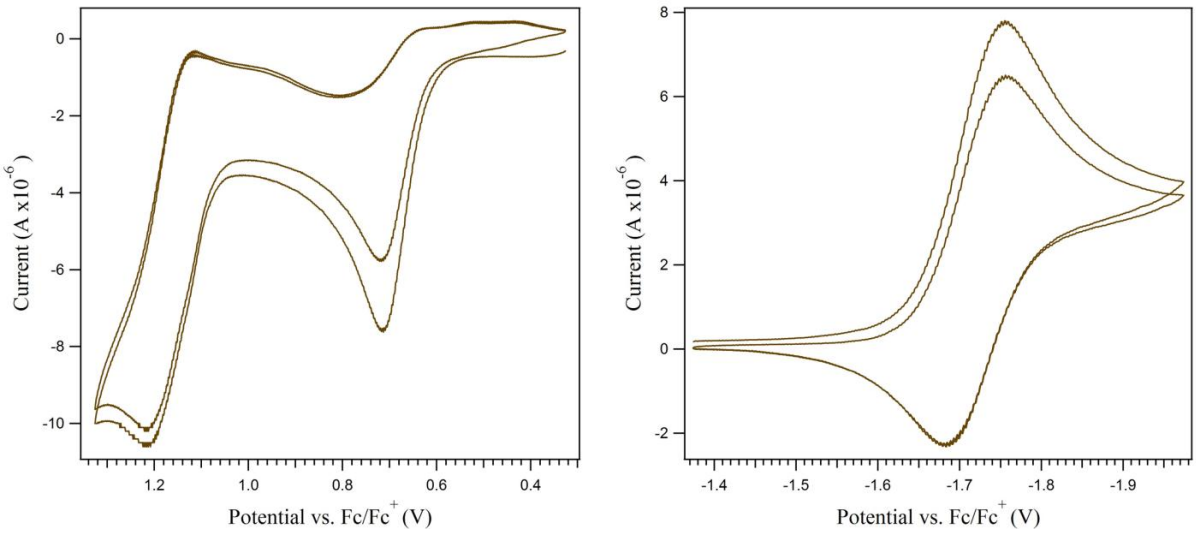

Figure 2.7. Cyclic voltammograms of **($_{BFP}^{H}L^{Mes}$)H**. Oxidation, left; reduction, right. For experimental details, see page 32.

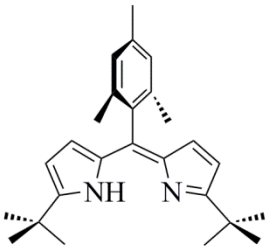

($_{Mes}^{H}$L^{tBu})H. Acetone solvent, 24 h reaction time. Isolation method B, purification method B; 77% yield. ^{1}H NMR (500 MHz, $CDCl_3$) δ ppm 1.41 (s, 18H, *t*Bu), 2.13 (s, 6H, *o*-Me [Mes]), 2.36 (s, 3H, *p*-Me [Mes]), 6.19 (d, *J* = 4.12 Hz, 2H, [pyrrole-C*H*]$_2$), 6.26 (d, *J* = 4.12 Hz, 2H, [pyrrole-C*H*]$_2$), 6.91 (s, 2H, *m*-H [Mes]), 12.91 (br. s, 1H, N-*H*). UV/Vis (CH_2Cl_2, 25 °C) λ_{max} = 447 nm, ε = 29,300 $M^{-1}cm^{-1}$. This compound has been reported elsewhere,[53a] so further characterization was not undertaken.

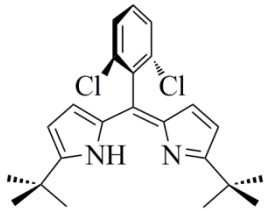

($_{DCP}^{H}$L^{tBu})H. Courtesy of ETH. UV/Vis (CH_2Cl_2, 25 °C) λ_{max} = 450 nm, ε = 33,800 $M^{-1}cm^{-1}$.

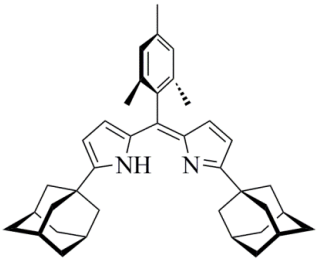

($_{Mes}^{H}$L^{Ad})H. Acetone solvent, 24 h reaction time. Isolation method A, purification method C; 57% yield. ^{1}H NMR (500 MHz, $CDCl_3$) δ ppm 1.76–1.88 (m, 12 H), 2.07 (d, *J* = 2.75 Hz, 12H), 2.12 (s, 12H), 2.35 (s, 3H, *p*-Me [Mes]), 6.18 (d, *J* = 4.12 Hz, 2H, [pyrrole-C*H*]$_2$), 6.26 (d, *J* = 3.66 Hz, 2H, [pyrrole-C*H*]$_2$), 6.90 (s, 2H, *m*-H [Mes]), 13.17 (br. s, 1H, N-*H*). UV/Vis

(CH_2Cl_2, 25 °C) λ_{max} = 453 nm, ε = 29,200 $M^{-1}cm^{-1}$. This compound has been reported elsewhere,[53a] so further characterization was not undertaken.

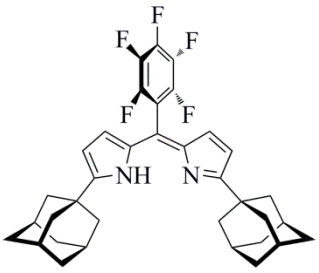

($_{C_6F_5}^{H}L^{Ad}$)H. Acetone solvent, 20 h reaction time. Isolation method A but with 80:20 hexanes:ethyl acetate; purification method C; 78.5% yield. ^{1}H NMR (500 MHz, $CDCl_3$) δ ppm 1.76–1.89 (m, apparent quartet, 12H), 2.05 (d, *J* = 2.29 Hz, 12H), 2.13 (br. s, 6H), 6.29 (d, *J* = 4.12 Hz, 2H, [pyrrole-C*H*]$_2$), 6.37 (d, *J* = 4.12 Hz, 2H, [pyrrole-C*H*]$_2$), 13.09 (br. s, 1H, N-*H*). ^{13}C NMR (125 MHz, $CDCl_3$) δ ppm 28.69, 35.78, 37.06, 42.01, 114.88, 120.93, 126.45, 138.94, 168.09; extensive C-F coupling obscures the ^{13}C signals of the C_6F_5 group. ^{19}F NMR (470 MHz, $CDCl_3$) δ ppm –161.98 (td, *J* = 21 Hz & 7 Hz, 2F, *m*-F), –153.87 (t, *J* = 7 Hz, 1F, *p*-F), –138.70 (dd, *J* = 21 Hz & 7 Hz, 2F, *o*-F). UV/Vis (CH_2Cl_2, 25 °C) λ_{max} = 461 nm, ε = 32,300 $M^{-1}cm^{-1}$. HR-MS (ESI$^+$, $^m/_z$ for $[M+H]^+$) calc'd for $[C_{35}H_{35}F_5N_2+H]$: 579.2793, found 579.3285.

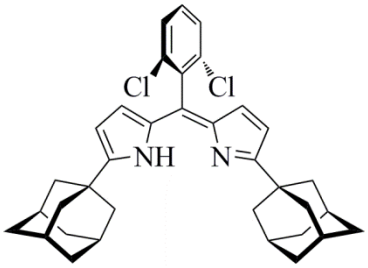

($_{DCP}^{H}L^{Ad}$)H. Acetone solvent, 1 h reaction time. Isolation method A, purification method A; 89.1% yield. ^{1}H NMR (500 MHz, $CDCl_3$) δ ppm 1.77–1.87 (m, 12H), 2.07 (d, *J* = 3.66 Hz, 12H), 2.12 (br. s, 6H), 6.24 (d, *J* = 4.0 Hz, 2H, [pyrrole-C*H*]$_2$), 6.26 (d, *J* = 4.0 Hz, 2H, [pyrrole-C*H*]$_2$), 7.31 (t, *J* = 7.8 Hz, 1H, *p*-H), 7.41 (d, *J* = 7.8 Hz, 2H, *m*-H), 13.03 (br. s, 1H, N-*H*). All

aromatic peaks show higher-order coupling. ^{13}C NMR (125 MHz, $CDCl_3$) δ ppm 28.51, 35.44, 36.87, 41.80, 113.84, 125.89, 127.71, 129.64, 131.81, 135.08, 135.97, 138.25, 166.73. UV/Vis (CH_2Cl_2, 25 °C) λ_{max} = 458 nm, ε = 15,300 $M^{-1}cm^{-1}$. HR-MS (ESI^+, $^m/_z$ for $[M+H]^+$) calc'd for $[C_{35}H_{38}Cl_2N_2+H]$: 557.2485, found 557.2538.

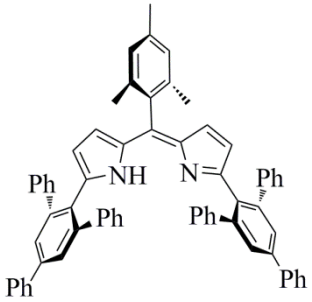

($_{\mathbf{Mes}}^{\mathbf{H}}\mathbf{L}^{\mathbf{Q}}$)H. Courtesy of ERK and MJWT. UV/Vis (CH_2Cl_2, 25 °C) λ_{max} = 507 nm, ε = 25,000 $M^{-1}cm^{-1}$. This compound has been reported elsewhere,[53a] so further characterization was not undertaken.

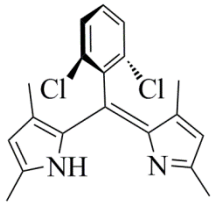

($_{\mathbf{DCP}}^{\mathbf{H;\,Me}}\mathbf{L}^{\mathbf{Me}}$)H. Performed *in situ* with the prior reaction, and PPTS was present. DCM solvent, 5 h reaction time. Isolated and purified by column chromatography using neutral alumina stationary phase and 50:50% ethyl acetate:hexanes mobile phase; 20% purified yield. ^{1}H NMR (500 MHz, C_6D_6) δ ppm 1.53 (d, *J* = 0.92 Hz, 6H, [pyrrole-3-position]Me), 2.03 (s, 6H, [pyrrole-5-position]Me), 5.79 (d, *J* = 0.61 Hz, 2H, [pyrrole-C*H*]$_2$), 6.47–6.60 (t, *J* = 8.3 Hz, 1H, *p*-H), 6.93 (d, *J* = 7.93 Hz, 2H, *m*-H), 13.73 (br. s, 1 H, N-*H*). ^{13}C NMR (125 MHz, C_6D_6) δ ppm 13.70, 15.81, 120.11, 128.23, 129.97, 131.89, 135.84, 135.93, 136.50, 138.57, 152.04. UV/Vis (CH_2Cl_2, 25 °C) λ_{max} = 451 nm, ε = 35,300 $M^{-1}cm^{-1}$.

Scheme 2.5. Chlorination of dipyrrins

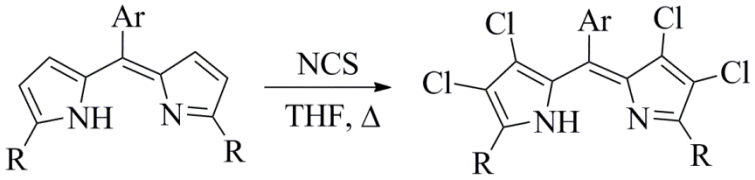

General procedure for chlorination. To a stirring solution of the dipyrrin in THF was added N-chlorosuccinimide (NCS, 6 equiv.); the reaction vessel was sealed and heated for 24 hours. If incomplete chlorination was observed by LC/MS, additional equivalents of NCS were added, and the reaction mixture was allowed to continue stirring at 60 °C for up to one week. Upon complete chlorination as determined by LC/MS, the solvent was removed in vacuo, and the residue was taken up in ethyl acetate, washed with saturated aqueous sodium bicarbonate, water, and brine, then dried over sodium or magnesium sulfate, filtered, and concentrated in vacuo to afford the tetrachlorodipyrrins.

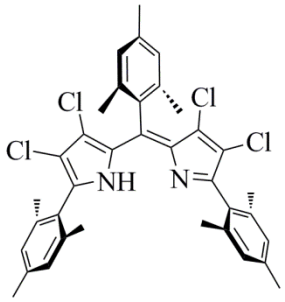

($_{Mes}^{Cl}$L^{Mes})H. Total 5 equivalents NCS, 70 °C, 24 h; 60% yield. ^{1}H NMR (500 MHz, $CDCl_3$) δ ppm 2.16 (s, 12H, [*o*-*Me*$_2$(C_6H_2Me)]$_2$ (flanking Mes)), 2.19 (s, 6H, *o*-*Me*$_2$(C_6H_2Me) [*meso*-Mes]), 2.33 (s, 6H, [*p*-*Me*($C_6H_2Me_2$)]$_2$ (flanking Mes)), 2.41 (s, 3H, *p*-*Me*($C_6H_2Me_2$) [*meso*-Mes]), 6.94 (s, 4H, [$Me_3C_6H_2$]$_2$ (flanking Mes)), 6.98 (s, 2H, $Me_3C_6H_2$ [*meso*-Mes]), 13.12 (br. s, 1H, N-*H*). ^{13}C NMR (125 MHz, $CDCl_3$) δ ppm 20.02, 20.20, 21.44, 21.60, 121.27, 127.54, 128.25, 128.59, 128.75, 129.73, 132.81, 136.21, 137.68, 138.77, 139.37, 140.06, 150.75. UV/Vis (CH_2Cl_2,

25 °C) λ_{max} = 480 nm, ε = 24,800 $M^{-1}cm^{-1}$. HR-MS (ESI$^+$, $^m/_z$ for $[M+H]^+$) calc'd for $[C_{36}H_{34}Cl_4N_2+H]$: 635.1549, found 635.1606.

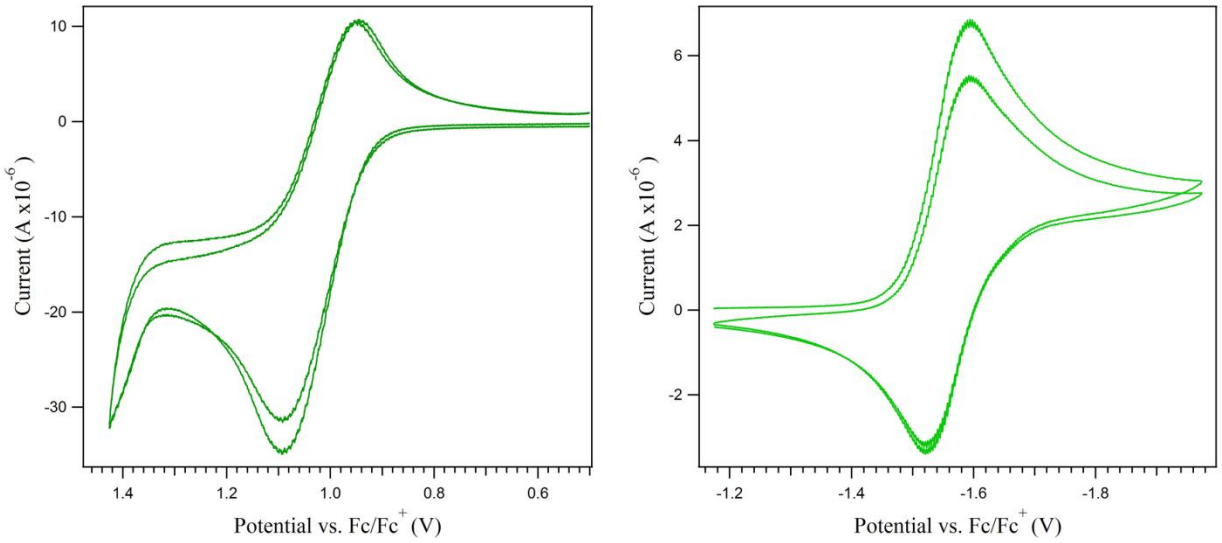

Figure 2.8. Cyclic voltammograms of **($^{Cl}_{Mes}$L^{Mes})H**. Oxidation, left; reduction, right. For experimental details, see page 32.

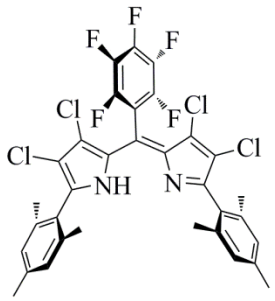

($^{Cl}_{C_6F_5}$L^{Mes})H. Total 10 equivalents of NCS, 60 °C, 48 hours; purified by trituration from cold pentanes; 58.3% yield. ^{1}H NMR (500 MHz, $CDCl_3$) δ ppm 2.17 (s, 12H, [*o*-*Me*$_2$(C_6H_2Me)]$_2$), 2.33 (s, 6H, [*p*-*Me*($C_6H_2Me_2$)]$_2$), 6.95 (s, 4H, [$Me_3C_6H_2$]$_2$), 12.77 (br. s., 1H, N*H*). ^{13}C NMR (125 MHz, $CDCl_3$) δ ppm 20.29, 21.44, 34.38, 122.86, 126.89, 127.52, 128.71, 132.84, 137.70, 139.88, 153.12; extensive C-F coupling obscures the ^{13}C signals of the C_6F_5 group. ^{19}F NMR

(375 MHz, $CDCl_3$) δ ppm –161.90 (td, *J*= 18.8 Hz & 3.75 Hz, 2F, *m*-F), –151.89 (t, *J* = 18.8 Hz, 1F, *p*-F), –139.66 (dd, *J* = 18.8 Hz & 7.5 Hz, 2F, *o*-F). UV/Vis (CH_2Cl_2, 25 °C) λ_{max} = 490 nm, ε = 27,900 $M^{-1}cm^{-1}$. HR-MS (ESI^+, $^m/_z$ for $[M+H]^+$) calc'd for $[C_{33}H_{23}Cl_4F_5N_2+H]$: 683.0608, found 683.0619.

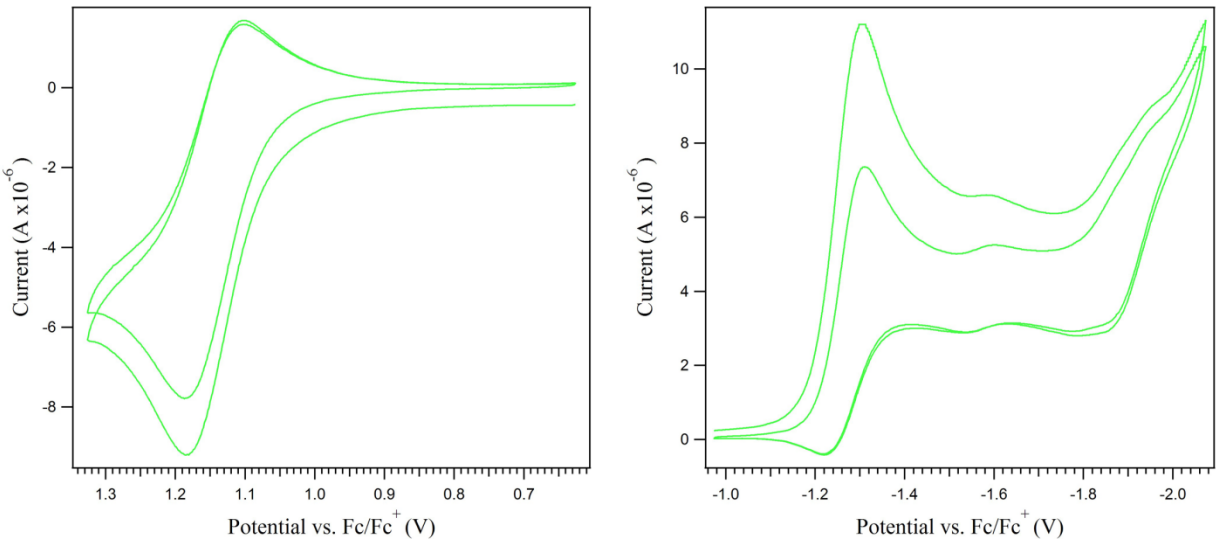

Figure 2.9. Cyclic voltammograms of **($_{C_6F_5}^{Cl}$L^{Mes})H**. Oxidation, left; reduction, right. For experimental details, see page 32.

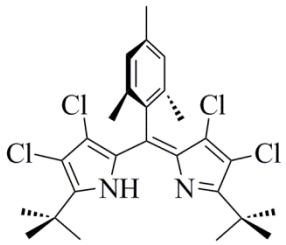

($_{Mes}^{Cl}$L^{tBu})H. Total 12 equiv. NCS, 60 °C, 120 hours; 35% yield. *Alternately:* Chlorination at room temperature with excess NCS in CCl_4 for 48 hours gives slightly improved yields. ^{1}H NMR (600 MHz, $CDCl_3$) δ ppm 1.53 (s, 18H, *t*Bu), 2.12 (s, 6H, *o*-Me [Mes]), 2.40 (s, 3H, *p*-Me [Mes]), 6.94 (s, *m*-H [Mes]), 13.25 (br. s, 1H, N-*H*). ^{13}C NMR (125 MHz, $CDCl_3$) δ ppm 20.08,

21.54, 28.48, 34.65, 118.59, 128.56, 128.71, 129.94, 130.24, 136.32, 138.46, 138.78, 158.37. UV/Vis (CH_2Cl_2, 25 °C) λ_{max} = 466 nm, ε = 25,900 $M^{-1}cm^{-1}$. HR-MS (ESI^+, $^m/_z$ for $[M+H]^+$) calc'd for $[C_{26}H_{30}Cl_4N_2+H]$: 511.1236, found 511.1339.

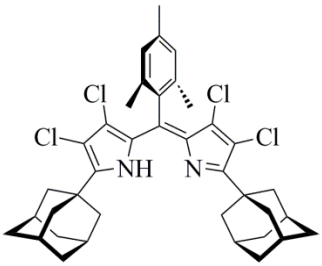

($^{Cl}_{Mes}L^{Ad}$)H. Total 12 equiv. NCS, 75 °C, 120 h, 24% isolated yield. ^{1}H NMR (600 MHz, $CDCl_3$) δ ppm 1.80–1.86 (m, 12H), 2.07 (s, 6H, *o*-Me [Mes]), 2.13 (br. s, 6H), 2.22 (d, *J* = 2.75, 12 H), 2.36 (s, 3H, *p*-Me [Mes]), 6.90 (s, 2H, *m*-H [Mes]), 13.36 (s, 1H, N-*H*). ^{13}C NMR (125 MHz, $CDCl_3$) δ ppm 20.07, 21.54, 28.60, 36.90, 36.97, 39.80, 118.31, 128.51, 128.52, 129.96, 130.42, 136.30, 138.38, 138.63, 157.90. UV/Vis (CH_2Cl_2, 25 °C) λ_{max} = 471 nm, ε = 36,900 $M^{-1}cm^{-1}$. HR-MS (ESI^+, $^m/_z$ for $[M+H]^+$) calc'd for $[C_{38}H_{42}Cl_4N_2+H]$: 667.2175, found 667.2226.

Scheme 2.6. Dibromination of dipyrrins

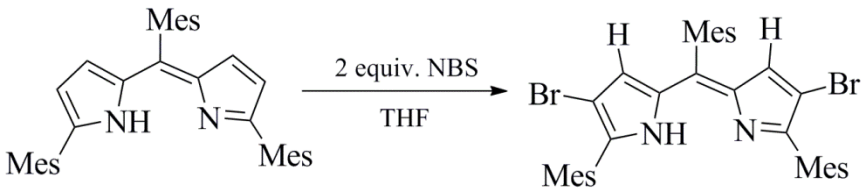

($^{Br;\,H}_{Mes}L^{Mes}$)H. Total 2.00 equivalents of NBS; the residue was taken up in a 1:1 mixture of ethyl acetate and diethyl ether instead of 100% ethyl acetate; 80.8% yield. ^{1}H NMR (500 MHz, $CDCl_3$) δ ppm 2.15 (s, 12H, [*o*-*Me*$_2$(C_6H_2Me)]$_2$ (flanking Mes)), 2.21 (s, 6H, *o*-*Me*$_2$(C_6H_2Me) [*meso*-Mes]), 2.33 (s, 6H, [*p*-*Me*($C_6H_2Me_2$)]$_2$ (flanking Mes)), 2.40 (s, 3H, *p*-*Me*($C_6H_2Me_2$) [*meso*-Mes]), 6.51 (s, 2H, [pyrrole C*H*]$_2$), 6.94 (s, 4H, [$Me_3C_6H_2$]$_2$ (flanking Mes)), 6.98 (s, 2H,

$Me_3C_6H_2$ [*meso*-Mes]), 12.16 (br. s., 1H, N*H*). ^{13}C NMR (125 MHz, $CDCl_3$) δ ppm 20.21, 20.24, 21.39, 21.45, 108.77, 125.41, 127.93, 128.20, 128.34, 129.41, 132.80, 136.89, 137.74, 138.14, 138.89, 139.91, 153.55. UV/Vis (CH_2Cl_2, 25 °C) λ_{max} = 471 nm, ε = 49,000 $M^{-1}cm^{-1}$. HR-MS (ESI^+, $^m/_z$ for $[M+H]^+$) calc'd for $[C_{36}H_{36}Br_2N_2+H]$: 655.1318, found 655.1365. Crystals suitable for X-ray diffraction were grown from slow evaporation of a concentrated solution in chloroform-*d*. The structure was solved in the monoclinic space group *C*2/*c*, with four molecules in the unit cell and half a molecule in the asymmetric unit. The 5-carbon of the dipyrrin and the *meso*-mesityl group reside on a crystallographic mirror plane. The N-H proton was refined using a riding model and was placed arbitrarily on a single nitrogen in the structure illustrated in Figure 2.1.

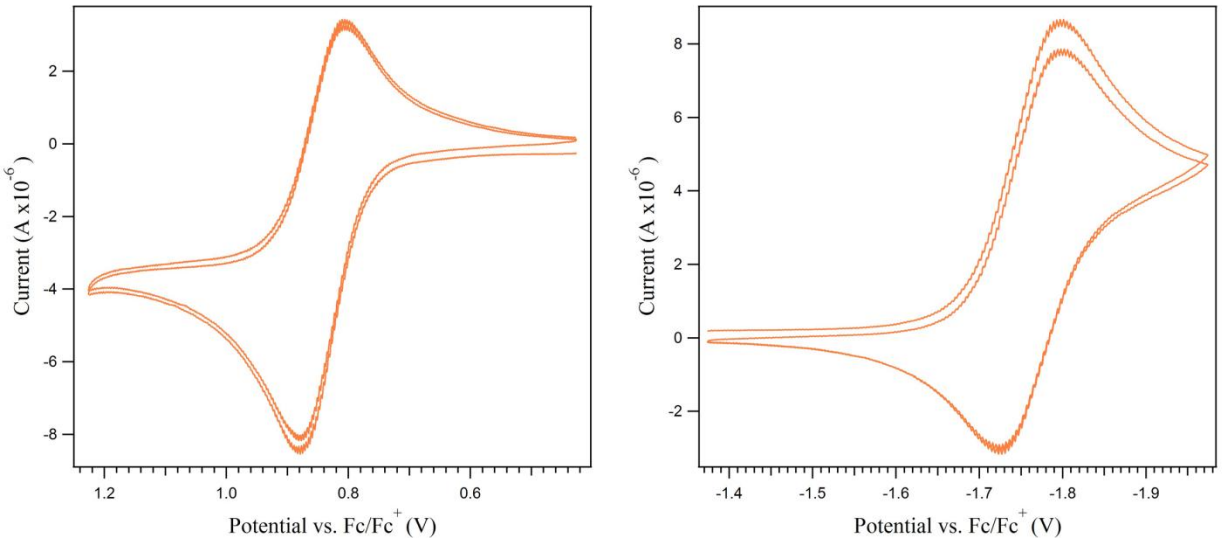

Figure 2.10. Cyclic voltammograms of $(^{Br;\,H}_{Mes}L^{Mes})H$. Oxidation, left; reduction, right. For experimental details, see page 32.

Scheme 2.7. Tetrabromination of dipyrrins

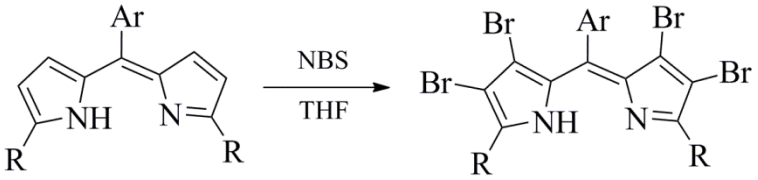

General procedure for tetrabromination. To a stirring solution of the dipyrrin in THF was added N-bromosuccinimide (NBS, 4+ equivalents), and the reaction mixture was allowed to stir at room temperature for up to 24 hours. The solvent was then removed in vacuo, and the residue was taken up in ethyl acetate, washed with saturated aqueous sodium bicarbonate, water, and brine, then dried over sodium or magnesium sulfate, filtered, and concentrated in vacuo to afford the tetrabromodipyrrins.

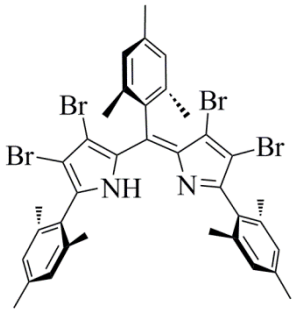

($_{Mes}^{Br}L^{Mes}$)H. Total 4.2 equivalents of NBS; 98% yield. ^{1}H NMR (500 MHz, $CDCl_3$) δ ppm 2.13 (s, 12H, [*o*-*Me*$_2$(C_6H_2Me)]$_2$ (flanking Mes)), 2.15 (s, 6H, *o*-*Me*$_2$(C_6H_2Me) [*meso*-Mes]), 2.33 (s, 6H, [*p*-*Me*($C_6H_2Me_2$)]$_2$ (flanking Mes)), 2.41 (s, 3H, *p*-*Me*($C_6H_2Me_2$) [*meso*-Mes]), 6.93 (s, 4H, [$Me_3C_6H_2$]$_2$ (flanking Mes)), 6.99 (s, 2H, $Me_3C_6H_2$ [*meso*-Mes]), 13.51 (br. s., 1H, N*H*). ^{13}C NMR (125 MHz, $CDCl_3$) δ ppm 20.11, 20.24, 21.45, 21.66, 113.91, 118.21, 128.49, 129.01, 129.23, 129.88, 134.74, 136.91, 137.54, 139.16, 139.26, 153.13. UV/Vis (CH_2Cl_2, 25 °C) λ_{max} = 485 nm, ε = 26,700 $M^{-1}cm^{-1}$. HR-MS (ESI$^+$, $^m/_z$ for $[M+H]^+$) calc'd for [$C_{36}H_{34}Br_4N_2$+H]: 810.9528, found 810.9602.

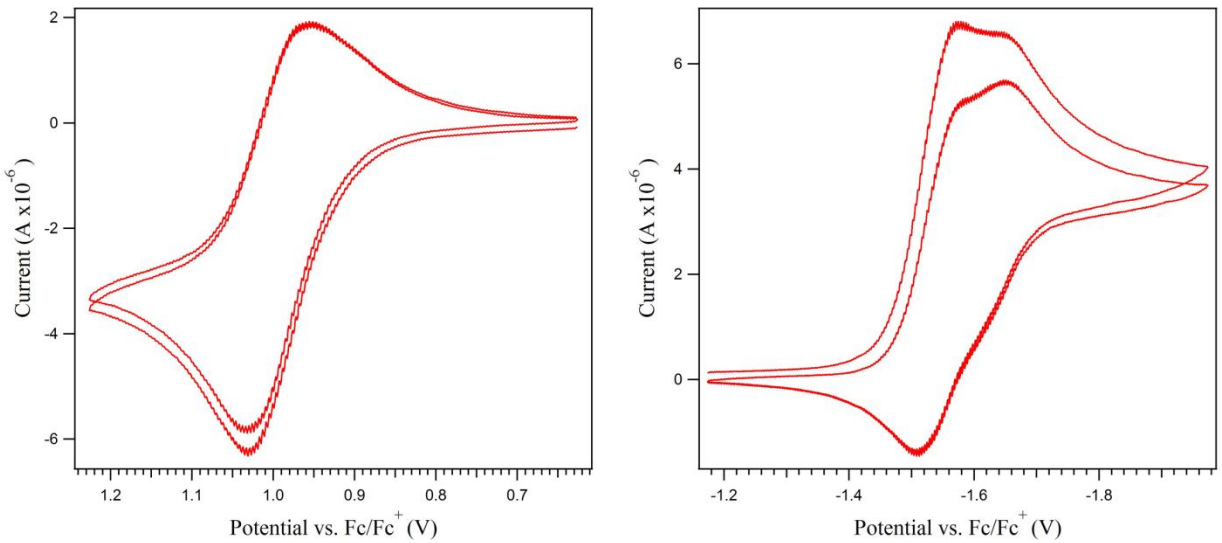

Figure 2.11. Cyclic voltammograms of **($^{Br}_{Mes}$L^{Mes})H**. Oxidation, left; reduction, right. For experimental details, see page 30.

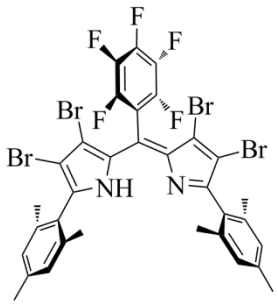

($^{Br}_{C_6F_5}$L^{Mes})H. Total 6.5 equiv. NBS, 48 h; triturated from cold methanol; 58.2% yield. ^{1}H NMR (500 MHz, $CDCl_3$) δ ppm 2.13 (s, 12H, [*o*-*Me*$_2$(C_6H_2Me)]$_2$), 2.33 (s, 6H, [*p*-*Me*($C_6H_2Me_2$)]$_2$), 6.93 (s, 4H, [$Me_3C_6H_2$]$_2$), 13.08 (br. s., 1H, N*H*). ^{13}C NMR (125 MHz, $CDCl_3$) δ ppm 20.34, 21.45, 29.95, 115.49, 117.80, 128.50, 128.61, 134.85, 137.55, 139.74, 155.43; extensive C-F coupling obscures the ^{13}C signals of the C_6F_5 group. ^{19}F NMR (375 MHz, $CDCl_3$) δ ppm –161.97 (td, *J* = 18.8 Hz & 3.75 Hz, 2F, *m*-F), –152.03 (t, *J* = 18.8 Hz, 1F, *p*-F), –139.24 (dd, *J* = 22.5 Hz & 7.5 Hz, 2F, *o*-F). UV/Vis (CH_2Cl_2, 25 °C) λ_{max} = 496 nm, ε = 30,700 $M^{-1}cm^{-1}$. HR-MS (ESI$^+$, $^m/_z$ for $[M+H]^+$) calc'd for [$C_{33}H_{23}Br_4F_5N_2$+H]: 858.8588, found 858.8742.

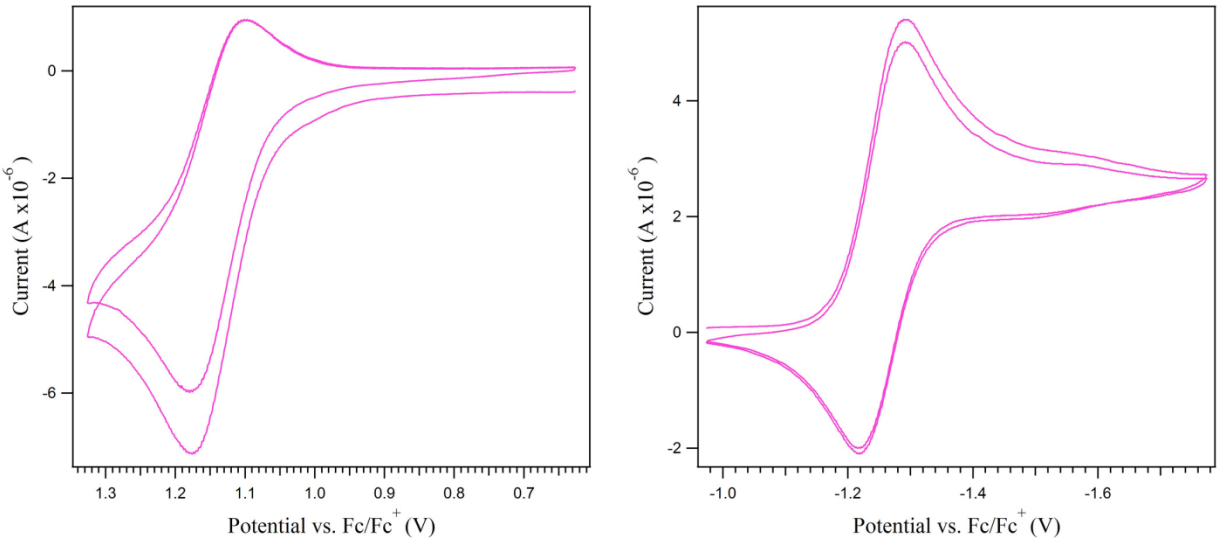

Figure 2.12. Cyclic voltammograms of **($_{C_6F_5}^{Br}$L^{Mes})H**. Oxidation, left; reduction, right. For experimental details, see page 32.

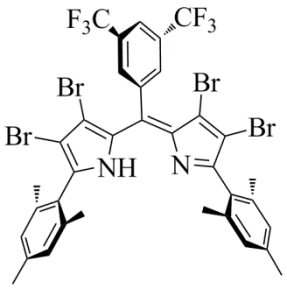

($_{BFP}^{Br}$L^{Mes})H. Total 6.5 equiv. NBS, 96 h; triturated from cold methanol; 12% yield. ^{1}H NMR (500 MHz, $CDCl_3$) δ ppm 2.14 (s, 12H, [*o*-*Me*$_2$(C_6H_2Me)]$_2$), 2.33 (s, 6H, [*p*-*Me*($C_6H_2Me_2$)]$_2$), 6.94 (s, 4H, [$Me_3C_6H_2$]$_2$), 7.97 (s, 2H, *o*-H [BFP]), 8.09 (s, 1H, *p*-H [BFP]), 13.31 (br. s, 1H, N-*H*). ^{13}C NMR (125 MHz, $CDCl_3$) δ ppm 20.37, 21.45, 29.96, 115.39, 118.60, 128.61, 128.69, 131.52, 132.67, 134.90, 135.94, 137.52, 139.67, 154.96. ^{19}F NMR (375 MHz, $CDCl_3$) δ ppm –63.16 (s, 6F, -C*F*$_3$). UV/Vis (CH_2Cl_2, 25 °C) λ_{max} = 492 nm, ε = 28,000 $M^{-1}cm^{-1}$. HR-MS (ESI$^+$, $^m/_z$ for [M+H]$^+$) calc'd for [$C_{35}H_{26}Br_4F_6N_2$+H]: 904.8806, found 904.8852.

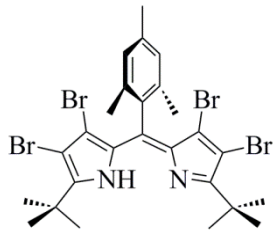

($_{Mes}^{Br}$L^{tBu})H. Total 4.0 equiv. NBS, 16 h; 72% yield. Recrystallized from cold ethyl acetate. ^{1}H NMR (500 MHz, $CDCl_3$) δ ppm 1.52 (s, 18H, *t*Bu), 2.04 (s, 6H, *o*-Me [Mes]), 2.37 (s, 3H, *p*-Me [Mes]), 6.91 (s, 2H, *m*-H [Mes]), 13.55 (br. s, 1H, N-*H*). ^{13}C NMR (125 MHz, $CDCl_3$) δ ppm 20.18, 21.60, 28.77, 34.89, 110.08, 120.17, 128.84, 130.18, 132.20, 137.07, 138.86, 139.68, 160.07. UV/Vis (CH_2Cl_2, 25 °C) λ_{max} = 472 nm, ε = 39,700 $M^{-1}cm^{-1}$. HR-MS (ESI$^+$, $^m/_z$ for $[M+H]^+$) calc'd for $[C_{26}H_{30}Br_4N_2+H]$: 686.9215, found 686.9207.

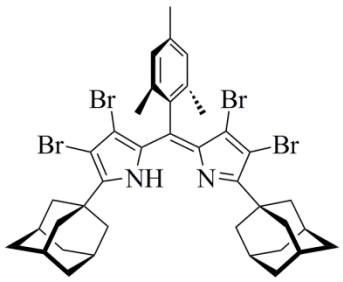

($_{Mes}^{Br}$L^{Ad})H. Total 5.0 equiv. NBS, 2.5 h; 66.3% yield. ^{1}H NMR (500 MHz, $CDCl_3$) δ ppm 1.83 (br. s, 12H), 2.03 (s, 6H, *o*-Me [Mes]), 2.13 (br. s, 6H), 2.26 (d, *J* = 2.75 Hz, 12H), 2.36 (s, 3H, *p*-Me [Mes]), 6.90 (s, 2H, *m*-H [Mes]), 13.65 (br. s, 1H, N-*H*). ^{13}C NMR (125 MHz, $CDCl_3$) δ ppm 20.18, 21.60, 28.66, 36.89, 37.19, 39.89, 109.55, 120.04, 128.81, 130.21, 132.32, 137.05, 138.81, 139.58, 159.50. UV/Vis (CH_2Cl_2, 25 °C) λ_{max} = 478 nm, ε = 36,100 $M^{-1}cm^{-1}$. HR-MS (ESI$^+$, $^m/_z$ for $[M+H]^+$) calc'd for $[C_{38}H_{42}Br_4N_2+H]$: 843.0154, found 842.9824.

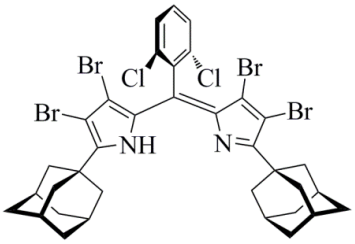

($_{DCP}^{Br}L^{Ad}$)H. Total 6.0 equiv. NBS, 18 h; 80% yield. ^{1}H NMR (500 MHz, $CDCl_3$) δ ppm 1.83 (br. s, 12H), 2.14 (br. s, 6H), 2.27 (br. s, 12H), 7.36–7.42 (m, 2H + 1H, aryl-*H*), 13.52 (s, 1H, N-*H*). ^{13}C NMR (125 MHz, $CDCl_3$) δ ppm 28.62, 36.85, 37.36, 39.80, 110.14, 119.50, 128.45, 131.22, 132.03, 132.36, 136.67, 160.56. UV/Vis (CH_2Cl_2, 25 °C) λ_{max} = 486 nm, ε = 39,400 $M^{-1}cm^{-1}$.

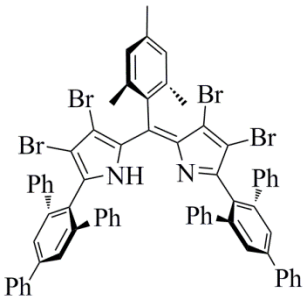

($_{Mes}^{Br}L^{Q}$)H. Total 4.1 equiv. NBS, 12 h; 72% yield. ^{1}H NMR (500 MHz, $CDCl_3$) δ ppm 1.92 (s, 6H), 2.33 (s, 3H), 6.88 (s, 2H), 7.00–7.08 (m, 16H), 7.11–7.20 (m, 4H), 7.45 (t, *J* = 7.4 Hz, 2H), 7.54 (t, *J* = 7.5 Hz, 4H), 7.77–7.89 (m, 8H), 12.07 (br. s., 1H). ^{13}C NMR (125 MHz, $CDCl_3$) δ ppm 19.35, 21.61, 117.06, 127.56, 127.61, 127.94, 128.05, 128.26, 128.79, 129.04, 129.27, 129.35, 129.90, 134.44, 136.54, 139.88, 139.95, 140.39, 140.69, 142.88, 143.64, 151.75. UV/Vis (CH_2Cl_2, 25 °C) λ_{max} = 520 nm, ε = 35,300 $M^{-1}cm^{-1}$. HR-MS (ESI^+, $^{m}/_{z}$ for $[M+H]^+$) calc'd for $[C_{66}H_{46}Br_4N_2+H]$: 1183.04673, found 1183.04968.

Scheme 2.8. Iodination under basic conditions

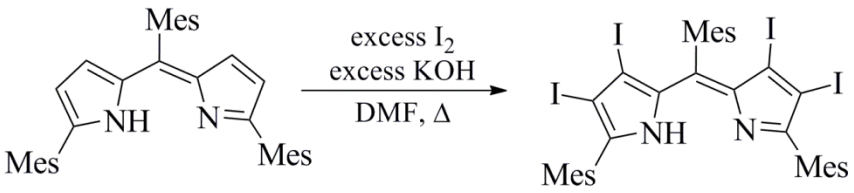

($_{Mes}^{I}$L^{Mes})H. To a darkened solution of **($_{Mes}^{H}$L^{Mes})H** (1.00 mmol) in dimethylformamide was added iodine (5.00 mmol) and solid potassium hydroxide (6.00 mmol) and the mixture was allowed to stir at room temperature for 16 hours, whereupon MS showed incomplete conversion, so the reaction vessel was heated to 75 °C and additional iodine and potassium hydroxide were added. After stirring for 48 hours, MS showed complete conversion, so the reaction was quenched with saturated aqueous sodium sulfite and poured into ethyl acetate. The resulting suspension was washed with saturated aqueous sodium bicarbonate and twice with water, and the solid suspended in the organic layer was collected by vacuum filtration and concentrated in vacuo to afford 677 mg (67.7%) of the title compound as a bright red-orange solid. ^{1}H NMR (500 MHz, $CDCl_3$) δ ppm 2.09 (s, 12H, [*o*-*Me*$_2$(C_6H_2Me)]$_2$ (flanking Mes)), 2.10 (s, 6H, *o*-*Me*$_2$(C_6H_2Me) [*meso*-Mes]), 2.33 (s, 6H, [*p*-*Me*($C_6H_2Me_2$)]$_2$ (flanking Mes)), 2.43 (s, 3H, *p*-*Me*($C_6H_2Me_2$) [*meso*-Mes]), 6.92 (s, 4H, [$Me_3C_6H_2$]$_2$ (flanking Mes)), 7.04 (s, 2H, $Me_3C_6H_2$ [*meso*-Mes]), 13.91 (br. s., 1H, N-*H*). ^{13}C NMR (125 MHz, $CDCl_3$) δ ppm 20.32, 20.34, 21.47, 21.74, 96.99, 97.91, 128.37, 129.80, 130.07, 131.15, 137.28, 138.41, 138.42, 139.05, 139.99, 140.87, 157.94. UV/Vis (CH_2Cl_2, 25 °C) λ_{max} = 503 nm, ε = 47,200 $M^{-1}cm^{-1}$. HR-MS (ESI^+, $^m/_z$ for $[M+H]^+$) calc'd for [$C_{36}H_{34}I_4N_2$+H]: 1002.8974, found 1002.9054. Crystals suitable for X-ray diffraction were grown from slow evaporation of a chloroform-*d* solution. The structure was solved in the

monoclinic space group $P2_1/n$, with four molecules in the unit cell and a single molecule in the asymmetric unit. The hydrogen atoms were arbitrarily placed on N2 in Figure 2.13.

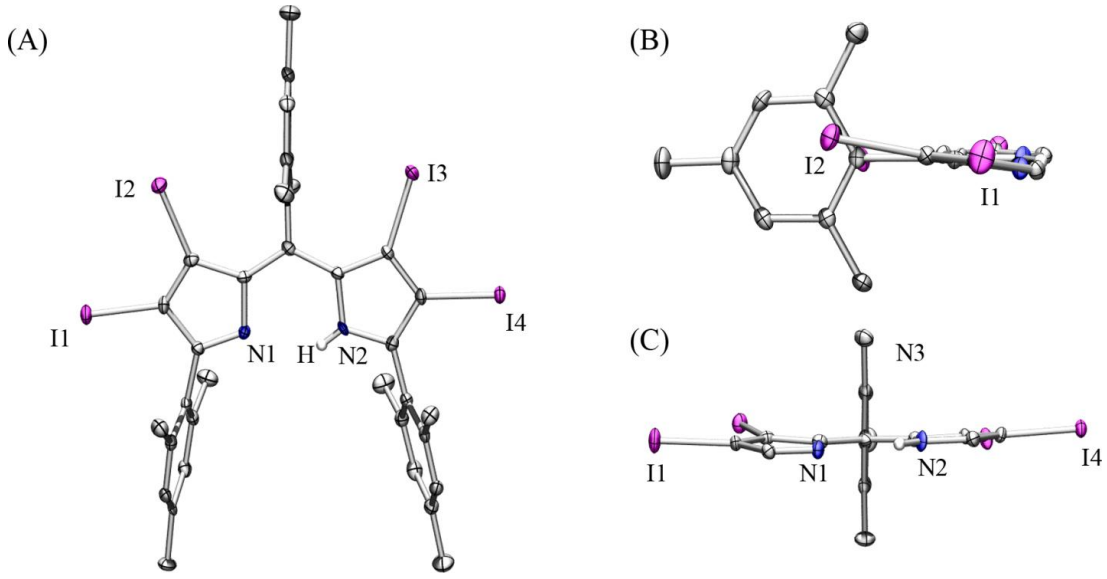

Figure 2.13. Solid-state structure of **($_{Mes}^{I}$L^{Mes})H** with ellipsoids set at the 50% probability level. Hydrogen atoms, except the N-H, have been omitted for clarity, and the N-H hydrogen has been arbitrarily placed on N2. (A) Whole molecule. (B) Side view, illustrating near-planarity of the dipyrrin core; flanking mesityl groups have been omitted for clarity. (C) Front view, illustrating the orthogonality of the dipyrrin with the *meso*-mesityl group (see Section 3.6 for further discussion); flanking mesityl groups have been omitted for clarity. Gray, C; blue, N; purple, I.

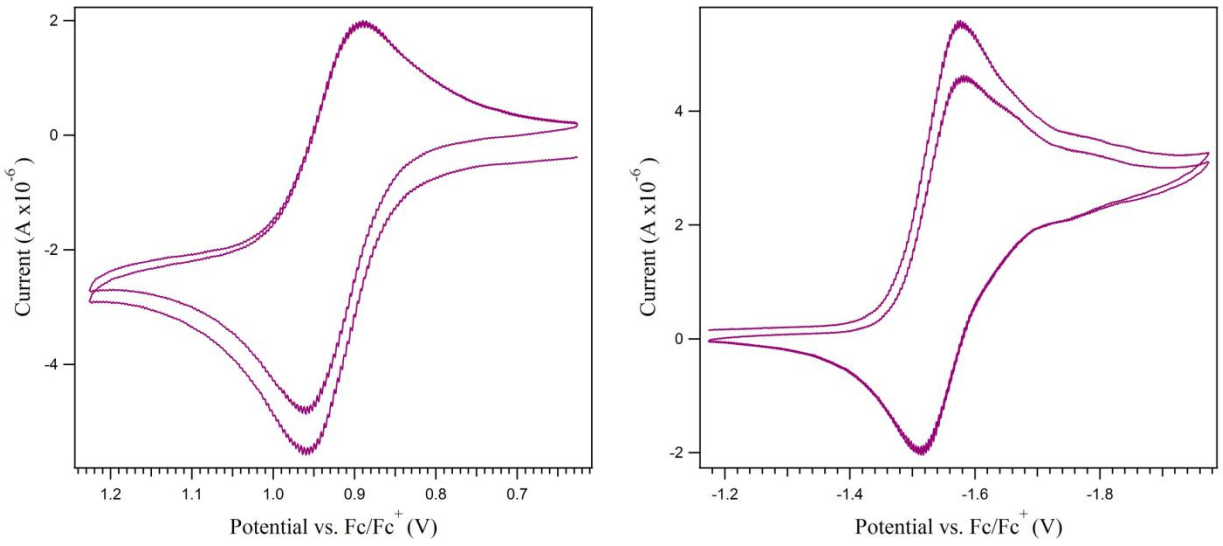

Figure 2.14. Cyclic voltammograms of **($_{Mes}^{I}$L^{Mes})H**. Oxidation, left; reduction, right. For experimental details, see page 32.

Scheme 2.9. Iodination under acidic conditions

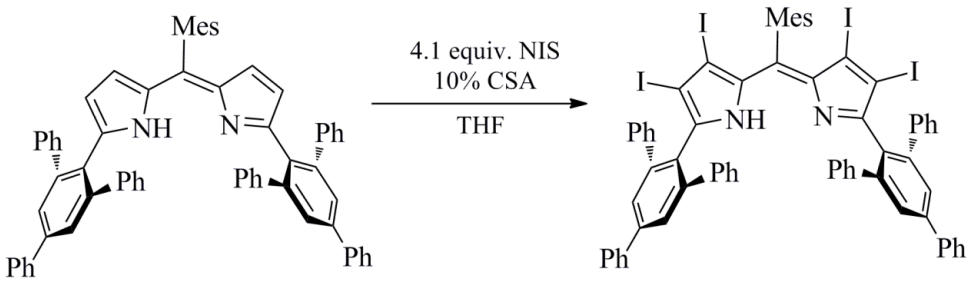

($_{\mathbf{Mes}}^{\mathbf{I}}$ L$^{\mathbf{Q}}$)H. To a darkened, stirring solution of **($_{\mathbf{Mes}}^{\mathbf{H}}$ L$^{\mathbf{Q}}$)H** (0.173 mmol) in anhydrous tetrahydrofuran was added N-iodo-succinimide (0.706 mmol) and catalytic camphor sulfonic acid (CSA). After stirring for 1 week at ambient temperature, the solvent was removed in vacuo. The residue was taken up in ethyl acetate, washed with saturated aqueous sodium bicarbonate, water, and brine, then dried over magnesium sulfate, filtered, and concentrated in vacuo. The residue was purified by passage through a neutral alumina plug eluting with dichloromethane, and dried in vacuo to afford the clean product in 65% yield. ^{1}H NMR (500 MHz, C_6D_6) δ ppm 2.10 (s, 6H, *o*-Me [Mes]), 2.21 (s, 3H, *p*-Me [Mes]), 6.89 (s, 2H, [pyrrole-C*H*]$_2$), 6.92–7.03 (m, 8H), 7.14 (s, 12H), 7.21 (d, *J* = 7.02 Hz, 6H), 7.35–7.45 (m, 4H), 7.74 (s, 4H), 12.80 (br. s, 1H, N-*H*). ^{13}C NMR (125 MHz) δ ppm 19.77, 21.44, 96.39, 99.20, 127.54, 128.06, 128.20, 129.03, 129.70, 130.95, 138.48, 139.67, 140.20, 140.35, 140.90, 142.10, 142.99, 143.77, 157.09. UV/Vis (CH_2Cl_2, 25 °C) λ_{max} = 539 nm, ε = 34,900 $M^{-1}cm^{-1}$.

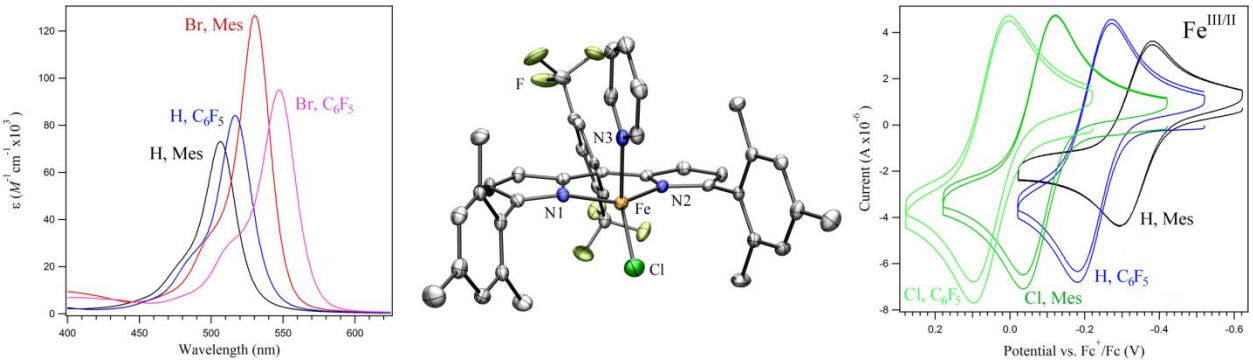

Chapter 3: Effects of Halogenation & *meso*-Fluoroarylation on Iron Dipyrrinato Complexes[66]

Iron(II) dipyrrinato complexes are interesting in their utility as catalysts for olefin aziridination and C-H amination.[53] The electronic, structural, and spectroscopic properties of these complexes can be rationally modified by varying: 1) pyrrole backbone substituents, X and X′; 2) the *meso*-Ar group; 3) the flanking R group; 4) the metal itself; or 5) the anionic ligand Y. Variations of the first four types are discussed throughout this dissertation. In this chapter, we will limit our discussion to the effects of halogenation and *meso*-fluoroarylation of Fe(II) dipyrrinato complexes (Figure 3.1).

[66] Chapter 3, Sections 3.1–3.5 were adapted with permission from Scharf, A. B.; Betley, T. A. *Inorg. Chem.* **2011**, *50*, 6837.

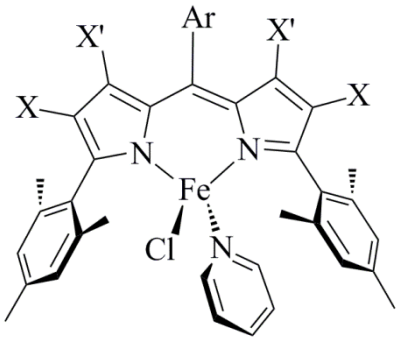

Figure 3.1. Generic structure of halogenated dipyrrinato iron(II) complexes described in Chapter 3. Ar = Mes, C_6F_5, or 3′,5′-bis(trifluoromethyl)phenyl (BFP). X; X′ = H, Cl, Br, or I.

3.1 Synthesis of Iron Dipyrrinato Complexes

The iron complexes discussed in this chapter were synthesized as illustrated in Scheme 3.1. The respective dipyrrins were deprotonated with LiHMDS and the resulting lithium salts[43,67] were metalated with $FeCl_2$ in thawing THF in the presence of excess pyridine. The resulting iron complexes were isolated by removal of the solvent in vacuo, dissolution in benzene, filtration through Celite, and concentration to give the products as red/green or orange/green dichroic powders or microcrystalline solids in good yields (Table 3.1).

Scheme 3.1. Synthesis of Fe(II) dipyrrinato complexes

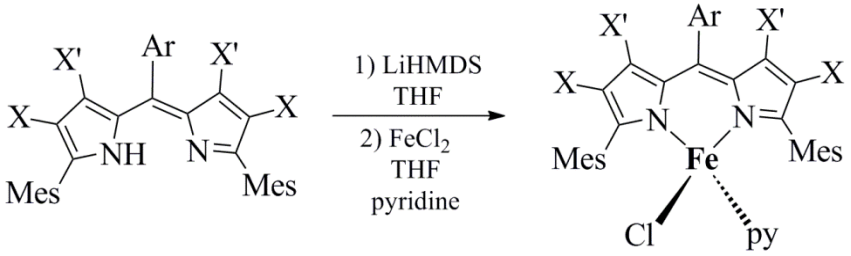

[67] Cipot-Wechsler, J.; Ali, A. A.-S.; Chapman, E. E.; Cameron, T. S.; Thompson, A. *Inorg. Chem.* **2007**, *46*, 10947.

Table 3.1. Iron(II) complexes discussed in Chapter 3

Number	Compound	Ar	X	X′	yield (%)[a]
1	**($_{Mes}^{H}$L^{Mes})FeCl(py)**	Mes	H	H	95
2	**($_{Mes}^{Cl}$L^{Mes})FeCl(py)**	Mes	Cl	Cl	77
3	**($_{Mes}^{Br; H}$L^{Mes})FeCl(py)**	Mes	Br	H	81
4	**($_{Mes}^{Br}$L^{Mes})FeCl(py)**	Mes	Br	Br	67
5	**($_{Mes}^{I}$L^{Mes})FeCl(py)**	Mes	I	I	51
6	**($_{C_6F_5}^{H}$L^{Mes})FeCl(py)**	C_6F_5	H	H	87
7	**($_{C_6F_5}^{Cl}$L^{Mes})FeCl(py)**	C_6F_5	Cl	Cl	81
8	**($_{C_6F_5}^{Br}$L^{Mes})FeCl(py)**	C_6F_5	Br	Br	76
9	**($_{BFP}^{H}$L^{Mes})FeCl(py)**	3′,5′-$(CF_3)_2C_6H_3$	H	H	89

[a] Isolated yield of final metalation step. Abbreviations used: Mes = 2′,4′,6′-trimethylphenyl, mesityl; BFP = 3′,5′-**b**is(tri**f**luoromethyl)**p**henyl.

Complexes **1**–**9** were all characterized by paramagnetic ^{1}H NMR spectroscopy, UV/Vis spectroscopy, cyclic voltammetry (CV), zero-field ^{57}Fe Mössbauer spectroscopy, and x-ray crystallography. Fluorine-containing molecules were also characterized by paramagnetic ^{19}F NMR spectroscopy.

3.2 Nuclear Magnetic Resonance Spectroscopy

^{1}H NMR spectra of Fe(II) dipyrrinato complexes **1**–**9** showed significant paramagnetic broadening due to the presence of high-spin Fe^{II} (S = 2);[68] typical spectra were observed in a spectral window of –40 to +60 ppm. The presence of halogens in the backbone positions slightly increased the peak-broadening. *meso*-Fluoroaryl dipyrrinato complexes **6**–**9** tended to give slightly sharper proton resonances than the *meso*-mesityl complexes **1**–**5**; no quantification of these peak-broadening phenomena was attempted. Halogens or fluoroaryl substituents did not significantly affect the chemical shift ranges of the protons in these species. However, the *meso*-bis-(trifluoromethyl)phenyl dipyrrinato complex **($_{BFP}^{H}$L^{Mes})FeCl(py) (9)** displayed a single,

[68] *NMR of Paramagnetic Molecules: Principles and Applications*; La Mar, G. N.; Horrocks, W. D., Jr.; Holm, R. H., Eds.; Academic Press: New York, 1973.

downfield proton resonance at 175 ppm that was absent in all other spectra; we tentatively assign this peak as the *ortho*-protons on the *meso*-aryl group, which are the closest protons in this molecule to the paramagnetic iron center, and should therefore experience the most significant paramagnetic shift.

^{19}F NMR spectra could also be obtained for those complexes with fluoroaryl groups in the *meso* position. Spectra of *meso*-perfluorophenyl dipyrrinato complexes **6–8** had a sharp peak for the *para* fluorine nuclei, a moderately broad peak for the *meta* fluorines, and an extremely broad peak for the *ortho* fluorines, as expected for increasing proximity to the paramagnetic Fe(II) center.[69] Interestingly, the ^{19}F NMR spectrum of **($_{BFP}^{H}$L^{Mes})FeCl(py) (9)** showed two distinct, equivalently broadened peaks, indicative of asymmetric environments for the two trifluoromethyl groups (Figure 3.2); this is indicative of hindered rotation of the *meso*-aryl group. No such hindered rotation is indicated by NMR of any other species studied here, including those in which hindered rotation may be expected, such as those bearing *meso*-(*o*-disubstituted)aryl and 3,7-dihalo substituents. It is unclear why complex **9** shows such hindered rotation while complexes **1–8** show no such restricted molecular motion on the NMR time scale. Notably, this hindered rotation is commonly cited as a contributing factor to enhanced luminescence from dipyrrinato species (Chapter 5), though very little evidence for this steric restriction has previously been shown from NMR experiments.[70]

[69] Belle, C.; Béguin, C.; Hamman, S.; Pierre, J.-L. *Coord. Chem. Rev.* **2009**, *253*, 963.
[70] (a) Birnbaum, E. R.; Hodge, J. A.; Grinstaff, M. W.; Schaefer, W. P.; Henling, L.; Labinger, J. A.; Bercaw, J. E.; Gray, H. B. *Inorg. Chem.* **1995**, *34*, 3625. (b) Song, B.; Yu, B.-S. *Bull. Kor. Chem. Soc.* **2003**, *24*, 981.

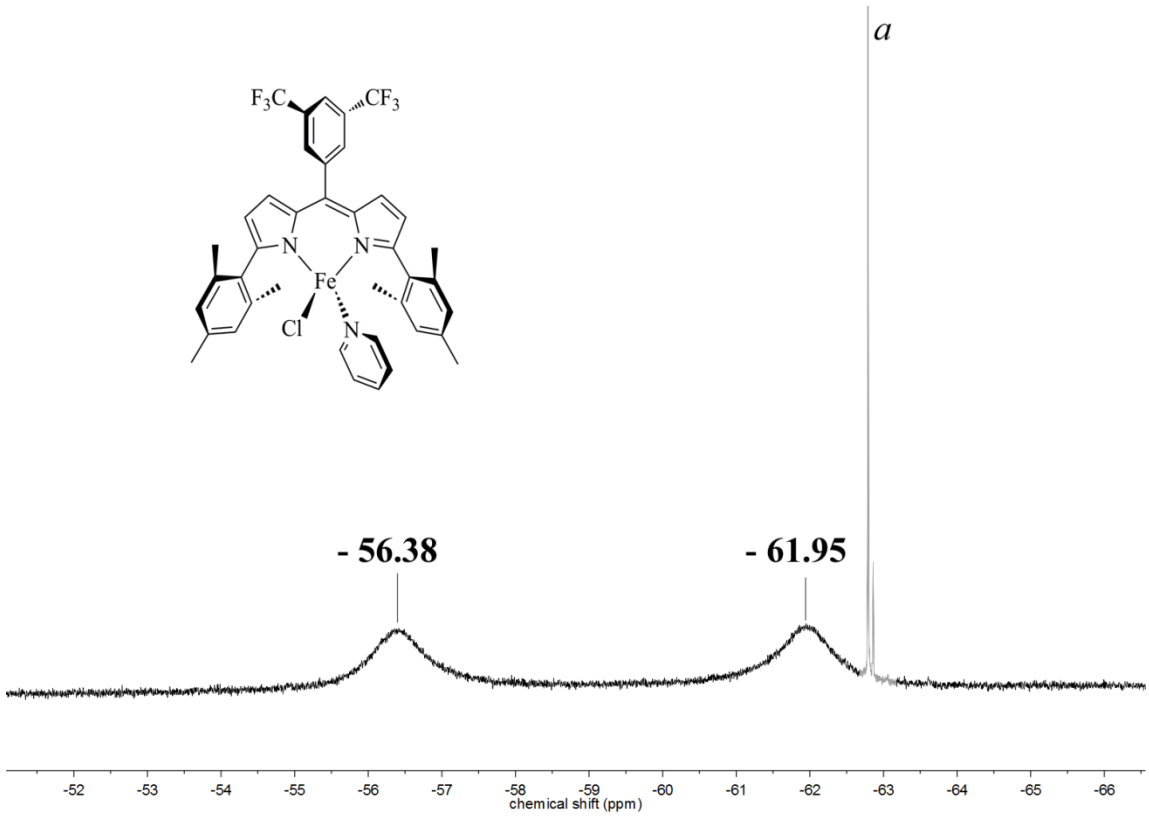

Figure 3.2. ^{19}F NMR spectrum of **($_{BFP}^{H}L^{Mes}$)FeCl(py) (9)**, showing two paramagnetically broadened peaks. [a] The sharp peaks at δ = −62.79 and −62.86 ppm are from residual amounts of free dipyrrin **($_{BFP}^{H}L^{Mes}$)H** and lithium salt **($_{BFP}^{H}L^{Mes}$)Li(THF)** present in the NMR sample; based on other characterization methods, the total amount of these other species is less than 5%.

3.3 Optical Properties

Metal dipyrrinato complexes typically display two intense absorption bands in the visible region of the electromagnetic spectrum. These ligand-based $\pi \rightarrow \pi^*$ transitions are typically more intense than in the corresponding free dipyrrins,[71] largely because of the rigidification of the π-system by chelation to a metal atom. The less intense of these absorptions is blue-shifted from the free dipyrrin absorption band, and generally appears as a shoulder under the more

[71] Motekaitis, R. J.; Martell, A. E. *Inorg. Chem.* **1970**, *9*, 1832.

prominent, slightly lower-energy $\pi \rightarrow \pi^*$ transition. These transitions can be attributed to closely-spaced $S_0 \rightarrow S_2$ and $S_0 \rightarrow S_1$ transitions within the ligand-based π-systems, respectively, where S_0 denotes the singlet ground state and S_1 and S_2 denote singlet excited states. The more intense absorptions occur with absorption maxima ranging from 506 nm for **($_{Mes}^{H}$L^{Mes})FeCl(py) (1)** to 548 nm for **($_{C_6F_5}^{Br}$L^{Mes})FeCl(py) (8)** (Figure 3.3). Like in the free dipyrrins (Section 2.2.3), the introduction of fluoroaryl groups to the *meso* position of the dipyrrinato ligand has only a small effect on the absorption spectra of the iron complexes. The substitution of the *meso*-mesityl group for 3′,5′-$(CF_3)_2C_6H_3$ (BFP) bathochromically shifts the λ_{max} by only 2.5 nm, and a *meso*-perfluorophenyl (C_6F_5) group shifts λ_{max}, on average, by 14.8 nm. Again paralleling the free dipyrrins, halogenation has a markedly larger effect on λ_{max}, with tetrachlorination (**2** and **7**), tetrabromination (**4** and **8**), and tetraiodination (**5**) increasing λ_{max} by 21.7, 27.7, and 39.6 nm, respectively. Dibromination (**3**) increases λ_{max} by 12.0 nm, roughly half the effect of tetrabromination, thus we can extrapolate that the introduction of bromides causes an approximately 6.9 nm bathochromic shift per bromine.

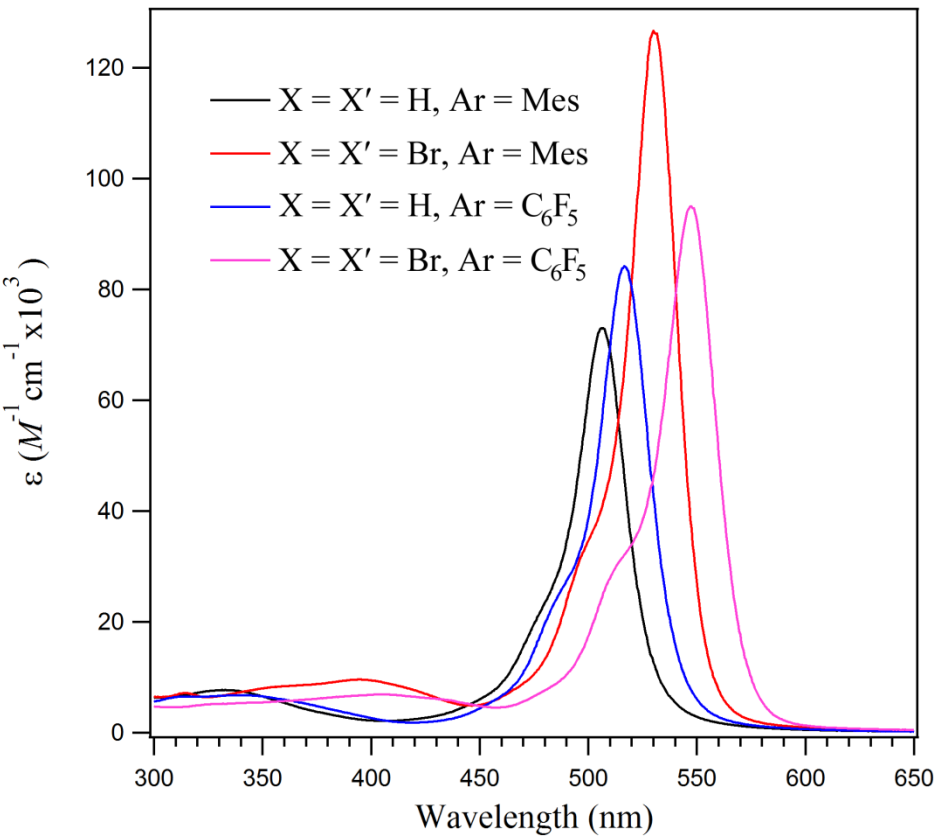

Figure 3.3. Representative UV/Vis spectra of halogenated dipyrrinato iron(II) complexes, obtained at room temperature in dichloromethane. The y-axis gives average ε values calculated from a minimum of four concentrations. Black, **1**; blue, **6**; red, **4**; pink, **8**.

Table 3.2. UV/Vis spectroscopic details for iron(II) dipyrrinato complexes

Number	Compound	λ_{max} (nm)[a]	ε ($M^{-1}cm^{-1}$)[b]
1	**($^{H}_{Mes}L^{Mes}$)FeCl(py)**	506.0	73,000
2	**($^{Cl}_{Mes}L^{Mes}$)FeCl(py)**	524.5	83,000
3	**($^{Br; H}_{Mes}L^{Mes}$)FeCl(py)**	528.0	97,000
4	**($^{Br}_{Mes}L^{Mes}$)FeCl(py)**	530.5	130,000
5	**($^{I}_{Mes}L^{Mes}$)FeCl(py)**	545.6	83,000
6	**($^{H}_{C_6F_5}L^{Mes}$)FeCl(py)**	516.7	84,000
7	**($^{Cl}_{C_6F_5}L^{Mes}$)FeCl(py)**	541.5	54,000
8	**($^{Br}_{C_6F_5}L^{Mes}$)FeCl(py)**	547.5	95,000
9	**($^{H}_{BFP}L^{Mes}$)FeCl(py)**	508.5	62,000

[a] UV/Vis spectra obtained in CH_2Cl_2 at 25 °C with a scan rate of 300 nm/min. [b] Average extinction coefficients calculated from a minimum of four concentrations.

3.4 Electrochemical Properties

The iron(II) complexes studied herein showed fully reversible $Fe^{III/II}$ couples by cyclic voltammetry (0.1 m*M* analyte concentration in THF; 0.3 *M* (nBu$_4$N)(PF$_6$) supporting electrolyte; scan rate = 100 mV/s; glassy carbon working electrode, nonaqueous Ag^+/Ag reference electrode, platinum wire counter electrode; nitrogen atmosphere, 25 °C), with separations between the anodic peak and the cathodic peak ranging from 86–99 mV (Table 3.3). Both backbone halogenation and *meso*-fluoroaryl substitution anodically shift the oxidation potential of the complexes relative to that of the parent complex **($_{Mes}^{H}L^{Mes}$)FeCl(py)**. The introduction of a *meso*-fluoroaryl group raised the oxidation potential by roughly +100 mV, while tetrahalogenation raised the potential by +257 mV in **($_{Mes}^{Cl}L^{Mes}$)FeCl(py)**, +241 mV in **($_{Mes}^{Br}L^{Mes}$)FeCl(py)**, and +166 mV in **($_{Mes}^{I}L^{Mes}$)FeCl(py)**, where less electronegative halogens impart a smaller anodic shift. As in the nonmetalated dipyrrins, these effects were additive, and the most difficult species to oxidize was **($_{C_6F_5}^{Cl}L^{Mes}$)FeCl(py)**, which displays a +386 mV anodic shift from the parent compound **($_{Mes}^{H}L^{Mes}$)FeCl(py)** (Figure 3.4).

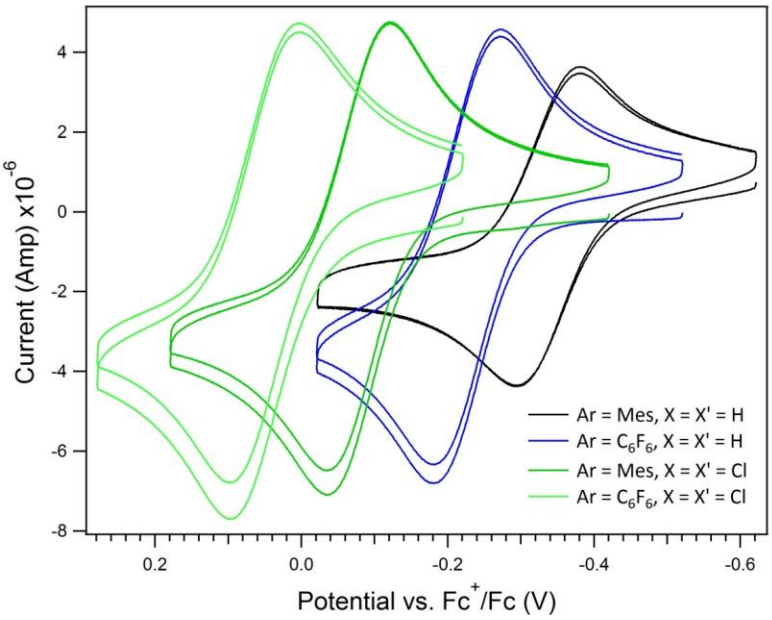

Figure 3.4. $Fe^{III/II}$ couples of representative complexes. Cyclic voltammograms obtained in THF with 0.3 *M* (nBu$_4$N)(PF$_6$) as supporting electrolyte with a scan rate of 100 mV/s. Black, **1**; blue, **6**; dark green, **2**; light green, **7**.

Table 3.3. Electrochemical data for iron(II) dipyrrinato complexes

Number	Compound	$E_{½}$ $Fe^{III/II}$ (mV)[a]	$\lvert E_{pc} - E_{pa} \rvert$ (mV)[b]
1	**($^{H}_{Mes}$L^{Mes})FeCl(py)**	–336	86
2	**($^{Cl}_{Mes}$L^{Mes})FeCl(py)**	–79	88
3	**($^{Br;\,H}_{Mes}$L^{Mes})FeCl(py)**	–154	93
4	**($^{Br}_{Mes}$L^{Mes})FeCl(py)**	–95	91
5	**($^{I}_{Mes}$L^{Mes})FeCl(py)**	–170	88
6	**($^{H}_{C_6F_5}$L^{Mes})FeCl(py)**	–227	92
7	**($^{Cl}_{C_6F_5}$L^{Mes})FeCl(py)**	+50	94
8	**($^{Br}_{C_6F_5}$L^{Mes})FeCl(py)**	+20	99
9	**($^{H}_{BFP}$L^{Mes})FeCl(py)**	–238	96

[a] Cyclic voltammetry performed in THF containing 0.3 *M* (nBu$_4$N)(PF$_6$) at 25 °C. Voltages are reported relative to $Fc^{+/0}$. [b] Separation between the voltages of the cathodic and anodic peak currents.

3.5 Mössbauer Spectroscopic Properties

Zero-field ^{57}Fe Mössbauer spectroscopy provides a unique opportunity to probe the electronic structure of iron complexes. Two parameters derived from Mössbauer spectra, the isomer shift (δ) and the quadrupole splitting ($|\Delta E_Q|$), provide information about the electronic environment of the iron center. The isomer shift provides information about the electron density at the iron nucleus as well as the spin state, and the quadrupole splitting is a reflection of the asymmetry of the electronic field gradient at the iron nucleus. Isomer shifts range from below 0 $^{mm}/_{s}$ for high-valent (Fe^{IV}) and/or low-spin complexes to above 2.2 $^{mm}/_{s}$ for iron in lower oxidation states and in high spin states.[72] The absolute value of the quadrupole splitting can range from 0 for species in spherically symmetric ligand fields to greater than 6 $^{mm}/_{s}$ for highly asymmetric species.[73]

All of the iron dipyrrinato complexes studied herein display isomer shifts consistent with other reported four-coordinate, high-spin Fe(II) species, and range from 0.86 to 0.89 $^{mm}/_{s}$ (Table 3.4). There is virtually no variation of this value upon modification of the ligand by halogenation or *meso*-fluoroarylation, suggesting that these two types of ligand modifications have little to no bearing on the oxidation state of the iron center.

Quadrupole splitting parameters ($|\Delta E_Q|$) for **1**–**9**, however, span a wide range of values, from a minimum of 1.35 $^{mm}/_{s}$ for **($^{Cl}_{C_6F_5}$L^{Mes})FeCl(py)** to a maximum of 3.24 $^{mm}/_{s}$ for **($^{Br}_{Mes}$L^{Mes})FeCl(py)**. Unlike for the optical and electrochemical trends described in Sections 3.3 and 3.4, no correlation between the quadrupole splitting and halogen size or electronegativity was observed. Since quadrupole splitting reflects the electronic field gradient at the iron nucleus and is therefore a function of the asymmetry around the iron center,[72] we surmised that the

[72] Drago, R. S. *Physical Methods for Chemists, 2nd ed.*; 2 ed.; Harcourt Brace Jovanovich College Publishers: Orlando, 1992.
[73] Evans, D. J. *Chem. Phys. Lett.* **1996**, *255*, 134, and references therein.

introduction of halogens to the backbone of the dipyrrin must induce geometric changes within the complexes. Indeed, due to steric interactions between the 3- and 7-substituents and the *o*-methyl substituents of the *meso*-mesityl group, the dipyrrinato ligands can be significantly distorted from planarity. This distortion can be measured by the geometric parameter χ, which is the dihedral angle between C3:C4:C6:C7. The magnitude of χ tracks reasonably well with the value of the $|\Delta E_Q|$; this correlation will be described in more detail in Section 3.6.

Table 3.4. Mössbauer spectroscopic data for iron(II) dipyrrinato complexes

Number	Compound	δ ($^{mm}/_{s}$)[a]	$\lvert\Delta E_Q\rvert$ ($^{mm}/_{s}$)[a]
1	**($^{H}_{Mes}$L^{Mes})FeCl(py)**	0.87	2.19
2	**($^{Cl}_{Mes}$L^{Mes})FeCl(py)**	0.87	2.90
3	**($^{Br;\ H}_{Mes}$L^{Mes})FeCl(py)**	0.86	1.46
4	**($^{Br}_{Mes}$L^{Mes})FeCl(py)**	0.88	3.24
5	**($^{I}_{Mes}$L^{Mes})FeCl(py)**	0.89	1.89
6	**($^{H}_{C_6F_5}$L^{Mes})FeCl(py)**	0.89	1.92
7	**($^{Cl}_{C_6F_5}$L^{Mes})FeCl(py)**	0.87	1.35
8	**($^{Br}_{C_6F_5}$L^{Mes})FeCl(py)**	0.89	2.24
9	**($^{H}_{BFP}$L^{Mes})FeCl(py)**	0.89	1.74

[a] Mössbauer spectra obtained on samples suspended in Paratone at 110 K and fit with Lorentzian functions in IGOR Pro.

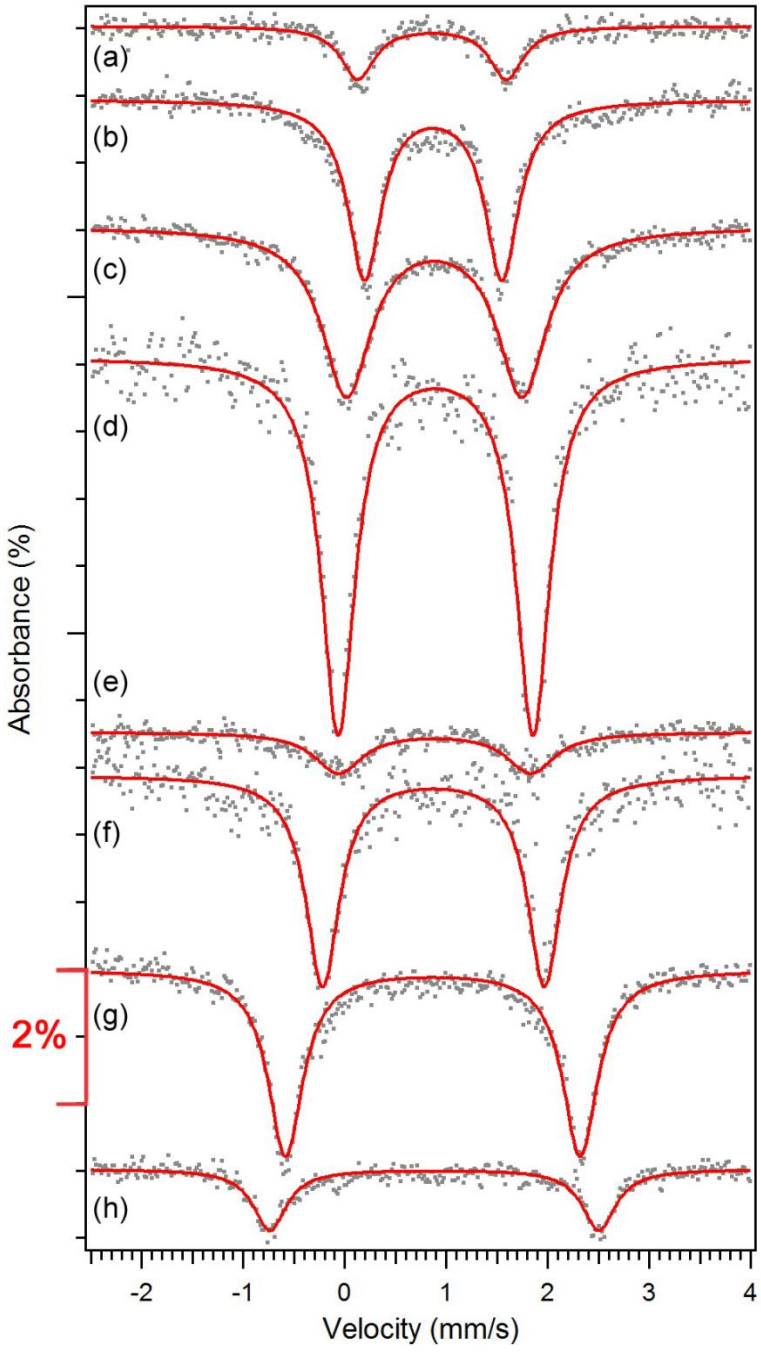

Figure 3.5. Zero-field ^{57}Fe Mössbauer spectra of iron(II) dipyrrinato complexes obtained at 110 K for the following compounds: **($^{Br;\,H}_{Mes}L^{Mes}$)FeCl(py)** (**a**); **($^{Cl}_{C_6F_5}L^{Mes}$)FeCl(py)** (**b**); **($^{H}_{BFP}L^{Mes}$)FeCl(py)** (**c**); **($^{H}_{C_6F_5}L^{Mes}$)FeCl(py)** (**d**); **($^{I}_{Mes}L^{Mes}$)FeCl(py)** (**e**); **($^{H}_{Mes}L^{Mes}$)FeCl(py)** (**f**); **($^{Cl}_{Mes}L^{Mes}$)FeCl(py)** (**g**); **($^{Br}_{Mes}L^{Mes}$)FeCl(py)** (**h**).

Table 3.5. Compiled characterization data of iron(II) dipyrrinato complexes

Number	Compound	Ar	X; X′	λ_{max} (nm)[a]	ε ($M^{-1}cm^{-1}$)[b]	$E_{½}$ $Fe^{III/II}$ (mV)[c]	δ ($^{mm}/_{s}$)[d]	$\lvert\Delta E_Q\rvert$ ($^{mm}/_{s}$)[d]
1	**($_{Mes}^{H}L^{Mes}$)FeCl(py)**	Mes	H; H	506.0	73,000	–336	0.87	2.19
2	**($_{Mes}^{Cl}L^{Mes}$)FeCl(py)**	Mes	Cl; Cl	524.5	83,000	–79	0.87	2.90
3	**($_{Mes}^{Br;\ H}L^{Mes}$)FeCl(py)**	Mes	Br; H	528.0	97,000	–154	0.86	1.46
4	**($_{Mes}^{Br}L^{Mes}$)FeCl(py)**	Mes	Br; Br	530.5	130,000	–95	0.88	3.24
5	**($_{Mes}^{I}L^{Mes}$)FeCl(py)**	Mes	I; I	545.6	83,000	–170	0.89	1.89
6	**($_{C_6F_5}^{H}L^{Mes}$)FeCl(py)**	C_6F_5	H; H	516.7	84,000	–227	0.89	1.92
7	**($_{C_6F_5}^{Cl}L^{Mes}$)FeCl(py)**	C_6F_5	Cl; Cl	541.5	54,000	+50	0.87	1.35
8	**($_{C_6F_5}^{Br}L^{Mes}$)FeCl(py)**	C_6F_5	Br; Br	547.5	95,000	+20	0.89	2.24
9	**($_{BFP}^{H}L^{Mes}$)FeCl(py)**	3,5-$(CF_3)_2C_6H_3$	H; H	508.5	62,000	–238	0.89	1.74

[a] UV/Vis spectra obtained in CH_2Cl_2 at 25 °C. [b] Average extinction coefficients calculated from a minimum of four concentrations. [c] Cyclic voltammetry performed in THF containing 0.3 *M* ($n$$Bu_4N$)($PF_6$) at 25 °C. [d] Mössbauer spectra obtained on samples suspended in Paratone at 110 K and fit with Lorentzian functions in IGOR Pro. For full experimental details, see Section 3.8.2.

3.6 Distortion of Ligands from Planarity

In the vast majority of crystallographically characterized dipyrrinato complexes, the conjugated dipyrrin core remains essentially planar, contributing to the overall stability of the ligand scaffold. However, it has been shown in the case of related macrocyclic porphyrin systems that halogenation of the β-positions of the pyrrole subunits can induce a significant structural distortion away from planarity of the conjugated system (Section 1.2.1), though this does not seem to be the case for the similar corrole ligand framework.[74] Given the structural similarities between these macrocycles and dipyrrins, it is unsurprising that the complexes of tetrahalogenated dipyrrins display structural distortions akin to those seen for the macrocyclic systems.

To our knowledge, there have been no systematic studies on how deviations from the planarity of iron porphyrin, corrole, dipyrrin, or related polypyrrolide complexes affect the ^{57}Fe Mössbauer isomer shift (δ) and quadrupole splitting (ΔE_Q). Since the quadrupole splitting is a reflection of the symmetry of the electronic field gradient at the iron nucleus, we surmised that desymmetrization of the ligand environment by distortions from planarity would have a significant effect on the quadrupole splitting, a trend we observe in a small series of variably halogenated iron(II) dipyrrinato complexes.

3.6.1 Crystallographic Characterization

Dichroic orange/green to red/green crystals of the Fe(II) dipyrrinato complexes were obtained upon sitting at –35 °C in mixtures of hexanes, benzene, and diethyl ether or

[74] (a) Alemayehu, A. B.; Hansen, L. K.; Ghosh, A. *Inorg. Chem.* **2010**, *49*, 7608. (b) Thomas, K. E.; Conradie, J.; Hansen, L. K.; Ghosh, A. *Inorg. Chem.* **2011**, *50*, 3247. (c) Thomas, K. E.; Alemayehu, A. B.; Conradie, J.; Beavers, C. M.; Ghosh, A. *Acc. Chem. Res.* **2012**, *45(8)*, 1203.

hexamethyldisiloxane for up to two months. **($_{Mes}^{H}$ L^{Mes})FeCl(py)**, **($_{Mes}^{Cl}$ L^{Mes})FeCl(py)**, **($_{Mes}^{Br}$L^{Mes})FeCl(py)**, and **($_{Mes}^{I}$L^{Mes})FeCl(py)** all crystallized in the monoclinic space group $P2_1/c$, while **($_{Mes}^{Br; H}$ L^{Mes})FeCl(py)** crystallized in the orthorhombic space group $Cmc2_1$, with a crystallographic mirror plane bisecting the molecule. The nonhalogenated, chlorinated, and brominated complexes crystallized without any solvent in the unit cell, while **($_{Mes}^{I}$L^{Mes})FeCl(py)** crystallized with one molecule of benzene for every two crystallographically equivalent iron complexes. Selected crystallographic data are shown in Table 3.6.

.

Table 3.6. Selected crystallographic information for *meso*-mesityl complexes

Parameter	$(^{H}_{Mes}L^{Mes})$FeCl(py) **1**	$(^{Cl}_{Mes}L^{Mes})$FeCl(py)[a] **2**	$(^{Br;\,H}_{Mes}L^{Mes})$FeCl(py) **3**	$(^{Br}_{Mes}L^{Mes})$FeCl(py) **4**	$(^{I}_{Mes}L^{Mes})$FeCl(py)·½C_6H_6 **5**
lattice	Monoclinic	Monoclinic	Orthorhombic	Monoclinic	Monoclinic
space group	$P2_1/c$	$P2_1/c$	$Cmc2_1$	$P2_1/c$	$P2_1/c$
a (Å)	8.000(3)	13.5394(9)	14.184(2)	13.662(3)	13.679(4)
b (Å)	21.723(7)	17.9754(13)	16.142(3)	18.202(4)	20.177(6)
c (Å)	20.764(7)	15.4992(10)	16.242(3)	15.660(3)	17.012(5)
α (°)	90	90	90	90	90
β (°)	100.927(6)	90.557(1)	90	90.437(4)	110.954(4)
γ (°)	90	90	90	90	90
R	0.0462	0.0343	0.0246	0.0411	0.0353

[a] Data obtained at the Advanced Photon Source (APS) at Argonne National Labs.

The crystal structures of all three tetrahalogenated complexes showed significant deviations from planarity of the dipyrrinato ligand, with the degree of deplanarization measured by the dihedral angle χ between C3-C4-C6-C7. The non-halogenated **($_{Mes}^{H}$L^{Mes})FeCl(py)** and C2,C8-dibrominated **($_{Mes}^{Br;\,H}$L^{Mes})FeCl(py)** structures showed minimal deviations from planarity with χ = 8.9(11)° and 0°,[75] respectively (Figure 3.6 and Figure 3.7, Table 3.7). The planarity of **($_{Mes}^{Br;\,H}$L^{Mes})FeCl(py)** was enforced by the relatively high crystallographic symmetry; a crystallographic mirror plane related the two pyrrole subunits. The tetrahalogenated structures showed significantly larger values of χ: 29.3(5)°, 29.6(15)°, and 15.7(12)° for **($_{Mes}^{Cl}$L^{Mes})FeCl(py)**, **($_{Mes}^{Br}$L^{Mes})FeCl(py)**, and **($_{Mes}^{I}$L^{Mes})FeCl(py)·½C$_6$H$_6$** (Figure 3.8, Figure 3.9, and Figure 3.10), respectively.

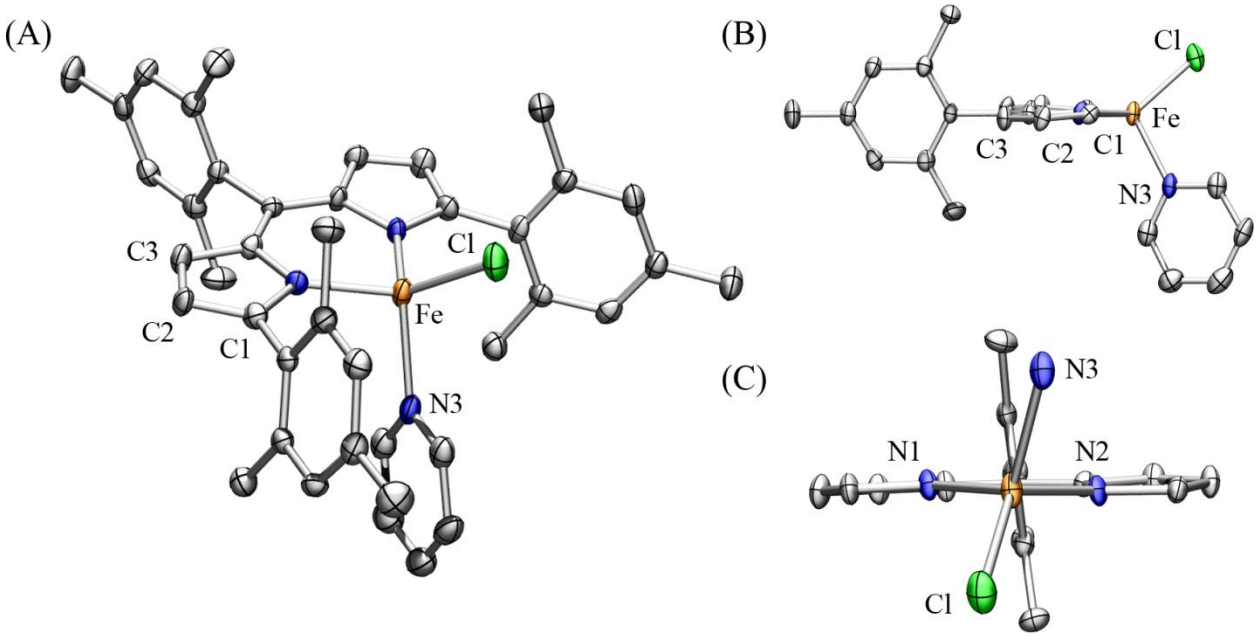

Figure 3.6. Solid-state structure of **($_{Mes}^{H}$L^{Mes})FeCl(py) (1)**. Thermal ellipsoids set at the 50% probability level. Hydrogen atoms have been omitted for clarity. (A) Whole molecule. (B) Side view, illustrating planarity of the dipyrrin core; flanking mesityl groups have been omitted for clarity. (C) Front view, illustrating the orthogonality of the dipyrrin with the *meso*-mesityl group; flanking mesityl groups and the pyridine carbons have been omitted for clarity. Gray, C; blue, N; green, Cl; orange, Fe.

[75] The high degree of crystallographic symmetry requires this angle to be 0°.

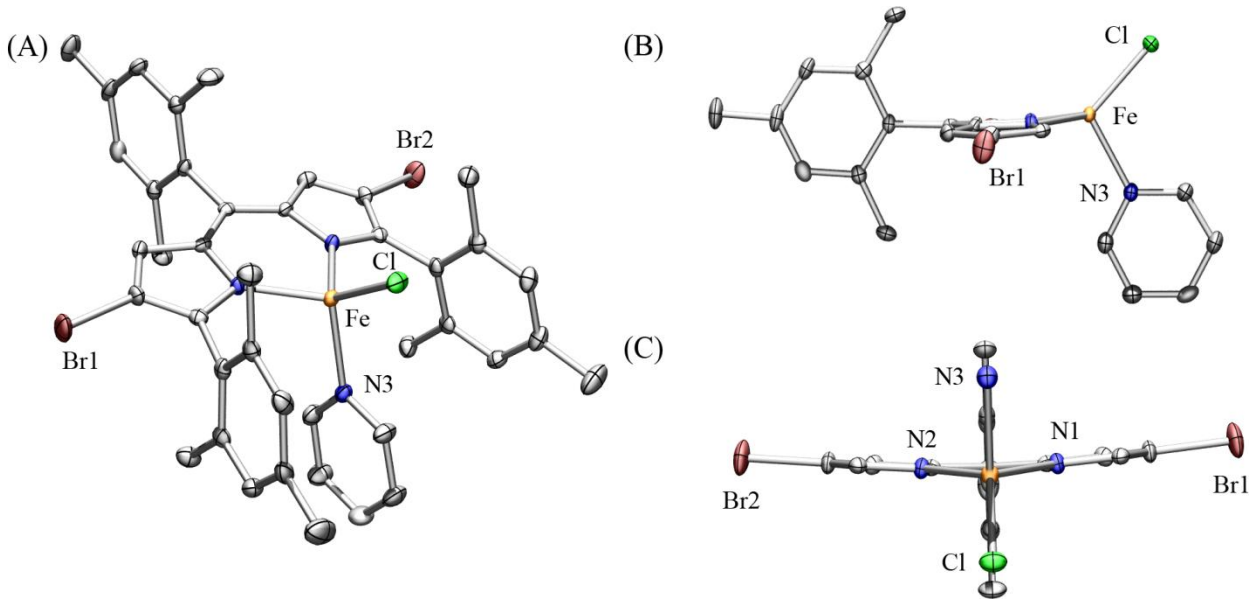

Figure 3.7. Solid-state structure of $(^{Br;\,H}_{Mes}L^{Mes})$**FeCl(py) (3)**. Thermal ellipsoids set at the 50% probability level. Hydrogen atoms have been omitted for clarity. (A) Whole molecule. (B) Side view, illustrating the near-planarity of the dipyrrin core; flanking mesityl groups have been omitted for clarity. (C) Front view, illustrating the orthogonality of the dipyrrin with the *meso*-mesityl group; flanking mesityl groups and the pyridine carbons have been omitted for clarity. Gray, C; blue, N; green, Cl; maroon, Br; orange, Fe.

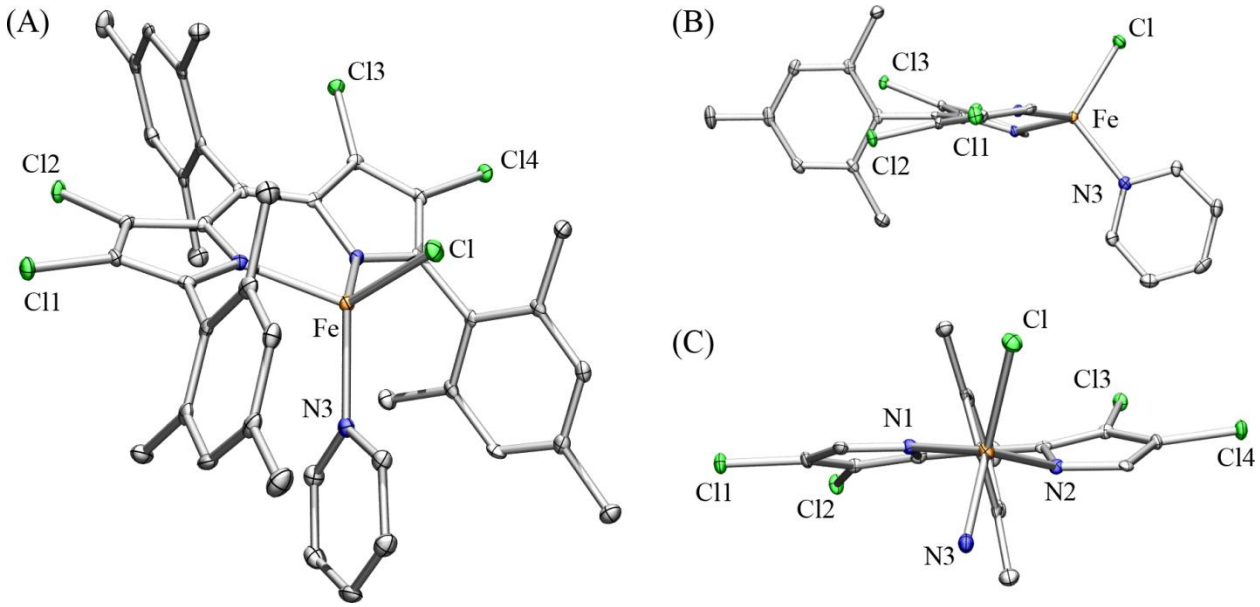

Figure 3.8. Solid-state structure of $(^{Cl}_{Mes}L^{Mes})$**FeCl(py) (2)**. Thermal ellipsoids set at the 50% probability level. Hydrogen atoms have been omitted for clarity. (A) Whole molecule. (B) Side view, illustrating the *non*-planarity of the dipyrrin core; flanking mesityl groups have been omitted for clarity. (C) Front view, illustrating the torquing of the *meso*-mesityl group relative to the dipyrrin; flanking mesityl groups and the pyridine carbons have been omitted for clarity. Gray, C; blue, N; green, Cl; orange, Fe. Data obtained at APS.

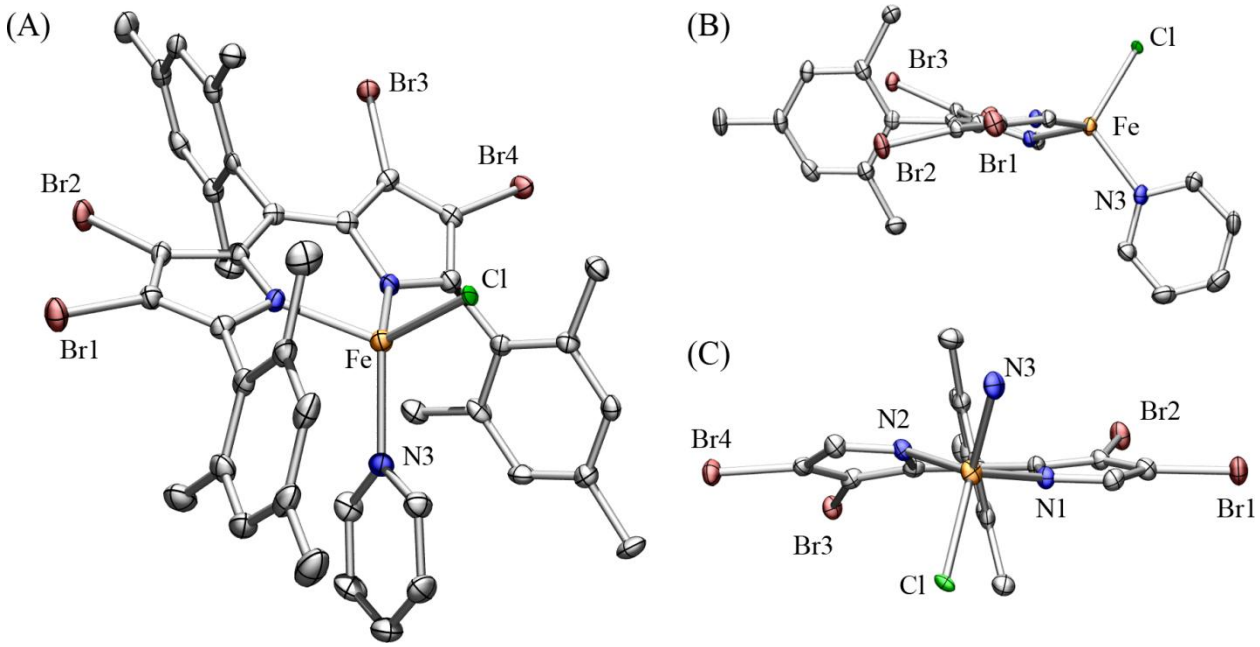

Figure 3.9. Solid-state structure of **($_{Mes}^{Br}$L^{Mes})FeCl(py) (4)**. Thermal ellipsoids set at the 50% probability level. Hydrogen atoms have been omitted for clarity. (A) Whole molecule. (B) Side view, illustrating the *non*-planarity of the dipyrrin core; flanking mesityl groups have been omitted for clarity. (C) Front view, illustrating the torquing of the *meso*-mesityl group relative to the dipyrrin; flanking mesityl groups and the pyridine carbons have been omitted for clarity. Gray, C; blue, N; green, Cl; maroon, Br; orange, Fe.

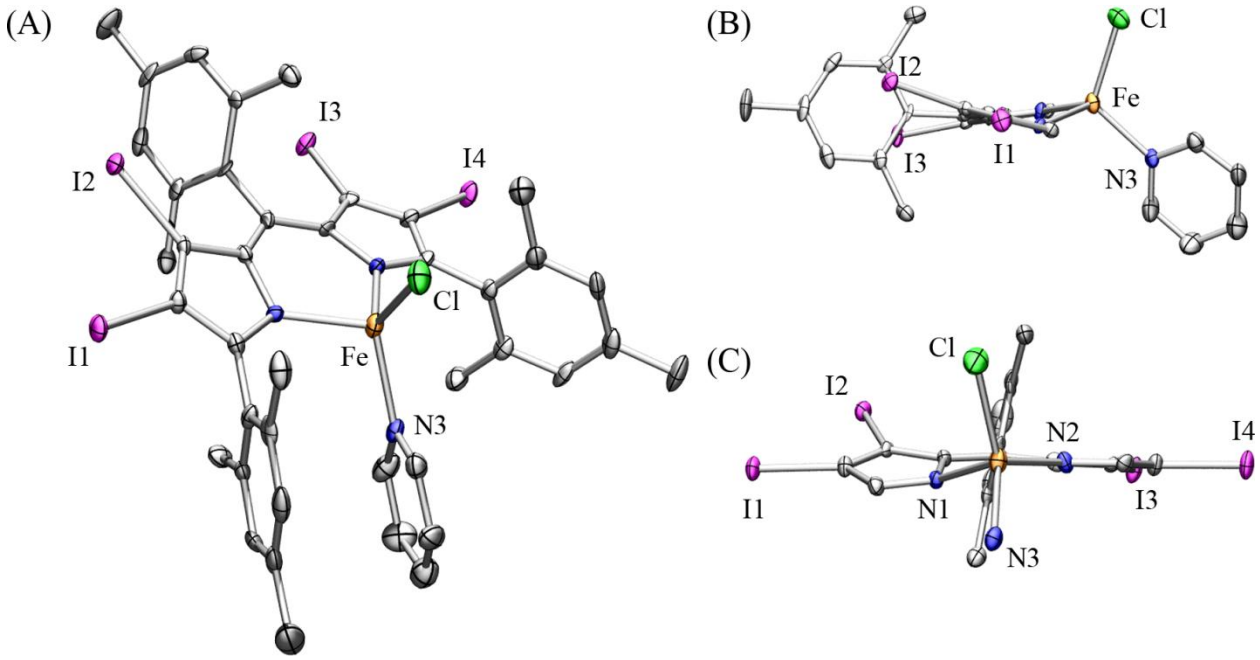

Figure 3.10. Solid-state structure of **($_{Mes}^{I}$L^{Mes})FeCl(py)·½C$_6$H$_6$ (5)**. Thermal ellipsoids set at the 50% probability level. Hydrogen atoms have been omitted for clarity. (A) Whole molecule. (B) Side view, illustrating the *non*-planarity of the dipyrrin core; flanking mesityl groups have been omitted for clarity. (C) Front view, illustrating the torquing of the *meso*-mesityl group relative to the dipyrrin; flanking mesityl groups and the pyridine carbons have been omitted for clarity. Gray, C; blue, N; green, Cl; purple, I; orange, Fe.

With the exception of the dibrominated compound **($^{Br;\ H}_{Mes}L^{Mes}$)FeCl(py)**, all the structures showed a twisting of the *meso*-mesityl substituent relative to the dipyrrin mean plane that indicates a steric interaction between the *o*-methyl groups of the mesityl ring and the substituents in the C3- and C7-positions of the dipyrrinato ligand [Figure 3.6(C) through Figure 3.10(C)]. This deviation from orthogonality was measured by subtracting 90° from the angle between the *meso*-mesityl plane and the N1:C5:N2 dipyrrin plane; the absolute values of these deviations from orthogonality are called ϕ and are reported in Table 3.7. Though the steric interaction should increase with larger halogen substituents, we believe that the correspondingly longer C–X bond lengths decrease the spatial proximity of the *o*-methyl groups with the halogen, so that the most significant steric interaction is with the medium-sized chlorine and bromine substituents, while the smaller hydrogen and larger iodine substituents are positioned further from the *o*-methyl groups, diminishing the steric interactions.

Table 3.7. Selected structural data for *meso*-mesityl complexes

Parameter	$(^{H}_{Mes}L^{Mes})$FeCl(py) **1**	$(^{Cl}_{Mes}L^{Mes})$FeCl(py)[a] **2**	$(^{Br;\,H}_{Mes}L^{Mes})$FeCl(py) **3**	$(^{Br}_{Mes}L^{Mes})$FeCl(py) **4**	$(^{I}_{Mes}L^{Mes})$FeCl(py)·½C_6H_6 **5**
Fe-N1 (Å)	2.026(3)	2.0364(17)	2.033(2)	2.022(4)	2.046(4)
Fe-N2 (Å)	2.043(3)	2.0336(17)	2.033(2)	2.031(4)	2.035(4)
Fe-N3 (py) (Å)	2.111(3)	2.0820(18)	2.080(3)	2.071(4)	2.079(5)
Fe-Cl1 (Å)	2.2540(14)	2.2395(6)	2.2314(10)	2.2660(13)	2.2422(18)
N1-Fe-N2 (°)	91.52(11)	89.70(7)	88.91(11)	90.30(16)	89.79(17)
N1-Fe-N3 (°)	99.94(12)	109.12(7)	105.18(8)	109.88(16)	108.13(17)
N1-Fe-Cl (°)	130.12(10)	118.44(5)	123.66(6)	116.38(12)	108.61(13)
N2-Fe-N3 (°)	118.36(13)	118.69(7)	105.18(8)	117.16(16)	118.74(18)
N2-Fe-Cl (°)	113.59(9)	111.28(5)	123.66(6)	111.61(12)	116.35(14)
N3-Fe-Cl (°)	103.87(10)	108.97(5)	107.53(9)	110.41(12)	112.07(13)
χ (°)	8.9(11)	29.3(5)	0[b]	29.6(15)	15.7(12)
ϕ (°)	9.6(11)	23.84(7)	0[b]	24.30(16)	19.96(17)

[a] Data obtained at APS. [b] These values are constrained to zero by the crystallographic symmetry of the molecule.

The steric interaction between the ortho-substituent on the *meso*-aryl group and the 3- and 7-substituents on the dipyrrin was corroborated by the fact that the structures of dipyrrinato complexes **6–8**, which bear a *meso*-perfluorophenyl substituent instead of a *meso*-mesityl substituent, display significantly smaller deviations from planarity, likely because of the smaller size of the *o*-fluorines of the perfluorophenyl group than the *o*-methyl groups of the mesityl unit. Their respective χ values are 5.0(4)°, 12.4(8)°, and 10.2(7)° for the non-halogenated, tetrachlorinated, and tetrabrominated complexes (Figure 3.11, Figure 3.12, and Figure 3.13, respectively).

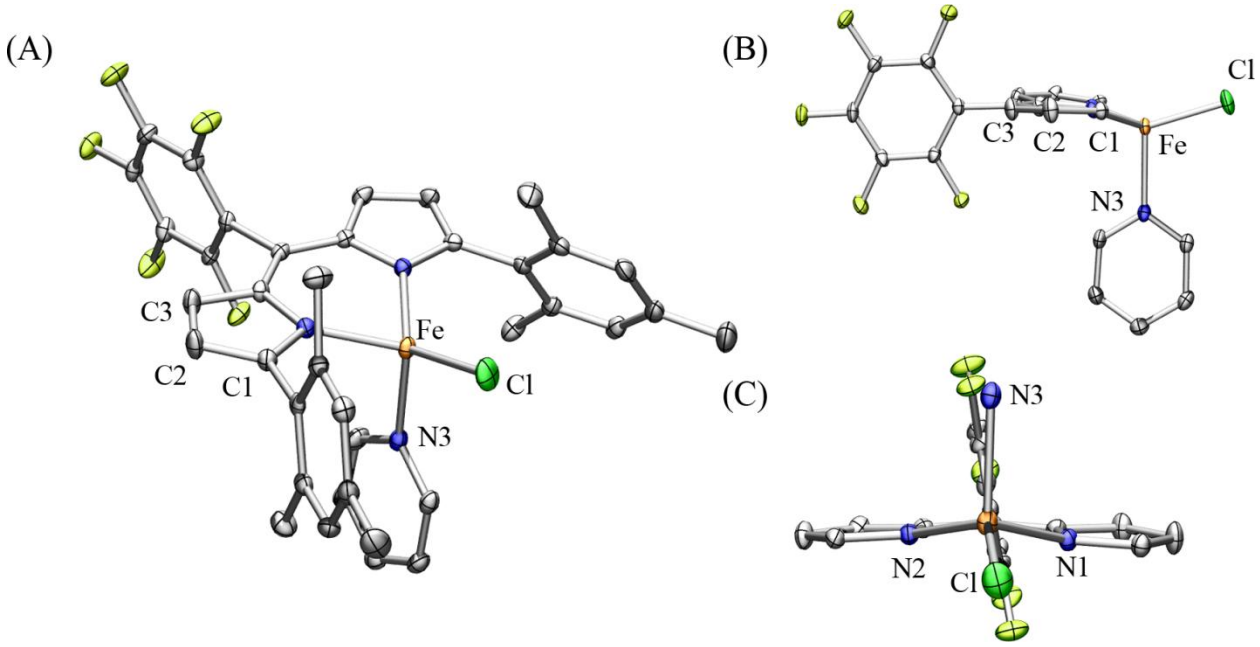

Figure 3.11. Solid-state structure of **($_{C_6F_5}^{H}$L^{Mes})FeCl(py) (6)**. Thermal ellipsoids set at the 50% probability level. Hydrogen atoms have been omitted for clarity. (A) Whole molecule. (B) Side view, illustrating the planarity of the dipyrrin core; flanking mesityl groups have been omitted for clarity. (C) Front view, illustrating the orthogonality of the dipyrrin with the *meso*-C_6F_5 group; flanking mesityl groups and the pyridine carbons have been omitted for clarity. Gray, C; blue, N; green, Cl; yellow-green, F; orange, Fe.

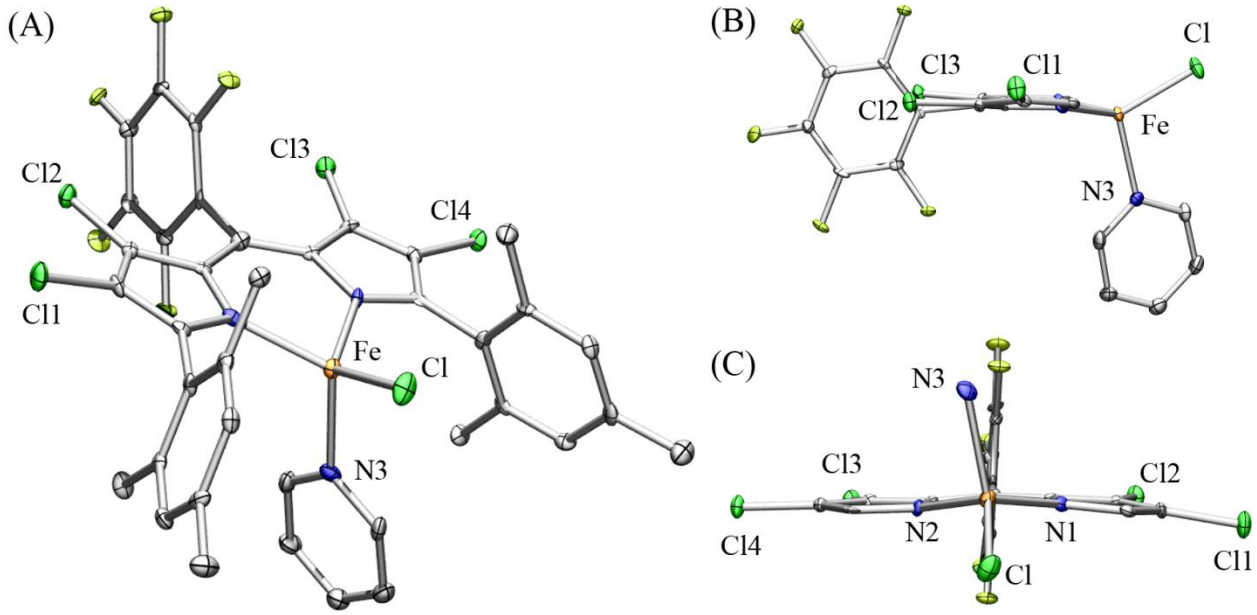

Figure 3.12. Solid-state structure of **($_{C_6F_5}^{Cl}$L^{Mes})FeCl(py) (7)**. Thermal ellipsoids set at the 75% probability level. Hydrogen atoms have been omitted for clarity. (A) Whole molecule. (B) Side view, illustrating the near-planarity of the dipyrrin core; flanking mesityl groups have been omitted for clarity. (C) Front view, illustrating the orthogonality of the dipyrrin with the *meso*-C_6F_5 group; flanking mesityl groups and the pyridine carbons have been omitted for clarity. Gray, C; blue, N; green, Cl; yellow-green, F; orange, Fe. Data obtained at APS.

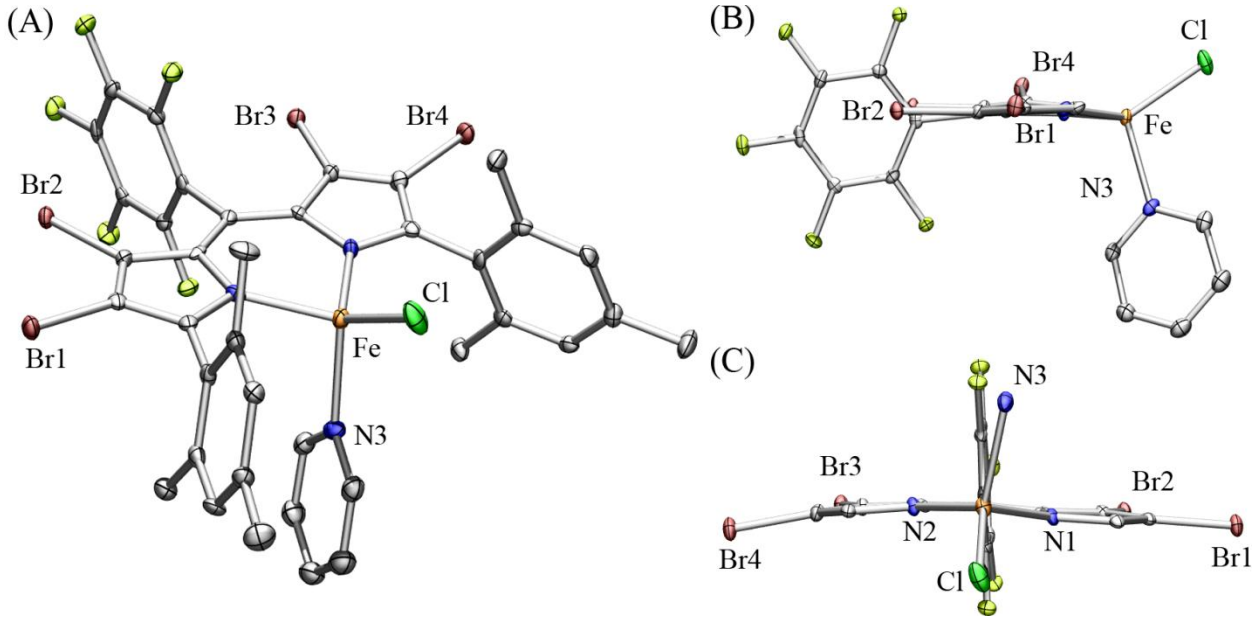

Figure 3.13. Solid-state structure of **($_{C_6F_5}^{Br}$L^{Mes})FeCl(py) (8)**. Thermal ellipsoids set at the 50% probability level. Hydrogen atoms have been omitted for clarity. (A) Whole molecule. (B) Side view, illustrating the near-planarity of the dipyrrin core; flanking mesityl groups have been omitted for clarity. (C) Front view, illustrating the orthogonality of the dipyrrin with the *meso*-C_6F_5 group; flanking mesityl groups and the pyridine carbons have been omitted for clarity. Gray, C; blue, N; green, Cl; yellow-green, F; orange, Fe. Data obtained at APS.

Interestingly, the free dipyrrin **($_{Mes}^{I}L^{Mes}$)H** (Figure 2.13) shows a significantly smaller deviation from planarity than its iron complex **($_{Mes}^{I}L^{Mes}$)FeCl(py)·½C_6H_6** (Figure 3.10). The value of χ for the free dipyrrin is only 9.5(14)°, more than 5° *less* distorted than in the iron complex. Additionally, there is virtually no torquing of the *meso*-mesityl group in the free dipyrrin; ϕ is only 4.71(17)°, smaller even than in the non-halogenated iron complex. The complex in which diethyl ether is bound to the iron atom instead of pyridine, **($_{Mes}^{I}L^{Mes}$)FeCl(OEt_2)**, also shows a significantly different degree of distortion; in this case, χ is 23.3(12)° and the *meso*-mesityl/dipyrrin torque angle ϕ is 20.07(15)°, both values that are greater than in the pyridine-ligated complex (Figure 3.14).

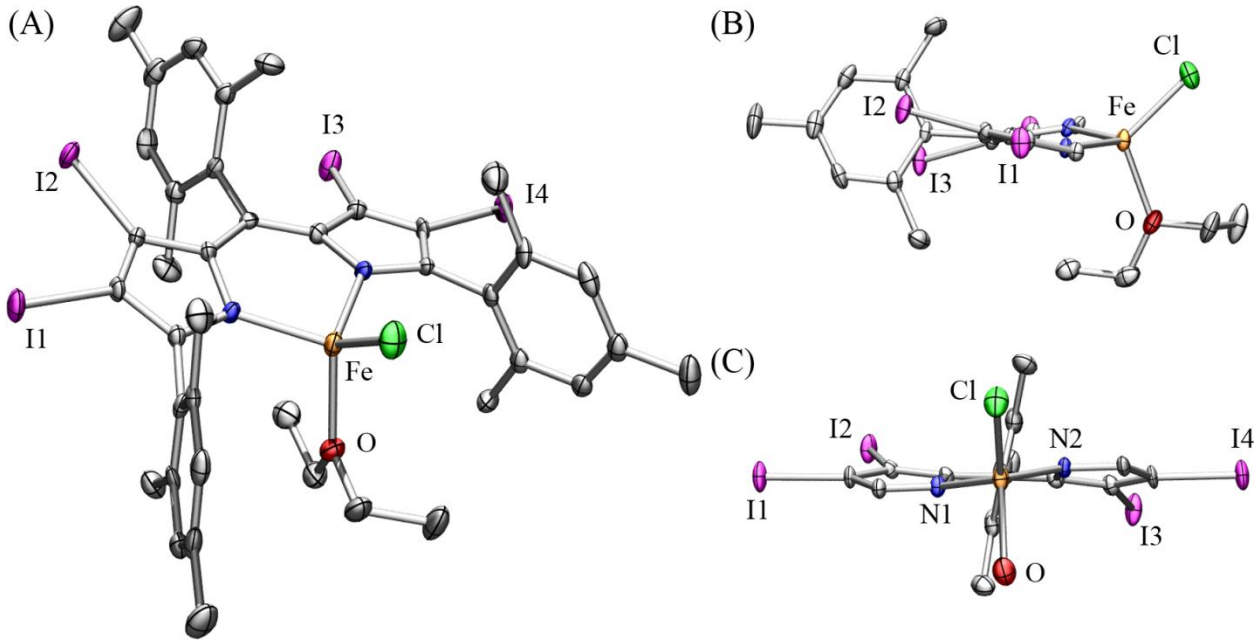

Figure 3.14. Solid-state structure of **($_{Mes}^{I}L^{Mes}$)FeCl(OEt_2)**. Thermal ellipsoids set at the 50% probability level. Hydrogen atoms have been omitted for clarity. (A) Whole molecule. (B) Side view, illustrating the *non*-planarity of the dipyrrin core; flanking mesityl groups have been omitted for clarity. (C) Front view, illustrating the torquing of the *meso*-mesityl group relative to the dipyrrin; flanking mesityl groups and the ether carbons have been omitted for clarity. Gray, C; blue, N; red, O; green, Cl; purple, I; orange, Fe.

3.6.2 Correlation of Structure with Mössbauer Spectra

Zero-field ^{57}Fe Mössbauer spectra provide two parameters that describe the electronic environment of the iron nucleus, the isomer shift (δ) and the quadrupole splitting ($|\Delta E_Q|$), as described in Section 3.5. Mössbauer spectra of the *meso*-mesityl iron(II) dipyrrinato complexes **1**–**5** showed isomer shifts ranging from 0.86–0.89 $^{mm}/_{s}$, consistent with high-spin Fe(II) in a pseudo-tetrahedral environment for all complexes. Absolute values of the quadrupole splitting, however, ranged from 1.46–3.24 mm/s, indicating significant differences in the electronic field gradient at the iron nuclei across the series.

In order to determine if a particular geometric feature of these molecules directly correlated with the quadrupole splitting, a number of geometric parameters were calculated and plotted against $|\Delta E_Q|$, including the dihedral angle χ (defined above), the angle ϕ (also described above), the angle between the two pyrrole mean planes, the dihedral angle between C–X bonds on the two pyrroles (X2-C3-C7-X3), the "tetrahedricity" at iron, τ_4,[76] defined by Equation 3.1 (where α and β are the two largest L–Fe–L angles in the molecule), the average Fe-$N_{dipyrrin}$ bond lengths, and the displacement of the iron from the dipyrrin mean plane.

$$\tau_4 = \frac{360° - (\alpha + \beta)}{141°} \qquad \text{(Eq. 3.1)}$$

While most of the geometric parameters had poor correlations with the quadrupole splitting, the value of χ did have a relatively close correlation with the quadrupole splitting, with an R^2 value of 0.87 for the line of best fit. The geometric parameters and their respective R^2 values can be found in Table 3.8. The four geometric parameters that showed the closest correlation with $|\Delta E_Q|$ are illustrated in Figure 3.15.

[76] Yang, L.; Powell, D. R.; Houser, R. P. *Dalton Trans.* **2007**, 955.

Table 3.8. Selected geometric parameters for *meso*-mesityl complexes & correlation with $|\Delta E_Q|$

Parameter	$(^{H}_{Mes}L^{Mes})$FeCl(py) **1**	$(^{Cl}_{Mes}L^{Mes})$FeCl(py)[a] **2**	$(^{Br;\,H}_{Mes}L^{Mes})$FeCl(py) **3**	$(^{Br}_{Mes}L^{Mes})$FeCl(py) **4**	$(^{I}_{Mes}L^{Mes})$FeCl(py)·½C_6H_6 **5**	R^2
$\|\Delta E_Q\|$ (mm/s)	**2.19**	**2.90**	**1.46**	**3.24**	**1.89**	
χ (°)	8.9(11)	29.3(5)	0[a]	29.6(15)	15.7(12)	**0.87**[d]
ϕ (°)	9.6(11)	23.84(7)	0[a]	24.30(16)	19.96(17)	**0.67**[d]
∡ between pyrrole mean planes (°)	5.69(16)	25.19(9)	–8.96(16)[c]	24.9(2)	20.4(2)	**0.64**[d]
torsion ∡ X2:C3:C7:X3 (°)	4.64(9)	30.17(10)	0[a]	32.4(2)	26.4(2)	**0.58**[d]
τ_4	0.79	0.87	0.80	0.90	0.89	0.37
avg. Fe-N_{dipyrr} bond length (Å)	2.035(4)	2.0349(24)	2.033(2)	2.027(6)	2.041(6)	0.14
displacement of Fe from dipyrrin mean plane (Å)	0.009(5)	0.178(3)	0.185(4)	0.196(6)	0.434(6)	0.08

[a] Data obtained at APS. [b] These values are required by the high symmetry of the solid-state structure to be 0°. [c] Both pyrrole units deviate in the same direction; this type of distortion is referred to as saddling. [d] These parameters are graphed against $|\Delta E_Q|$ in Figure 3.15.

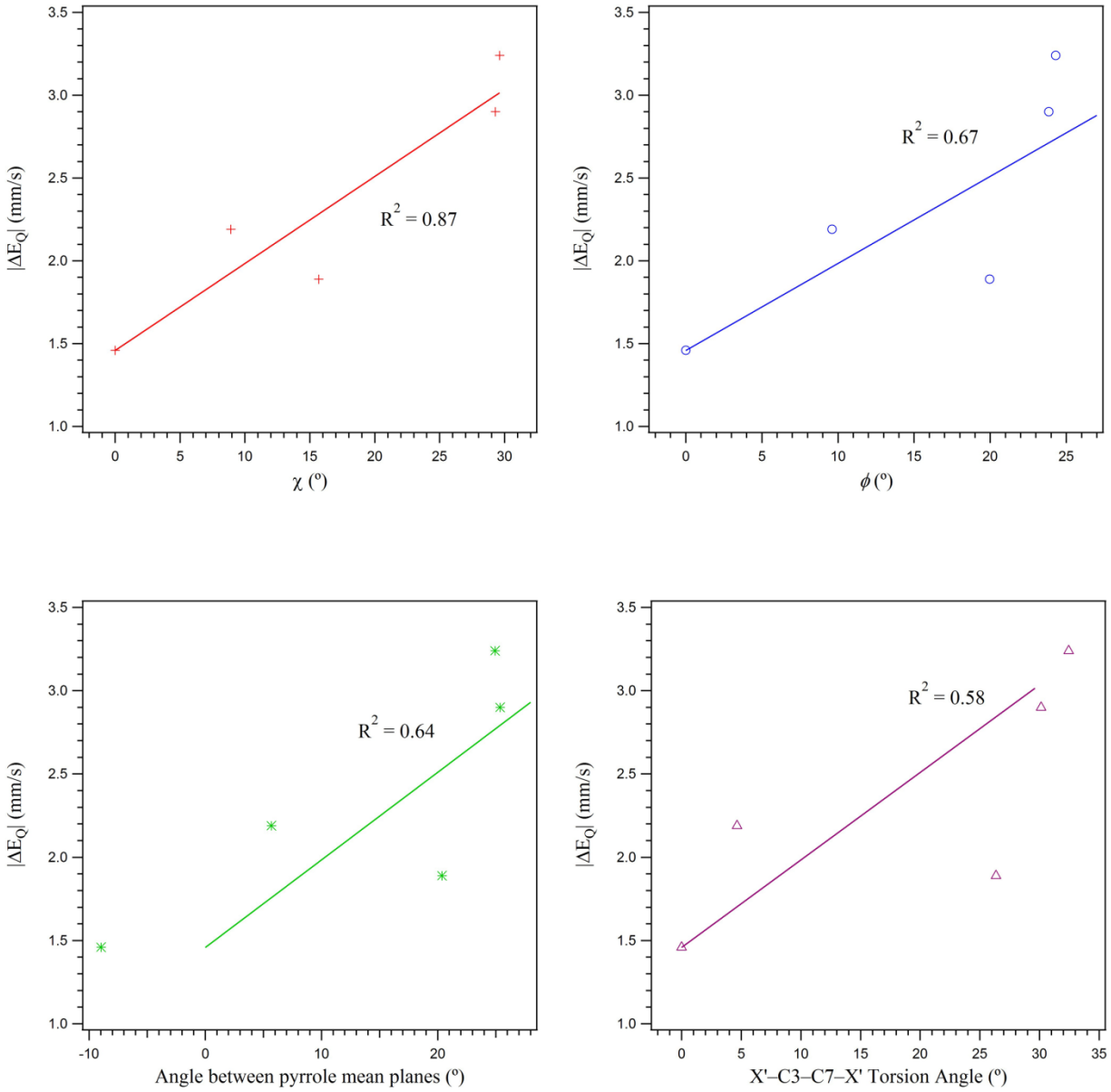

Figure 3.15. Graphical correlations of geometric parameters with $|\Delta E_Q|$. Top left: χ vs. $|\Delta E_Q|$; top right: ϕ vs. $|\Delta E_Q|$; bottom left: pyrrole mean plane ∠ pyrrole mean plane vs. $|\Delta E_Q|$; bottom right: X2-C3-C7-X3 dihedral ∠ vs. $|\Delta E_Q|$.

3.6.3 Density Functional Theory Calculations

The calculation of the ^{57}Fe Mössbauer parameters δ (the isomer shift) and ΔE_Q (the quadrupole splitting) by density functional theory (DFT) has been a challenge in recent years, and various functionals and basis sets can give widely different results. Our methods were based on the recent analysis of several basis sets and functionals by Lippard and coworkers, published

recently.[77] Calculations of Mössbauer parameters for the iron(II) dipyrrinato complexes described in Section 3.6 were carried out utilizing the ORCA 2.8 program package,[78] employing a variety of basis sets and functionals. Single-point calculations performed on the crystallographically determined geometries with the B3LYP hybrid functional[79] reproduced the experimental isomer shifts (δ) remarkably well for all complexes described herein, with the largest deviation being 0.03 $^{mm}/_{s}$. The quadrupole splittings ($|\Delta E_Q|$) determined with this functional, however, were not consistent with experimentally obtained values, overestimating them by as much as 2.5 $^{mm}/_{s}$. In an attempt to reproduce the quadrupole splitting values obtained experimentally, further computations were undertaken with various functionals and basis sets. The best results were obtained on structures that were optimized using the BP86 functional, and the Mössbauer parameters were subsequently calculated using the O3LYP hybrid functional[80] with SVP basis sets for C and H, CP(PPP) basis set for Fe,[81] pVTZ basis set for I, and TZVP basis sets[82] for all other atoms. Despite these optimizations, calculated values were still significantly higher than experimentally obtained, ranging from 0.1 $^{mm}/_{s}$ too high for **($^{Br}_{Mes}$L^{Mes})FeCl(py)** to as much as 1.4 $^{mm}/_{s}$ for **($^{I}_{Mes}$L^{Mes})FeCl(py)**.

[77] Bochevarov, A. D.; Friesner, R. A.; Lippard, S. J. *J. Chem. Theory Comput.* **2010**, *6*, 3735.
[78] Neese, F. ORCA – An ab initio, Density Functional and Semi-Empirical Electronic Structure Package, 2.8; Universitat Bonn: Bonn, Germany, 2010.
[79] (a) Schafer, A.; Horn, H.; Ahlrichs, R. *J. Chem. Phys.* **1992**, *97*, 2571. (b) Lee, C. T.; Yang, W. T.; Parr, R. G. *Phys Rev B* **1988**, *33*, 785. (c) Becke, A. D. *J. Chem. Phys.* **1993**, *98*, 5648.
[80] Handy, N. C. and Cohen, A. J. *J. Mol. Phys.* **2001**, *99*, 403.
[81] Neese, F. *Inorg. Chim. Acta* **2002**, *337*, 181.
[82] Schafer, A.; Huber, C.; Ahlrichs, R. *J. Chem. Phys.* **1994**, *100*, 5829.

Table 3.9. Experimental and computational Mössbauer parameters

Compound	Method (functional, structure, convergence criteria)	δ ($^{mm}/_{sec}$)	ΔE_Q ($^{mm}/_{sec}$)	$\Delta(\lvert\Delta E_Q\rvert)$
$(^{H}_{Mes}L^{Mes})FeCl(py)$ **1**	Experimental	**0.87**	**±2.19**	
	Single-point (B3LYP, xtal)	0.89	2.925	0.735
	Single-point (TPSSH, opt)	–0.36	3.832	1.642
	Single-point (O3LYP, opt)	8.28	**2.410**	**0.220**
	Single-point (B3LYP, opt, ext)		2.695	0.505
	Single-point (PBE, opt)	0.18	3.999	1.809
	Single-point (BP86, opt)		3.999	1.809
	Optimized (BP86; B3LYP, opt)	0.87	4.001	1.811
$(^{Cl}_{Mes}L^{Mes})FeCl(py)$ **2**	Experimental	**0.87**	**±2.90**	
	Single-point (B3LYP, xtal)	0.90	3.837	0.937
	Single-point (O3LYP, xtal)		3.615	0.715
	Single-point (O3LYP, opt)		**3.378**	**0.478**
	Optimized (BP86)	0.87	3.741	0.841
$(^{Br_2}_{Mes}L^{Mes})FeCl(py)$ **3**	Experimental	**0.86**	**±1.46**	
	Single-point (B3LYP, xtal)	0.88	3.896	2.436
	Single-point (O3LYP, opt)		**2.429**	**0.969**
	Optimized (BP86)	0.88	3.940	2.480
$(^{Br_4}_{Mes}L^{Mes})FeCl(py)$ **4**	Experimental	**0.88**	**±3.24**	
	Single-point (B3LYP, xtal)	0.89	3.835	0.595
	Single-point (B3LYP, xtal, vt)		3.835	0.595
	Single-point (O3LYP, opt, vt)		**3.350**	**0.110**
	Optimized (BP86)	0.86	3.685	0.445
$(^{I}_{Mes}L^{Mes})FeCl(py)$ **5**	Experimental	**0.89**	**±1.89**	
	Single-point (B3LYP, xtal)	0.90	3.655	1.765
	Single-point (O3LYP, opt, vt)		**3.308**	**1.418**
	Optimized (BP86)	0.86	3.597	1.707

Gray text indicates numerical outputs that were not calibrated to our internal set of isomer shifts using Equation 3.2. Red text indicates the closest correlation between experimental and calculated quadrupole splitting values. "Xtal" denotes crystallographically determined atomic coordinates; "opt" indicates that the structures were optimized using the BP86 functional, and the resulting atomic coordinates were used as input in the subsequent calculation. Convergence criteria occasionally had to be tightened beyond the default criteria in order to converge at a meaningful value; "vt" indicates very tight and "ext" indicates extremely tight convergence criteria.

The ORCA program package that was used to calculate ΔE_Q employs Equation 3.2 to calculate the isomer shift (δ), which the electron density at the iron nucleus, ρ_0, to the isomer shift; this requires calibration to a set of experimentally determined values of *a*, *b*, and *C*. The values of these constants were determined from a series of dipyrromethanato, dipyrrinato, and tris(pyrrolyl)ethane complexes synthesized in our lab.

$$\delta = a(\rho_0 - C) + b \qquad \text{(Eq. 3.2)}$$

The experimentally determined values used in these calculations were a = –0.402 $au^3 \cdot mm \cdot s^{-1}$, b = 8.605 mm, and C = 11797.145 au^{-3}.

The ORCA package also uses Equation 3.3 to determine the expected quadrupole splitting.

$$\Delta E_Q = \tfrac{1}{2} e Q V_{zz} \sqrt{1 + \tfrac{1}{3}\eta^2} \qquad \text{(Eq. 3.3)}$$

The values *e* (the elementary charge) and *Q* (the nuclear quadrupole moment of ^{57}Fe, taken to be 0.16 barn[83]) are constants, but V_{zz}, the principal tensor component of the electronic field gradient in the z-direction at the iron nucleus, and the asymmetry parameter η (defined as $\eta = (V_{xx} - V_{yy})/V_{zz}$), are both calculated separately by the program. The calculated values of V_{zz} and η were examined to determine if they had a better correlation with the crystallographically determined geometric variations than the calculated quadrupole splitting; no improved correlation was observed.

In an attempt to isolate single structural changes and ascertain their effects on the calculated quadrupole splitting, simplified and idealized structures of the molecules in question were used in further calculations, in which all the mesityl substituents were replaced by

[83] Sinnecker, S.; Slep, L. D.; Bill, E.; Neese, F. *Inorg. Chem.* **2005**, *44*, 2245.

hydrogens and the dipyrrin was forced into total planarity *in silico* (Figure 3.16). While maintaining full planarity of the simplified dipyrrinato ligand, the effect of halogenation was probed at the B3LYP level of theory; no change in the calculated isomer shift was observed, and halogenation uniformly increased the quadrupole splitting by ~1.2 $^{mm}/_{s}$, regardless of the identity of the halogen (Table 3.10), contrary to the observed trends for both the dibrominated (**3**) and tetraiodinated (**5**) complexes, which showed smaller quadrupole splittings than the non-halogenated compound (**1**).

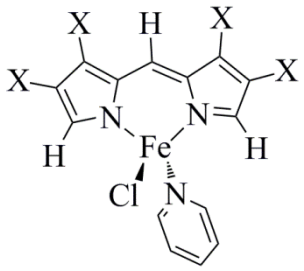

$(^{X}_{H}L^{H})FeCl(py)$

Figure 3.16. Simplified structure used to evaluate the effect of halogenation on the DFT calculation of Mössbauer parameters.

Table 3.10. Calculated quadrupole splittings for halogenated iron(II) dipyrrinato complexes

Compound	X	ΔE_Q ($^{mm}/_{s}$)
$(^{H}_{H}L^{H})FeCl(py)$	H	2.676 (3.975)[a]
$(^{Cl}_{H}L^{H})FeCl(py)$	Cl	3.872
$(^{Br}_{H}L^{H})FeCl(py)$	Br	3.870 (3.757)[b]
$(^{I}_{H}L^{H})FeCl(py)$	I	3.879

A fully planar dipyrrinato core with all mesityl substituents replaced by hydrogens was used in each of these single-point calculations, which were performed using the B3LYP functional. [a] Value obtained with non-stringent convergence criteria. [b] Results using the O3LYP functional.

The effect of changing χ was then probed using a similar technique on a simplified, non-halogenated system (Figure 3.17). The fully planar dipyrrin ligand bearing hydrogens instead of mesityl groups was modified by increasing χ in 5° increments while freezing the positions of the iron and other ligands, and Mössbauer parameters were calculated at the B3LYP level of theory for each variation. Though a self-consistent trend in the quadrupole splitting was observed in the series of calculations, it was the *opposite* trend than experimentally seen (Figure 3.18). Experimentally, an increase in χ corresponded with an increase in $|\Delta E_Q|$, but calculations showed a decrease in $|\Delta E_Q|$ with increasing χ (Table 3.11). It is unclear why calculations have provided such contrary results, but we hope that these findings can be used to improve the accuracy of DFT methods for the calculation of Mössbauer parameters.

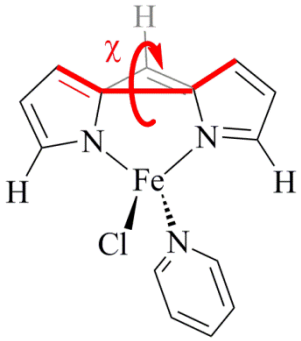

Figure 3.17. Illustration of the systematic variation in χ that was used to calculate Mössbauer parameters.

Table 3.11. Calculated effect of χ on $|\Delta E_Q|$.

χ (°)	ΔE_Q ($^{mm}/_{sec}$)
0 (vt) [a]	2.676
5 (vt) [a]	2.673
10	2.663
15	3.969[b]
20	2.622
25 (vt) [a]	2.588
30 (vt) [a]	2.549
35	2.509
40	–2.469[c]
45	–2.433[c]
50	–2.403[c]

Relative positions of the Fe, Cl, and pyridine units were frozen and the dihedral angle χ was increased in increments of 5°, while maintaining the planarity of each pyrrole subunit; Mössbauer parameters were then calculated. [a] Very tight (vt) convergence parameters had to be used in these cases in order to reproduce the self-consistent trend; in other cases, weaker convergence criteria were used to minimize computational expense. With lower tightness of convergence criteria, ΔE_Q values of ~3.97 mm/s were observed for these angles χ. [b] Despite attempts to increase the tightness of the convergence criteria, no values lower than 3.9 $^{mm}/_{s}$ could be obtained for χ = 15°. [c] The sign of the quadrupole splitting switches between χ = 35° and χ = 40°; this is likely due to a change in the iron orbitals that are involved in bonding with the dipyrrinato ligand.

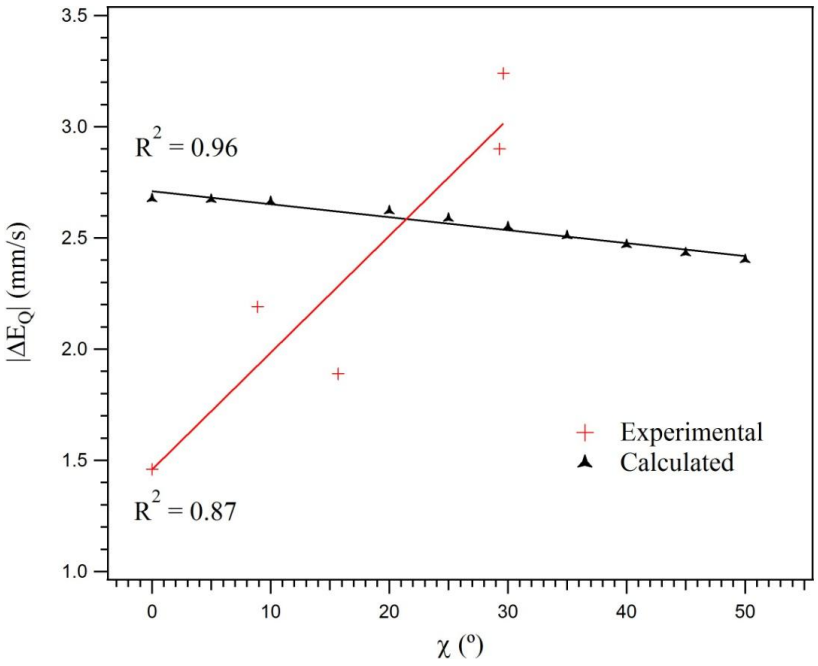

Figure 3.18. Graphical comparison of the experimental and DFT-calculated trends in χ vs. $|\Delta E_Q|$.

3.7 Conclusions

The effects of halogenation and *meso*-fluoroarylation on the electronic, spectroscopic, and structural properties of iron(II) dipyrrinato complexes has been explored. The UV/Vis absorption spectra are bathochromically shifted for both halogenated and *meso*-fluoroarylated complexes **2**–**9** relative to the non-halogenated *meso*-mesityl complex **1**. The oxidation potential of the fully-reversible $Fe^{III/II}$ couple in these iron(II) dipyrrinato complexes is also sensitive to halogenation and *meso*-fluoroarylation; the incorporation of these electron-withdrawing substituents can increase the oxidation potential by as much as +386 mV. While neither halogenation nor *meso*-fluoroarylation affected the Mössbauer isomer shift (δ), large variations in the quadrupole splitting ($|\Delta E_Q|$) were seen for the halogenated complexes **2**–**5**. Crystallographic analysis showed a correlation between the degree of deplanarization of the

dipyrrin, as measured by the dihedral angle χ, with the quadrupole splitting, though these correlations were not borne out by DFT calculations.

3.8 Experimental Methods

3.8.1 General Synthetic Considerations

All syntheses of iron complexes were carried out in the absence of water and dioxygen in an MBraun inert atmosphere drybox under a dinitrogen atmosphere. All glassware was oven dried for a minimum of 1 h and cooled in an evacuated antechamber prior to use in the drybox. Bulk solvents used inside the glovebox (tetrahydrofuran, benzene, diethyl ether, and *n*-hexane) were dried and deoxygenated on a Glass Contour System (SG Water) and stored over 4 Å molecular sieves prior to use. Anhydrous *n*-pentane and pyridine were purchased from Aldrich and used as received in the glovebox. Anhydrous hexamethyldisiloxane (Aldrich) and benzene-d_6 (Cambridge Isotope Labs) were degassed by a minimum of three freeze-pump-thaw cycles and stored over 4 Å molecular sieves prior to use. Anhydrous transition metal compounds were purchased from Strem and used as received. Celite® 545 (Baker), tetra-*n*-butylammonium hexafluorophosphate (Alfa Aesar) and zinc chloride (Aldrich) for use in the glovebox were dried in a Schlenk flask for 24 h under dynamic vacuum while heating to at least 150 °C.

3.8.2 Characterization and Physical Measurements

Nuclear magnetic resonance experiments were performed on Varian Mercury 400 or Varian Unity/Inova 500 spectrometers. ^{1}H NMR chemical shifts are reported relative to $SiMe_4$ using the chemical shift of residual solvent peaks as reference. ^{19}F chemical shifts are reported relative to external $CFCl_3$. Spectra were processed using the ACDLabs SpecManager v. 12 software package.

UV/Visible spectra were recorded on a Varian Cary 50 UV/Visible Spectrometer, with a scan rate of 100–300 nm/min. Extinction coefficients were determined from a minimum of four concentrations per sample, and were calculated by a linear regression fit of the absorbance vs. concentration data.

Cyclic voltammetry experiments were carried out using a CH Instruments CHI660C Electrochemical Workstation. The supporting electrolyte was 0.3 *M* (nBu$_4$N)(PF$_6$) in tetrahydrofuran. A glassy carbon working electrode, platinum wire counter electrode, and a non-aqueous Ag^+/Ag reference electrode (10 m*M* $AgNO_3$ in acetonitrile) were used. The concentration of each analyte was ~0.1 m*M*. Scan rates were 100–500 $^{mV}/_{s}$, depending on the sample. Each scan was referenced to internal Fc^+/Fc; when overlapping redox waves or electron transfer between species in solution obscured the reference peaks, external Fc^+/Fc was used instead.

Elemental analyses were carried out at Complete Analysis Laboratories, Inc. (Parsippany, NJ).

Zero-field ^{57}Fe Mössbauer spectra were recorded on a Janis Research Company SVT-100 constant-acceleration spectrometer operating at 110 K. Samples were prepared as suspensions in Paratone-N oil. Spectral fits were performed with WaveMetrics IGOR Pro v. 6.1.2.1.

X-ray crystallographic characterization was performed at one of two locations. In-house data was collected at the at the Harvard Center for Crystallographic Studies. Data was obtained on a Bruker three-circle platform goniometer equipped with an Apex II CCD and an Oxford cryostream cooling device. Radiation was from a graphite fine focus sealed tube Mo Kα (λ = 0.71073 Å) source. Crystals were mounted on a cryoloop or glass fiber pin using

Paratone-N oil. Structures were collected at 100 K. Data for small or poorly diffracting crystals were obtained on the ChemMatCARS beamline at the Advanced Photon Source (APS) at Argonne National Labs (Argonne, IL), operating at 15 K (or 50 K for **($_{C_6F_5}^{Cl}$L^{Mes})FeCl(py)**). For data collected at APS, absorption parameters, *f′*and *f″*, for all heavy atoms (C, N, O, F, Cl, Br, Fe) were adjusted to the appropriate values for the synchrotron wavelength of 0.41328 Å (or 0.44280 Å for **($_{C_6F_5}^{Cl}$L^{Mes})FeCl(py)**) during refinement. All data was collected as a series of φ and ω scans. All data was integrated using SAINT and scaled with a multi-scan absorption correction using SADABS.[64] The structures were solved by direct methods or Patterson maps using SHELXS-97 and refined against F^2 on all data by full matrix least squares with SHELXL-97.[65] All non-hydrogen atoms were refined anisotropically. Hydrogen atoms were placed at idealized positions and refined using a riding model. Full experimental details for all compounds characterized by x-ray diffraction can be found in the Appendix.

3.8.3 Synthetic Procedures

Scheme 3.2. Deprotonation of dipyrrins

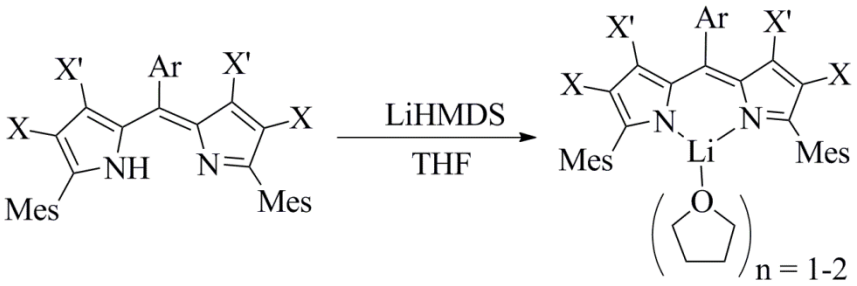

General procedure for deprotonation. To a stirring solution of the dipyrrin in anhydrous THF at liquid nitrogen temperature or room temperature was added lithium hexamethyl disilazide (LiHMDS, 1.0 equiv.) as a 1.0 *M* solution in hexanes. The solution was allowed to stir for up to

24 hours, and the solvent was removed in vacuo to afford the lithium dipyrrinato salts as THF adducts. Yields were uniformly quantitative.

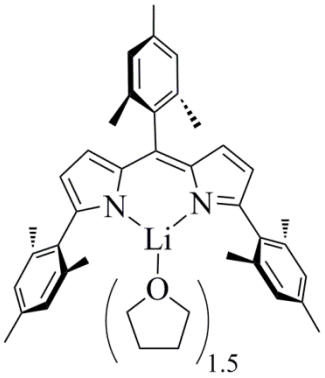

($_{Mes}^{H}L^{Mes}$)Li(THF)$_{1.5}$. ^{1}H NMR (500 MHz, C_6D_6) δ ppm 1.00 (m, 6H, O(CH$_2$)$_2$(C*H*$_2$)$_2$), 2.10 (s, 6H, [*p*-*Me*($C_6H_2Me_2$)]$_2$ (flanking Mes)), 2.25 (s, 3H, *p*-*Me*($C_6H_2Me_2$) [*meso*-Mes]), 2.28 (s, 12H, [*o*-*Me*$_2$(C_6H_2Me)]$_2$ (flanking Mes)), 2.45 (s, 6H, *o*-*Me*$_2$(C_6H_2Me) [*meso*-Mes]), 2.81 (br. s., 6H, O(C*H*$_2$)$_2$(CH$_2$)$_2$), 6.40 (d, *J* = 4.12 Hz, 2H, [pyrrole-C*H*]$_2$), 6.72 (s, 4H, [$Me_3C_6H_2$]$_2$ (flanking Mes)), 6.89 (s, 2H, $Me_3C_6H_2$ [*meso*-Mes]), 6.93 (d, *J* = 4.12 Hz, 2H, [pyrrole-C*H*]$_2$).

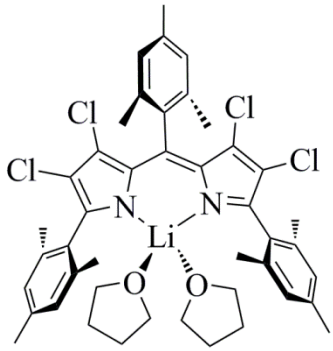

($_{Mes}^{Cl}L^{Mes}$)Li(THF)$_2$. ^{1}H NMR (400 MHz, C_6D_6) δ ppm 1.07 (m, 8H, O(CH$_2$)$_2$(C*H*$_2$)$_2$), 1.99 (s, 6H, [*p*-*Me*($C_6H_2Me_2$)]$_2$ (flanking Mes)), 2.07 (s, 12H, [*o*-*Me*$_2$(C_6H_2Me)]$_2$ (flanking Mes)), 2.21 (s, 3H, *p*-*Me*($C_6H_2Me_2$) [*meso*-Mes]), 2.39 (s, 6H, *o*-*Me*$_2$(C_6H_2Me) [*meso*-Mes]), 2.92 (m, 8H, O(C*H*$_2$)$_2$(CH$_2$)$_2$), 6.57 (s, 4H, [$Me_3C_6H_2$]$_2$ (flanking Mes)), 6.93 (s, 2H, $Me_3C_6H_2$ [*meso*-Mes]).

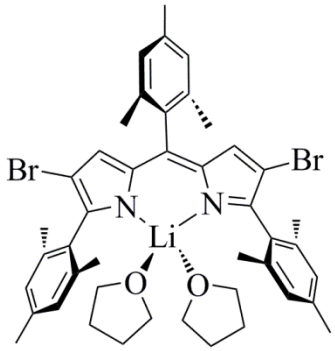

($^{Br;\ H}_{Mes}L^{Mes}$)Li(THF)$_2$. ^{1}H NMR (400 MHz, C_6D_6) δ ppm 1.26 (m, 8H, O(CH$_2$)$_2$(C*H*$_2$)$_2$), 2.21 (2, 6H, [*p*-*Me*($C_6H_2Me_2$)]$_2$ (flanking Mes)) , 2.34 (s, 12H, [*o*-*Me*$_2$(C_6H_2Me)]$_2$ (flanking Mes)), 2.38 (s, 3H, *p*-*Me*($C_6H_2Me_2$) [*meso*-Mes]), 2.47 (s, 6H, *o*-*Me*$_2$(C_6H_2Me) [*meso*-Mes]), 3.16 (m, 8H, O(C*H*$_2$)$_2$(CH$_2$)$_2$), 6.82 (s, 4H, [$Me_3C_6H_2$]$_2$ (flanking Mes)), 6.95 (s, 2H, $Me_3C_6H_2$ [*meso*-Mes]), 7.29 (s, 2H, [pyrrole-C*H*]$_2$).

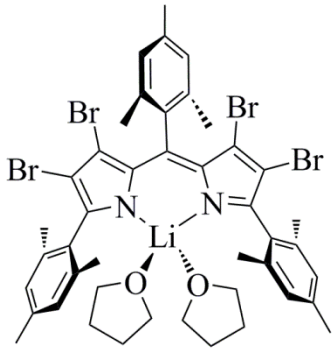

($^{Br}_{Mes}L^{Mes}$)Li(THF)$_2$. ^{1}H NMR (400 MHz, C_6D_6) δ ppm 1.11 (t, *J* = 6.22 Hz, 8H, O(CH$_2$)$_2$(C*H*$_2$)$_2$), 2.00 (s, 6H, [*p*-*Me*($C_6H_2Me_2$)]$_2$ (flanking Mes)), 2.05 (s, 12H, [*o*-*Me*$_2$(C_6H_2Me)]$_2$ (flanking Mes)), 2.23 (s, 3H, *p*-*Me*($C_6H_2Me_2$) [*meso*-Mes]), 2.34 (s, 6H, *o*-*Me*$_2$(C_6H_2Me) [*meso*-Mes]), 2.99 (t, *J* = 6.22 Hz, 8H, O(C*H*$_2$)$_2$(CH$_2$)$_2$), 6.57 (s, 4H, [$Me_3C_6H_2$]$_2$ (flanking Mes)), 6.93 (s, 2H, $Me_3C_6H_2$ [*meso*-Mes]).

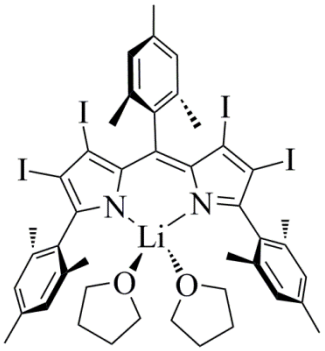

($_{Mes}^{I}$L^{Mes})Li(THF)$_2$. ^{1}H NMR (500 MHz, C_6D_6) δ ppm 1.15 (dt, *J* = 6.56 & 3.13 Hz, 8H, O(CH$_2$)$_2$(C*H*$_2$)$_2$), 2.04 (s, 6H, [*p*-*Me*(C$_6$H$_2$Me$_2$)]$_2$ (flanking Mes)), 2.05 (s, 12H, [*o*-*Me*$_2$(C$_6$H$_2$Me)]$_2$ (flanking Mes)), 2.28 (s, 6H, *o*-*Me*$_2$(C$_6$H$_2$Me) [*meso*-Mes]), 2.30 (s, 3H, *p*-*Me*(C$_6$H$_2$Me$_2$) [*meso*-Mes]), 2.99 (m, 8H, O(C*H*$_2$)$_2$(CH$_2$)$_2$), 6.61 (s, 4H, [Me$_3$C$_6$*H*$_2$]$_2$ (flanking Mes)), 6.98 (s, 2H, Me$_3$C$_6$*H*$_2$ [*meso*-Mes]).

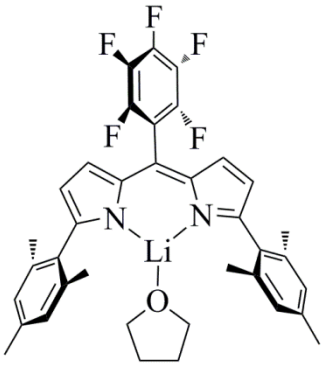

($_{C_6F_5}^{H}$L^{Mes})Li(THF)$_1$. ^{1}H NMR (500 MHz, C_6D_6) δ ppm 0.91 (dt, *J* = 6.79 & 3.16 Hz, 4H, O(CH$_2$)$_2$(C*H*$_2$)$_2$), 2.08 (s, 6H, [*p*-*Me*(C$_6$H$_2$Me$_2$)]$_2$), 2.18 (s, 12H, [*o*-*Me*$_2$(C$_6$H$_2$Me)]$_2$), 2.58 (m, 4H, O(C*H*$_2$)$_2$(CH$_2$)$_2$), 6.43 (d, *J* = 3.97 Hz, 2H, [pyrrole-C*H*]$_2$), 6.68 (s, 4H, [Me$_3$C$_6$*H*$_2$]$_2$), 6.71 (d, *J* = 3.97 Hz, 2H, [pyrrole-C*H*]$_2$).

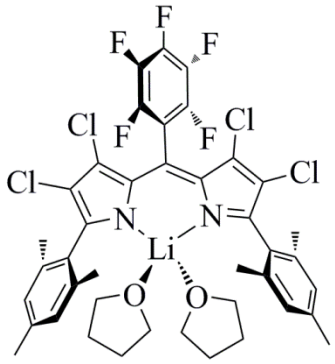

($_{C_6F_5}^{Cl}$L^{Mes})Li(THF)$_2$. ^{1}H NMR (500 MHz, C_6D_6) δ ppm 1.05 (m, 8H, O(CH$_2$)$_2$(C*H*$_2$)$_2$), 1.97 (s, 12H, [*o*-*Me*$_2$(C$_6$H$_2$Me)]$_2$), 1.99 (s, 6H, [*p*-*Me*(C$_6$H$_2$Me$_2$)]$_2$), 2.87 (m, 8H, O(C*H*$_2$)$_2$(CH$_2$)$_2$), 6.55 (s, 4H, [Me$_3$C$_6$*H*$_2$]$_2$).

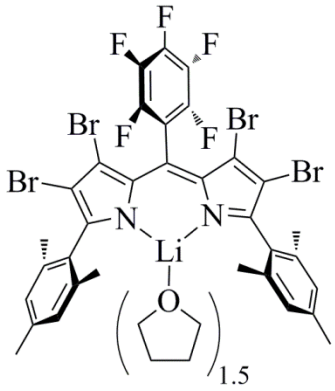

($_{C_6F_5}^{Br}$L^{Mes})Li(THF)$_{1.5}$. ^{1}H NMR (500 MHz, C_6D_6) δ ppm 0.94 (dt, *J* = 6.48, 3.32 Hz, 6H, O(CH$_2$)$_2$(C*H*$_2$)$_2$), 1.92 (s, 12H, [*o*-*Me*$_2$(C$_6$H$_2$Me)]$_2$), 1.97 (s, 6H, [*p*-*Me*(C$_6$H$_2$Me$_2$)]$_2$), 2.61 (t, *J* = 6.25 Hz, 6H, O(C*H*$_2$)$_2$(CH$_2$)$_2$), 6.53 (s, 4H, [Me$_3$C$_6$*H*$_2$]$_2$).

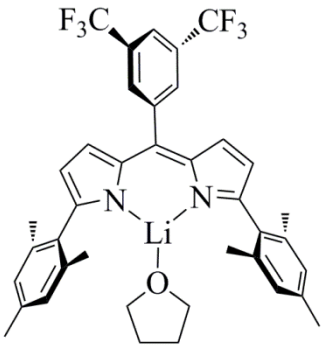

($_{BFP}^{H}$L^{Mes})Li(THF)$_1$. ^{1}H NMR (500 MHz, C_6D_6) δ ppm 0.99 (dt, *J* = 6.79 & 3.16 Hz, 4H, $O(CH_2)_2(CH_2)_2$), 2.10 (s, 6H, [*p*-*Me*($C_6H_2Me_2$)]$_2$), 2.25 (s, 12H, [*o*-*Me*$_2$(C_6H_2Me)]$_2$), 2.76 (m, 4H, $O(CH_2)_2(CH_2)_2$), 6.37 (d, *J* = 3.66 Hz, 2H, [pyrrole-C*H*]$_2$), 6.49 (d, *J* = 3.97 Hz, 2H, [pyrrole-C*H*]$_2$), 6.71 (s, 4H, [$Me_3C_6H_2$]$_2$), 7.82 (s, 1H, *p*-*H*($C_6H_2(CF_3)_2$), 7.84 (s, 2H, *o*-*H*$_2$($C_6H_1(CF_3)_2$)).

Scheme 3.3. Metalation of lithium dipyrrinato complexes with $FeCl_2$

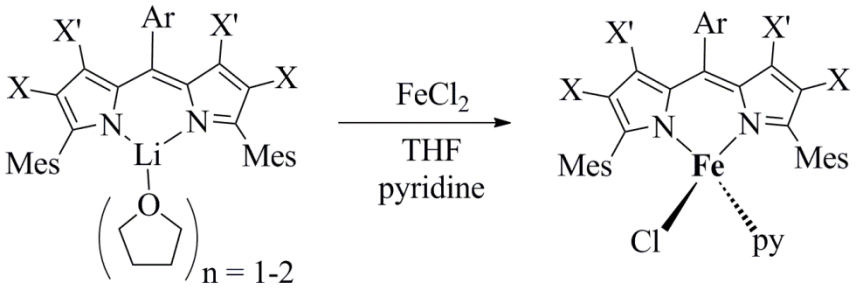

General procedure for metalation with $FeCl_2$. To a stirring solution of the lithium dipyrrinato salt in THF was added metal chloride (1.1 equiv.) and a few drops of pyridine. After stirring for up to 24 hours, the solvent was removed in vacuo and the residue was taken up in benzene, filtered through a plug of diatomaceous earth, and concentrated in vacuo to afford the metal dipyrrinato complexes.

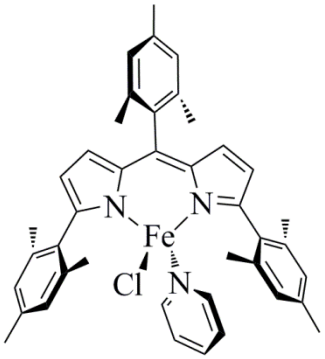

($_{Mes}^{H}$L^{Mes})FeCl(py) (1). 95% isolated yield. ^{1}H NMR (500 MHz, C_6D_6) δ ppm –21.37 (br. s), −10.33 (br. s), –2.06 (br. s), 2.41 (s), 5.08 (s), 23.09 (s), 27.27 (br. s), 40.93 (s), 50.88 (s). UV/Vis (CH_2Cl_2, 25 °C) λ_{max} = 506 nm, ε = 73,000 $M^{-1}cm^{-1}$. Mössbauer (Paratone, 110 K) $\delta = 0.87$ $^{mm}/_{s}$, $|\Delta E_Q|$ = 2.19 $^{mm}/_{s}$. Anal. calc'd for $C_{41}H_{42}ClFeN_3$: C, 73.71; H, 6.34; N, 6.29. Found: C, 73.66; H, 6.33; N, 6.29. Crystals suitable for X-ray diffraction were grown from concentrated diethyl ether/hexane solutions at −35 °C. The structure was solved in the monoclinic space group $P2_1/c$, with four molecules in the unit cell and a single molecule in the asymmetric unit.

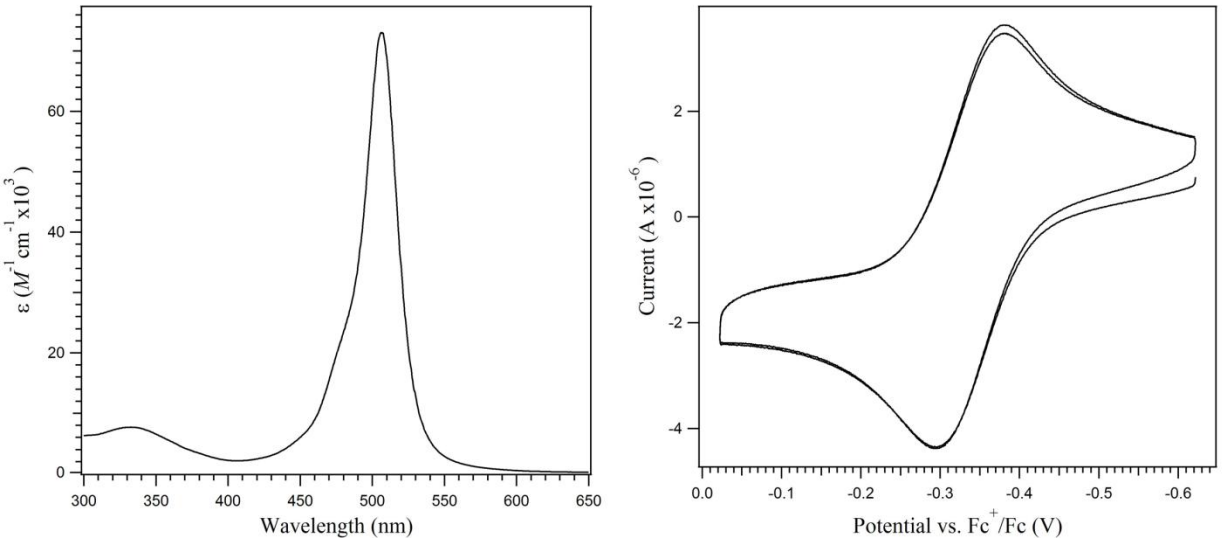

Figure 3.19. UV/Vis spectrum, left, and cyclic voltammogram, right, of **($_{Mes}^{H}$L^{Mes})FeCl(py)**. The cyclic voltammogram illustrates the $Fe^{III/II}$ couple. For full experimental details, see page 93.

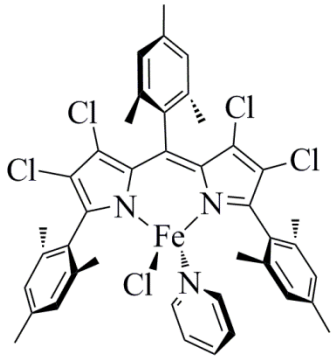

($_{Mes}^{Cl}$L^{Mes})FeCl(py) (2). 77% isolated yield. ^{1}H NMR (500 MHz, C_6D_6) δ ppm −12.24 (br. s), −5.79 (br. s), 3.72 (s), 6.22 (s), 38.35 (s). UV/Vis (CH_2Cl_2, 25 °C) λ_{max} = 524.5 nm, ε = 83,000 $M^{-1}cm^{-1}$. Mössbauer (Paratone, 110 K) $\delta = 0.87$ $^{mm}/_{s}$, $|\Delta E_Q|$ = 2.90 $^{mm}/_{s}$. Anal. calc'd for $C_{41}H_{38}Cl_5FeN_3$: C, 61.11; H, 4.75; N, 5.21. Found: C, 61.16; H, 4.75; N, 5.27. Microcrystalline material suitable for X-ray diffraction using the synchrotron source at APS were grown from a concentrated solution in diethyl ether and hexamethyldisiloxane. The structure was solved in the monoclinic space group $P2_1/c$, with four molecules in the unit cell and a single molecule in the asymmetric unit.

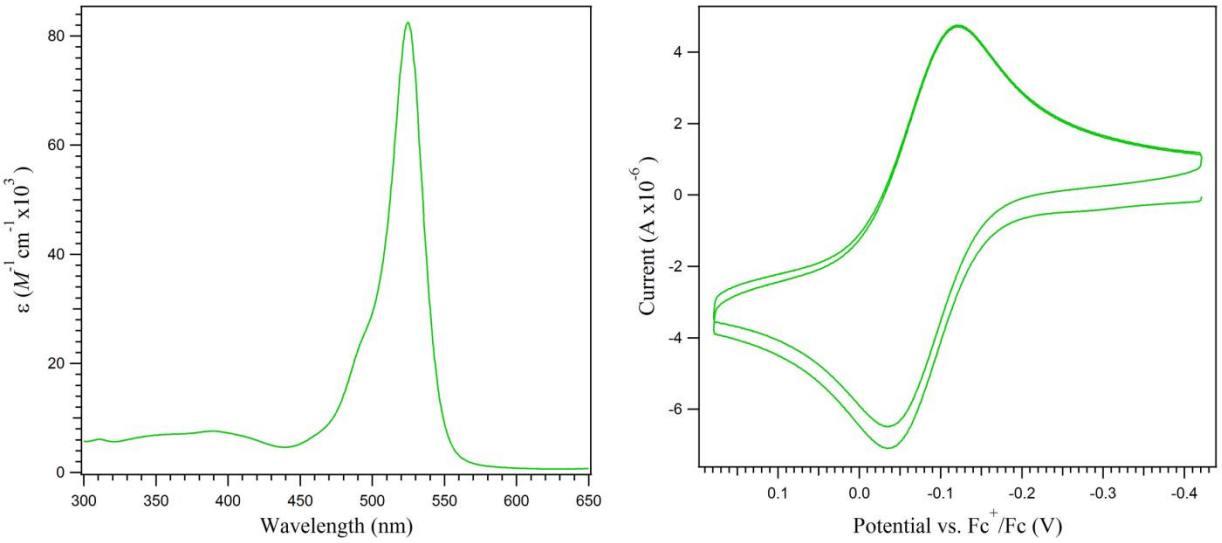

Figure 3.20. UV/Vis spectrum, left, and cyclic voltammogram, right, of **($_{Mes}^{Cl}$L^{Mes})FeCl(py)**. The cyclic voltammogram illustrates the $Fe^{III/II}$ couple. For full experimental details, see page 93.

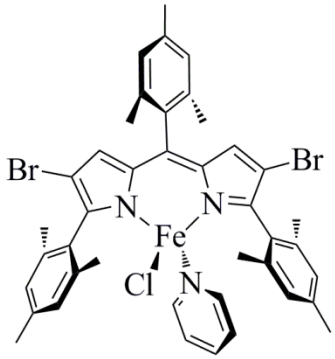

($^{Br;\ H}_{Mes}$L^{Mes})FeCl(py) (3). 81% isolated yield. ^{1}H NMR (500 MHz, C_6D_6) δ ppm −14.96 (br. s), −1.64 (br. s), 2.24 (s), 4.96 (s), 11.22 (br. s), 24.39 (s), 34.58 (br. s). UV/Vis (CH_2Cl_2, 25 °C) λ_{max} = 528.0 nm, ε = 97,000 $M^{-1}cm^{-1}$. Mössbauer (Paratone, 110 K) $\delta = 0.86$ $^{mm}/_{s}$, $|\Delta E_Q| = 1.44$ $^{mm}/_{s}$. Anal. calc'd for $C_{41}H_{40}Br_2ClF_5FeN_3$: C, 59.63; H, 4.88; N, 5.09. Found: C, 59.60; H, 4.79; N, 5.21. Crystals suitable for X-ray diffraction were grown from concentrated solutions in diethyl ether/hexanes at –35 °C. The structure was solved in the orthorhombic space group C*mc*2_1, with four molecules in the unit cell and one half the molecule in the asymmetric unit. The iron, chloride, and pyridine ligands all reside on a crystallographic mirror plane.

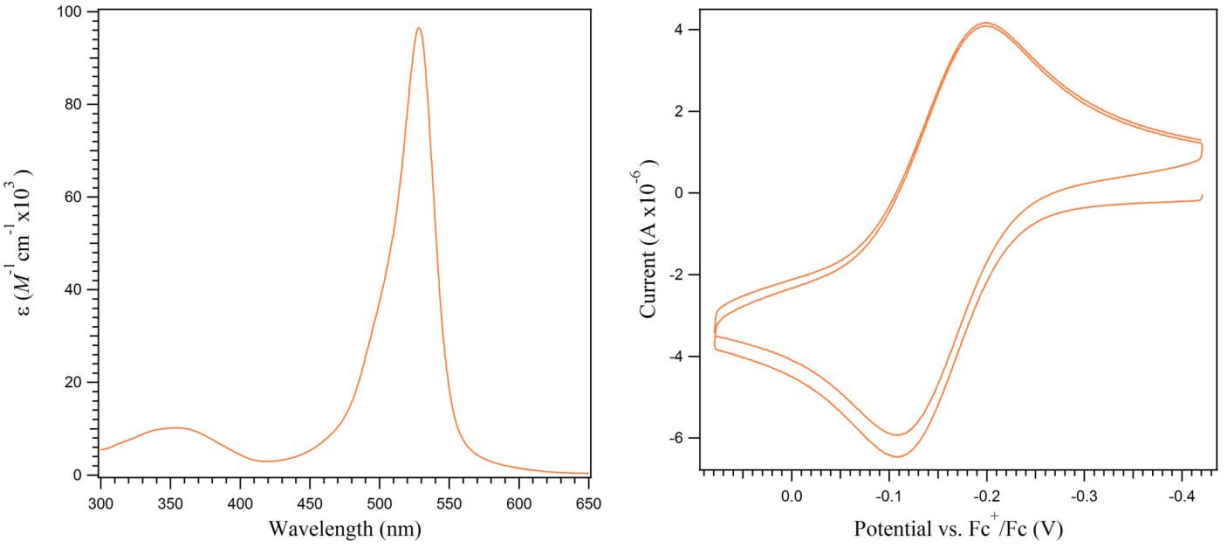

Figure 3.21. UV/Vis spectrum, left, and cyclic voltammogram, right, of **($^{Br;\ H}_{Mes}$L^{Mes})FeCl(py)**. The cyclic voltammogram illustrates the $Fe^{III/II}$ couple. For full experimental details, see page 93.

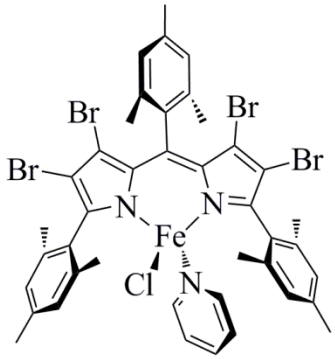

($_{Mes}^{Br}$L^{Mes})FeCl(py) (4). 67% isolated yield. ^{1}H NMR (500 MHz, C_6D_6) δ ppm −27.46 (br. s), −14.00 (br.s), −5.62 (s), 4.05 (s), 4.72 (s), 6.38 (s), 13.57 (br. s), 38.39 (s). UV/Vis (CH_2Cl_2, 25 °C) λ_{max} = 530.5 nm, ε = 130,000 $M^{-1}cm^{-1}$. Mössbauer (Paratone, 110 K) δ = 0.88 $^{mm}/_{s}$, $|\Delta E_Q|$ = 3.24 $^{mm}/_{s}$. Anal. calc'd for $C_{41}H_{38}Br_4ClFeN_3$: C, 50.06; H, 3.89; N, 4.27. Found: C, 49.93; H, 3.88; N, 4.24. Crystals suitable for X-ray diffraction were grown from concentrated solutions in THF/hexamethyldisiloxane at –35 °C. The structure was solved in the monoclinic space group $P2_1/c$, with four molecules in the unit cell and a single molecule in the asymmetric unit.

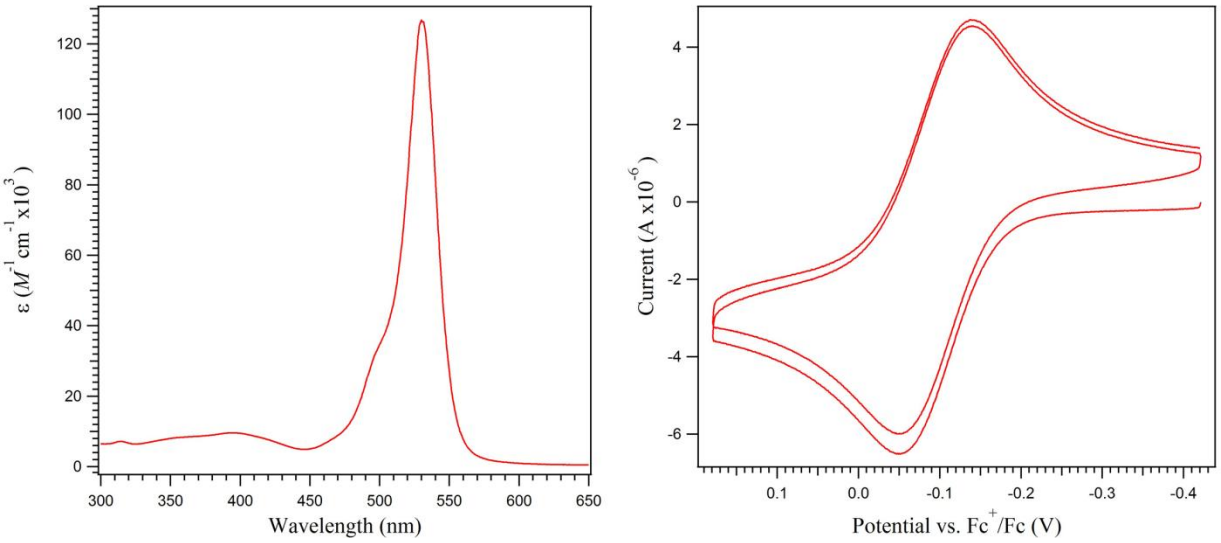

Figure 3.22. UV/Vis spectrum, left, and cyclic voltammogram, right, of **($_{Mes}^{Br}$L^{Mes})FeCl(py)**. The cyclic voltammogram illustrates the $Fe^{III/II}$ couple. For full experimental details, see page 93.

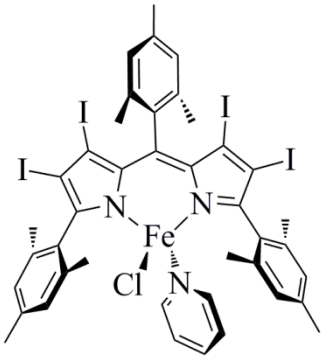

($_{Mes}^{I}$L^{Mes})FeCl(py) (5). 51% isolated yield. ^{1}H NMR (500 MHz, C_6D_6) δ ppm −30.20 (br. s), −11.73 (br. s.), −3.99 (br. s), 1.86 (s), 2.01 (s), 2.13 (s), 2.21 (s), 4.50 (s), (6.54 (s), 14.71 (s), 38.31 (br. s). UV/Vis (CH_2Cl_2, 25 °C) λ_{max} = 545.6 nm, ε = 83,000 $M^{-1}cm^{-1}$. Mössbauer (Paratone, 110 K) δ = 0.89 $^{mm}/_{s}$, $|\Delta E_Q|$ = 1.89 $^{mm}/_{s}$. Anal. calc'd for $C_{41}H_{38}ClFeI_4N_3$: C, 42.03; H, 3.27; N, 3.59. Found: C, 41.99; H, 3.19; N, 3.53. Crystals suitable for X-ray diffraction were grown from a concentrated solution in hexanes at –35 °C. The structure was solved in the monoclinic space group $P2_1/c$, with four molecules in the unit cell and a single molecule in the asymmetric unit. There was half a molecule of benzene in the asymmetric unit, bisected by a crystallographic mirror plane.

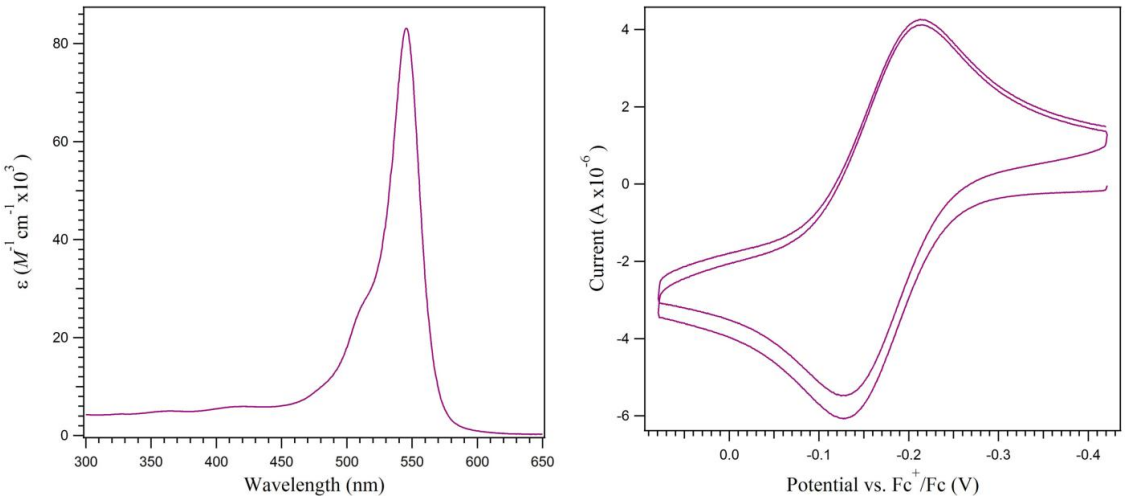

Figure 3.23. UV/Vis spectrum, left, and cyclic voltammogram, right, of **($_{Mes}^{I}$L^{Mes})FeCl(py)**. The cyclic voltammogram illustrates the $Fe^{III/II}$ couple. For full experimental details, see page 93.

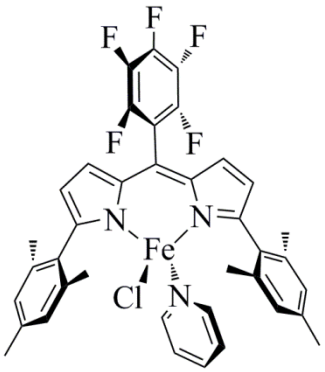

($_{C_6F_5}^{H}$L^{Mes})FeCl(py) (6). 87% isolated yield. ^{1}H NMR (500 MHz, C_6D_6) δ ppm −19.31 (br. s), 1.34 (s), 3.21 (s), 26.45 (s), 41.10 (s), 51.25 (s). ^{19}F NMR (376 MHz, C_6D_6) δ ppm −151.12 (br. s, 2F, *m*-F), −149.27 (t, *J* = 22.5 Hz, 1F, *p*-F). UV/Vis (CH_2Cl_2, 25 °C) λ_{max} = 516.7 nm, ε = 84,000 $M^{-1}cm^{-1}$. Mössbauer (Paratone, 110 K) δ = 0.89 $^{mm}/_{s}$, $|\Delta E_Q|$ = 1.92 $^{mm}/_{s}$. Anal. calc'd for $C_{38}H_{31}ClF_5FeN_3$: C, 63.75; H, 4.36; N, 5.87. Found: C, 63.81; H, 4.25; N, 5.79. Crystals suitable for X-ray diffraction were grown by slow evaporation of concentrated chloroform-*d* solution at ambient temperature. The structure was solved in the monoclinic space group $P2_1/c$, with four molecules in the unit cell and a single molecule in the asymmetric unit.

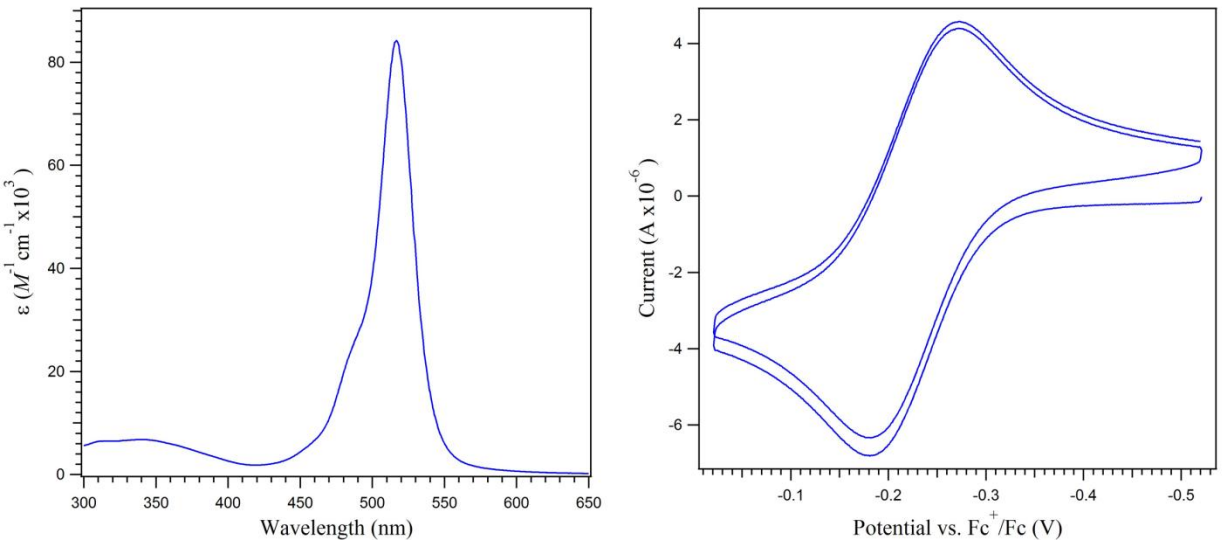

Figure 3.24. UV/Vis spectrum, left, and cyclic voltammogram, right, of **($_{C_6F_5}^{H}$L^{Mes})FeCl(py)**. The cyclic voltammogram illustrates the $Fe^{III/II}$ couple. For full experimental details, see page 93.

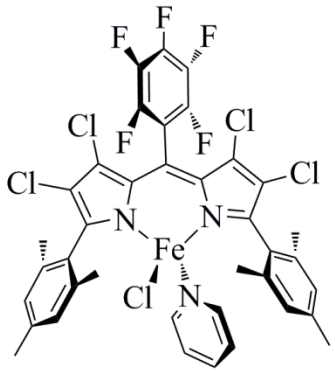

($_{C_6F_5}^{Cl}$L^{Mes})FeCl(py) (7). 81% isolated yield. ^{1}H NMR (500 MHz, C_6D_6) δ ppm −24.54 (br. s), −21.66 (br. s), −6.68 (br. s), 1.30 (s), 5.10 (s), 37.79 (br. s). ^{19}F NMR (376 MHz, C_6D_6) δ ppm −155.06 (br. s, 2F, *m*-F), −145.93 (m, 1F, *p*-F), −124.83 (br. s, 2F, *o*-F). UV/Vis (CH_2Cl_2, 25 °C) λ_{max} = 541.5 nm, ε = 54,000 $M^{-1}cm^{-1}$. Mössbauer (Paratone, 110 K) $\delta = 0.87$ $^{mm}/_{s}$, $|\Delta E_Q| = 1.35$ $^{mm}/_{s}$. Anal. calc'd for $C_{38}H_{27}Cl_5F_5FeN_3$: C, 53.46; H, 3.19; N, 4.92. Found: C, 53.37; H, 3.26; N, 4.86. Microcrystalline material suitable for X-ray diffraction analysis at the synchrotron radiation source at APS was grown from concentrated diethyl ether/hexanes solutions at ambient temperature. The structure was solved in the monoclinic space group $P2_1/c$, with four molecules in the unit cell and a single molecule in the asymmetric unit.

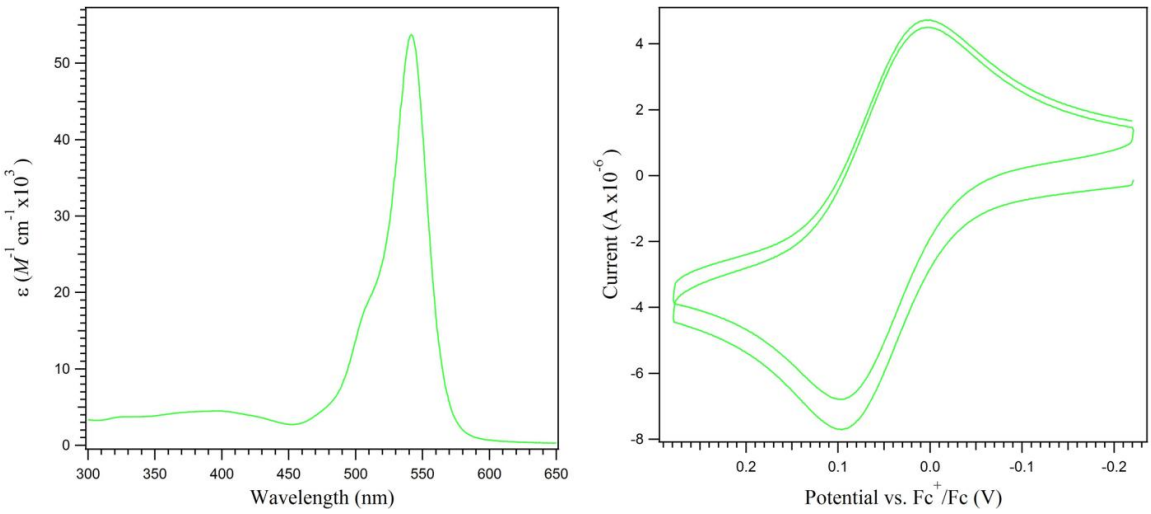

Figure 3.25. UV/Vis spectrum, left, and cyclic voltammogram, right, of **($_{C_6F_5}^{Cl}$L^{Mes})FeCl(py)**. The cyclic voltammogram illustrates the $Fe^{III/II}$ couple. For full experimental details, see page 93.

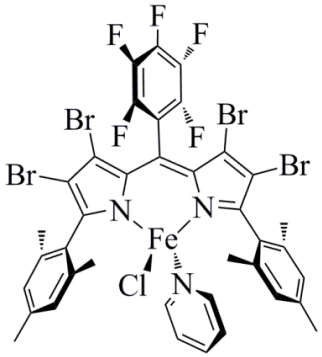

($_{C_6F_5}^{Br}$L^{Mes})FeCl(py) (8). 76% isolated yield. ^{1}H NMR (500 MHz, C_6D_6) δ ppm −25.08 (br. s), −5.37 (br. s), 0.18 (s), 1.87 (m), 5.59 (s), 33.58 (br. s). ^{19}F NMR (376 MHz, C_6D_6) δ ppm −155.00 (br. s, 2F, *m*-F), −146.21 (t, *J* = 22.5 Hz, 1F, *p*-F), −123.24 (br. s, 2F, *o*-F). UV/Vis (CH_2Cl_2, 25 °C) λ_{max} = 547.5 nm, ε = 95,000 $M^{-1}cm^{-1}$. Mössbauer (Paratone, 110 K) δ = 0.89 $^{mm}/_{s}$, $|\Delta E_Q|$ = 2.24 $^{mm}/_{s}$. Anal. calc'd for $C_{38}H_{27}Br_4ClF_5FeN_3$: C, 44.24; H, 2.64; N, 4.07. Found: C, 44.24; H, 2.71; N, 4.10. Microcrystalline material suitable for X-ray diffraction analysis at the synchrotron source at APS was grown from concentrated diethyl ether/hexamethyldisiloxane at –35 °C. The structure was solved in the monoclinic space group $P2_1/c$, with four molecules in the unit cell and a single molecule in the asymmetric unit.

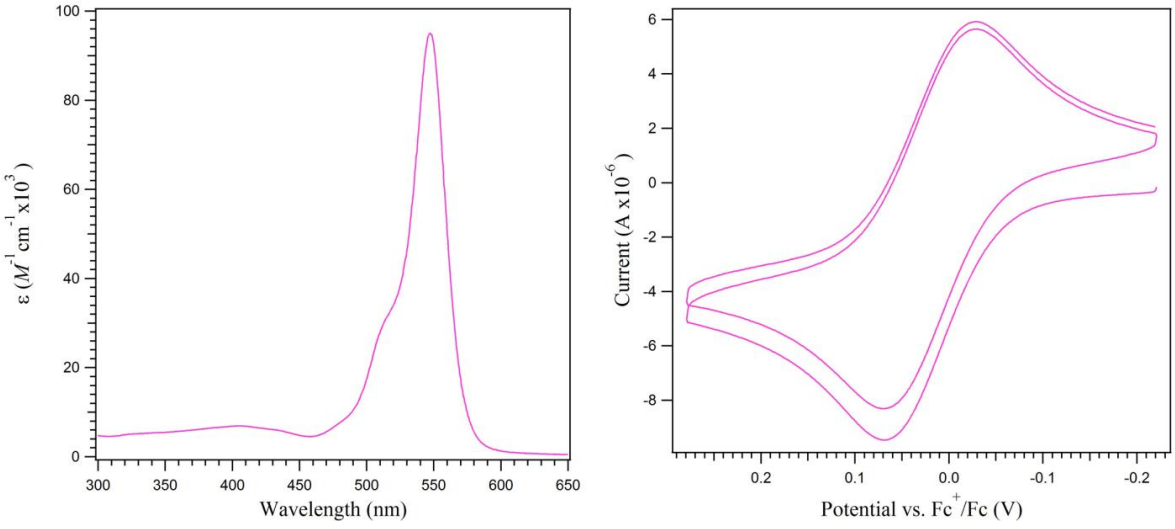

Figure 3.26. UV/Vis spectrum, left, and cyclic voltammogram, right, of **($_{C_6F_5}^{Br}$L^{Mes})FeCl(py)**. The cyclic voltammogram illustrates the $Fe^{III/II}$ couple. For full experimental details, see page 93.

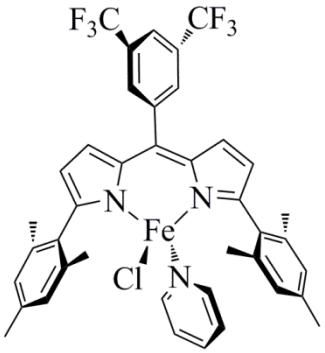

($_{BFP}^{H}L^{Mes}$)FeCl(py) (9). 89% isolated yield. ^{1}H NMR (500 MHz, C_6D_6) δ ppm −22.13 (br. s), −8.99 (br. s), −3.61 (br. s), 2.12 (s), 11.97 (s), 19.74 (s), 32.98 (br. s), 40.10 (s), 50.81 (s), 174.76 (br. s). ^{19}F NMR (376 MHz, C_6D_6) δ ppm −61.95 (br. s, 3F), −56.38 (br. s, 3F). UV/Vis (CH_2Cl_2, 25 °C) λ_{max} = 516.7 nm, ε = 64,000 $M^{-1}cm^{-1}$. Mössbauer (Paratone, 110 K) $\delta = 0.89$ $^{mm}/_{s}$, $|\Delta E_Q| = 1.74$ $^{mm}/_{s}$. Anal. calc'd for $C_{40}H_{34}ClF_6FeN_3$: C, 63.05; H, 4.50; N, 5.51. Found: C, 62.97; H, 4.41; N, 5.46. Microcrystalline material suitable for X-ray diffraction analysis at the synchrotron source at APS was grown by slow evaporation of a saturated solution in THF. The structure was solved in the triclinic space group $P\bar{1}$, with two molecules in the unit cell and a single molecule in the asymmetric unit.

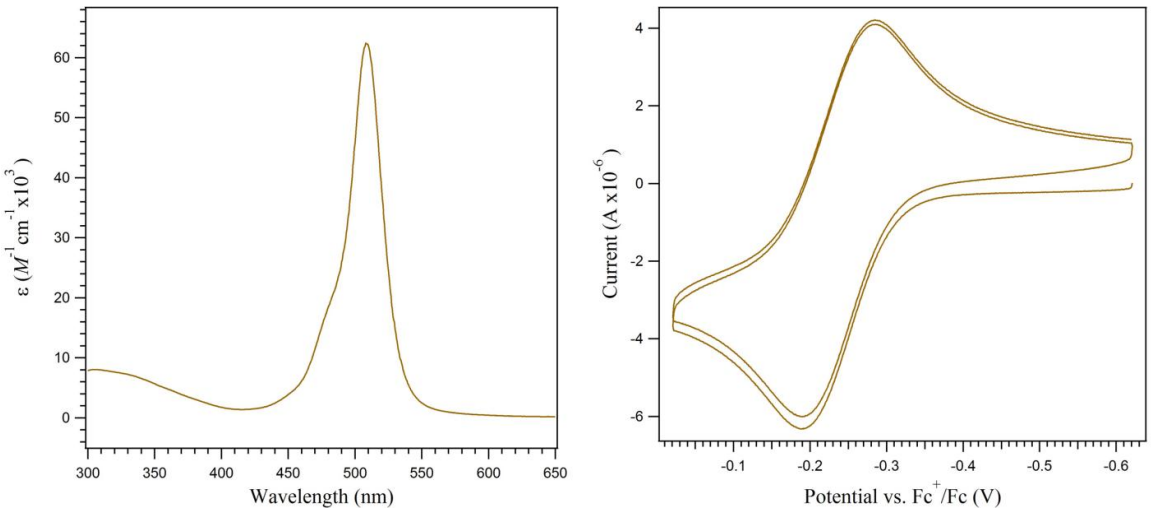

Figure 3.27. UV/Vis spectrum, left, and cyclic voltammogram, right, of **($_{BFP}^{H}L^{Mes}$)FeCl(py)**. The cyclic voltammogram illustrates the $Fe^{III/II}$ couple. For full experimental details, see page 93.

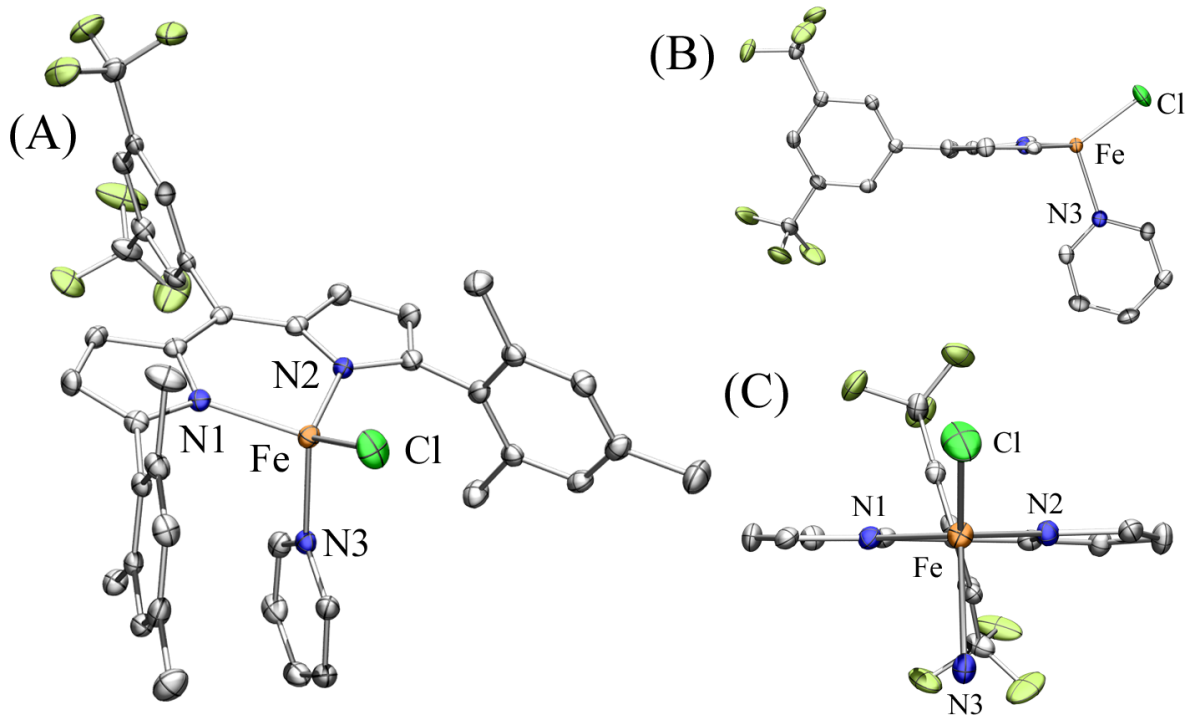

Figure 3.28. Solid-state structure of **($_{BFP}^{H}$L^{Mes})FeCl(py)**. Thermal ellipsoids set at the 50% probability level. Hydrogen atoms have been omitted for clarity. (A) Whole molecule. (B) Side view, illustrating the planarity of the dipyrrin core; flanking mesityl groups have been omitted for clarity. (C) Front view, illustrating the torquing of the *meso*-aryl group relative to the dipyrrin; flanking mesityl groups and the pyridine carbons have been omitted for clarity. Gray, C; blue, N; yellow-green, F; green, Cl; orange, Fe. Data obtained at APS.

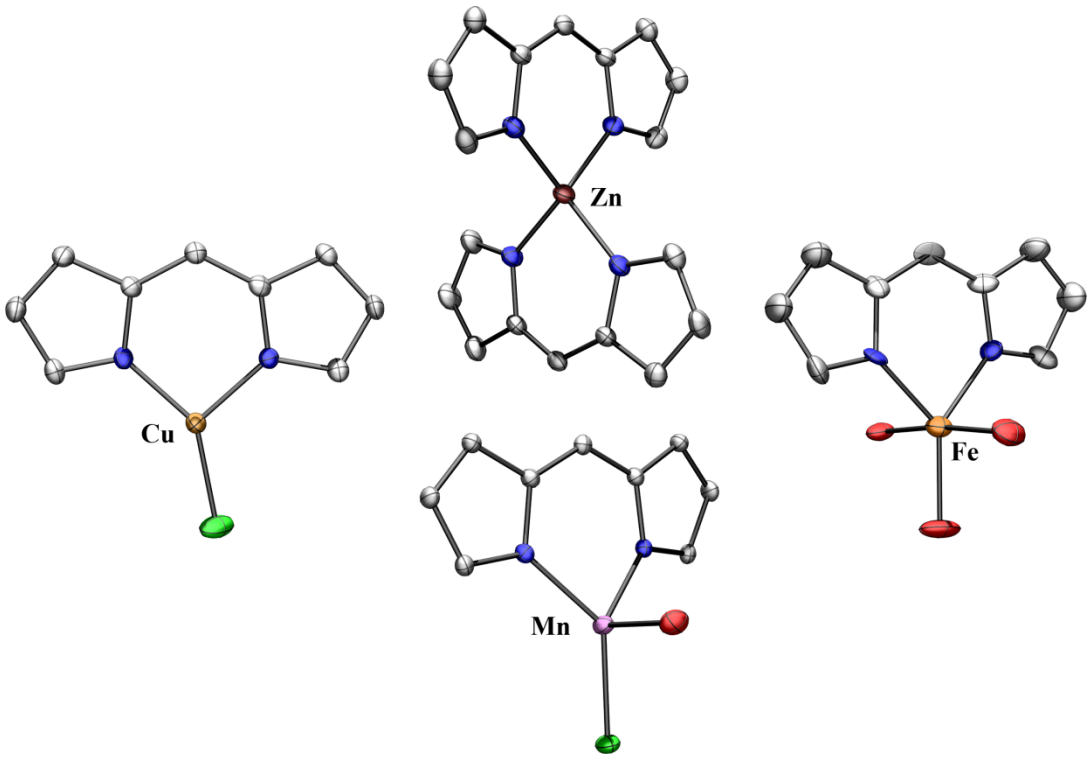

Chapter 4: Coordination Number in Dipyrrinato Complexes

Dipyrrins have become more widely utilized as ligands in transition metal complexes in recent years,[40] largely for their highly variable architectures and ability to bind metals in a variety of geometries. This variability results in a wide range of accessible coordination numbers and electronic structures. A detailed understanding of these geometries and their associated orbital energy diagrams will aid in the design of dipyrrinato transition metal complexes with desirable properties, such as modifiable absorption and emission, tunable redox properties, and catalytic activity.

4.1 General Synthesis of Transition Metal Dipyrrinato Complexes

Dipyrrinato transition metal complexes can be easily synthesized in a two-step procedure (Scheme 4.1). First, the dipyrrin is deprotonated with either phenyllithium or lithium hexamethyl disilazide (LiHMDS) in hydrocarbon or ethereal solvent. Removal of the solvent and organic byproduct can be performed in vacuo, allowing the isolation of the lithium chelates in quantitative yield. If the deprotonation is performed in ethereal solvent, the lithium cation is typically bound by 1–2 molecules of solvent. Subsequent transmetalation with a metal halide salt in coordinating solvent (diethyl ether, THF, or pyridine) is typically rapid and clean; the lithium halide byproduct can be easily removed by filtration though diatomaceous earth (Celite), eluting with benzene. Homoleptic bis(dipyrrinato) metal complexes can be formed if R = Me and only 0.5 equivalents of metal halide are used; if one equivalent of metal chloride is used, heteroleptic complexes are obtained (Scheme 4.2). The resulting metal dipyrrinato complexes are generally stable in the solid state at −35 °C, which the exception of the tetrahalodipyrrinato metal halide THF or diethyl ether adducts, which decompose slowly at −35 °C over the course of days. The corresponding pyridine adducts, however, are stable indefinitely at room temperature in the solid state. All complexes described herein decompose slowly in solution, or upon exposure to ambient atmosphere, oxygen, or water.

All of the metal dipyrrinato complexes studied here were characterized by ^{1}H NMR, elemental analysis, and whenever possible, X-ray crystallography. In the cases of diamagnetic complexes, ^{13}C NMR spectra were also obtained. Where appropriate, the complexes were also characterized by ^{19}F NMR, cyclic voltammetry (Section 3.4), zero-field ^{57}Fe Mössbauer spectroscopy (Section 3.5), and luminescence spectroscopy (Chapter 5).

Scheme 4.1. Synthesis of metal(II) dipyrrinato complexes

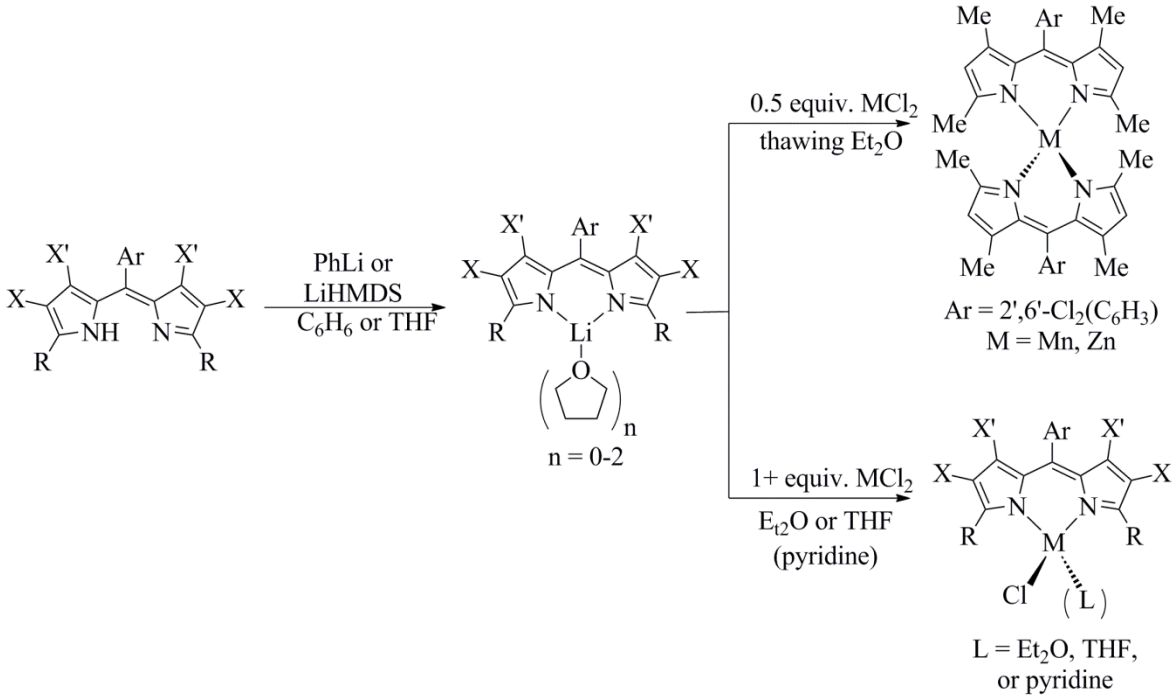

Table 4.1. Transition metal dipyrrinato complexes synthesized

Compound	R	Ar	X	X′	M(oxid. st.)	L
$(^{H}_{Mes}L^{Mes})$**MnCl(THF)**	Mes	Mes	H	H	Mn(II)	THF
$(^{H}_{Mes}L^{Mes})$**FeCl(py)**[a]	Mes	Mes	H	H	Fe(II)	py
$(^{Cl}_{Mes}L^{Mes})$**FeCl(py)**[a]	Mes	Mes	Cl	Cl	Fe(II)	py
$(^{Br;\ H}_{Mes}L^{Mes})$**FeCl(py)**[a]	Mes	Mes	Br	H	Fe(II)	py
$(^{Br}_{Mes}L^{Mes})$**FeCl(py)**[a]	Mes	Mes	Br	Br	Fe(II)	py
$(^{I}_{Mes}L^{Mes})$**FeCl(py)**[a]	Mes	Mes	I	I	Fe(II)	py
$(^{I}_{Mes}L^{Mes})$**FeCl(OEt$_2$)**	Mes	Mes	I	I	Fe(II)	Et_2O
$(^{H}_{C_6F_5}L^{Mes})$**FeCl(py)**[a]	Mes	C_6F_5	H	H	Fe(II)	py
$(^{Cl}_{C_6F_5}L^{Mes})$**FeCl(py)**[a]	Mes	C_6F_5	Cl	Cl	Fe(II)	py
$(^{Br}_{C_6F_5}L^{Mes})$**FeCl(py)**[a]	Mes	C_6F_5	Br	Br	Fe(II)	py
$(^{H}_{BFP}L^{Mes})$**FeCl(py)**[a]	Mes	3′,5′-$(CF_3)_2C_6H_3$	H	H	Fe(II)	py
$(^{H}_{Mes}L^{Q})$**FeCl(THF)**	2′,4′,6′-$Ph_3C_6H_2$	Mes	H	H	Fe(II)	THF
$(^{H}_{Mes}L^{Q})$**MnCl(THF)**	2′,4′,6′-$Ph_3C_6H_2$	Mes	H	H	Mn(II)	THF
$(^{H}_{Mes}L^{Q})$**CuCl**	2′,4′,6′-$Ph_3C_6H_2$	Mes	H	H	Cu(II)	—
$(^{H}_{Mes}L^{Q})$**Cu**	2′,4′,6′-$Ph_3C_6H_2$	Mes	H	H	Cu(I)	—
$(^{H}_{Mes}L^{Q})$**ZnCl(THF)**	2′,4′,6′-$Ph_3C_6H_2$	Mes	H	H	Zn(II)	THF
$(^{I}_{Mes}L^{Q})$**MnCl(THF)**	2′,4′,6′-$Ph_3C_6H_2$	Mes	I	I	Mn(II)	THF
$(^{H;\ Me}_{DCP}L^{Me})$**ZnCl(THF)**	Me	2′,6′-$Cl_2C_6H_3$	H	Me	Zn(II)	THF
$(^{H;\ Me}_{DCP}L^{Me})_2$**Zn**	Me	2′,6′-$Cl_2C_6H_3$	H	Me	Zn(II)	[b]
$(^{H;\ Me}_{DCP}L^{Me})_2$**Mn**	Me	2′,6′-$Cl_2C_6H_3$	H	Me	Mn(II)	[b]

[a] The synthesis and characterization of these complexes was described in detail in Section 2.4.3. [b] In the homoleptic complexes, two dipyrrinato ligands complete the coordination environment around the metal; no halides or solvents are bound.

4.2 Three-Coordinate Structures

Three-coordinate transition metal complexes are generally limited to those with very bulky ligands supporting the metal ion. This is true in the case of dipyrrinato complexes as well, where the extremely crowded environment provided by the 2′,4′,6′-triphenylphenyl flanking unit ("Q") of the dipyrrinato ligand can support 3-coordinate metals. We have crystallographically characterized 3-coordinate Fe(I), Co(I), Cu(I), Fe(II), Cu(II), and Co(III)[84] complexes bearing this ligand. Additionally, we have spectroscopic evidence that a 3-coordinate Mn(II) complex is accessible in non-coordinating solvents (Section 5.2), though we have been unable to confirm this crystallographically. Notably, Cu(I) complexes of even smaller dipyrrinato ligands also tend to adopt 3-coordinate structures, as evidenced by the complex **($_{Mes}^{H}L^{Mes}$)Cu(py)**, despite the tendency of other metals chelated by this ligand to adopt four-coordinate geometries (Section 4.3). Additionally, Fe(II) complexes of smaller dipyrrinato ligands can also support three-coordinate structures if the anionic ligand is especially bulky, as in the cases of **($_{Mes}^{H}L^{Mes}$)Fe(N(SiMe$_3$)$_2$)** and **($_{Mes}^{H}L^{Mes}$)Fe(CH$_2$SiMe$_3$)** whose large bis(trimethylsilyl)amido and (trimethylsilyl)methyl ligands, respectively, prevent coordination of a fourth exogenous ligand (Figure 4.1).

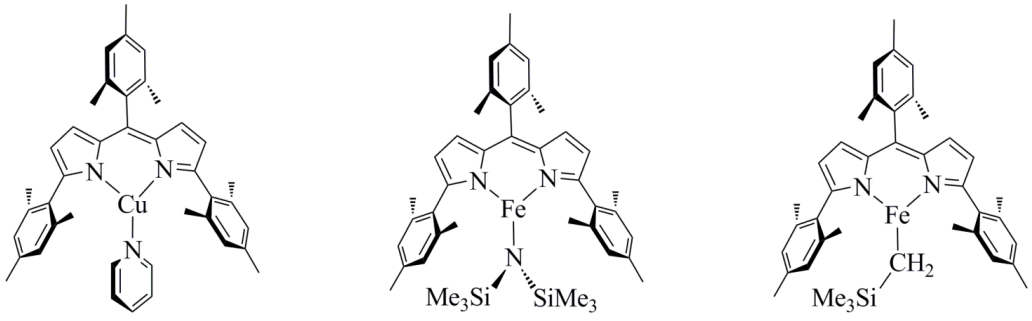

Figure 4.1. Three-coordinate complexes with mesityl flanking groups on the dipyrrinato ligand: **($_{Mes}^{H}L^{Mes}$)Cu(py)** (courtesy of ERK), left, **($_{Mes}^{H}L^{Mes}$)Fe(N(SiMe$_3$)$_2$)** (GAE), center, and **($_{Mes}^{H}L^{Mes}$)Fe(CH$_2$SiMe$_3$)** (ARB), right.

[84] King, E. R.; Sazama, G. T.; Betley, T. A. *J. Am. Chem. Soc.* **2012**, *134*, 17858.

The geometries of these three-coordinate complexes are constrained by the relatively small bite angle of the dipyrrinato ligand, which is typically near 90°; this prevents the formation of symmetric trigonal planar structures with bond angles of 120°. This ligand arrangement yields an idealized C_{2v} structure. The method of angular overlap,[54] which allows the construction of d and f [85] orbital splitting diagrams based on the geometric overlap of ligand orbitals with metal-based orbitals, provides a σ-only d-orbital splitting diagram with the d_{xz} orbital at 1.5 e_σ (bearing the entirety of the bonding with the dipyrrinato ligand), d_{z^2} at 1 e_σ, and the remaining d orbitals essentially non-bonding in a σ-capacity (Figure 4.2). Here, e_σ is the energetic destabilization of a given d orbital due to direct σ-overlap of the ligand orbital involved in bonding, and is defined here as the destabilization of a d_{z^2} orbital by direct overlap with a ligand p_z orbital.

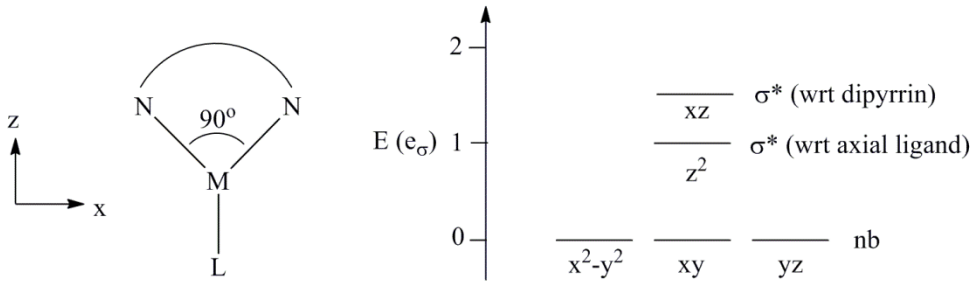

Figure 4.2. Idealized geometry and d-orbital splitting diagram [86] for C_{2v}, pseudo-trigonal planar structures.

[85] Warren, K. *Inorg. Chem.* **1977**, *16(8)*, 2008.

[86] Conventionally, the d-orbital splitting diagrams of these 3-coordinate structures regard the z-axis as perpendicular to the trigonal plane; we believe the axes presented here better represent the electronic structure of these complexes.

Three-coordinate monovalent Fe(I), Co(I), and Cu(I) complexes of the bidentate dipyrrinato ligands have distorted trigonal planar geometries with a neutral ligand in the third coordination site. If a strong enough donor ligand is added during the synthesis, this third coordination site is usually occupied by that exogenous ligand (pyridine, acetonitrile, tetrahydrofuran, diethyl ether). However, in the cases of **($_{Mes}^{H}L^{Q}$)Fe·2C$_6$H$_6$** and **($_{Mes}^{H}L^{Q}$)Cu·3C$_6$H$_6$**, which have no additional ligands bound, one of the flanking phenyl groups of the dipyrrinato ligand occupies this third coordination site. In the Fe(I) case, the flanking phenyl group binds η^6, but in the case of the more electron-rich Cu(I), the phenyl group is bound η^2. Deviations from idealized trigonal planar geometries (with 90°, 135°, and 135° angles) can be attributed to steric constraints of the ligand binding.

Table 4.2. Selected geometric parameters of monovalent, three-coordinate complexes

Compound	N-M-N ∠ (°)	N-M-L (1) ∠ (°)	N-M-L (2) ∠ (°)	Σ∠ (°)	Source
($_{Mes}^{H}L^{Q}$)Li(OEt$_2$)	99.20(13)	130.40(7)	130.40(7)	360.0	erk065
($_{Mes}^{H}L^{Q}$)Fe·2C$_6$H$_6$	89.2(2)	130.2(6)[a]	119.7(8)[a]	339.2	erk103
($_{Mes}^{H}L^{Q}$)Co(py)	95.82(16)	132.09(8)	132.09(8)	360.0	**ref 84**
($_{Mes}^{H}L^{Mes}$)Cu(py)	97.30(4)	131.14(10)	131.47(7)	359.9	erk018
($_{Mes}^{H}L^{Q}$)Cu·3C$_6$H$_6$	96.17(11)	111.08(17)[b]	143.81(17)[b]	351.1	abs418

[a] Angles to the η^6 phenyl group are calculated to the phenyl group centroid. [b] Angles to the η^2 phenyl group are calculated to the centroid of the C-C bond bound to the metal.

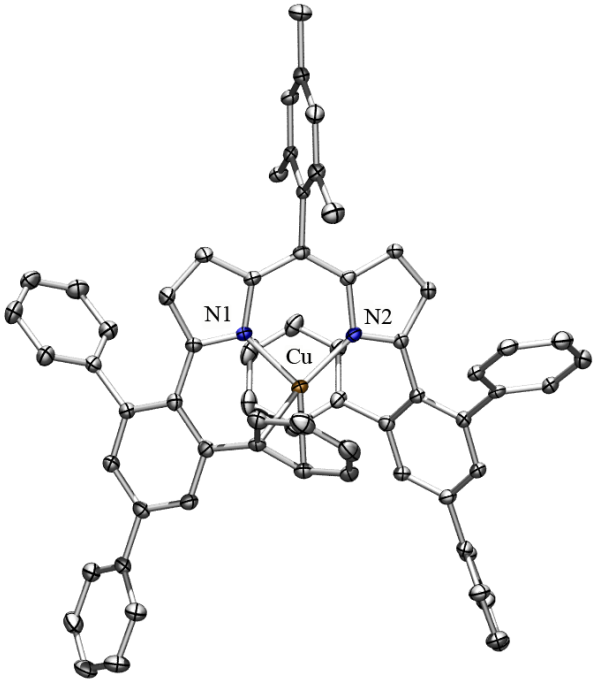

Figure 4.3. Solid-state structure of $(_{Mes}^{H}L^{Q})Cu{\cdot}3C_6H_6$. Hydrogen atoms and solvent molecules have been omitted for clarity. Ellipsoids set at the 50% probability level. Gray, C; blue, N; gold, Cu.

Divalent, three-coordinate dipyrrinato metal complexes bear an anionic ligand completing the pseudo-trigonal planar coordination environment around the metal ion. These complexes can undergo Jahn-Teller distortions if the d_{xz} and d_{z^2} are roughly degenerate (as is the case with the very weak-field dipyrrinato ligand), in which the anionic ligand deviates from the molecular z-axis (defined by the M–C5 line) (Figure 4.4). Such a distortion is observed in the Cu(II) complex $(_{Mes}^{H}L^{Q})CuCl$, in which the chloride ligand deviates from the z-axis by 11.5(21)° (Figure 4.5). The complex $(_{Mes}^{H}L^{Q})FeCl$, which was isolated as a bis-benzene solvate, shows no appreciable Jahn-Teller distortion, despite an electron configuration that could lead to such a phenomenon. However, a Jahn-Teller distortion in the iron complex would not likely involve the anti-bonding d_{z^2} orbital, but would involve the non-bonding orbitals $d_{x^2-y^2}$, d_{xy}, and d_{yz}; even should a Jahn-Teller distortion occur within these orbitals, it would not likely be manifest in the solid-state structure. In fact, only high-spin d^4, low-spin d^7, and d^9 complexes would be expected

to show physically significant Jahn-Teller distortions in this coordination environment, and then only under the assumption of near-degeneracy of the d_{xz} and d_{z^2} orbitals.

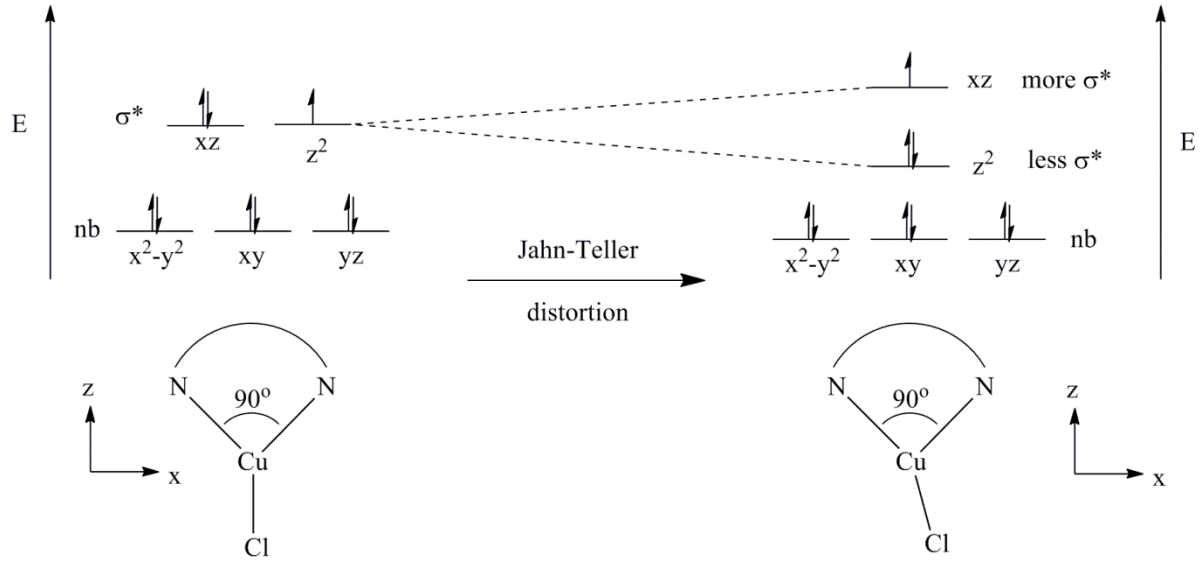

Figure 4.4. Electronic and structural Jahn-Teller distortion in a Cu(II), d^9 pseudo-trigonal planar dipyrrinato complex.

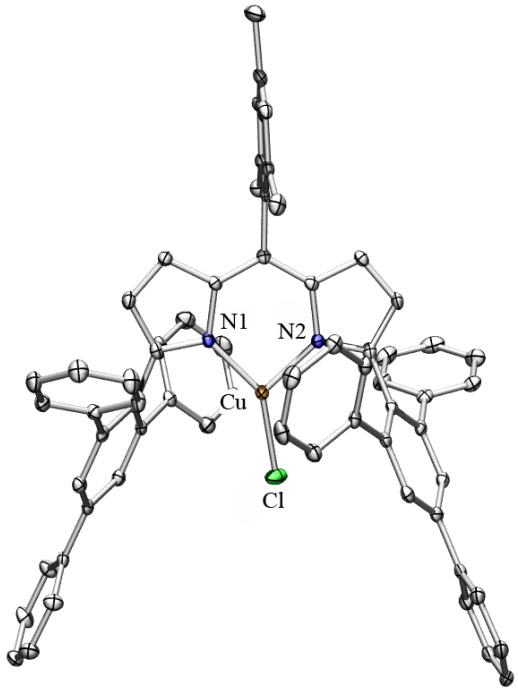

Figure 4.5. Solid-state structure of **($_{Mes}^{H}L^{Q}$)CuCl**, emphasizing the Jahn-Teller distortion in the N-Cu-Cl bond angle. Hydrogen atoms have been omitted for clarity. Ellipsoids set at the 50% probability level. Gray, C; blue, N; green, Cl; gold, Cu.

Table 4.3. Selected geometric parameters of divalent, three-coordinate complexes

Compound	N-M-N ∠ (°)	N-M-L (1) ∠ (°)	N-M-L (2) ∠ (°)	Σ∠ (°)	JT distortion (°)	Source
$(^{H}_{Mes}L^{Mes})Fe(N(SiMe_3)_2)$	92.35(9)	129.17(10)	134.24(10)	355.8	2.54	gae009
$(^{H}_{Mes}L^{Mes})Fe(CH_2SiMe_3)$	93.84(16)	127.5(2)	138.4(2)	359.7	5.60	arb001
$(^{H}_{Mes}L^{Q})FeCl\cdot 2C_6H_6$	96.1(3)	131.96(14)	131.96(14)	360.1	0	**ref 53a**
$(^{H}_{Mes}L^{Q})CuCl$	95.55(10)	121.29(8)	143.12(8)	360.0	11.52	abs418

The more electrophilic (earlier) three-coordinate metal complexes of Mn(II), Fe(II), and Co(II) can be prepared only in the absence of donor solvents, as they are readily bound by exogenous donor solvents like THF or pyridine, producing clean four-coordinate materials, though these may be in equilibrium with their three-coordinate counterparts in solution in the absence of excess coordinating solvent (Section 5.2). The more electron-rich copper complexes do not readily bind moderate donor solvents like THF, and three-coordinate structures can even be isolated cleanly from THF solutions.

4.3 Four-Coordinate Structures

The majority of previously described transition metal complexes of dipyrrinato ligands have been homoleptic species with very small flanking R groups on the dipyrrinato ligand.[40] Indeed, as we have demonstrated, bis(dipyrrinato) Zn(II) and Mn(II) complexes can be formed if R = Me and a 2:1 mole ratio of ligand to metal are combined at low temperature (Scheme 4.2).

Scheme 4.2. Synthesis of homoleptic bis(dipyrrinato) complexes

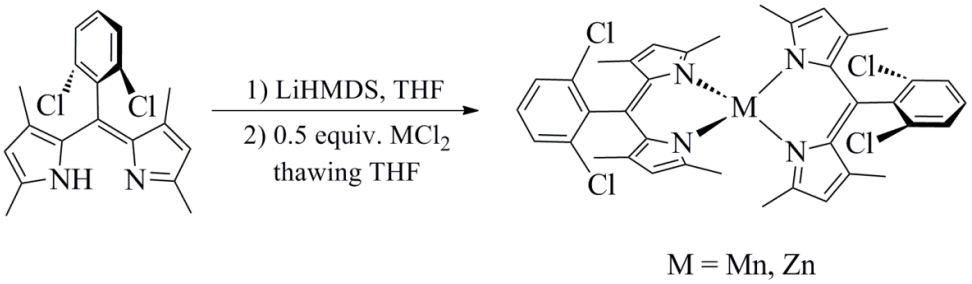

M = Mn, Zn

These homoleptic complexes are highly absorptive in the visible region of the electromagnetic spectrum, with molar extinction coefficients on the order of 10^6 $M^{-1}cm^{-1}$, approaching the maximum known absorptivities. These types of molecules are interesting both for practical applications as dyes, as well as for theoretical investigation of the relationship between proximal chromophores, which can lead to exciton coupling and Davydov coupling. In the homoleptic complexes **$(^{H;\,Me}_{DCP}L^{Me})_2Zn{\cdot}½(OEt_2)$** and **$(^{H;\,Me}_{DCP}L^{Me})_2Mn$**, the angles between the mean planes of the two dipyrrinato ligands are 90.8(6)° and 87.9(5)°, respectively, as determined by X-ray crystallography (Figure 4.6). It is currently unknown whether exciton coupling can occur with the condition of rigorous orthogonality of two proximal chromophores, and investigations of this phenomenon are currently being undertaken.[87]

[87] Yuen-Zhou, J.; Krich, J. J.; Mohseni, M.; Aspuru-Guzik, A. *Proc. Natl. Acad. Sci. U.S.A.*, **2011**, *108*, 17615.

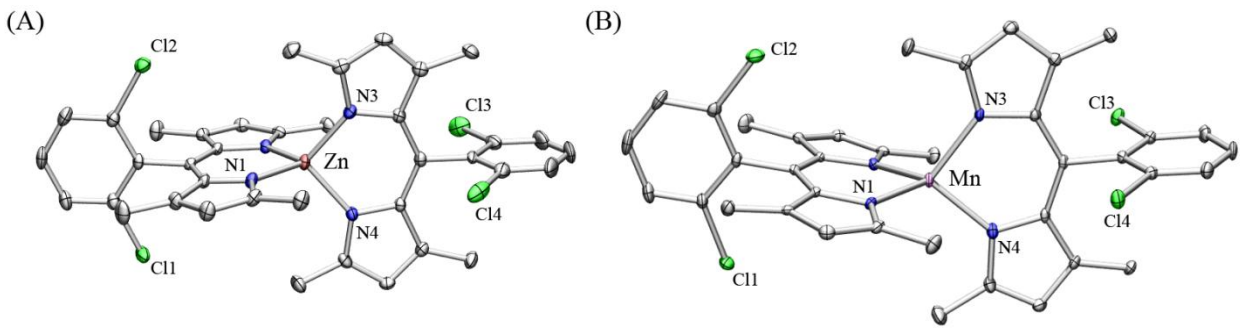

Figure 4.6. Solid-state structures of (A) **($^{H;\,Me}_{DCP}L^{Me})_2Zn\cdot½(OEt_2)$** and (B) **($^{H;\,Me}_{DCP}L^{Me})_2Mn$**. There are two crystallographically independent molecules in the asymmetric unit of **($^{H;\,Me}_{DCP}L^{Me})_2Zn\cdot½(OEt_2)$** which do not differ significantly in any structural parameters; only one is shown. Hydrogen atoms and solvent molecules are omitted for clarity. Ellipsoids set at the 50% probability level. Gray, C; blue, N; green, Cl; brown, Zn; orchid, Mn.

We have synthesized a wide variety of heteroleptic four-coordinate transition metal dipyrrinato complexes in our lab, mostly of divalent metals bearing a chloride ligand and a solvento ligand bound to the metal center. The geometries of these four-coordinate structures are constrained by the bite angle of the dipyrrinato ligand, as described for three-coordinate structures in Section 4.2. The geometric extremes possible with this constraint are a pseudo-trigonal pyramidal or monovacant trigonal bipyramid structure, best exemplified by **($^{H}_{Mes}L^{Q}$)MnCl(THF)** (Figure 4.9A) and a pseudo-tetrahedral structure, as observed in the homoleptic zinc complex described above, and best exemplified by **($^{Br}_{Mes}L^{Mes}$)FeCl(py)** (Figure 4.9B). These geometric extremes give rise to d-orbital splitting diagrams with idealized C_s (Figure 4.7) and C_{2v} symmetry (Figure 4.8), respectively.

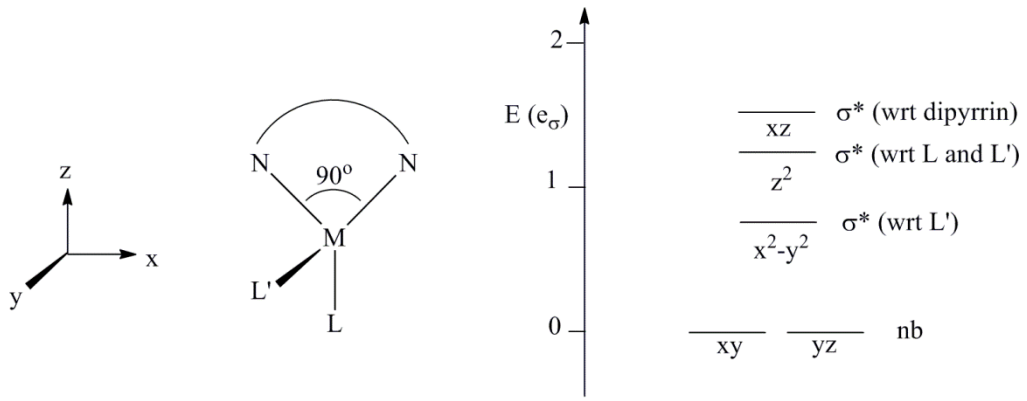

Figure 4.7. Idealized geometry and d-orbital splitting diagram for C_s, monovacant trigonal bipyramidal four-coordinate structures.

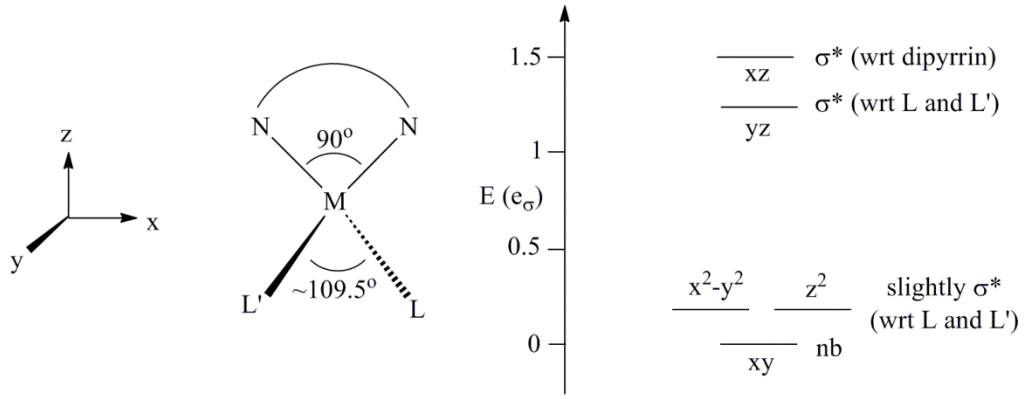

Figure 4.8. Idealized geometry and d-orbital splitting diagram for C_{2v}, pseudo-tetrahedral four-coordinate structures.

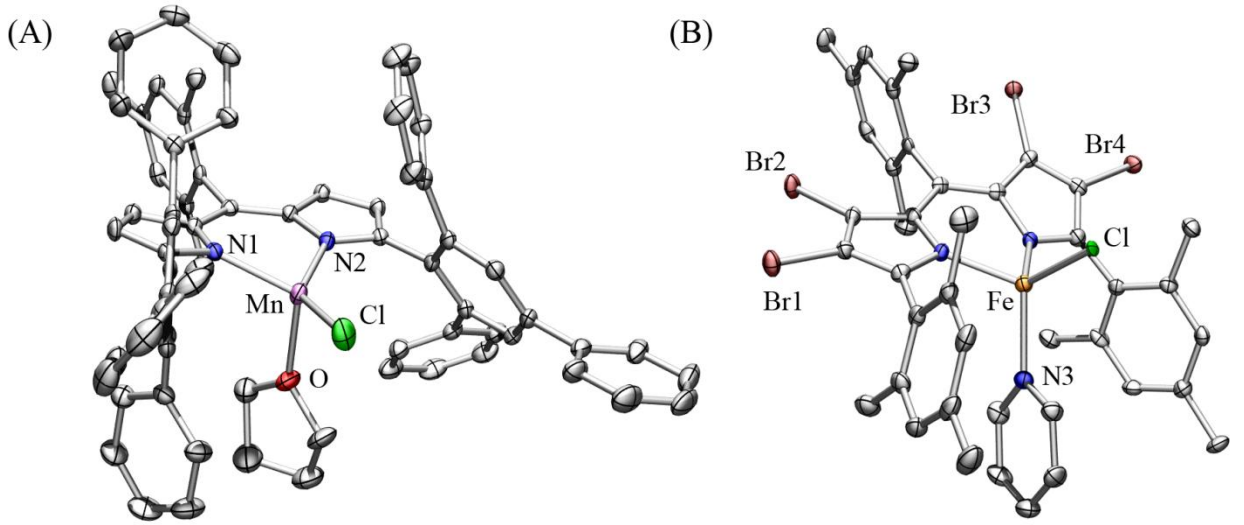

Figure 4.9. Solid-state structures of (A) **($_{Mes}^{H}$L^{Q})MnCl(THF)**, the four-coordinate structure with the structure closest to a monovacant trigonal bipyramid, and (B) **($_{Mes}^{Br}$L^{Mes})FeCl(py)**, the four-coordinate structure with the most nearly tetrahedral structure among the dipyrrinato complexes studied herein. Thermal ellipsoids set at 50% probability. Hydrogen atoms have been omitted for clarity. Gray, C; blue, N; red, O; green, Cl; maroon, Br; orchid, Mn; orange, Fe.

In the cases of homoleptic bis(dipyrrinato) complexes, with nearly orthogonal arrangements of the dipyrrin planes and near-90° chelate angles, an idealized D_{2d} structure results. The d_{xz} and d_{yz} orbitals are truly degenerate and anti-bonding with respect to both dipyrrinato ligands, and structurally-manifest Jahn-Teller distortions could arise for high-spin d^4, low-spin d^7, and d^9 complexes (Figure 4.10). Since the homoleptic manganese and zinc complexes prepared in our lab are high-spin d^5 and d^{10}, respectively, we do not expect to see significant Jahn-Teller distortions; indeed, the zinc complex shows near-perfect D_{2d} symmetry in the solid state. The manganese complex, however, does exhibit a slight canting of one of the dipyrrinato ligands, causing a deviation from D_{2d} symmetry; given the high-spin d^5 configuration of this complex, we attribute this distortion to crystal-packing effects rather than Jahn-Teller effects.

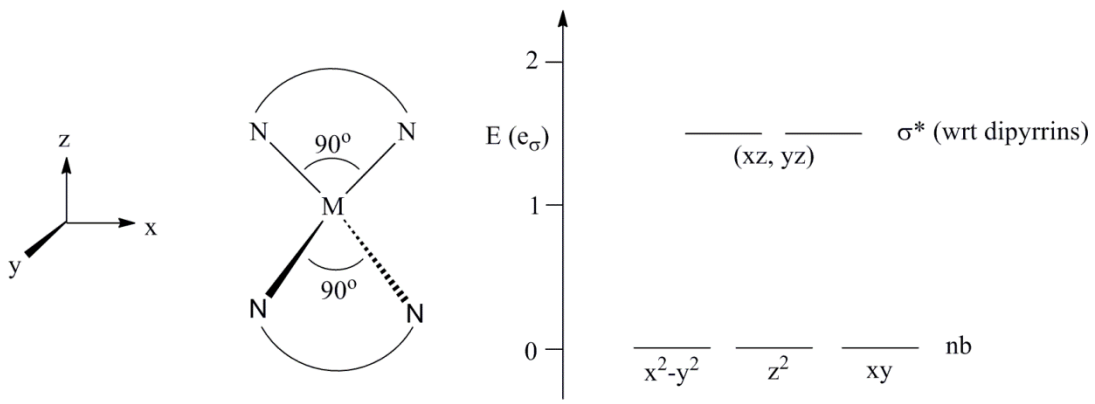

Figure 4.10. Idealized geometry and d-orbital splitting diagram for D_{2d}, pseudo-tetrahedral four-coordinate homoleptic structures.

Several geometric indices have been proposed to quantitatively describe four-coordinate complexes, whose potential geometries include tetrahedral (T_d), square planar (D_{4h}), trigonal pyramidal (C_{3v}), see-saw (C_{2v}), or lower-symmetry deviations from these idealized geometries. The most general of these parameters is τ_4,[76] is defined by Equation 3.1.

$$\tau_4 = \frac{360° - (\alpha + \beta)}{141°} \qquad \text{(Eq. 3.1)}$$

Here, α and β are the two largest ligand-metal-ligand bond angles; perfectly tetrahedral structures have $\tau_4 = 1.0$ ($\alpha = \beta = 109.5°$), perfectly square planar structures have $\tau_4 = 0$ ($\alpha = \beta = 180°$), and perfect monovacant trigonal bipyramidal structures have $\tau_4 = 0.85$ ($\alpha = \beta = 120°$). Notably, a given τ_4 value does not define a specific geometry; there are a number of possible geometries with a given τ_4. A second geometry index, the tetrahedral character for donor-acceptor interactions, THC_{DA}, was developed by Höpfl[88] to describe four-coordinate boron atoms, whose extreme geometries are tetrahedral and trigonal pyramidal; since those are the two geometric extremes for heteroleptic dipyrrinato complexes, we also examined this geometric parameter to analyze four-coordinate structures. THC_{DA} is defined by Equation 4.4.

[88] Höpfl, H. *J. Organomet. Chem.* **1999**, *581*, 129.

$$THC_{DA} = \left[1 - \frac{\sum_n |109.5 - \theta_n|^\circ}{90^\circ}\right] \times 100\% \qquad \text{(Eq. 4.4)}$$

Here, θ_n are the L–M–L bond angles (of which there are six in four-coordinate structures); perfectly tetrahedral structures have THC_{DA} = 100% and perfectly trigonal pyramidal structures have THC_{DA} = 0%. The structures of dipyrrinato complexes are constrained by the chelating bite angle of the dipyrrin, as described above; for a "perfectly" trigonal pyramidal molecule with this constraint (bond angles within the equatorial plane of 90°, 135°, and 135°, and an apical ligand at exactly 90° from the equatorial ligands), the value of THC_{DA} is −43%; this geometry is better described as a monovacant trigonal bipyramid. For comparison, a perfectly square planar molecule has THC_{DA} = −143%, a value that has little meaning. For this reason, we prefer to use τ_4 as the more applicable four-coordinate geometry index, but we have included THC_{DA} values in Table 4.4 for reference, keeping in mind that the full applicable scale for four-coordinate dipyrrinato complexes runs from −143% to 100%.

Despite a wide range of geometries for four-coordinate structures, we see no predictable trends between the identity of the bound metal, halogenation of the ligand, the identity of the *meso*-aryl substituent, or any other readily identifiable feature of the complexes with the tetrahedricity parameter τ_4 or the tetrahedral character for donor-acceptor interactions (THC_{DA}).

Table 4.4. Selected geometric parameters of divalent, four-coordinate complexes

Compound	N1-M-N2 ∠ (°)	N1-M-Cl ∠ (°)	N1-M-L ∠ (°)	N2-M-Cl ∠ (°)	N2-M-L ∠ (°)	Cl-M-L ∠ (°)	τ_4	THC_{DA} (%)	Source
$(^{H}_{Mes}L^{Mes})$MnCl(THF)	92.32(1)	114.67(7)	118.89(6)	114.67(7)	118.89(6)	98.69(2)	0.87	36.5	abs392b
$(^{H}_{Mes}L^{Q})$MnCl(THF)	90.56(7)	125.55(5)	103.69(6)	135.18(5)	96.67(7)	98.74(5)	***0.70***[d]	***–0.1***[d]	abs443
$(^{H}_{DCP}L^{Ad})$FeCl(OEt$_2$)	98.84(11)	118.98(11)	102.6(2)	118.72(12)	106.89(18)	109.1(2)	0.87	56.4	**ref 53b**
$(^{H}_{Mes}L^{Mes})$FeCl(py)	91.52(11)	130.12(10)	99.94(12)	113.59(9)	118.36(13)	103.87(10)	0.79	25.8	abs1031
$(^{Br;\ H}_{Mes}L^{Mes})$FeCl(py)	88.91(11)	123.66(6)	105.18(8)	123.66(6)	105.18(8)	107.53(9)	0.80	33.9	abs1026
$(^{Cl}_{Mes}L^{Mes})$FeCl(py)	89.70(7)	118.44(5)	109.12(7)	111.28(5)	118.69(7)	108.97(5)	0.87	54.9	abs[a]
$(^{Br}_{Mes}L^{Mes})$FeCl(py)	90.30(16)	116.38(12)	109.88(16)	111.61(12)	117.16(16)	110.41(12)	***0.90***[d]	***58.7***[d]	abs1025
$(^{I}_{Mes}L^{Mes})$FeCl(py)	89.79(17)	108.61(13)	108.13(17)	116.35(14)	118.74(18)	112.07(13)	0.89	54.9	abs1104
$(^{I}_{Mes}L^{Mes})$FeCl(OEt$_2$)	91.60(13)	122.00(12)	102.40(15)	116.61(12)	109.94(15)	111.99(11)	0.86	47.2	abs1029
$(^{H}_{BFP}L^{Mes})$FeCl(py)	91.32(9)	124.25(7)	102.00(9)	123.80(7)	102.36(9)	109.24(7)	0.79	31.0	abs211[a]
$(^{H}_{C_6F_5}L^{Mes})$FeCl(py)	90.62(6)	120.07(5)	102.57(6)	130.74(5)	102.66(6)	106.22(6)	0.77	24.7	abs1106
$(^{Cl}_{C_6F_5}L^{Mes})$FeCl(py)	89.48(1)	122.62(8)	112.98(12)	124.61(8)	99.56(11)	105.40(9)	0.80	24.9	abs[a]
$(^{Br}_{C_6F_5}L^{Mes})$FeCl(py)	89.26(12)	123.98(10)	99.37(13)	123.71(10)	110.99(13)	106.67(10)	0.80	29.6	abs[a]
$(^{H}_{Mes}L^{Mes})$CoCl(THF)	94.41(7)	112.78(6)	116.13(7)	115.38(6)	118.52(7)	100.52(5)	0.89	45.7	erk014
$(^{H}_{Mes}L^{Q})$CoCl(py)[b]	96.03(6) 95.66(7)	130.22(5) 113.26(5)	103.83(6) 112.86(7)	114.81(5) 131.64(5)	109.48(6) 103.13(6)	101.35(5) 100.12(5)	0.82 0.82	40.7 34.6	**ref 84**
$(^{H}_{Mes}L^{Mes})$NiCl(py)	94.14(18)	124.68(15)	98.8(2)	123.10(15)	100.2(2)	111.05(15)	0.80	27.0	erk016
$(^{H;\ Me}_{DCP}L^{Me})_2$Zn·½(OEt$_2$)[b,c]	94.34(9) 94.87(9)	118.55(9) 119.75(9)	117.93(9) 115.07(9)	116.16(9) 117.58(9)	117.61(9) 116.85(9)	94.20(9) 94.53(9)	0.87 0.87	30.2 32.4	abs403
$(^{H;\ Me}_{DCP}L^{Me})_2$Mn[c]	90.09(9)	117.48(9)	118.23(9)	122.65(8)	120.97(10)	90.36(9)	0.83	11.3	abs474

[a] Data obtained at APS. [b] Two crystallographically independent molecules were present in the asymmetric unit; geometric parameters for both are reported. [c] Given the different coordination sphere, the bond angles in the homoleptic complex do not correspond to the column headers; the ~94° angles are the dipyrrin chelate angles, and the others represent angles between dipyrrins. [d] These values represent the extrema of the τ_4 and THC_{DA} values calculated here.

4.4 Five-Coordinate Structures

Very few five-coordinate dipyrrinato transition metal complexes have been reported. One class of five-coordinate complexes involves pendant donors on the flanking arms (R-groups) of the dipyrrinato ligands, such as in the 2-(pyrrolyl)dipyrrinato derivates called prodigiosenes.[89] A few five-coordinate dipyrrinato complexes of copper(II) have also been reported, in which the *meso*-aryl substituent bears a relatively strong donor moiety; these types of architectures result in coordination oligomers or polymers.[52b] In the case of large, non-donor flanking R groups as described here, five-coordinate binding modes are extremely rare. However, even in the presence of R-groups as large as mesityl or adamantyl, when the metal is bound by an especially weak X-type ligands such as triflate, two solvent molecules can be accommodated in the coordination sphere of the bound metal. Again, the constraints of the dipyrrinato ligand bite angle change the ideal geometry from a regular trigonal bipyramidal structure to an idealized C_{2v} structure in which the z-axis contains the two pseudo-axial ligands;[90] this results in a d-orbital arrangement with little degeneracy (Figure 4.12).

[89] (a) Thompson, A.; Bennett, S.; Gillis, H. M.; Wood, T. E. *J. Porphyrins Phthalocyanines* **2008**, *12*, 918. (b) Crawford, S. M.; Al-Sheikh, A. A.; Cameron, T. S.; Thompson, A. *Inorg. Chem.* **2011**, *50*, 8207.

[90] The z-axis described here does not correspond to the principal axis of symmetry; this convention is used in a range of pseudo-C_{2v} five-coordinate structures bearing bidentate ligands.

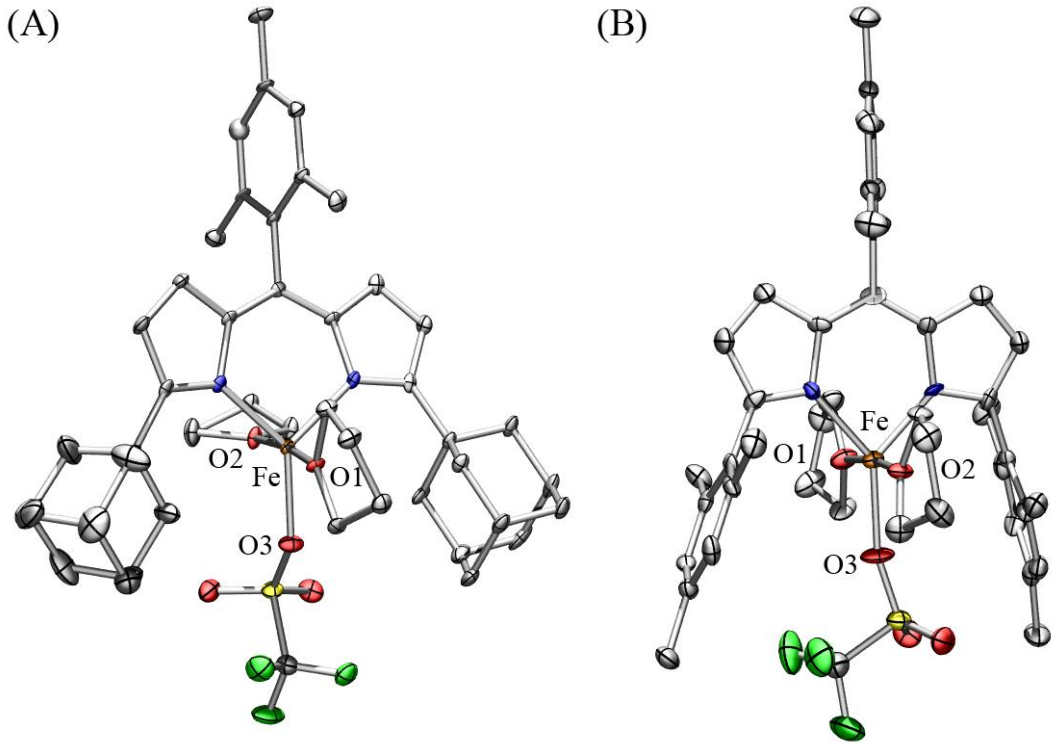

Figure 4.11. Solid-state structures of (**A**) ($^{H}_{Mes}$**L**^{Mes})**Fe(OTf)(THF)**$_2$, (courtesy of ERK), and (**B**) ($^{H}_{Mes}$**L**^{Ad})**Fe(OTf)(THF)**$_2$ (courtesy of DAI**)**. Hydrogen atoms have been omitted for clarity. Ellipsoids set at the 50% probability level. Gray, C; blue, N; red, O; yellow, S; green, F; orange, Fe.

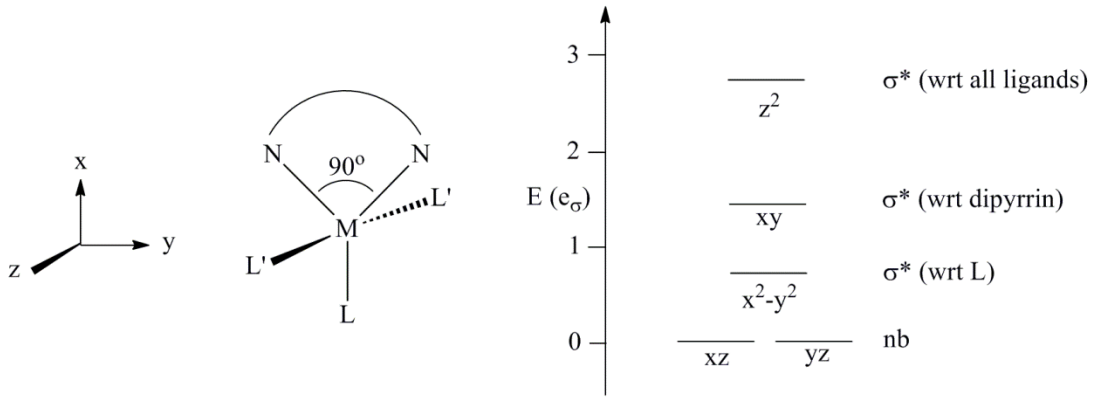

Figure 4.12. Idealized geometry and d-orbital splitting diagram for C_{2v}, five-coordinate dipyrrinato complexes.

4.5 Six-Coordinate Structures

Only a few six-coordinate dipyrrinato complexes of first-row transition metals have been reported to date, and include homoleptic tris(dipyrrinato) cobalt(III),[91] iron(III),[92] and manganese(III)[93] complexes, and a heteroleptic bis(dipyrrinato)Cr^{III}(acac) complex.[94] Several tris(dipyrrinato) complexes of the Group 13 trications have been described by Cohen.[3b,c,4] Additionally, a number of six-coordinate dipyrrinato complexes of second- and third-row transition metals have been reported.[40] Presumably, the small ionic radii of the first-row transition metals, their typical +1 or +2 charges, the relatively high electron count of the mid- to late-transition metals studied herein, and the size of the majority of the dipyrrins used to chelate transition metals, preclude the binding of six ligands. All reported six-coordinate structures have been nearly ideal octahedra with local D_{3d} symmetry, and have idealized σ-only d-orbital splitting diagrams with the common 2-over-3 arrangement.

Structurally-manifest Jahn-Teller distortions in these octahedral complexes are expected for high-spin d^4, low-spin d^7, and d^9 complexes. To the best of our knowledge, no crystallographically characterized dipyrrinato complexes exhibit these distortions, though the high-spin, homoleptic Mn(III), d^4 complexes reported by Murakami, et al.[93] show splitting of UV/Vis absorption peaks, which they attribute to Jahn-Teller distortions from ideal (local) O_h symmetry to D_{4h} symmetry.

---

[91] (a) Brückner, C.; Zhang, Y.; Rettig, S. J.; Dolphin, D. *Inorg. Chim. Acta* **1997**, *263*, 279. (b) Halper, S. R.; Cohen, S. M. *Inorg. Chem.* **2005**, *44*, 486. (c) Halper, S. R.; Do, L.; Stork, J. R.; Cohen, S. M. *J. Am. Chem. Soc.* **2006**, *128*, 15255.

[92] (a) Cohen, S. M.; Halper, S. R. *Inorg. Chim. Acta* **2002**, *341*, 12. (b) Halper, S. R.; Cohen, S. M. *Chem. - Eur. J.* **2003**, *9*, 4661.

[93] Murakami, Y.; Matsuda, Y.; Sakata, K. *Inorg. Chem.* **1971**, *10*, 1728.

[94] Murakami, Y.; Matsuda, Y.; Iiyama, K. *Chem. Lett.* **1972**, *1*, 1069.

4.6 Conclusions

Changes in the size of the flanking R group in of dipyrrinato ligands can lead to coordination numbers other than the four-coordinate structures most commonly seen in dipyrrinato transition metal complexes. With very large R groups or electron rich metals (e.g. Cu^{I}), three-coordinate geometries are often favored, as seen in the majority of complexes bearing the extremely large $(_{Mes}^{H}L^{Q})^{-}$ ligand (Section 4.2). Exceptionally small R groups, when paired with trivalent metals, can also allow the formation of six-coordinate complexes (Section 4.5).

Very weak anionic ligands bound to divalent metals can also affect the coordination number by enhancing the electrophilicity of the metal center, thereby inducing multiple solvent molecules to bind; this leads to five-coordinate complexes with local C_{2v} symmetry at the metal (Section 4.4).

4.7 Experimental Methods

4.7.1 General Synthetic Considerations

All syntheses of transition metal complexes were carried out in the absence of water and dioxygen in an MBraun inert atmosphere drybox under a dinitrogen atmosphere. All glassware was oven dried for a minimum of 1 h and cooled in an evacuated antechamber prior to use in the drybox. Bulk solvents used inside the glovebox (tetrahydrofuran, benzene, diethyl ether, and *n*-hexane) were dried and deoxygenated on a Glass Contour System (SG Water) and stored over 4 Å molecular sieves prior to use. Anhydrous hexamethyldisiloxane (Aldrich) and benzene-d_6 (Cambridge Isotope Labs) were degassed by a minimum of three freeze-pump-thaw cycles and stored over 4 Å molecular sieves prior to use. Anhydrous transition metal compounds were purchased from Strem and used as received. Celite® 545 (Baker) and zinc chloride (Aldrich) for

use in the glovebox were dried in a Schlenk flask for 24 h under dynamic vacuum while heating to at least 150 °C.

4.7.2 Characterization and Physical Measurements

Nuclear magnetic resonance experiments were performed on Varian Mercury 400 or Varian Unity/Inova 500 spectrometers. ^{1}H and ^{13}C NMR chemical shifts are reported relative to $SiMe_4$ using the chemical shift of residual solvent peaks as reference. Spectra were processed using the ACDLabs SpecManager v. 12 software package.

Elemental analyses were carried out at Complete Analysis Laboratories, Inc. (Parsippany, NJ).

X-ray crystallographic characterization was performed at one of two locations. In-house data was collected at the at the Harvard Center for Crystallographic Studies. Data was obtained on a Bruker three-circle platform goniometer equipped with an Apex II CCD and an Oxford cryostream cooling device. Radiation was from a graphite fine focus sealed tube Mo Kα (λ = 0.71073 Å) or Cu Kα (λ = 1.5418 Å) source. Crystals were mounted on a cryoloop or glass fiber pin using Paratone-N oil. Structures were collected at 100 K. Data for small or poorly diffracting crystals were obtained on the ChemMatCARS beamline at the Advanced Photon Source (APS) at Argonne National Labs (Argonne, IL), operating at 15 K. For data collected at APS, absorption parameters, *f′*and *f″*, for all heavy atoms (C, N, O, F, Cl, Br, Fe) were adjusted to the appropriate values for the synchrotron wavelength of 0.41328 Å during refinement. All data was collected as a series of φ and ω scans. All data was integrated using SAINT and scaled with a multi-scan absorption correction using SADABS.[64] The structures were solved by direct methods or Patterson maps using SHELXS-97 and refined against F^2 on all data by full matrix least squares with SHELXL-97.[65] All non-hydrogen atoms were refined anisotropically.

Hydrogen atoms were placed at idealized positions and refined using a riding model. Other details of individual crystal structure determinations are discussed below. Full experimental details for all compounds characterized by x-ray diffraction can be found in the Appendix.

4.7.3 Synthetic Procedures

Syntheses and characterization data of dipyrrinato iron(II) chloride pyridine complexes of the form **($^{X;\,X'}_{Ar}$L^{Mes})FeCl(py)** and their precursor lithium salts **($^{X;\,X'}_{Ar}$L^{Mes})Li(THF)$_n$** can be found in Section 3.8.3.

Scheme 4.3. Deprotonation of dipyrrins

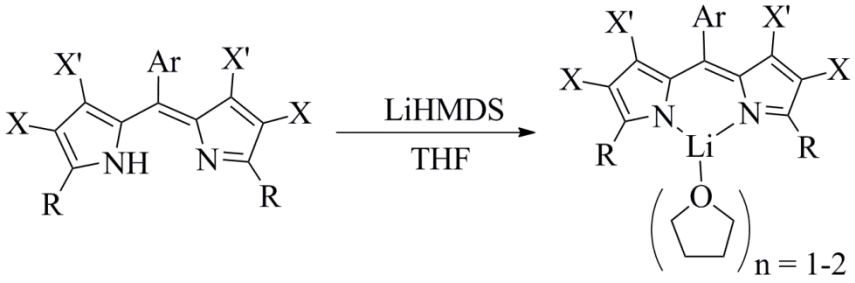

General procedure for deprotonation. To a stirring solution of the dipyrrin in anhydrous THF at liquid nitrogen temperature or room temperature was added lithium hexamethyl disilazide (LiHMDS, 1.0 equiv.) as a 1.0 *M* solution in hexanes. The solution was allowed to stir for up to 24 hours, and the solvent was removed in vacuo to afford the lithium dipyrrinato salts as THF adducts. Yields were uniformly quantitative.

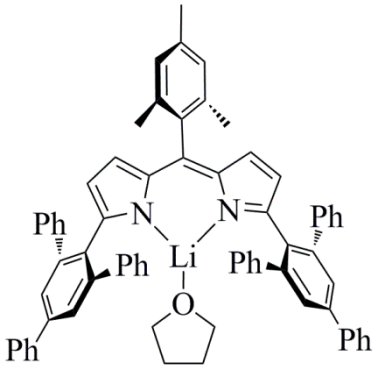

($_{Mes}^{H}L^{Q}$)Li(THF). ^{1}H NMR (500 MHz, C_6D_6) δ ppm 1.24 (br. s, 4H, O(CH_2)$_2$(CH_2)$_2$), 2.22 (s, 3H, *p*-Me [Mes]), 2.23 (s, 6H, *o*-Me[Mes]), 3.36 (br. s, 4H, O(CH_2)$_2$(CH_2)$_2$), 5.84 (dd, *J* = 4.0 & 0.9 Hz, [pyrrole-C*H*]$_2$), 6.30 (dd, *J* = 4.0 & 0.9 Hz, [pyrrole-C*H*]$_2$), 6.82 (s, 2H, *m*-H[Mes]), 7.15 (br. m, 22H, aryl), 7.55 (d, 4H, *o*-H[*p*-Ph]$_2$), 7.71 (s, 4H, *m*-H[2′,4′,6′-Ph]C_6H_2).

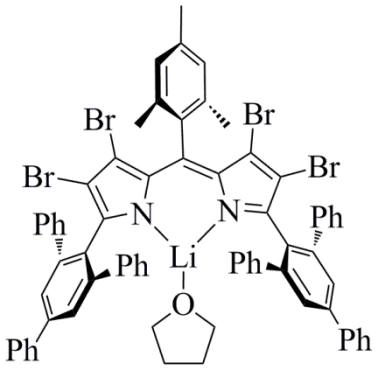

($_{Mes}^{Br}L^{Q}$)Li(THF)$_1$. ^{1}H NMR (500 MHz, C_6D_6) δ ppm 1.20 (br. s., 4 H), 2.22 (s, 3H), 2.25 (s, 6H), 3.24 (br. s, 4H), 6.95 (s, 2H), 6.95–7.01 (m, 8H), 7.03 (d, *J* = 7.32 Hz, 4H), 7.14 (s, 6H), 7.22 (d, *J* = 7.32 Hz, 12H), 7.45 (d, *J* = 7.32 Hz, 4H), 7.69 (s, 4H).

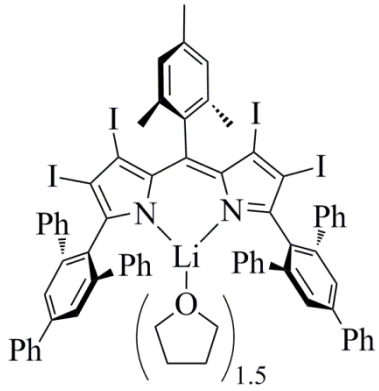

($_{Mes}^{I}L^{Q}$)Li(THF)$_{1.5}$. ^{1}H NMR (500 MHz, C_6D_6) δ ppm 1.31 (br. s, 6H), 2.18 (s, 6H), 2.26 (s, 3H), 3.43 (br. s, 6H), 6.89–6.97 (m, 10H), 7.00 (q, *J* = 7.52 Hz, 6H), 7.14 (s, 8H), 7.19–7.26 (m, 12H), 7.45 (d, *J* = 7.32 Hz, 4H), 7.72 (s, 4H).

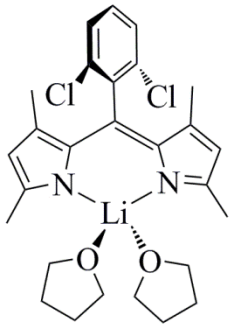

($_{DCP}^{H;\ Me}L^{Me}$)Li(THF)$_2$. ^{1}H NMR (400 MHz, C_6D_6) δ ppm 1.22 (dt, *J* = 6.64 & 3.24 Hz, 8H, $O(CH_2)_2(CH_2)_2$), 1.72 (s, 6H, [pyrrole-3-position]Me), 2.22 (s, 6H, [pyrrole-5-position]Me), 3.39 (m, 8H, $O(CH_2)_2(CH_2)_2$) 6.19 (s, 2H, [pyrrole-C*H*]$_2$) 6.55 (t, *J* = 8.09 Hz, 1H, *p*-H) 7.00 (d, *J* = 8.24 Hz, 2H, *m*-H).

Scheme 4.4. Metalation of lithium dipyrrinato complexes

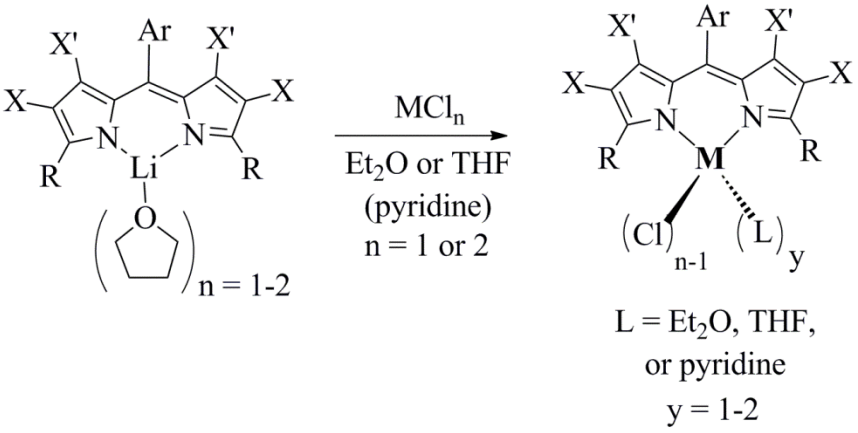

General procedure for metalation. To a stirring solution of the lithium dipyrrinato salt in THF was added metal chloride (1.1 equiv.). After stirring for up to 24 hours, the solvent was removed in vacuo and the residue was taken up in benzene, filtered through a plug of diatomaceous earth, and concentrated in vacuo to afford the metal dipyrrinato complexes.

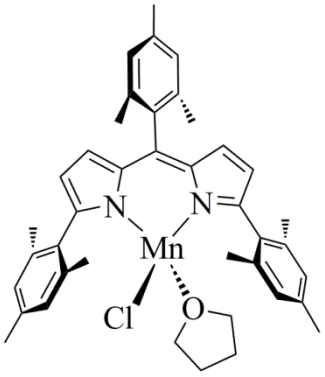

($_{Mes}^{H}$L^{Mes})MnCl(THF). 83% isolated yield. NMR silent. Crystals suitable for X-ray diffraction analysis were grown from vapor-diffusion of hexanes into a concentrated THF solution at room temperature. The structure was solved in the monoclinic space group $P2_1/m$. The manganese, chloride, oxygen, and *meso*-mesityl group resided on a crystallographic mirror plane. However, the quality of the data was exceptionally poor due to severe twinning.

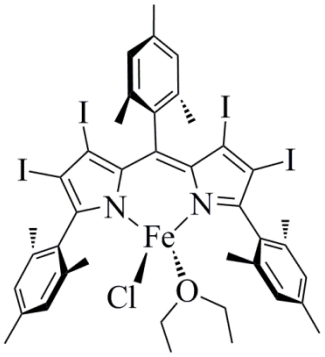

($_{Mes}^{I}L^{Mes}$)FeCl(OEt$_2$). This material decomposed over the course of two days in solution at −35 °C, and only a few crystals suitable for X-ray analysis were obtained. The structure was solved in the monoclinic space group $P2_1/n$, with four molecules in the unit cell and a single molecule in the asymmetric unit.

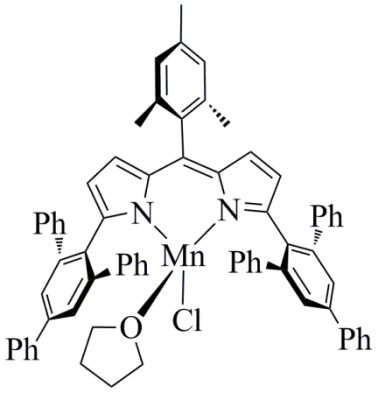

($_{Mes}^{H}L^{Q}$)MnCl(THF). 92% isolated yield. NMR silent. Anal. calc'd for $C_{70}H_{57}ClMnN_2O$: C, 81.42; H, 5.56; N, 2.71. Found: C, 81.36; H, 5.63; N, 2.59. Crystals suitable for X-ray analysis were grown from THF/hexane solution at −35 °C. The structure was solved in the monoclinic space group $C2/c$, with eight molecules in the unit cell and a single molecule in the asymmetric unit. A disordered molecule of solvent was also present in the asymmetric unit, which was treated as a diffuse contribution to the overall scattering without specific atom placements by PLATON/SQUEEZE.[95]

[95] Spek, A. L. Acta Crystallogr., Sect. D: Biol. Crystallogr. **2009**, 65, 148-155.

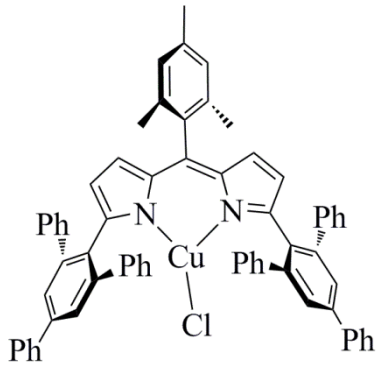

($_{Mes}^{H}$L^{Q})CuCl. 65% isolated yield. NMR silent. Anal. calc'd for $C_{66}H_{49}ClCuN_2$: C, 81.80; H, 5.10; N, 2.89. Found: C, 81.68; H, 4.99; N, 2.83. Crystals suitable for X-ray characterization were grown from saturated hexane solution at −35 °C. The structure was solved in the monoclinic space group *C*2/*c*, with eight molecules in the unit cell and a single molecule in the asymmetric unit.

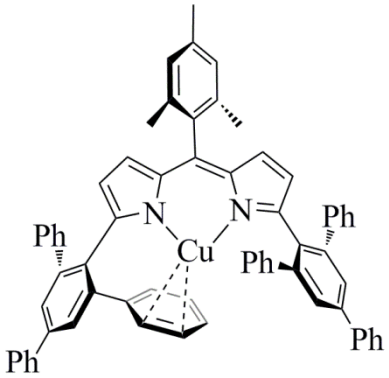

($_{Mes}^{H}$L^{Q})Cu. 88% isolated yield. ^{1}H NMR (500 MHz, C_6D_6) δ ppm 2.15 (s, 6H), 2.17 (s, 3H), 5.86 (d, *J* = 3.97 Hz, 2H), 6.20 (d, *J* = 3.97 Hz, 2H), 6.74 (s, 2H), 6.90–7.00 (m, 12H), 7.10 (dd, *J* = 8.08 & 1.37 Hz, 8H), 7.17 (d, *J* = 7.32 Hz, 2H), 7.20–7.26 (m, 4H), 7.47–7.55 (m, 4H), 7.69 (s, 4H). ^{13}C NMR (125 MHz, C_6D_6), δ ppm 19.82, 21.06, 121.37, 135.17, 126.10, 127.36, 127.56, 127.77, 127.81, 128.29, 128.44, 129.09, 134.23, 136.43, 136.53, 136.75, 137.64, 140.52, 140.62, 140.74, 142.75, 145.13, 155.48. Anal. calc'd for $C_{66}H_{49}CuN_2$: C, 84.90; H, 5.29; N, 3.00.

Found: C, 84.81; H, 5.38; N, 2.95. Crystals suitable for X-ray diffraction analysis were grown from concentrated hexanes solutions at −35° C. The structure was solved in the triclinic space group $P\bar{1}$, with two molecules in the unit cell and a single molecule in the asymmetric unit. The asymmetric unit also contained three molecules of benzene.

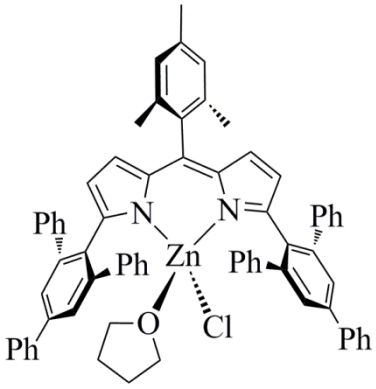

($_{Mes}^{H}$L^{Q})ZnCl(THF). 90% isolated yield. ^{1}H NMR (500 MHz, C_6D_6) δ ppm 1.32 (br. s, 4H), 1.94 (s, 5H), 2.17 (s, 3H), 3.53 (br. s, 4H), 5.86 (d, *J* = 3.97 Hz, 2H), 6.12 (d, *J* = 3.97 Hz, 2H), 6.73 (s, 2H), 6.99–7.24 (m, 19H), 7.33–7.46 (m, 12H), 7.71 (s, 4H); the residual solvent peak was obscured by the ligand aryl proton peaks, so referencing to the solvent peak is potentially inaccurate. Anal. calc'd for $C_{70}H_{57}ClZnN_2O$: C, 80.61; H, 5.51; N, 2.69. Found: C, 80.49; H, 5.44; N, 2.56.

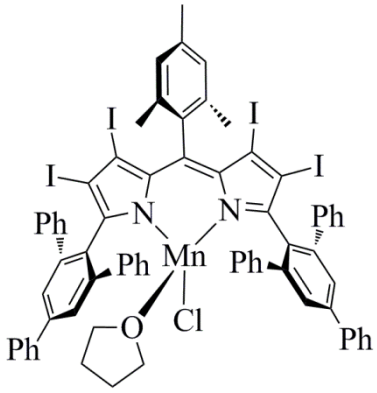

($_{Mes}^{I}L^{Q}$)MnCl(THF). 71% isolated yield. NMR silent. Only clean free ligand was observed in the HR-MS, and elemental analysis was hampered by the extreme water- and air-sensitivity of the material.

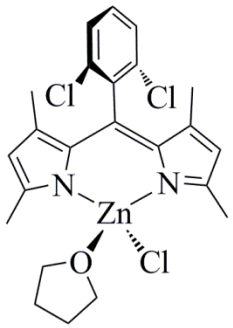

($_{DCP}^{H;\ Me}L^{Me}$)ZnCl(THF). 86% isolated yield. ^{1}H NMR (500 MHz, C_6D_6) δ ppm 1.12 (m, 4H), 1.46 (s, 6H), 2.49 (s, 6H), 3.54 (t, *J* = 6.56 Hz, 4H), 5.85 (s, 2H), 6.52 (t, *J* = 8.08 Hz, 1H, *p*-H), 6.90 (d, *J* = 7.93 Hz, 2H, *m*-H).

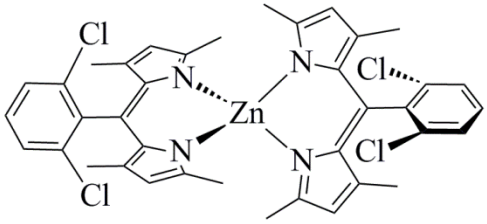

($^{H;\,Me}_{DCP}L^{Me}$)$_2$Zn. 78% isolated yield. ^{1}H NMR (500 MHz, C_6D_6) δ ppm 1.55 (s, 12H), 2.17 (s, 12H), 5.88 (s, 4H), 6.55 (t, *J* = 8.24 Hz, 2H, *p*-H), 6.97 (d, *J* = 8.24 Hz, 4H, *m*-H). HR-MS (ESI$^+$, $^m/_z$ for $[M+H]^+$) calc'd for $[C_{38}H_{34}Cl_4N_4Zn+H]$: 751.0902, found 751.0890. Crystals suitable for X-ray diffraction analysis were grown from a concentrated solution in diethyl ether at −35 °C. The structure was solved in the triclinic space group $P\bar{1}$, with eight molecules in the unit cell and two crystallographically inequivalent molecules in the asymmetric unit. The asymmetric unit also contained a single, disordered molecule of diethyl ether, which significantly worsened the quality of the data.

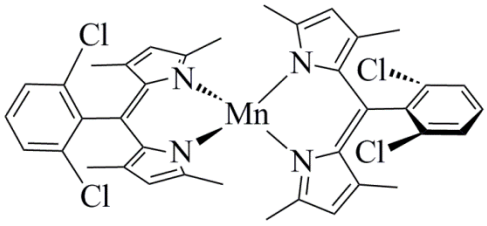

($^{H;\,Me}_{DCP}L^{Me}$)$_2$Mn. 68% isolated yield. NMR silent. Crystals suitable for X-ray diffraction analysis were grown from a 90:10 hexanes:THF solution at −35 °C. The structure was solved in the triclinic space group $P\bar{1}$, with two molecules in the unit cell and a single molecule in the asymmetric unit. The unit cell also contained half of a disordered solvent molecule, which was treated as a diffuse contribution to the overall scattering with PLATON/SQUEEZE.[95]

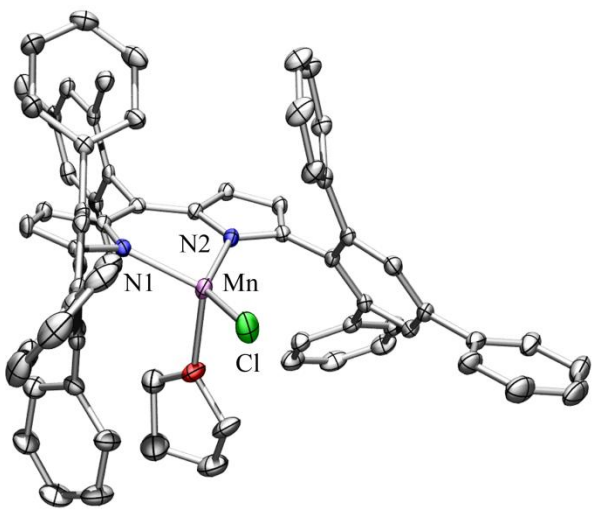

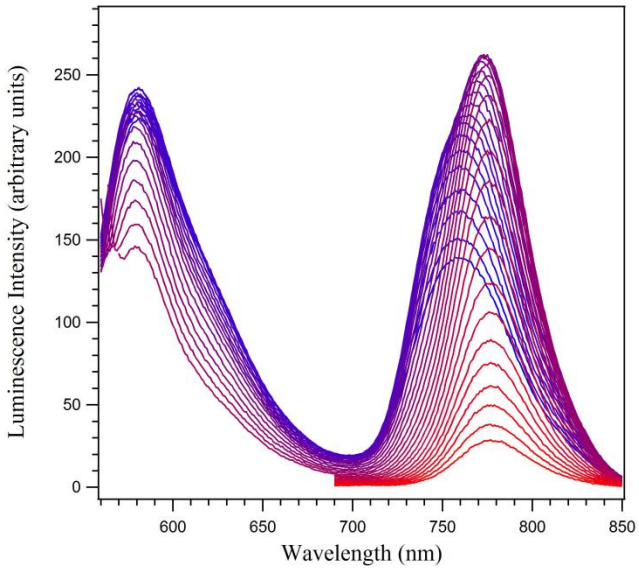

Chapter 5: Luminescence from Dipyrrins and Dipyrrinato Chelates

The photophysical and photochemical properties of dipyrrins and dipyrrinato chelates have been well-studied, and those molecules have been used in light-harvesting arrays[96] and as fluorescence labels in biological systems,[97] among many other applications. Examples of main-group chelates that display appreciable luminescence include the widely used boron-difluoride dipyrrin (BODIPY) dyes,[42] as well as chelates of Mg, Ca, Al, Ga, In, Si, and Sn.[47] A number of closed-shell transition metal complexes of dipyrrinato ligands have also been shown to luminesce, notably several complexes of Zn(II), which have been shown to efficiently fluoresce with quantum yields (Φ_F) as high as 0.83,[97b] where the quantum yield is defined as the number of emitted photons divided by the number of absorbed photons. The phosphorescence of dipyrrinato

[96] Yu, L.; Muthukumaran, K.; Sazanovich, I. V.; Kirmaier, C.; Hindin, E.; Diers, J. R.; Boyle, P. D.; Bocian, D. F.; Holten, D.; Lindsey, J. S. *Inorg. Chem.* **2003**, *42*, 6629.

[97] (a) Filatov, M. A.; Lebedev, A. Y.; Mukhin, S. N.; Vinogradov, S. A.; Cheprakov, A. V. *J. Am. Chem. Soc.* **2010**, *132*, 9552. (b) Ikeda, C.; Ueda, S.; Nabeshima, T. *Chem. Commun.* **2009**, 2544. (c) Wilson, C. J.; James, L.; Mehl, G. H.; Boyle, R. W. *Chem. Commun.* **2008**, 4582.

complexes of diamagnetic second- and third-row transition metals has been observed for Rh(III), Re(I), Ir(III), Pd(II), and Pt(II), and is uniformly weaker than the room-temperature fluorescence of analogous complexes, with the maximum reported Φ_P of 0.115.[98]

Luminescence from dipyrrinato complexes is virtually always due to a ligand-based $\pi^* \rightarrow \pi$ emission, which is generally enhanced by extension of the π system of the ligand,[2a] introduction of a bulky aryl group at the *meso* position,[99] or rigidification of the ligand by chelation to a (closed shell) metal (or boron) atom. Though fluorescence is the dominant mode of emission for most dipyrrin-based systems, those in which inter-system crossing is enhanced by spin-orbit coupling – usually by the presence of a heavy metal – have also been shown to phosphoresce.[47] To the best of our knowledge, every appreciably luminescent ($\Phi \geq 0.01$) dipyrrinato complex described to date has been diamagnetic. While several paramagnetic dipyrrinato complexes have been reported,[100] their emission spectra have rarely been described, and when they have, the luminescence has been exceptionally weak. Both dia- and paramagnetic luminophores have potential utility as metal sensors, in imaging applications,[101] and for paramagnetic luminophores especially, as hybrid optical/MRI imaging agents akin to those recently described by Li, et al.[102]

---

[98] Hanson, K.; Tamayo, A.; Diev, V. V.; Whited, M. T.; Djurovich, P. I.; Thompson, M. E. *Inorg. Chem.* **2010**, *49*, 6077.

[99] Kee, H. L.; Kirmaier, C.; Yu, L.; Thamyongkit, P.; Youngblood, W. J.; Calder, M. E.; Ramos, L.; Noll, B. C.; Bocian, D. F.; Scheidt, W. R.; Birge, R. R.; Lindsey, J. S.; Holten, D. *J. Phys. Chem. B* **2005**, *109*, 20433.

[100] (a) Cohen, S. M.; Halper, S. R. *Inorg. Chim. Acta* **2002**, *341*, 12. (b) King, E. R.; Betley, T. A. *Inorg. Chem.* **2009**, *48*, 2361. (c) King, E. R.; Hennessy, E. T.; Betley, T. A. *J. Am. Chem. Soc.* **2011**, *133*, 4917. (d) King, E. R.; Sazama, G. T.; Betley, T. A. *J. Am. Chem. Soc.* **2012**, *134*, 17858. (e) Hennessy, E. T.; Betley, T. A. *Science* **2013**, *340*, 591. (f) Halper, S. R.; Malachowski, M. R.; Delaney, H. M.; Cohen, S. M. *Inorg. Chem.* **2004**, *43*, 1242. (g) Choi, S. H.; Kim, K.; Jeon, J.; Meka, B.; Bucella, D.; Pang, K.; Khatua, S.; Lee, J.; Churchill, D. G. *Inorg. Chem.* **2008**, *47*, 11071. (h) Choi, S. H.; Kim, K.; Lee, J.; Do, Y.; Churchill, D. G. *J. Chem. Cryst.* **2007**, *37*, 315. (i) Yang, L.; Zhang, Y.; Yang, G.; Chen, Q.; Ma, J. S. *Dyes Pigm.* **2004**, *62*, 27. (j) Scharf, A. B.; Betley, T. A. *Inorg. Chem.* **2011**, *50*, 6837. (k)

[101] Di, W.; Velu, S. K. P.; Lascialfari, A.; Liu, C.; Pinna, N.; Arosio, P.; Sakka, Y.; Qin, W. *J. Mater. Chem.* **2012**, *22*, 20641.

[102] Mitchell, N.; Kalber, T. L.; Cooper, M. S.; Sunassee, K.; Chalker, S. L.; Shaw, K. P.; Ordidge, K. L.; Badar, A.; Janes, S. M.; Blower, P. J.; Lythgoe, M. F.; Hailes, H. C.; Tabor, A. B. *Biomaterials* **2013**, *34*, 1179.

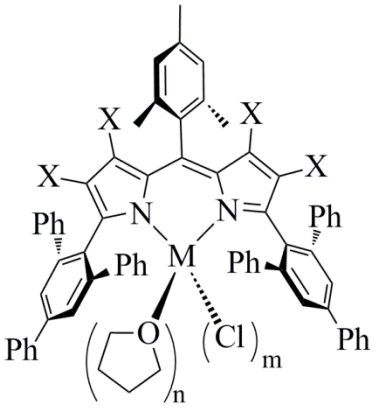

M = H, Li(I), Mn(II), Fe(II), Cu(II), Cu(I), Zn(II)
X = H, Br, I
n = 0-2
m = 0, 1

Figure 5.1. Generic structure of complexes studied in Chapter 5, abbreviated $(_{Mes}^{X}L^{Q})MCl_{m}(THF)_{n}$, where X is the 2,3,7,8-substituent on the dipyrrin, Mes is the mesityl group in the *meso* position, Q is the 2′,4′,6′-(triphenyl)phenyl flanking group, M is the chelated metal (or hydrogen atom), n is the number of THF ligands on the metal, and m is the number of chloride ligands on the metal.

5.1 Fluorescence

In our exploration of the reactivity of iron(II) dipyrrinato complexes for the inter-[53] and intra-molecular[21a] amination of C-H bonds, we synthesized the extremely bulky monoanionic ligand 2,9-bis(2′,4′,6′-triphenylphenyl)-5-mesityl-dipyrrinato [abbreviated $(_{Mes}^{H}L^{Q})^{-}$, where H is the 2,3,7,8-substituent, Mes is the mesityl group in the *meso* position, and Q is the 2,9-substituent], which allowed us to isolate an Fe(III) iminyl radical that we hypothesized to be the active aminating species in that reaction pathway.[53a] We noticed in the course of these studies that both the protio dipyrrin, $(_{Mes}^{H}L^{Q})H$, (Φ_F = 0.16, vs. Rhodamine 6G in absolute ethanol,[103] against which all subsequent quantum yields are reported) and its lithium salt, $(_{Mes}^{H}L^{Q})Li(THF)_2$ (Φ_F = 0.51), were visibly luminescent in benzene solution, though none of the iron complexes were noticeably luminescent. (Φ_F is the quantum yield of fluorescence, defined for a

[103] Magde, D.; Wong, R.; Seybold, P. G. *Photochem. Photobiol.* **2002**, *75*, 327.

luminophore as the number of protons emitted divided by the number of protons absorbed, as described in Section 1.2.3.) Given the importance of related chromophores in a wide array of applications, we were interested to explore whether transition metal chelates of this and related ligands would exhibit luminescence. To this end, we synthesized the closed-shell Zn(II) and Cu(I) dipyrrinato complexes **($_{Mes}^{H}L^{Q}$)ZnCl(THF)** and **($_{Mes}^{H}L^{Q}$)Cu**, respectively, anticipating that they should in fact luminesce, like the analogous lithium complex (Figure 5.2).

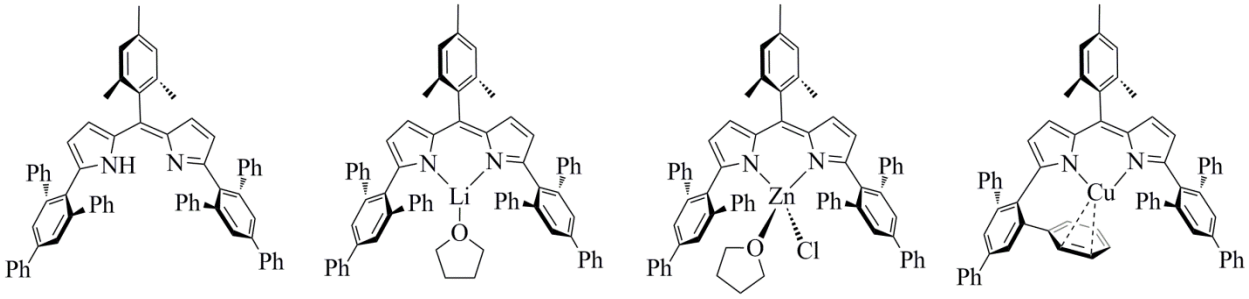

Figure 5.2. Closed-shell, fluorescent derivatives of the dipyrrinato ligand **($_{Mes}^{H}L^{Q}$)**$^{-}$.

Unsurprisingly, the zinc complex showed significant fluorescence at room temperature (Φ_F = 0.67) in benzene solution, but complexation of the dipyrrinato ligand to Cu(I) had a significant quenching effect on the fluorescence of the ligand (Φ_F ~ 0.03). We attribute this difference in fluorescence intensity to the significant difference in the coordination environment around the d^{10} ions; in the zinc complex, ^{1}H NMR indicates a four-coordinate species with THF bound to a presumably pseudo-tetrahedral zinc ion. Crystallographic characterization of the Cu(I) complex showed a three-coordinate Cu(I) atom with one of the flanking phenyl units bound in an η^2 fashion to the metal in the solid state (Figure 4.3 and Figure 5.2). Proton NMR in benzene-d_6 did not show desymmetrization of the ligand, so presumably the η^2-bound phenyl group is fluxional in solution. Notably, the emission spectrum of **($_{Mes}^{H}L^{Q}$)Cu** showed excitation wavelength dependence (Figure 5.3), indicative of the presence of multiple emissive species

present in solution, consistent with the hypothesis that the solution-state structure of **($_{Mes}^{H}$L^{Q})Cu** is fluxional. Addition of acetonitrile to the solution results in a single emission spectrum, consistent with the formation of a static 3- or 4-coordinate acetonitrile adduct, which displays only very weak fluorescence (Figure 5.4). The presence of multiple species in non-coordinating solvents makes the determination of quantum yields challenging, but we can estimate Φ by comparison to other similar spectra obtained in this study.

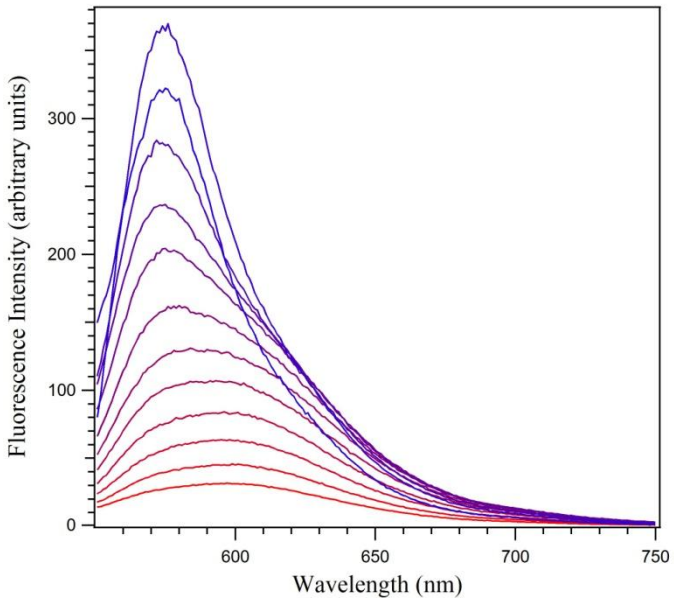

Figure 5.3. Excitation-dependent emission spectra of **($_{Mes}^{H}$L^{Q})Cu** in benzene without coordinating solvent. Spectra were recorded in 10 nm increments of excitation wavelength from 450 nm (red traces) to 560 nm (blue traces). λ_{max}(fluorescence) = 597 nm for excitation at 450 nm; λ_{max}(fluorescence) = 575 nm for excitation at 560 nm.

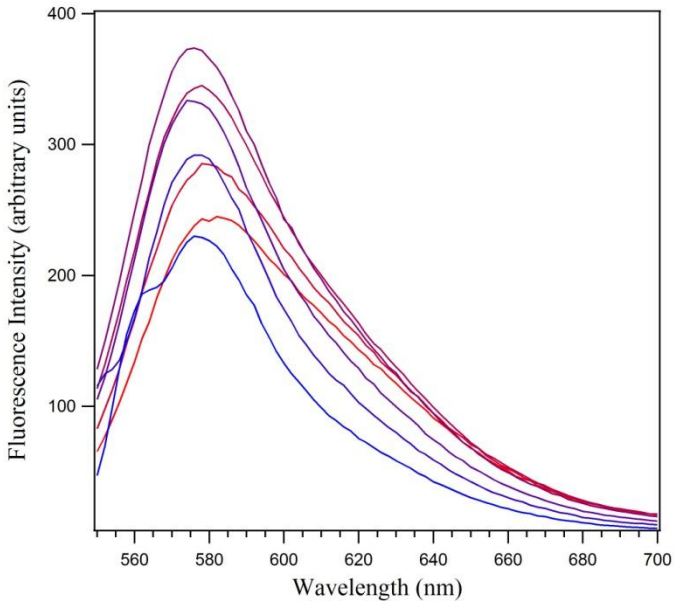

Figure 5.4. Excitation-dependent emission spectra of **($_{Mes}^{H}L^{Q}$)Cu** in benzene with added acetonitrile. Spectra were recorded in 10 nm increments of excitation wavelength from 500 nm (red traces) to 560 nm (blue traces). λ_{max}(fluorescence) = 576 ± 1 nm for all excitation wavelengths. The complex with acetonitrile bound is markedly less luminescent than the unsolvated complex (Figure 5.3). Some peak shape dependence on the excitation wavelength can be seen, but we attribute this to the broad excitation/absorption spectra of this species rather than an equilibrium mixture of various adducts.

Given the absence of paramagnetic, luminescent dipyrrinato complexes in the literature, we synthesized several open-shell complexes of the fluorescent ligand **($_{Mes}^{H}L^{Q}$)**$^{-}$. While the Fe(II) complex showed only extremely weak fluorescence (Φ_F < 0.001), both the Mn(II) and Cu(II) complexes **($_{Mes}^{H}L^{Q}$)MnCl(THF)** and **($_{Mes}^{H}L^{Q}$)CuCl** luminesced at room temperature in benzene solutions. Though there was appreciable quenching of the luminescence in both complexes relative to the metal-free ligand **($_{Mes}^{H}L^{Q}$)H**, presumably due to the unpaired electrons in the metal's d orbitals,[104] fluorescence with appreciable quantum yield (Φ_F) was observed for both species. Fluorescence spectral details of the derivatives of **($_{Mes}^{H}L^{Q}$)**$^{-}$ are compiled in Table 5.1.

[104] Formosinho, S. J. *Mol. Photochem.* **1976**, *7*, 13.

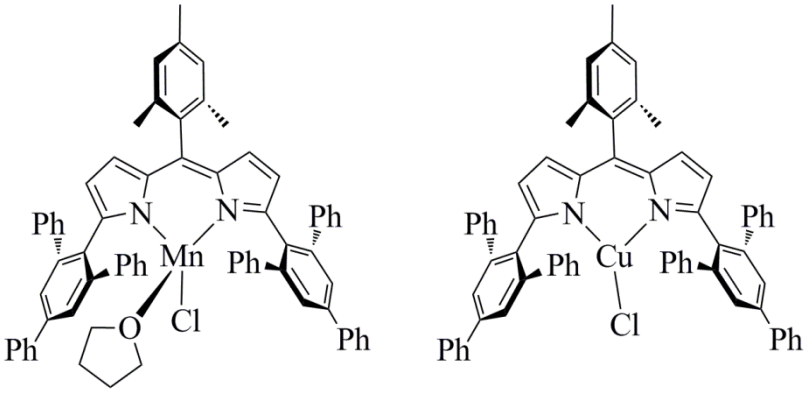

Figure 5.5. Open-shell, paramagnetic, fluorescent derivatives of the dipyrrinato ligand $(^{H}_{Mes}L^{Q})^{-}$. The drawings accurately represent the solid-state structures as determined by X-ray crystallography (Figure 4.5 and Figure 4.9, respectively).

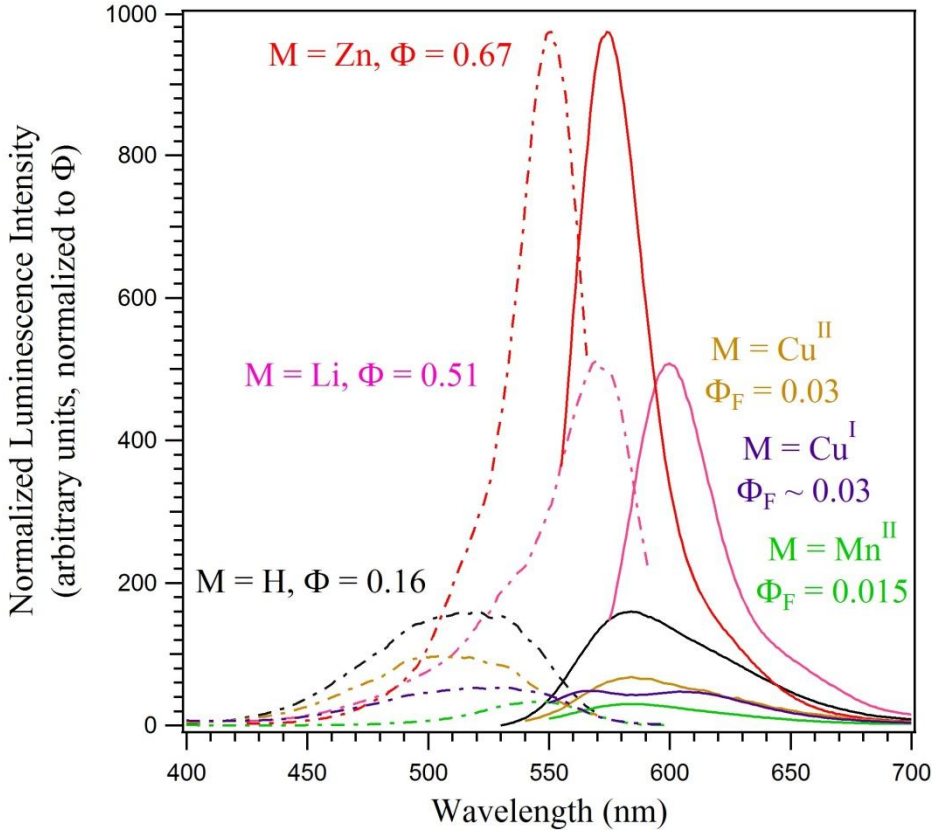

Figure 5.6. Fluorescence spectra of derivatives of $(^{H}_{Mes}L^{Q})^{-}$ (taken in benzene solution at 298 K). Dashed lines are excitation spectra obtained with emission detected at λ_{max}(em), and solid lines are emission spectra obtained with excitation at λ_{max}(ex). Black, $(^{H}_{Mes}L^{Q})$**H**; pink, $(^{H}_{Mes}L^{Q})$**Li(THF)$_2$**; red, $(^{H}_{Mes}L^{Q})$**ZnCl(THF)**; gold, $(^{H}_{Mes}L^{Q})$**CuCl**; purple, $(^{H}_{Mes}L^{Q})$**Cu**; green, $(^{H}_{Mes}L^{Q})$**MnCl(THF)**. Intensities are normalized to Φ and are reported on an arbitrary y-axis.

Table 5.1. Fluorescence spectral details for derivatives of $(^{H}_{Mes}L^{Q})^{-}$

Complex	λ_{max} (ex, nm)[a]	λ_{max} (em, nm)[b]	Stokes shift (nm)	Φ_F[c]	*S*
$(^{H}_{Mes}L^{Q})H$	520	584	64	0.16	0
$(^{H}_{Mes}L^{Q})Li(THF)_2$	570	600	30	0.51	0
$(^{H}_{Mes}L^{Q})MnCl(THF)$	535	579	44	0.015	$^{5}/_{2}$
$(^{H}_{Mes}L^{Q})FeCl(THF)$	519	583	64	<0.001	2
$(^{H}_{Mes}L^{Q})CuCl$	504 (br)	588	64	0.03	$^{1}/_{2}$
$(^{H}_{Mes}L^{Q})Cu$[d]	532 544	567 605	35 61	~0.03	0
$(^{H}_{Mes}L^{Q})ZnCl(THF)$	550	574	24	0.67	0

[a] Excitation maximum. [b] Emission maximum. [c] Quantum yields were determined by comparison to Rhodamine 6G in absolute ethanol ($\Phi_F = 0.95 \pm 0.005$).[103] [d] Two emission and excitation maxima were observed for $(^{H}_{Mes}L^{Q})Cu$; it is unclear how the two emissive species differ. All spectra were obtained in benzene solutions at 298 K.

5.2 Phosphorescence

Notably, $(^{H}_{Mes}L^{Q})MnCl(THF)$ also showed appreciable near-infrared (NIR, λ_{max} = 757 nm) phosphorescence, a very rare phenomenon for paramagnetic complexes in solution at room temperature. Room temperature phosphorescence in the solution state is uncommon because the excited state lifetime of molecular phosphors is generally quite long ($>10^{-4}$ s); non-radiative decay processes usually compete effectively with phosphorescent emission on these time scales, especially at high temperatures and in fluid media, where collisional and vibrational relaxation are enhanced. Second, the presence of permanent paramagnets in or near a luminophore typically increases the rate of intersystem crossing,[104] both

in the singlet → triplet and triplet → singlet directions; for this reason, deoxygenated solvents must often be used to observe phosphorescence.

In benzene solutions, pure samples of **($_{\mathbf{Mes}}^{\mathbf{H}}$ L$^{\mathbf{Q}}$)MnCl(THF)** showed excitation wavelength-dependent phosphorescence emission maxima (Figure 5.7), an apparent violation of Kasha's Rule,[105] which says that emission from a singlet or triplet manifold always occurs from the lowest-energy singlet or triplet state, respectively. This rule implies that the emission spectra of pure molecules should not show dependence on the excitation wavelength. As determined by X-ray crystallography, **($_{\mathbf{Mes}}^{\mathbf{H}}L^{\mathbf{Q}}$)MnCl(THF)** exists as a four-coordinate monovacant trigonal bipyramidal THF adduct in the solid state (Figure 4.9), so we surmised that the complex's excitation wavelength-dependent phosphorescence spectrum could be due to an equilibrium mixture of the 4-coordinate THF adduct and the 3-coordinate complex **($_{\mathbf{Mes}}^{\mathbf{H}}L^{\mathbf{Q}}$)MnCl** with dissociated THF. Addition of excess THF to a benzene solution of **($_{\mathbf{Mes}}^{\mathbf{H}}$ L$^{\mathbf{Q}}$)MnCl(THF)** supported this hypothesis, as the excitation wavelength dependence disappeared under these conditions, presumably by pushing the equilibrium heavily toward the THF adduct (Figure 5.8). Other possible structures for **($_{\mathbf{Mes}}^{\mathbf{H}}L^{\mathbf{Q}}$)MnCl** include a bis-μ-Cl dimer, though this is unlikely under the extremely dilute (~10^{-7} *M*) conditions, various ligand phenyl group adducts (η^2, η^6, bis-η^2, etc.), or benzene solvento species. Without structural or NMR evidence for the identity of this species, we hesitate to assign its structure definitively.

[105] Kasha, M. *Discuss. Faraday Soc.* **1950**, *9*, 14.

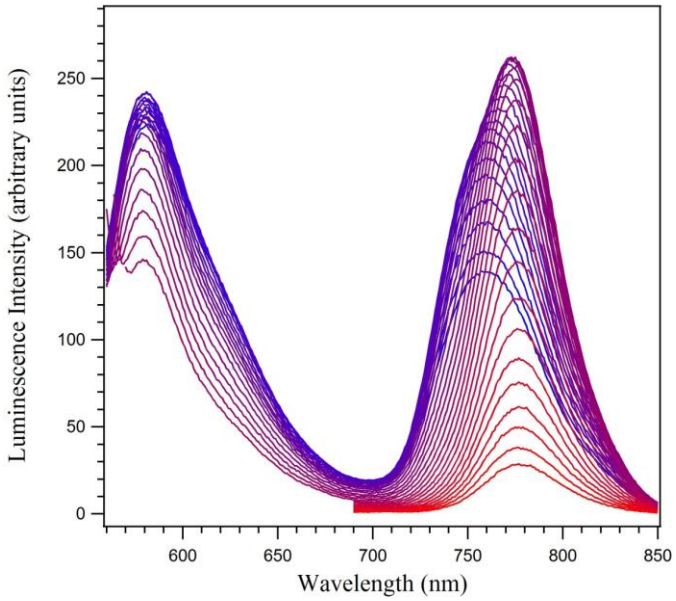

Figure 5.7. Excitation dependent emission spectra of **($_{Mes}^{H}$L^{Q})MnCl(THF)** in benzene, in the absence of exogeneous THF. Emission spectra were collected for excitation wavelengths in 2 nm increments from 520 nm (blue traces) to 580 nm (red traces). λ_{max}(fluorescence) = 579 ± 1 nm for all excitation wavelengths; λ_{max}(phosphorescence) = 757 nm for excitation at 520 nm; λ_{max}(phosphorescence) = 777 nm for excitation at 580 nm.

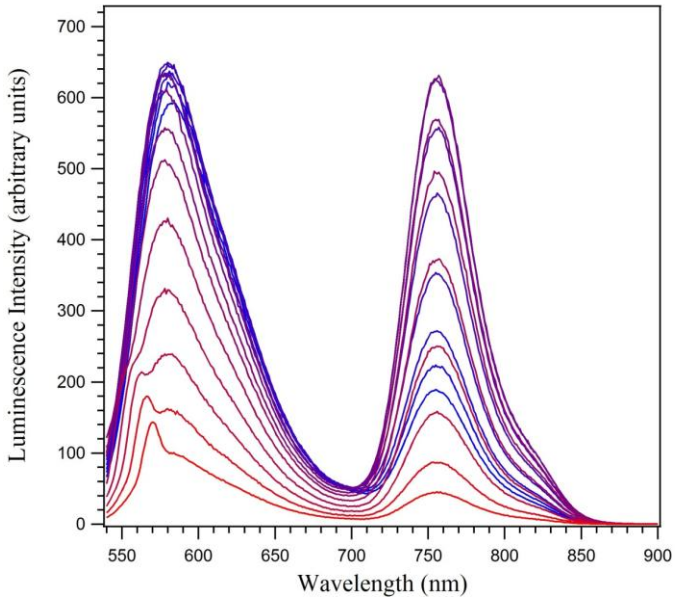

Figure 5.8. Excitation dependent emission spectra of **($_{Mes}^{H}$L^{Q})MnCl(THF)** in benzene, in the presence of exogeneous THF. Emission spectra were collected for excitation wavelengths in 2 nm increments from 520 nm (blue traces) to 580 nm (red traces). λ_{max}(fluorescence) = 579 ± 1 nm and λ_{max}(phosphorescence) = 757 nm for all excitation wavelengths. The small shoulders in the fluorescence emission curves at long excitation wavelengths are due to bleed-over from the excitation source.

The complex **($_{Mes}^{H}$L^{Q})MnCl(THF)** is, to the best of our knowledge, the first appreciably phosphorescent molecular complex of Mn(II). While Mn(II) is often used as a dopant in phosphorescent glasses,[106] and in nanoparticles[107] and quantum dots,[108] reports of solution-state, room-temperature phosphorescence from a molecular species containing manganese are virtually nonexistent. There is a single report of the phosphorescence of Mn(II) tetraphenylporphyrin, which showed weak NIR phosphorescence (λ_{max} = 840 nm, $\Phi_P = 3 \times 10^{-4}$) in methylcyclohexane glass at 77 K,[109] and a few reports of discrete molecular manganese species exhibiting solid-state phosphorescence.[110]

To ascertain whether phosphorescence could be enhanced to a greater degree, the 2,3,7,8-tetrabrominated and tetraiodinated dipyrrins **($_{Mes}^{Br}$L^{Q})H** and **($_{Mes}^{I}$L^{Q})H**, respectively, were synthesized (Section 2.4.3). Halogenation is known to increase the rate of intersystem crossing in luminescent molecules by enhancing spin-orbit coupling,[37] thereby increasing the proportion of phosphorescence to fluorescence. Indeed, the lithium complexes **($_{Mes}^{Br}$L^{Q})Li(THF)** and **($_{Mes}^{I}$L^{Q})Li(THF)$_{1.5}$** displayed measurable phosphorescence in solution at room temperature, albeit with significantly lower quantum yields than for fluorescence emission. We can attribute the quenching of fluorescence upon introduction of halogens to two phenomena: the enhancement of spin-orbit coupling, and the deplanarization of the conjugated system of *meso*-mesityl dipyrrins with halogens in the 4- and 7-positions (Section 3.6.1). Despite these effects, on complexation of the tetraiodinated ligand to Mn(II), phosphorescence was totally quenched, and the only observable emission was by fluorescence, albeit quite weakly (Φ_F = 0.02).

[106] Feuerhelm, L. N.; Sibley, S. M.; Sibley, W. A. *J. Solid State Chem.* **1984**, *54*, 164.
[107] (a) Pradhan, N.; Sarma, D. D. *J. Phys. Chem. Lett.* **2011**, *2*, 2818. (b) Isobe, T. *Hyomen Kagaku* **2001**, *22*, 315.
[108] Gan, C. Z., Yanpeng; Battaglia, David; Peng, Xiaogang; Xiao, Min *Appl. Phys. Lett.* **2008**, *92*, 241111.
[109] Harriman, A. J. Chem. Soc., Faraday Trans. 1, **1980**, 76, 1978.
[110] Oelkrug, D. W., A. *Ber. Bunsen-Ges.* **1972**, *76*, 1088.

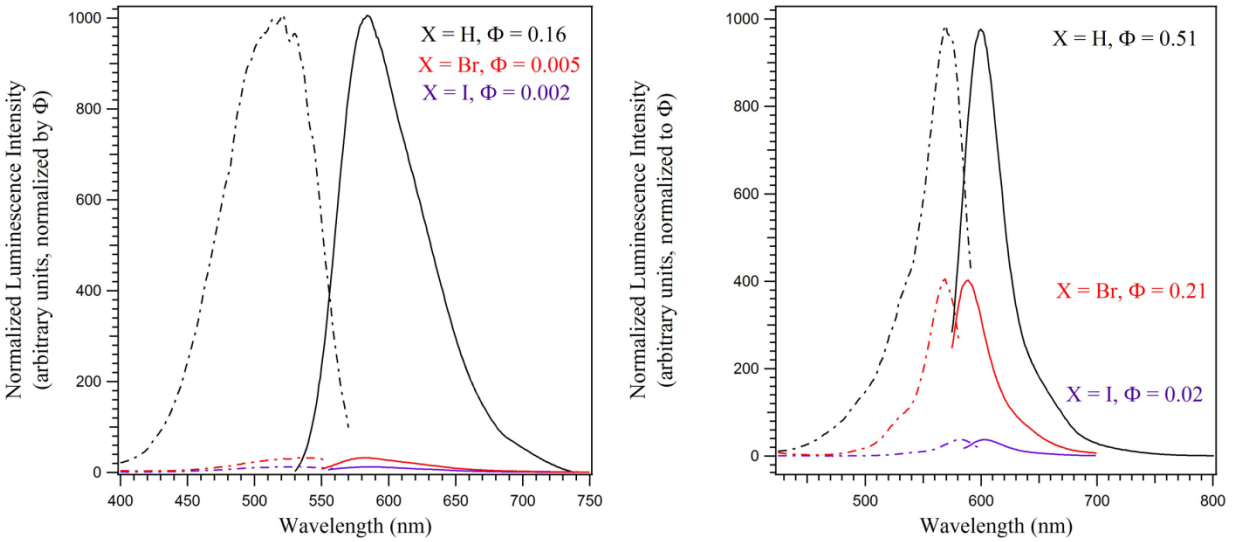

Figure 5.9. Fluorescence spectra of halogenated species. Left: black, $(^{H}_{Mes}L^{Q})H$; red, $(^{Br}_{Mes}L^{Q})H$; purple $(^{I}_{Mes}L^{Q})H$. Right: black, $(^{H}_{Mes}L^{Q})Li(THF)_2$; red, $(^{Br}_{Mes}L^{Q})Li(THF)$; purple $(^{I}_{Mes}L^{Q})Li(THF)_{1.5}$. Intensities are normalized to Φ and are reported on an arbitrary y-axis. All spectra obtained in benzene solutions at 298 K.

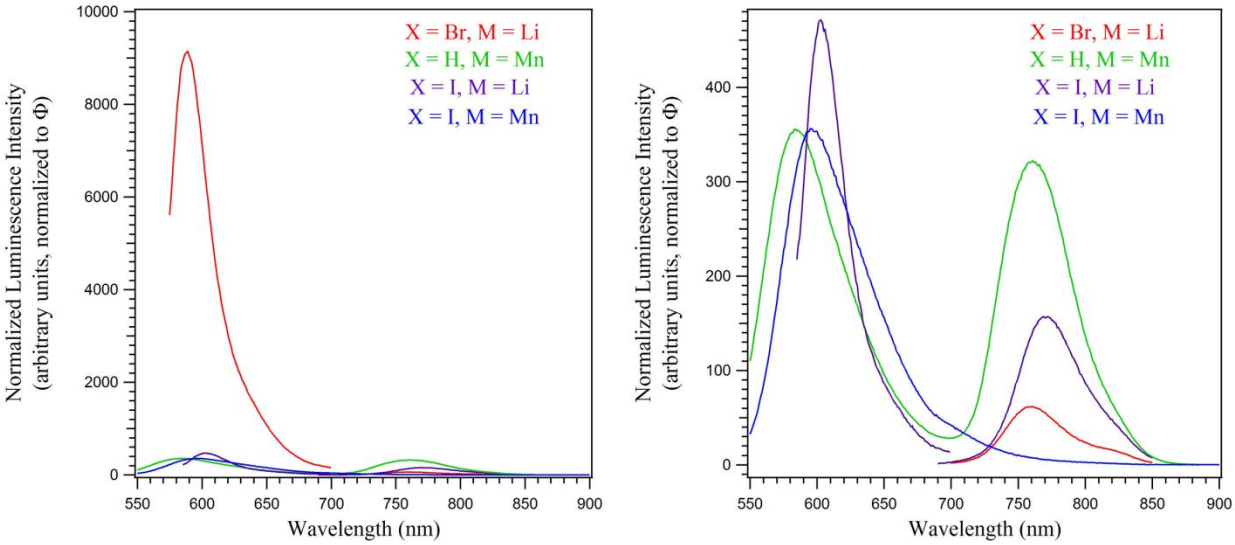

Figure 5.10. Emission spectra of phosphorescent species. Red, $(^{Br}_{Mes}L^{Q})Li(THF)$; purple, $(^{I}_{Mes}L^{Q})Li(THF)_{1.5}$; green, $(^{H}_{Mes}L^{Q})MnCl(THF)$; blue, $(^{I}_{Mes}L^{Q})MnCl(THF)$. Left: normalized emission spectra for all species; right: magnified emission spectra of all species, omitting the fluorescence emission curve of $(^{Br}_{Mes}L^{Q})Li(THF)$, which dwarfs the other emission intensities. All spectra obtained in benzene solutions at 298 K.

Table 5.2. Luminescence spectral details of halogenated and phosphorescent species

Complex	λ_{max} (ex, nm)[a]	λ_{max} (em, nm)[b]	Stokes shifts (nm)[c]	Φ_F[d]	Φ_P[d]	Φ_F/Φ_P
$(^{Br}_{Mes}L^{Q})H$	535	583	48	0.005	--	--
$(^{Br}_{Mes}L^{Q})Li(THF)$	569	589, 760	20, 191	0.21	0.002	105
$(^{I}_{Mes}L^{Q})H$	532	585	53	0.002	--	--
$(^{I}_{Mes}L^{Q})Li(THF)_{1.5}$	583	603, 772	20, 189	0.017	0.008	2.1
$(^{H}_{Mes}L^{Q})MnCl(THF)$[e]	535	579, 757	44, 222	0.015	0.015	1.0
$(^{I}_{Mes}L^{Q})MnCl(THF)$	534	595	61	0.02	--	--

[a] Excitation maximum. [b] Emission maxima for fluorescence and phosphorescence, respectively. [c] For fluorescence and phorphorescence, respectively. [d] Quantum yields were determined by comparison to Rhodamine 6G in absolute ethanol ($\Phi_F = 0.95 \pm 0.005$).[103] [e] These data are taken from the solution with added THF, and we presume that under these conditions the 4-coordinate THF adduct is the dominant species in solution. All spectra obtained in benzene solutions at 298 K.

5.3 Conclusions

Using the luminescent dipyrrinato ligands $(^{H}_{Mes}L^{Q})^{-}$, $(^{Br}_{Mes}L^{Q})^{-}$, and $(^{I}_{Mes}L^{Q})^{-}$, a variety of luminescent metal complexes were synthesized and characterized by fluorescence and phosphorescence spectroscopies. Chelation to closed-shell metal ions such as Li(I) and Zn(II) markedly enhanced the luminescence intensities of the chromophores; **$(^{H}_{Mes}L^{Q})ZnCl(THF)$** had a quantum yield of fluorescence (Φ_F) of 0.67, one of the highest quantum yields reported to date for dipyrrinato metal complexes. Notably, fluorescence emission was incompletely quenched by coordination of the dipyrrin to the paramagnetic metal centers Mn(II) and Cu(II), giving rise to the first paramagnetic dipyrrinato complexes with appreciable fluorescence intensity.

Room temperature, solution-state phosphorescence was also observed from the Mn(II) complex **$(^{H}_{Mes}L^{Q})MnCl(THF)$**, the first reported molecular species containing manganese to phosphoresce at room temperature ($\Phi_P = 0.015$). The introduction of halogens onto the periphery of the dipyrrinato ligand also allowed the observation of room-temperature, solution-state phosphorescence from both the free halogenated dipyrrins and their lithium chelates, albeit with

markedly lower quantum yields than for fluorescence. These molecular luminophores may find application in fluorescence labeling, metal sensing, or hybrid optical/MRI imaging agents.

5.4 Experimental Details for Luminescence Spectroscopy

Luminescence measurements were performed on a Varian Cary Eclipse fluorescence spectrophotometer operating at 298 K. Instrument settings (emission and excitation slit widths, PMT detector voltage) were optimized for each individual sample. Relative quantum yields of optically dilute solutions (absorbance < 0.1, concentrations ~10^{-6}–10^{-7} *M* in benzene) were calculated in comparison to dilute solutions of Rhodamine 6G in absolute ethanol ($\Phi = 0.95 \pm 0.005$)[103] according to Equation 5.1.[111]

$$\Phi_x = \Phi_r \left(\frac{A_r}{A_x}\right)\left(\frac{I_r}{I_x}\right)\left(\frac{D_x}{D_r}\right)\left(\frac{n_x}{n_r}\right)^2 \qquad \text{(Eq. 5.1)}$$

Here, *A* is the absorbance at the excitation wavelength, *I* is the intensity of the incident light, *D* is the integrated area under the emission curve (calculated by trapezoidal or rectangular numerical integration of the spectrum in Microsoft Excel), *n* is the refractive index of the solvent, and subscripts *x* and *r* denote the analyte and reference solutions, respectively. For identical instrument configurations between analyte and reference solutions, I_r/I_x was considered to be unity. However, for weakly-emitting samples ($\Phi < 0.05$), the instrument settings used to obtain acceptable excitation and emission spectra of the analyte gave over-range fluorescence intensities for the Rhodamine 6G reference solution. In these cases, either the voltage of the PMT detector was lowered or the slit widths were decreased for the reference solution measurement, and the intensity ratios I_r/I_x were calculated by linear calibration of the instrument response to the altered measurement conditions. Quantum yields are reported with ±0.10 error

[111] Crosby, G. A.; Demas, J. N. *J. Phys. Chem.* **1971**, *75*, 991.

intervals, as is customary for values determined by comparison with chemical quantum yield standards, as opposed to those determined by a more direct method such as actinometry.

Appendix: Experimental details for crystallographic data collection

Crystal Data	$(^{Br;\,H}_{Mes}L^{Mes})H$	$(^{I}_{Mes}L^{Mes})H$	$(^{H}_{BFP}L^{Mes})FeCl(py)$	$(^{H}_{Mes}L^{Mes})FeCl(py)$	$(^{Cl}_{Mes}L^{Mes})FeCl(py)$
Chemical formula	$C_{36}H_{36}Br_2N_2$	$C_{36}H_{34}I_4N_2$	$C_{40}H_{34}ClF_6FeN_3$	$C_{41}H_{42}ClFeN_3$	$C_{41}H_{38}Cl_5FeN_3$
M_r	656.49	1002.25	762.00	668.08	805.84
Crystal system, space group	Monoclinic, $C2/c$	Monoclinic, $P2_1/n$	Triclinic, $P\bar{1}$	Monoclinic, $P2_1/c$	Monoclinic, $P2_1/c$
Temperature (K)	100	100	100	100	15
a, b, c (Å)	8.845 (3), 14.897 (5), 23.629 (8)	13.085 (2), 21.806 (4), 13.361 (2)	8.0378 (8), 13.8834 (13), 16.5650 (15)	8.000 (3), 21.723 (7), 20.764 (7)	13.5394 (9), 17.9754 (13), 15.4992 (10)
β (°)	100.233 (5)	110.615 (2)	96.774 (2), 100.237 (2), 93.746 (2)	100.927 (6)	90.557 (1)
V (Å^3)	3064.1 (18)	3568.3 (10)	1799.3 (3)	3543 (2)	3772.0 (4)
Z	4	4	2	4	4
Radiation type	Mo $K\alpha$	Mo $K\alpha$	Synchrotron, λ = 0.41328 Å	Mo $K\alpha$	Synchrotron, λ = 0.41328 Å
μ (mm^{-1})	2.67	3.52	0.30	0.53	0.41
Crystal size (mm)	0.03 × 0.02 × 0.01	0.08 × 0.07 × 0.05	0.12 × 0.01 × 0.01	0.04 × 0.02 × 0.02	not meas.
Data collection					
Radiation source	fine-focus sealed tube	fine-focus sealed tube	synchrotron	fine-focus sealed tube	synchrotron
Monochromator	graphite	graphite	diamond 1 1 1	graphite	diamond 1 1 1
T_{min}, T_{max}	0.924, 0.974	0.766, 0.844	0.965, 0.997	0.979, 0.989	0.950, 0.975
No. of measured, independent and observed [$I > 2\sigma(I)$] reflections	17853, 2931, 2601	54250, 6801, 5686	29174, 6421, 5122	33965, 6848, 5055	58533, 8085, 6476
R_{int}	0.080	0.055	0.050	0.098	0.081
$(\sin\theta/\lambda)_{max}$ (Å^{-1})	0.612	0.611		0.613	0.641
Refinement					
$R[F^2 > 2\sigma(F^2)]$, $wR(F^2)$, S	0.077, 0.221, 1.07	0.026, 0.057, 1.02	0.045, 0.110, 1.05	0.046, 0.104, 0.99	0.034, 0.080, 1.01
No. of reflections	2931	6801	6421	6848	8085
No. of parameters	189	396	466	425	460
No. of restraints	0	0	0	0	0
$\Delta\rho_{max}$, $\Delta\rho_{min}$ (e Å^{-3})	1.41, -1.43	0.92, -0.83	0.51, -0.36	0.26, -0.63	0.37, -0.37

Crystal Data	$(^{Br;\ H}_{Mes}L^{Mes})$FeCl(py)	$(^{Br}_{Mes}L^{Mes})$FeCl(py)	$(^{I}_{Mes}L^{Mes})$FeCl(py)·½C_6H_6	$(^{H}_{C_6F_5}L^{Mes})$FeCl(py)	$(^{Cl}_{C_6F_5}L^{Mes})$FeCl(py)
Chemical formula	$C_{41}H_{40}Br_2ClFeN_3$	$C_{41}H_{38}Br_4ClFeN_3$	$C_{44}H_{41}ClFeI_4N_3$	$C_{38}H_{31}ClF_5FeN_3$	$C_{38}H_{27}Cl_5F_5FeN_3$
M_r	825.88	983.68	1210.70	715.96	853.73
Crystal system, space group	Orthorhombic, $Cmc2_1$	Monoclinic, $P2_1/c$	Monoclinic, $P2_1/c$	Monoclinic, $P2_1/c$	Monoclinic, $P2_1/c$
Temperature (K)	100	100	100	100	50
a, b, c (Å)	14.184 (2), 16.142 (3), 16.242 (3)	13.662 (3), 18.202 (4), 15.660 (3)	13.679 (4), 20.177 (6), 17.012 (5)	14.3797 (11), 22.8598 (16), 10.4289 (8)	14.792 (2), 22.507 (3), 11.6134 (15)
β (°)	90	90.437 (4)	110.954 (4)	103.402 (1)	109.957 (3)
V (Å^3)	3718.6 (10)	3894.0 (14)	4385 (2)	3334.8 (4)	3634.1 (8)
Z	4	4	4	4	4
Radiation type	Mo $K\alpha$	Mo $K\alpha$	Mo $K\alpha$	Mo $K\alpha$	Synchrotron, λ = 0.44280 Å
μ (mm^{-1})	2.66	4.59	3.26	0.59	0.44
Crystal size (mm)	0.04 × 0.03 × 0.03	0.03 × 0.01 × 0.01	0.03 × 0.02 × 0.02	0.06 × 0.05 × 0.05	0.01 × 0.01 × 0.01
Data collection					
Radiation source	fine-focus sealed tube	fine-focus sealed tube	fine-focus sealed tube	fine-focus sealed tube	synchrotron
Monochromator	graphite	graphite	graphite	graphite	diamond 1 1 1
T_{min}, T_{max}	0.901, 0.925	0.875, 0.956	0.909, 0.938	0.965, 0.971	0.996, 0.996
No. of measured, independent and observed [$I > 2\sigma(I)$] reflections	27531, 3683, 3331	54273, 7681, 5309	65880, 8372, 6053	50124, 6344, 5029	41689, 6671, 4657
R_{int}	0.053	0.107	0.100	0.050	0.128
$(\sin\theta/\lambda)_{max}$ (Å^{-1})	0.611	0.618	0.611	0.611	0.611
Refinement					
$R[F^2 > 2\sigma(F^2)]$, $wR(F^2)$, S	0.025, 0.052, 1.04	0.041, 0.097, 1.01	0.035, 0.073, 1.00	0.033, 0.079, 1.03	0.045, 0.099, 1.01
No. of reflections	3683	7681	8372	6344	6671
No. of parameters	244	460	487	439	463
No. of restraints	1	0	0	0	0
$\Delta\rho_{max}$, $\Delta\rho_{min}$ (e Å^{-3})	0.23, -0.38	1.22, -0.63	0.80, -0.88	0.30, -0.36	0.44, -0.43
Absolute structure	Flack H D (1983), Acta Cryst. A39, 876-881				
Flack parameter	-0.005 (7)				

Crystal Data	$(^{Br}_{C_6F_5}L^{Mes})FeCl(py)$	$(^{I}_{Mes}L^{Mes})FeCl(OEt_2)$	$(^{H}_{Mes}L^{Q})MnCl(THF)$	$(^{H}_{Mes}L^{Q})CuCl$
Chemical formula	$C_{38}H_{27}Br_4ClF_5FeN_3$	$C_{40}H_{43}ClFeI_4N_2O$	$C_{70}H_{57}ClMnN_2O$	$C_{66}H_{49}ClCuN_2$
M_r	1031.57	1166.66	1032.57	969.06
Crystal system, space group	Monoclinic, $P2_1/c$	Monoclinic, $P2_1/n$	Monoclinic, $C2/c$	Monoclinic, $C2/c$
Temperature (K)	15	102	100	100
a, b, c (Å)	14.9860 (12), 22.2943 (19), 11.8486 (9)	13.139 (5), 22.930 (9), 15.371 (6)	36.126 (5), 18.734 (3), 20.883 (3)	34.093 (2), 17.7142 (12), 23.3196 (16)
β (°)	109.835 (2)	115.072 (6)	121.829 (2)	131.542 (1)
V (Å^3)	3723.8 (5)	4195 (3)	12008 (3)	10541.0 (13)
Z	4	4	8	8
Radiation type	Synchrotron, λ = 0.41328 Å	Mo $K\alpha$	Mo $K\alpha$	Mo $K\alpha$
μ (mm^{-1})	2.58	3.40	0.31	0.51
Crystal size (mm)	0.02 × 0.01 × 0.01	0.06 × 0.04 × 0.04	0.02 × 0.01 × 0.01	0.08 × 0.02 × 0.02
Data Collection				
Radiation source	synchrotron	fine-focus sealed tube	fine-focus sealed tube	fine-focus sealed tube
Monochromator	diamond 1 1 1	graphite	graphite	graphite
T_{min}, T_{max}	0.950, 0.975	0.822, 0.876	0.994, 0.997	0.961, 0.990
No. of measured, independent and observed [$I > 2\sigma(I)$] reflections	76550, 8050, 6037	60895, 7771, 5357	92395, 11420, 7830	66515, 10364, 6570
R_{int}	0.090	0.141	0.089	0.118
$(\sin\theta/\lambda)_{max}$ (Å^{-1})	0.642	0.612	0.611	0.617
Refinement				
$R[F^2 > 2\sigma(F^2)]$, $wR(F^2)$, S	0.036, 0.087, 1.06	0.032, 0.064, 0.91	0.048, 0.107, 1.05	0.049, 0.108, 1.01
No. of reflections	8050	7771	11420	10364
No. of parameters	475	453	679	634
No. of restraints	0	0	0	0
$\Delta\rho_{max}$, $\Delta\rho_{min}$ (e Å^{-3})	2.24, -0.82	0.64, -0.90	0.47, -0.37	0.96, -0.56

Crystal Data	$(^{H}_{Mes}L^{Q})Cu\cdot 3C_6H_6$	$(^{H;\,Me}_{DCP}L^{Me})_2Zn\cdot ½(OEt_2)$	$(^{H;\,Me}_{DCP}L^{Me})_2Mn$
Chemical formula	$C_{84}H_{67}CuN_2$	$C_{78}H_{39}Cl_8N_8O_{0.5}Zn_2$	$C_{38}H_{34}Cl_4MnN_4$
M_r	1167.94	1398.53	743.43
Crystal system, space group	Triclinic, $P\bar{1}$	Triclinic, $P\bar{1}$	Triclinic, $P\bar{1}$
Temperature (K)	100	100	293
a, b, c (Å)	12.446 (4), 14.203 (4), 20.614 (6)	15.2368 (2), 17.1536 (3), 17.4594 (3)	7.9767 (4), 14.3759 (7), 16.8151 (9)
β (°)	74.427 (5), 84.895 (5), 64.576 (5)	108.276 (1), 110.637 (1), 104.620 (1)	106.542 (1), 93.652 (1), 93.649 (1)
V (Å^3)	3168.6 (17)	3701.43 (10)	1837.91 (16)
Z	2	4	2
Radiation type	Mo $K\alpha$	Cu $K\alpha$	Mo $K\alpha$
μ (mm^{-1})	0.39	5.02	0.68
Crystal size (mm)	0.03 × 0.03 × 0.02	not measured	not measured
Data collection			
Radiation source	fine-focus sealed tube	fine-focus sealed tube	fine-focus sealed tube
Monochromator	graphite	graphite	graphite
T_{min}, T_{max}	0.988, 0.992		
No. of measured, independent and observed [$I > 2\sigma(I)$] reflections	48198, 12132, 7057	76551, 12110, 9613	26580, 6273, 5196
R_{int}	0.103	0.056	0.039
$(\sin\theta/\lambda)_{max}$ (Å^{-1})	0.613	0.593	0.589
Refinement			
$R[F^2 > 2\sigma(F^2)]$, $wR(F^2)$, S	0.058, 0.148, 1.01	0.038, 0.097, 1.03	0.091, 0.273, 1.05
No. of reflections	12132	12110	6273
No. of parameters	787	910	432
No. of restraints	0	0	0
$\Delta\rho_{max}$, $\Delta\rho_{min}$ (e Å^{-3})	0.82, -0.55	0.82, -0.47	6.85, -0.38